

Development of a nanofluidic particle size sorter and its biomedical applications

Inauguraldissertation

zur

Erlangung der Würde eines Doktors der Philosophie

vorgelegt der

Philosophisch-Naturwissenschaftlichen Fakultät

der Universität Basel

von

Thomas Mortelmans

Basel, 2022

Genehmigt von der Philosophisch-Naturwissenschaftlichen Fakultät auf
Antrag von

Prof. Dr. Roderick Lim

Dr. Yasin Ekinci

Prof. Dr. Richard Neher

Dr. Thomas Pfohl

Basel, den 21 Juni 2022

Prof. Dr. Marcel Mayor

Dekan

“Nothing in life is to be feared; it is only to be understood. Now is the time to understand more, so that we may fear less” – *Marie Curie*

Abstract

Immunoassays are methods that allow for highly specific and sensitive assessment of a large variety of analytes in different bio-fluids, such as cell lysate, serum, or urine. Unfortunately, conventional immunoassay-associated techniques are characterized by lengthy operational protocols, high-reagent consumption, and require the use of centralized laboratories. To this extent, micro- and nanofluidic devices have gained significant interest in biomedical research due to their rapid sample processing with precise fluid control and low volume requirements. Their reduced dimensions enable the miniaturization of the whole device for lab-on-a-chip applications. In typical two-dimensional microfluidic devices, the height of the channel (out-of-plane dimension) remains constant. However, a new degree of freedom is obtained when the height is varied, enabling more complex functionalities. Furthermore, traditional microfluidic devices, to operate, often require peripheral infrastructures, such as a syringe or pressure pump. This significantly hinders their portability and applicability in resource-limited environments.

The research presented within this doctoral dissertation investigated the use of micro- and nanofluidic systems with channel variations in all three dimensions to overcome the drawbacks of conventional laboratory-based immunoassays and those of active fluidic systems. More specifically, a thermoplastic device with a vertically tapered channel was developed for size-dependent separation and immobilization of bio-functionalized particles. The immobilized particles were, in turn, used for on-chip fluorescent immunosorbent assays in the framework of various biomedical applications. The device is passively operated to reduce operational requirements and uses surface-tension effects in conjunction with specialized capillary constructs to provide a steady, homogeneous, and reproducible liquid flow.

A key device component is its nano functionality in the vertical rather than lateral axis. This unique feature allows for low aspect ratio patterning, reduces resolution requirements, and greatly simplifies downstream fabrication processes. However, the integration of these uniquely defined fluidic geometries required the use and adaptation of state-of-the-art nanofabrication protocols. An in-depth experimental characterization of grayscale e-beam lithography (g-EBL) enabled highly controllable 3D structuring of the resist material with nanoscale topography variations but on the millimeter length scale. The accuracy of the adapted g-EBL protocol was used in conjunction with thermoplastic patterning methods, such as nanoimprint lithography and injection molding, to fabricate nanofluidic devices with extremely shallow channel dimensions in an upscalable and cost-effective manner. The developed process was optimized to go from device ideation to fluidic application within a single day, enabling rapid prototyping of various geometrical parameters.

The 3D fluidic devices were used to address various shortcomings in different biomedical applications. Firstly, as the doctoral research was performed during the COVID-19 pandemic, a critical technological development was the device's application toward rapid and quantifiable antibody detection. It was shown that the size-dependent particle trapping properties could be leveraged to perform multiplexed antibody detection of SARS-CoV-2 and Influenza A associated antibodies on distinctly functionalized particles with a high degree of sensitivity and specificity. The multiplexing capabilities of the device were extended by using secondary antibodies labeled with different fluorophores that targeted either short-term (IgM) or long-term (IgG) antibodies. This fluidic platform provided a viable alternative for the widely implemented rapid antibody and antigen tests, characterized by a limited sensitivity and only provided a binary (*yes/no*) result.

Furthermore, a major drawback of rapid antibody tests and their lab-based counterparts is their need for whole blood pre-processing and serum isolation. Such procedures can lengthen the performed assay and severely impact its sensitivity and specificity. This shortcoming was overcome by making the device compatible with whole blood on-chip immunoassays through the adaptation of the 3D channel profile. The latter enabled unhindered passage of the whole blood constituents, such as red blood cells. The fluidic assay could be read-out in less than 10 min and provided the same nanomolar sensitivity compared to a pure buffer solution.

Lastly, the multiplexed assay characteristics of the device were further extended by parallelizing different fluidic channels in the framework of sepsis diagnosis. More specifically, conventional culture methods are lengthy and, therefore, significantly decrease patient survivability. This is especially true for sepsis. A physiological hallmark of sepsis development is deregulated cytokine release, which can be used as a potential disease predictor to provide accelerated disease diagnosis. It was shown that by using individually loadable channels, five-fold concurrent cytokine detection was possible within a single field of view of the microscope. These devices were characterized by picomolar analyte sensitivity with reaction times less than 20 min.

The result of the doctoral research is a 3D fluidic device that overcomes many shortcomings in various immunoassay fields, ranging from viral antibody detection to cytokine quantification. Furthermore, its cost-effective fabrication facilitates bridging the gap between academia and industry to bring rapid, sensitive, and straightforward immunoassays from the lab to the patient's bedside. Its innovative and passive approach to size-dependent particle immobilization further paves the way for application in many biomedical research fields, ranging from neurology, hematology, and sports physiology.

Declaration

Self-Citations

During the course of my Ph.D. at the University of Basel and the Paul Scherrer Institute, two papers were published, and three are in preparation. All of these manuscripts, as well as a second author paper, are fully implemented in this thesis.

Chapter 2

Mortelmans, T.; Kazazis, D.; Guzenko, V. A.; Padeste, C.; Braun, T.; Stahlberg, H.; Li, X.; Ekinci, Y. Grayscale E-Beam Lithography: Effects of a Delayed Development for Well-Controlled 3D Patterning. *Microelectron. Eng.* **2020**, 225

Chapter 3

Ayhan F.; Mortelmans T.; Ekinci Y.; Kazazis D. Dry development of poly(methyl methacrylate), *in preparation*

Chapter 4

Mortelmans, T.; Kazazis, D.; Werder J.; Kristiansen P.M.; Ekinci, Y. Poly(methyl methacrylate) and cyclic olefin polymer injection molded 3D nanofluidic devices for particle sorting, *in preparation*

Chapter 5

Mortelmans, T.; Kazazis, D.; Padeste, C.; Berger, P.; Li, X.; Ekinci, Y. Poly(Methyl Methacrylate)-Based Nanofluidic Device for Rapid and Multiplexed Serological Antibody Detection of SARS-CoV-2. *ACS Appl. Nano Mater.* **2022**.

Chapter 6

Mortelmans, T.; Marty B.; Kazazis D.; Padeste, C.; Li X.; Ekinci, Y. A three-dimensional microfluidic capillary system for rapid on-bead multiplexed immunoassays in whole blood, *in preparation*

Chapter 7

Mortelmans, T.; Štefanić S.; Kazazis D.; Marty B.; Padeste C.; Li X.; Ekinci, Y. Multiplexed detection of cytokines in 3D nanofluidics with picomolar sensitivity, *in preparation*

Individual contributions

Thomas Mortelmans performed the nanofabrication, device design, and experiments. He performed the data analysis and made the scientific illustrations. Thomas wrote the doctoral thesis, paper manuscripts and co-authored the manuscript presented in Chapter 2 as the second author. Here, he contributed to the experimental design, e-beam exposures, and to the writing of the manuscript.

Furkan Ayhan was a master student supervised by Thomas Mortelmans and performed the experiments regarding the manuscript presented in Chapter 2. He also contributed to the writing of the associated manuscript.

Balz Marty was a master student supervised by Thomas Mortelmans and contributed experimentally to the results presented in Chapter 6 and Chapter 7.

Celestino Padeste, Philipp Berger, Dimitrios Kazazis, Xiaodan Li and Yasin Ekinci advised and guided the experiments. They provided insightful input, discussion, and co-authored publications.

Abbreviations

2D	Two dimensional
3D	Three dimensional
3D PEC	3D proximity effect correction
AFM	Atomic force microscopy
BSA	Bovine Serum Albumin
CET	Cryo-electron tomography
COC	Cyclic olefin copolymer
DOE	Diffraction optical elements
EBL	E-beam lithography
ELISA	Enzyme-linked immunosorbent assays
EDTA	Ethylenediaminetetraacetic acid
EUV	Extreme ultraviolet
FIBD	Focused ion-beam induced deposition
F.O.V.	Field-of-view
FLISA	Fluorescent immunosorbent assay
FT-IR	Fourier-transformation infrared spectroscopy
T _g	Glass transition temperature
g-EBL	Grayscale e-beam lithography
HRP	Horse Raddish Peroxidase
Ig	Immunoglobulin
ICP	Inductively coupled plasma
IPA	Isopropanol
IIM	Isothermal molding
LFA	Lateral flow assay
LOD	Limit-of-detection
MIBK	Methyl isobutyl ketone
PBS	Phosphate buffered saline

PMMA	Poly(methyl methacrylate)
POC	Point-of-care
PSF	Point-spread function
PDMS	Poly(dimethyl siloxane)
PVA	Poly(vinyl alcohol)
PS	Polystyrene
PEB	Post-exposure bake
PSA	Prostate specific antigen
RIE	Reactive ion-etching
ROC	Receiver operator characteristic analysis
RBD	Receptor binding domain
RBC	Red blood cell
Re	Reynolds Number
RMS	Root mean square roughness
SEM	Scanning electron microscopy
SPR	Surface plasmon resonance
t-SPL	Thermal scanning probe lithography
TEM	Transmission electron microscopy
UV	Ultraviolet
UV/O ₃	Ultraviolet/Ozone
VIM	Variothermal molding
XPS	X-ray photoelectron spectroscopy

Table of contents

Abstract	i
Declaration	iv
Abbreviations	vi
Table of contents	viii
1 Introduction	1
1.1 Motivation	2
1.2 Thesis outline and overview	3
1.3 Immunoassays	7
1.3.1 General overview	7
1.3.2 On-bead immunoassays	9
1.3.3 Lateral flow assays	11
1.4 Micro – and nanofluidics	15
1.4.1 History, background, and physical considerations	15
1.4.2 Bead-based microfluidic systems	17
1.4.3 Fluidic systems as point-of-care diagnostics	19
1.5 Fabrication methods	24
1.5.1 Optical and electron beam lithography	24
1.5.2 Grayscale patterning	27
1.5.3 Thermoplastic upscaling	29
2 Grayscale lithography for 3D patterning	34
2.1 Abstract	34
2.2 Introduction	35
2.3 Methods	36
2.3.1 Dose-response behavior of PMMA 950K	36
2.3.2 Grayscale electron beam lithography	37
2.3.3 Metrology	38

2.4	Results and discussion	39
2.4.1	Change in dose-response behavior over time	39
2.4.2	Influence of PEB on contrast curve of PMMA 950K	42
2.4.3	A practical example: changing a 3D shape by application of a PEB	44
2.5	Conclusion and outlook	46
2.6	Acknowledgments	46
3	<u>Dry development of poly(methyl methacrylate)</u>	48
3.1	Abstract	48
3.2	Introduction	49
3.3	Methods	52
3.3.1	Measurement of the plasma etch rate of PMMA	52
3.3.2	Pattern transfer to Si	54
3.4	Results and discussion	56
3.4.1	PMMA etch-rate dependence on electron dose	56
3.4.2	Dry development of PMMA and pattern transfer to Si	58
3.5	Conclusions	62
3.6	Acknowledgments	63
3.7	Author contributions	63
4	<u>Thermoplastic injection molding for nanofluidic device fabrication</u>	66
4.1	Abstract	66
4.2	Introduction	67
4.3	Experimental section	70
4.3.1	Grayscale e-beam lithography and nickel-shim fabrication	70
4.3.2	Injection molding and device bonding	71
4.3.3	Particle trapping experiments	73

4.4	Results and discussion	74
4.4.1	Geometry of 3D nanofluidic devices and injection molded parts	74
4.4.2	Pattern transfer fidelity and roughness transfer	76
4.4.3	Nanoparticle trapping in injection-molded fluidics	79
4.5	Conclusion and outlook	83
4.6	Acknowledgments	85
4.7	Author contributions	85
5	<u>A 3D nanofluidic device for SARS-CoV-2 antibody detection</u>	88
<hr/>		
5.1	Abstract	88
5.2	Introduction	89
5.3	Methods	90
5.3.1	Grayscale e-beam lithography	90
5.3.2	Nanofluidic master fabrication and nanoimprint lithography	91
5.3.3	Poly(vinyl alcohol) (PVA) functionalization and bonding	92
5.3.4	Trapping of calibration grade fluorescent polystyrene particles	92
5.3.5	Fluorescence microscopy	93
5.3.6	Preparation of Dynabeads M-280 and MyOne T1 with spike-RBD and hemagglutinin	93
5.3.7	Serological immunoassay – limit-of-detection and test validation	94
5.3.8	Antibody and disease multiplexing	96
5.4	Results and discussion	97
5.4.1	Design, fabrication, and functionalization of a 3D nanofluidic particle sorter	97
5.4.2	Size-dependent separation of a multi-particle mixture	101
5.4.3	Evaluation of on-chip capillary immunoassays for SARS-CoV-2 IgG antibodies	103
5.4.4	Test validation with COVID-19 patient serum	105
5.4.5	Multiplexed detection of SARS-CoV-2 IgG and IgM antibodies	107
5.4.6	Particle multiplexing for concurrent detection of SARS-CoV-2 and Influenza A antibodies	108

5.5	Conclusions	111
5.6	Supporting Information	113
5.7	Acknowledgments	113
5.8	Author contributions	113
6	<u>Multiplexed immunoassays in whole blood</u>	116
6.1	Abstract:	116
6.2	Introduction	117
6.3	Methods	120
6.3.1	Device design and grayscale e-beam patterning	120
6.3.2	Fabrication of daughter stamps and devices with nanoimprint lithography	120
6.3.3	Device functionalization and bonding	122
6.3.4	Capillary filling as a function of wedge profile	122
6.3.5	Bovine Serum Albumin (BSA) bead functionalization and pre-trapping	123
6.3.6	Time-lapse of BSA immunoassay	123
6.3.7	Limit-of-detection (LOD) of BSA antibodies	124
6.3.8	Multiplexed detection of horseradish peroxidase (HRP) and BSA in whole blood	125
6.4	Results and Discussion	127
6.4.1	Design of a capillary device with a 3D profile	127
6.4.2	Adapting the 3D channel profile for uninterrupted flow of whole blood	129
6.4.3	Preparation of 3D microfluidic devices to enable on-chip immunoassays	132
6.4.4	Rapid one-drop detection of anti-BSA antibodies directly in whole blood	134
6.4.5	On-chip immunoassays reveal a 2 nM limit-of-detection	136
6.4.6	Passive particle size-separation enabling facile two-fold multiplexed antibody detection	139
6.5	Conclusions and Outlook	142
6.6	Acknowledgments	144

6.7	Author contributions	144
7	<u>The power of one F.O.V.: five-fold concurrent cytokine detection</u>	146
7.1	Abstract	146
7.2	Introduction	147
7.3	Methods	150
7.3.1	Enzyme-linked immunosorbent assays	150
7.3.2	Fabrication of a 3D nanofluidic particle sorter	152
7.3.3	Trapping of calibration grade particles	153
7.3.4	Pre-trapping of bio-functionalized particles	153
7.3.5	On-chip limit-of-detection of cytokines	154
7.3.6	Multiplexed screening of cytokines with one field-of-view	154
7.4	Results and discussion	155
7.4.1	The geometry and operation of a multiplexed nanofluidic device	155
7.4.2	On-chip detection of cytokines with picomolar sensitivity	159
7.4.3	Five-fold multiplexed detection of cytokines with one micrograph	164
7.5	Conclusions and outlook	168
7.6	Acknowledgments	169
7.7	Author contributions	169
8	<u>Conclusions and outlook</u>	172
8.1	Conclusions and considerations	173
8.1.1	g-EBL exposed PMMA permits nanoscale topography control and dry development	173
8.1.2	Upscalable device fabrication is enabled via thermoplastic patterning	175
8.1.3	3D nanofluidic devices for viral antibody detection	176
8.1.4	Whole blood immunoassays through adaptation of channel topography	178
8.1.5	Three-dimensional multiplexing: color, size, and channel	179

8.2	Outlook	180
8.2.1	Mobile fluorescence detection	180
8.2.2	Further optimization of the nanofluidic devices	183
8.2.3	Biomedical applications	185
8.2.4	Alternate application of e-beam patterned fluidics: horizontal nanopores	187
8.3	Concluding statement	190
9	References	194
10	Publications	220
10.1	Publications in peer-reviewed journals	220
10.2	Publications in preparation	220
10.3	Annual reports	220
10.4	Poster presentations	221
10.5	Talks	222
11	Acknowledgments	224
12	Curriculum Vitae	231
13	Appendix	234

Introduction

1

1. Introduction

1.1 Motivation

The outbreak of SARS-CoV-2 highlighted the importance of point-of-care (POC) diagnostics, as well as reliable and cost-effective tests to monitor the viral spread and contain pandemics, epidemics, and endemics.¹⁻³ One of the most widely applied devices for rapid and cost-effective antibody or antigen detection is the lateral flow assay (LFA).^{4,5} This technology provided a viable and portable alternative to the more elaborate laboratory-based enzyme-linked immunosorbent assays (ELISA), which require large sample volumes and time-consuming procedures. Nevertheless, LFAs have several significant shortcomings, such as limited sensitivity, specificity,⁶ and control over sample flow⁷. Apart from disease diagnosis, immunoassays and immunosensors are widely used in various clinical and biomedical research fields.^{8,9} This evidences the need to miniaturize the lab on a chip to address the aforementioned shortcomings. To do so, micro and nanofluidics are of significant interest as their unique geometrical properties enable a high degree of control over the fluid flow profile¹⁰ and permit various schemes for multiplexed analyte detection.¹¹⁻¹⁴ Yet, most micro – and nanofluidic devices employ external syringes or pressure pumps, hindering their widespread usage. Consequently, devices which are purely self-powered by capillary forces are beneficial in increasing their portability and applicability.¹⁵⁻¹⁷

This thesis aims to explore the fabrication, characterization, and application of capillary-powered 3D nanofluidic devices in the framework of POC diagnostics and immunoassays. We developed a device that employs size-dependent immobilization of bio-functionalized particles to perform rapid and multiplexed on-chip fluorescent immunosorbent assays.

The presented device highly depends on the integration of various nanofabrication techniques, ranging from grayscale electron beam lithography to nanoimprint lithography and injection molding. To this extent, substantial

1.2. Thesis outline and overview

efforts went into fully exploring each avenue to develop not only a viable device but also to establish a fabrication process with nanoscale topography precision and a high degree of upscalability. Furthermore, the device was combined with a modular assay detection scheme that allows for a high reagent and target analyte flexibility.

The outcome of the presented work is an immunosensor that is low-cost (potentially less than a dollar in high-volume manufacturing), rapid (less than 10 minutes), multiplexed (up to 5 analytes at once), simple to use (passive operation), characterized by a high sensitivity (down to 100 pM) and is compatible with different biofluids (such as whole blood). The device developed during this doctoral research can pave the way for applications in a large variety of scientific fields, ranging from diagnostics to neurology and drug discovery.

1.2 Thesis outline and overview

In **Chapter 1**, the thesis structure is outlined, and the state of the research on immunoassays is discussed. Their working principle is summarized as well as relevant applications, such as ELISAs or LFAs. This is followed by an overview of their shortcomings and how innovative technologies, such as micro and nanofluidics, can overcome these. A short introduction to the history of microfluidics is given, and their relevant physical properties are discussed. Subsequently, the requirements for microfluidics to be applied in POC diagnostics and relevant design considerations are identified. The chapter is completed with an overview of the different fabrication methods used for micro and nanofluidics, ranging from conventional optical lithography to grayscale e-beam lithography and upscaling of device fabrication.

Chapter 2 discusses the use of grayscale e-beam lithography for precise 3D micro structuring of e-beam resist with a low contrast development scheme. An extensive experimental characterization of the resist's post-exposure behavior is presented. This explains, with a unified equation, how the resulting

1. Introduction

topography depends on the time between electron beam exposure and subsequent development (t_{ED}). It is shown that the greater the electron dose, the greater the dependence on t_{ED} . The equation also shows that at large t_{ED} -values little variation in pattern depth occurs. Lastly, the influence of temperature on pattern depth is shown via the application of a post-exposure bake.

In **Chapter 3**, the dry (plasma) development of grayscale exposed poly(methyl methacrylate) (PMMA) is described. It outlines how the PMMA etch rate is dose-dependent, enabling negative-tone processing. The required e-beam dose used for patterning is significantly lower in comparison to that of conventional negative-tone processing in a wet development scheme. This technique is also used to perform simultaneous development and pattern transfer into a silicon substrate by using an SF_6/O_2 -plasma. The practical implications of the dry development method are shown by the fabrication of binary and grayscale structures in silicon with only e-beam lithography and subsequent reactive ion etching.

In **Chapter 4**, it is explained how grayscale e-beam patterned resists may be used for the fabrication of a nickel shim to enable upscalable device fabrication in thermoplastic materials. The results show that due to the pattern transfer process, the pattern roughness decreases while the 3D profile is well maintained. The nickel shim was used to injection mold the nanofluidic devices into PMMA and cyclic olefin polymer (COP). To demonstrate the functionality of the injection molded devices, size-dependent trapping of five different particle sizes was performed while only requiring a 4 μ l sample volume. Lastly, the dependency of particle trapping position on material characteristics and its design implications are discussed.

Chapter 5 outlines the application of 3D nanofluidic devices for multiplexed detection of viral antibodies in patient serum. The device's geometrical layout, consisting of nanoscale topography variations on a millimeter length scale, is

described. Further, the required material functionalization is explained to perform size-dependent trapping of bio-functionalized nanoparticles. It is then shown how the functionalized devices can be used as an on-chip fluorescence-linked immunosorbent assay for highly sensitive and specific SARS-CoV-2 antibody detection. The particle size-sorting is subsequently used to extend the device's multiplexing capabilities to detect SARS-CoV-2 and Influenza A-related antibodies concurrently.

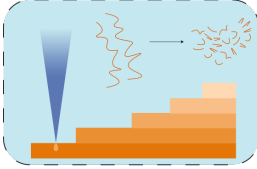
In **Chapter 6**, the pre-trapping of antigen-functionalized particles inside PMMA-based nanofluidic devices is discussed. Subsequently, it is shown how this enables rapid on-chip immunoassays, reaching nanomolar sensitivities in less than 10 minutes without washing steps. The 3D channel profile is subsequently modulated to allow for red blood cells to flow through the device, enabling whole blood immunoassays. It is demonstrated that the presence of red blood cells has no detrimental effect on the sensitivity of the assay.

Chapter 7 will highlight the use of a multiplexed 3D nanofluidic system for the detection the simultaneous detection of five cytokines with picomolar sensitivity. The device design and the relevant nanoparticle functionalization and pre-loading strategies are discussed. Lastly, the nanofluidic immunoassay is benchmarked against a conventional ELISA assay, and its shortcomings are considered.

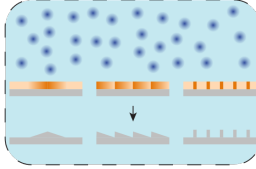
Finally, **Chapter 8**, will provide a short summary of the results presented in this thesis and an outlook on future applications and improvements of 3D nanofluidic immunoassays. Additionally, a brief discussion of another technology developed using the fabrication methods established in this thesis is given.

1. Introduction

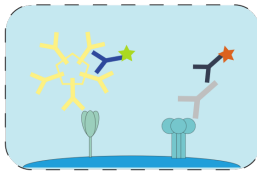
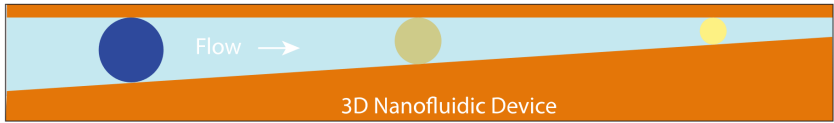
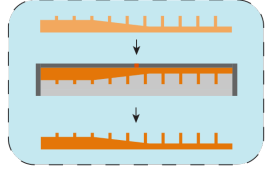
Chapter 2
Grayscale
E-beam Lithography



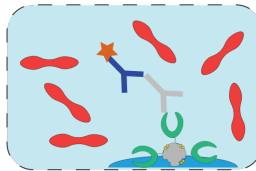
Chapter 3
Dry Development
of PMMA



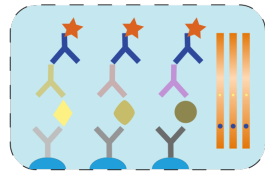
Chapter 4
Injection Molding
3D Nanofluidics



Chapter 5
Multiplexed
Antibody detection



Chapter 6
Whole blood
Immunoassays



Chapter 7
Rapid Cytokine
Quantification

1.3 Immunoassays

1.3.1 General overview

Immunoassays are biochemical methods that measure the presence, the concentration of biomolecules, or their specific binding using analyte (antigen) specific antibodies.^{9,12} Thanks to the highly specific molecular recognition capabilities, they have become one of the most popular test methods for many applications in medicine¹⁸, biomedical research¹⁴, forensics, and industrial production, such as in the food industry¹⁹. There are many different immunoassay approaches, but they can be generally classified into two distinct sub-classes: competitive and non-competitive assays. In the former, the analyte in the sample competes with a labeled analyte variant at a known concentration for antibody binding. The labeled analyte can either be added to the sample or pre-immobilized on a substrate surface (Fig. 1.1a).²⁰ When the labeled analyte is pre-immobilized, the sample is added directly onto the substrate together with detection antibodies containing a reporter molecule, such as a fluorophore. The detection antibodies will bind to both the pre-immobilized analytes on the surface as well as those in solution stemming from the sample. The higher the analyte concentration in the added sample, the lower the fraction of detection antibodies that will bind to the analyte on the substrate's surface. As a consequence, there is an inverse relationship between the obtained signal and sample antigen concentration.²¹ Alternatively, it is possible to perform non-competitive assaying (Fig. 1.1b).²² In this case, a sample is added to a substrate, and its biomolecules are immobilized on its surface. This can either be done electrostatically or via analyte-specific capture antibodies.¹⁴ Subsequently, a detection antibody that binds to the immobilized analyte is added to enable analyte quantification. Furthermore, in both sub-classes, it is possible to perform direct and indirect sensing of the analyte (Fig. 1c-d). In direct sensing, the primary antibody against the analyte is labeled with a reporter molecule, enabling immediate analysis. In indirect sensing, the primary antibody does not contain a reporter

1. Introduction

molecule and an additional step is required for analysis. More specifically, a secondary antibody labeled with a reporter molecule, specific for the host species of the primary antibody, is used. In doing so, an additional degree of amplification is obtained, resulting in a higher sensitivity.⁹ In the presented work, non-competitive indirect immunoassays are used in an on-chip and on-bead format.

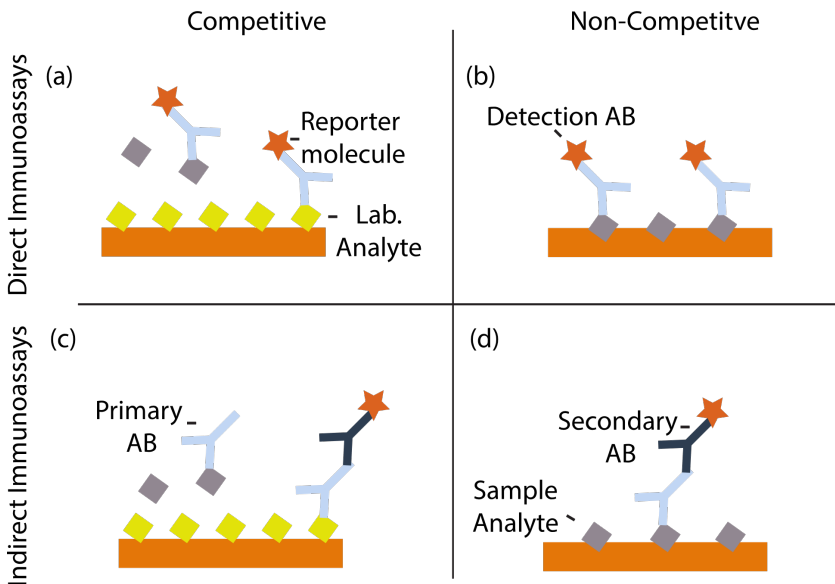


Figure 1.1. Overview of different immunoassays. (a) *Direct competitive immunoassay.* A labeled or known amount of antigen is immobilized on the substrate's surface. The sample, as well as a detection antibody, are added onto the substrate. The detection antibody will bind to both the antigen on the substrate's surface and that originating from the sample in solution. (b) *direct non-competitive immunoassays.* The analyte is immobilized on top of the surface of the substrate. This can be detected using a detection antibody conjugated with a reporter molecule. (c) *Indirect competitive immunoassays.* The sample, together with a primary unlabeled antibody, is added to the substrate. After washing, the substrate is incubated with a secondary detection antibody conjugated with a reporter molecule. (d) *Indirect non-competitive assay.* Analyte detection through the combination of a primary and secondary antibody.

1.3. Immunoassays

Additionally, the assay's read-out mechanism can be based on different biophysical and biochemical processes, such as enzyme-linked immunosorbent assays (ELISA)⁸, fluorescence-linked immunosorbent assays, or fluoroimmunoassay (FLISA)²³ and chemiluminescent immunoassays²⁴. The enzymatic amplification step of ELISAs makes it the most extensively used technique in medical laboratories.²⁵ The signal amplification step enables ELISA to detect analytes in the picomolar regime²⁶, allowing for quantitative monitoring of several biomarkers, such as cytokines, with low homeostatic concentrations.²⁷ Its colorimetric-based read-out mechanism also requires less advanced infrastructure in comparison to alternative immunosorbent assays such as the FLISA.²⁸ However, even though ELISA is the gold standard regarding sensitivity and specificity, it requires large sample volumes and offers little multiplexed analyte detection.

1.3.2 On-bead immunoassays

To overcome the drawbacks of conventional laboratory-based immunoassays, bead-based assays have attracted increasing attention. They enable the surface functionalization and washing steps to be greatly simplified. Additionally, they provide an increased sample (surface) to volume ratio and sample concentration capabilities. This results in immunoassays with reduced fluid requirements, increased throughput, and ameliorated the limit of detection.^{29,30} For example, the use of (nano)beads consisting of polymeric brushes has been shown to enable a 270-fold improvement in detection limit as compared to standard ELISA.³¹ Most importantly, they offer simple multiplexing advantages, in which concurrent measurement of multiple analytes from a single sample is performed.³² Bead-based immunoassays exist in various forms, of which surface coverage assays are most widely implemented due to their ease of functionalization, cost-effectiveness, and facile operation.³³ However, the use of solid surfaces can have unwanted effects, such as fouling and inefficient analyte diffusion. To this extent,

1. Introduction

alternate methods, such as homogenous solution bead-based assays, have been extensively developed over the last decades.³⁴

The most commercially successful example of this assay type is the Luminex technology.^{35–37} This platform uses polystyrene particles of similar sizes with different internalized dye concentrations to give them a distinct color. Each color represents a distinct functionalization with an analyte-specific capture antibody. This enables simultaneous detection of 100 different analytes (Fig. 1.2).

The Luminex experimental protocol involves sequential incubation, washing, and labeling steps, which makes it largely similar to that of conventional ELISA and FLISA. Once the assay is completed, the beads are injected into a flow cytometer, where two lasers simultaneously detect the bead color (analyte identification) as well as the fluorescence of the reporter molecule (test outcome). The use of a flow cytometer for read-out makes the technology expensive and not widely applicable. Due to this, it has been mostly applied and validated in human medicine, but it has yet to breakthrough in other fields, such as the food and animal industry.³⁸ Moreover, flow cytometry is a standalone system, which hampers its integration into a total analysis system.

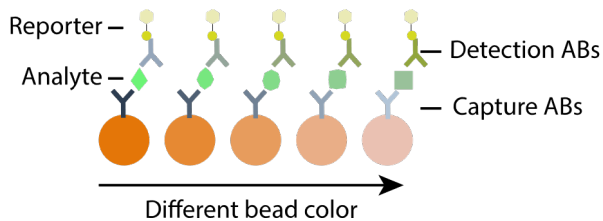


Figure 1.2. Luminex-assay principle. Beads of similar size but different colors are functionalized with capture antibodies against different analytes. A sandwich assay is performed by the addition of analyte-specific detection antibodies containing a biotin moiety. The latter functions as a substrate for a streptavidin-phycoerythrin complex, functioning as a reporter molecule.

1.3. Immunoassays

1.3.3 Lateral flow assays

Nevertheless, even though they offer exciting multiplexing possibilities, bead-based immunoassays share many shortcomings with conventional lab-based assays, such as their lengthy and cumbersome protocol, high reagent consumption, and large required sample volume (> 100 μL). These inherently limit the application of these techniques in resource-limited environments or when rapid disease diagnosis is needed.³⁹ Thus, a more portable, simplistic, and low-cost detection method has been developed in the form of a so-called lateral flow immunoassay (LFA). The technology also uses antibodies as a detection method but does so in a compacted paper-based format (Fig. 1.3a). An LFA typically consists of several different components mounted on a backing card. Firstly, the sample is added to the sample pad. Here, surfactants and buffer salts prepare the solution for further processing steps. Afterward, the sample flows through the conjugate pad, releasing analyte-specific antibodies conjugated with colloidal gold nanoparticles. The nanoparticles enable optical (i.e. by eye) detection of the antibody-antigen binding interaction. To prevent electrostatic interaction of the gold nanoparticles with the sample or other LFA components, they are usually pre-blocked with bovine serum albumin (BSA).⁴⁰ Subsequently, the flow will continue along the nitrocellulose-based membrane. This membrane contains two distinctly functionalized areas: the test and control lines. The former contains analyte-specific antibodies that enable the capturing of the detection of the antibody-analyte complex. The latter consists of antibodies specific to the host species of the detection antibodies, e.g. anti-goat or anti-mouse. Therefore, the gold nanoparticle conjugated detection antibody should always be immobilized at this position. An absorbent pad is included at the end of the test to enable a continuous fluid flow.⁴¹ After a supplier specified incubation period, the possible test outcomes are positive (Fig. 1.3b), negative (Fig. 1.3c) or invalid (Fig. 1.3d).

1. Introduction

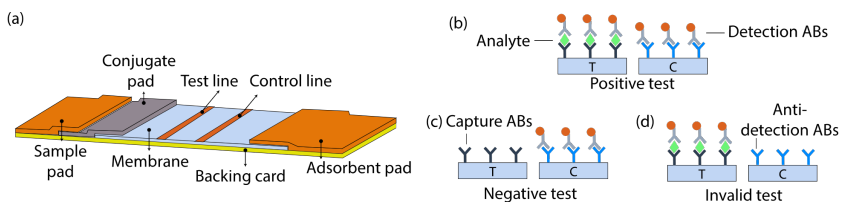


Figure 1.3. Lateral flow assays. (a) A schematic overview of the various components in an LFA test strip. The LFA-test can be read-out in three different ways: positive (b), negative (c), or invalid (d).

Unfortunately, LFAs have low sensitivities (i.e., μM to nM ^{42–44}), meaning a negative result can also represent a sub-threshold antigen (analyte) concentration. This significantly hampers the use of LFAs for early-stage disease recognition.⁴⁵ To address this, several alternate LFA-based methods were developed with increased sensitivity or multiplexing capabilities to detect several diseases simultaneously.^{45–48} A major review of these developments is outside of the scope of this work, but several exciting improvements are highlighted. For example, in the field of colorimetric (or conventional) LFAs (Fig. 1.4a), dual-labelling has been reported as a viable signal amplification method to improve the LOD by several orders of magnitude (Fig. 1.4b).^{49,50} This is an elegant solution that circumvents the use of larger gold nanoparticles, which are inherently unstable and aggregate after several days.⁵¹ In the work of Mei et al., the BSA-blocking step of the gold nanoparticles was leveraged as an additional target for secondary anti-BSA antibodies conjugated with gold nanoparticles. Hence, the gold nanoparticle density for a given analyte concentration is increased, leading to an elevated optical density.

Interestingly, recent developments have shown that alternate gold nanoparticle morphologies, such as gold nano-popcorns, offer advantages over conventional nanospheres. These popcorn-like particles are hierarchical structures with multiple rough edges. This unique geometry gives rise to different surface plasmon resonance (SPR) properties and effectively

1.3. Immunoassays

enhances their optical contrast. This phenomenon was used by Serebrennikova et al. to achieve a five-fold improvement in the LOD for procalcitonin (a biomarker for bacterial infections) compared to a gold nanosphere-based LFA.⁵² Furthermore, it is possible to use the immobilized gold nanoparticles as a catalyst for the reduction of metal ions, such as silver, in a post-assay treatment step. In doing so, the nanoparticles serve as a nucleation site for silver growth and enable particle enlargement. Consequently, the contrast is improved even further. This was used by Rodriguez et al. for a three-fold amelioration of the LOD in an LFA for prostate specific antigen (PSA).⁵³

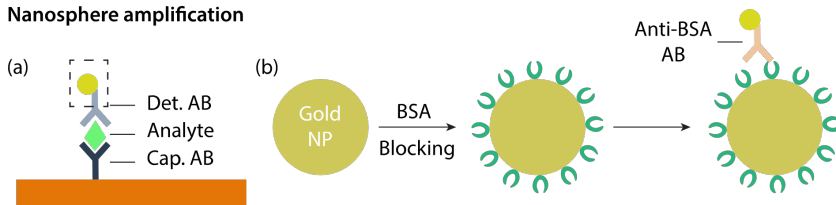
Alternatively, other metals, such as IrO₂, have recently gained increasing attention due to their better optical contrast in comparison to gold nanospheres.⁵⁴ Also, other nanomaterials, such as graphene oxide⁵⁵ and carbon nanotubes⁵⁶ have been used to push the limits of colorimetric LFAs. They are highly stable, are characterized by a large surface area, and can be easily synthesized and functionalized.⁵⁷

Furthermore, rather than improving the LOD of LFAs with signal amplification or contrast enhancement methods, it is possible to use a different read-out mechanism to increase the assay's performance further. The most relevant to the presented work is fluorescence-based detection. This technique is characterized by an ameliorated signal-to-noise ratio, sensitivity, and signal linearity compared to colorimetric assaying and allows for signal quantification.⁵⁸ To enable analyte detection, the employed detection antibody is conjugated with a fluorescent molecule rather than a gold nanosphere. This molecule can be controllably excited by light of a specific wavelength, after which light of a longer wavelength is emitted. The emitted light can be subsequently filtered out by advanced optics before it reaches the detector.⁵⁹ Usually, this means that LFA read-out requires a centralized laboratory with benchtop fluorescent readers. However, various portable fluorescent read-out systems have been developed over the last few years to enable cost-effective

1. Introduction

and rapid analysis of the test and control lines, such as smartphone-based fluorescence microscopy.^{58,60} Furthermore, other fluorescent nanomaterials, such as quantum dots, offer superior brightness and photostability over conventional organic dyes. This pushed LFA-based detection to the femtomolar range.⁶¹

Nanosphere amplification



Material enhancement

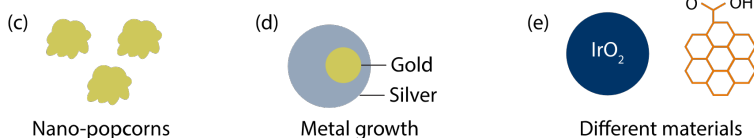


Figure 1.4. Overview of advances in lateral flow assays. (a) Classical LFA gold nanosphere detection mechanism. (b) Secondary labeling with an anti-BSA gold nanoparticle conjugated antibody allows for signal amplification due to increased optical density (c) Nano-popcorns are characterized by unique SPR properties, enabling geometrically induced contrast enhancement (d) Gold nanoparticle induced silver reduction and subsequent nucleation allow for localized post-assay particle growth (e) Different materials such as Iridium Oxide or Graphene Oxide offer exciting advantages over gold nanospheres.

Despite the noteworthy developments regarding their sensitivity and read-out mechanisms, the traditional gold nanosphere-based LFAs remained the dominant choice during the SARS-CoV-2 pandemic attributable to their low costs and ease of use.⁶²

Moreover, gold nanosphere LFAs, albeit portable and cost-effective, offer little multiplexing capabilities or quantitative read-out. As such, it is of interest to

1.4. Micro – and nanofluidics

combine their advantages with other technologies, like bead-based platforms, to bring lab-grade immunoassays to the patient's bedside and address an unmet need in the current diagnostic landscape. A possible candidate to do so are micro- and nanofluidic-based detection systems and devices. This technology allows for the integration and miniaturization of various laboratory handlings while reducing incubation times, enabling precise and controlled fluid manipulations and different multiplexing strategies.²⁹

1.4 Micro – and nanofluidics

1.4.1 History, background, and physical considerations

In the 1950s, powered by advances in the semiconductor industry, there was a large interest to design miniaturized analytical and electrical systems. This led to the development of photolithography, coming from the Greek *photo*, *lithos*, and *graphia*, which respectively translate into 'light', 'stone', and 'writing'. Essentially, light was used to write microscopical features onto a solid crystalline material. It was because of these efforts that researchers at Stanford University in the 1970s were able to fabricate a miniaturized gas chromatography system on a silicon wafer.⁶³ This was later extended by Andreas Manz at Ciba in Basel to fully integrate an entire laboratory system on a chip and gave it the well-known name of "total chemical analysis systems" or μ -TAS.⁶⁴

In conjunction with the development of photolithography, one of the driving forces behind the widespread adaptation of the micro – and nanofluidic systems can be attributed to the introduction of poly(dimethyl siloxane) (PDMS) as a suitable material by Georges Whitesides and David Duffy in 1998.⁶⁵ The hardware required to fabricate PDMS-based devices is relatively low-cost and can be integrated into a small laboratory. This made the technology widely accessible. Moreover, PDMS has several favorable properties that allow for implementation in various fields, such as low interfacial energy, chemical inertness and high thermal stability.⁶⁶

1. Introduction

Over the last decades, the technology has significantly matured, and the benefit of micro- and nanofluidic devices is widely recognized in numerous scientific areas. These devices provide promising and innovative solutions for simple reagent delivery and handling of small sample volumes while simultaneously reducing contamination, minimizing analysis times, providing signal amplification, and portable solutions and multiplexed analysis.^{67,68} Furthermore, in many cases, such as that of on-chip immunoassays, the reduced device dimensions and the microscopically small detection volume result in an extremely localized signal while retaining a low background.^{69,70}

To fully appreciate the benefit of micro- and nanofluidic systems, it is necessary to briefly discuss some of the relevant physical equations. Firstly, one of the most important numbers that serve as an indication of the flow pattern in these systems is the Reynolds Number (Re)⁷¹:

$$Re = \frac{\rho v L}{\mu} \quad (1)$$

where ρ is the fluid density, v is the velocity, L is the characteristic linear dimension, and μ is the dynamic viscosity. Fundamentally, what it describes is the ratio of the inertial to viscous forces. From the equation, it can be deduced that upon a reduction of L , the Reynolds Number will decrease. It is generally accepted that when $Re > 4000$, the system is characterized by a so-called turbulent flow, and when $Re < 2000$, laminar flow occurs.⁷² Due to the small size of microfluidic systems, their Re values are usually less than < 100 , meaning laminar flow is dominant.¹⁰ This has several advantages over turbulent flow, such as controllable fluid flow behavior and dominant diffusive mixing behavior. Consequently, reaction kinetics in microfluidic systems become highly predictable.⁷² The diffusion time of molecules inside these fluidic channels can be approximated by the following equation⁷³:

1.4. Micro – and nanofluidics

$$t \approx \frac{x^2}{2D} \quad (2)$$

Here, x is the distance traveled by a molecule along a certain axis after time t . The associated molecular diffusion constant is given by D . This implies that for molecules with the same diffusion constant, the diffusion time scales with the square of the traveled distance. Therefore, upon reduction of the device dimensions, the time it takes for molecules to diffuse across a characteristic device dimension is reduced, leading to accelerated reaction times. Theoretically, this would imply that devices with smaller dimensions are more favored due to enhanced mixing properties and reaction kinetics. Nevertheless, several geometrical and practical constraints exist and should be taken into consideration when designing micro – and nanofluidic devices. For example, fluidic resistivity increases with a cubic dependency as the channel height decreases, drastically decreasing the flow rate.⁷⁴ Furthermore, as will be discussed in the main body of this thesis, the fabrication of devices with a sub-micron height is a challenging endeavor.

1.4.2 Bead-based microfluidic systems

As previously mentioned, it would be of interest to use microfluidic systems to increase the portability of multiplexed bead-based assays. To do so, beads can be integrated into microfluidic devices as solid support structures, offering a significant amplification of the bio-functionalized surface-to-volume ratio.³⁰ In order to function as an integrated analyte capture support, the beads need to be appropriately functionalized, with either disease-specific antigens⁷⁵ (Fig. 1.5a) or analyte-specific capture antibodies⁷⁶ (Fig. 1.5b). This can be done by using a variety of modification strategies, such as covalent attachment through surface-modified or pre-activated bead surfaces. However, these are either characterized by low particle stability or low coupling specificity, hampering their applicability in microfluidic systems.⁷⁷ In this regard, bio-activated surfaces offer an attractive substitute. For example, the

1. Introduction

streptavidin-biotin system has been widely applied for the bio-functionalization of beads. Herein, the beads are conjugated with streptavidin, a tetrameric protein of bacterial origin.⁷⁸ Streptavidin has a high binding affinity for biotin attributable to the formation of hydrogen bridges, sulfur and hydroxyl interactions, and partial protein re-organization.⁷⁹ This makes the streptavidin-biotin complex one of the strongest non-covalent biological binding interactions.⁸⁰ Moreover, it makes the functionalization of streptavidin-coated beads highly selective and straightforward. One just needs to add a biotinylated reagent (e.g. antibody or antigen) to a bead-containing solution and mix properly.¹¹ This gives streptavidin-based bead functionalization a plug-and-play approach, offering a high degree of flexibility and customizability.

Once the particles are correctly prepared, they need to be controllably immobilized or trapped. A variety of techniques to do so exist, of which two are briefly highlighted. Firstly, if magnetic beads are employed, it is possible to use magnetic field modulation to locally trap the particles in the flow path (Fig. 1.5c). Microfluidic devices utilizing this method have been shown to reach a picomolar LOD for rapid cytokine screening.⁸¹ As an additional advantage, it is possible to move the magnetic field during device operation to increase the washing efficiency after labeling.⁸² Nevertheless, the pre-requisite that the particles should be magnetic poses a significant constraint on available particle sizes and properties. Hence, microfluidic devices which use less material-dependent particle trapping methods, such as geometrical trapping (Fig. 1.5d), are favored. This can be done by placing constricting posts⁷ or lines⁸³ smaller than the employed particle size in the flow path. By using a separate inflow path for the functionalized particles, it is possible to integrate multiple particle trapping positions in a single device. In doing so, one can perform on-device bead-based multiplexed immunoassays. This method has been leveraged to perform FLISA-based detection of a cardiac biomarker at an LOD of 150 pM after an incubation period of 45 min.⁷ Yet, even though this

1.4. Micro – and nanofluidics

method is highly versatile, it requires sequential loading of particle sizes, reducing its ease of use. To this extent, the idea of the device presented in this thesis was to perform geometrical particle trapping with a single inlet. A more in-depth explanation of the ideal device is given in sub-chapter 1.4.3.

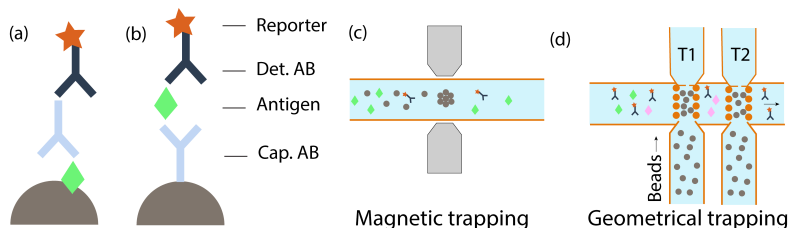


Figure 1.5. Bead-based microfluidic immunoassays. Schematic representation of antibody (a) and antigen (b) screening. (c) Magnetic trapping of functionalized particles (gray) (d) Two-inflow system for geometrical particle trapping. T1 performs an assay for analyte X, whereas T2 screens for analyte Y.

The above discussion showed that the combination of microfluidics and bead-based assays offers a large degree of flexibility concerning analyte choice, trapping mechanisms, and read-out system. This makes them an ideal candidate to contribute to the POC diagnostic landscape to rapidly and cost-effectively screen for a large variety of biomarkers in a multiplexed and facile manner.

1.4.3 Fluidic systems as point-of-care diagnostics

POC tests are diagnostic tools that do not necessitate central laboratories or advanced equipment and can be performed without trained personnel. To this extent, they must be simple to use, rapid, and have a high degree of portability.⁸⁴ Furthermore, they must be inexpensive and compatible with low sample volumes so that they can be applied in resource-limited environments.⁴⁴ These requirements fit well with the characteristics of micro- and nanofluidic analysis systems as they allow for facile integration of the lab

1. Introduction

on a chip.⁸⁵ However, a significant drawback that hampers the use of microfluidic systems as POC tests is that they often require large peripheral infrastructure. For example, pressure or syringe pumps are commonly used to control the fluid flow, whereas advanced electronics are needed to perform signal acquisition and analysis. This is not only costly but significantly decreases the portability of these miniaturized systems.⁸⁶ Consequently, so-called self-powered microfluidics are of interest. These systems make use of capillary effects to manipulate and direct fluid movement with a high degree of control. These effects originate from the surface tension of a liquid, the channel geometry, and the surface chemistry of the device material.⁸⁷ Thus, by changing the geometry throughout the device, one can intelligently design passive devices without the need for real-time flow control. An example of such a device design and its various components is given in Figure 1.6. Here, several important microfluidic elements are highlighted.

Firstly, the inflow (I-1) serves as a port to add samples onto the chip's surface. Usually, before entering the main fluidic channel, a valve is placed to modulate the capillary pressure to reduce liquid backflow. After the fluid enters the main channel, it can trigger the release of a liquid that can be pre-loaded in a reservoir compartment (I-2). Pre-mature flow from the reservoir into the main channel is prevented by a retention valve (ret. valve) with a higher capillary pressure. The liquid stored in the reservoir can be used to deliver the required detection antibodies into the system in a controlled and reliable manner. In doing so, a true one-step immunoassay can be performed.

Afterward, the fluid typically moves through a resistor section, which is used to further control the capillary pressure within the device by providing a pressure drop. Moreover, as the flow in a microfluidic environment is laminar, mixing of the sample in a microfluidic device is largely based on diffusive processes. For this reason, a fluidic resistor can be included not only as an additional flow control mechanism but also as a mixer.⁸⁸ Once properly mixed, the liquid, now consisting of the sample and detection antibodies, will pass

into the assaying area. Here, depending on the immunoassay format, it is possible to screen for either disease-specific antibodies by pre-patterning antigens or for specific analytes (antigens) by employing capture antibodies. In addition to performing immunoassays on-chip, it also is possible to perform DNA-based biosensing, but this is outside the scope of the thesis.⁸⁹ For fluid to continuously flow over the assay area, a steady flow rate is required. As a result, most capillary-based devices contain integrated capillary pumps. These are usually an array of densely packed structures to provide a sufficiently high capillary pressure to enable fluid flow while simultaneously enabling a large filling capacity.⁹⁰

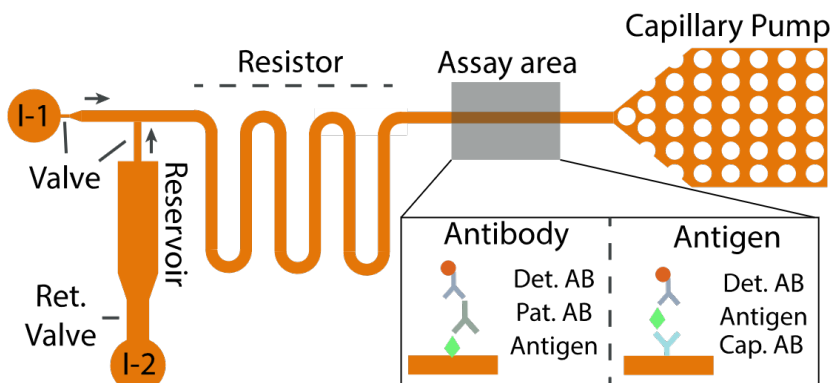


Figure 1.6. Microfluidic POC-test and its various components. Adapted with permission from Olanrewaju et al.⁷⁴

Capillary-powered POC-microfluidic devices have been used to detect various analytes rapidly and quantitatively and have translated into commercial applications. For example, Gervais et al. developed a microfluidic device to detect a cardiac biomarker at an LOD of 8 pM within 14 min. Their device remained stable up to 6 months after fabrication.¹⁶ This innovation directly led to the foundation of 1Drop Diagnostics, that now offers multiplexed detection of biomarkers in capillary whole blood.⁹¹ Likewise, efforts towards the combination of capillary micro- and nanofluidics by Durand et al.^{92,93} laid the

1. Introduction

foundation for Abionic, a multi-million dollar enterprise offering simultaneous detection of 14 biomarkers in under 5 minutes.⁹⁴ The unique combination of both fluidic regimens in capillary-based devices facilitated sub-picomolar detection of ferritin in human plasma without the need for a washing step.⁹⁵

Nevertheless, a drawback of such autonomous systems is that once device fabrication is finalized, there is no possibility to further adapt the flow path. This means that new devices and prototypes have to be developed for each alteration to screen for the influence of different fabrication or assay parameters. Moreover, a method to assess the flow properties inside the device is usually absent. This is important as fabrication defects that are not visible by the naked eye might lead to complications such as fluidic shortcutting⁹⁶ or corner-flow⁹⁷, effectively invalidating the performed assay. In this regard, it is important to mention recent developments by the research group of Emmanuel Delamarche at IBM. Here, they intelligently include abrupt height differences inside a fluidic channel to stop the fluid flow at pre-defined points due to pinning effects. These pinning points are coated with an electrically conducting material, to which a voltage can be applied. Upon the application of a voltage, electro-wetting can be triggered to overcome the pinning effect and enable continued fluid flow. This principle can be leveraged to design unique flow paths via a smartphone-based application within the same portable device. This yields a high degree of post-fabrication control over the flow. Also, the inclusion of electrically conducting elements enables flow monitoring through capacitance changes inside the devices and is provided in real-time.⁹⁸ This is an excellent example of how height control is of the utmost importance in capillary microfluidic systems and how this enables more advanced and precise fluid manipulations.

The height modulation presented by Delamarche et al. is binary, rather than a gradual modulation. The core idea of this thesis is to fabricate topographically changing nano – and microfluidic channels to perform size-dependent particle immobilization. These particles can be, in turn, used to

perform multiplexed immunoassays on three distinct levels (Fig. 1.7). Firstly, it is possible to perform color multiplexing via the use of uniquely labeled (green/red) detection antibodies. In such a way, it is possible to detect short-term (IgM) and long-term (IgG) antibodies on a single immobilized particle. Secondly, each particle size can be used to perform a distinct immunoassay, e.g. for different diseases. Thirdly, by placing 3D fluidic channels next to each other, it is possible to perform parallelized multiplexed immunoassays.

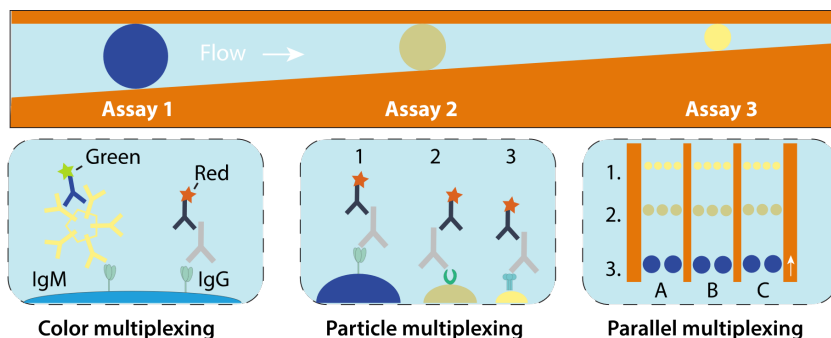


Figure 1.7. Multiplexed immunoassays in a 3D nanofluidic device.

Color multiplexing is used in **Chapter 5** to perform a FLISA for short-term (IgM) and long-term (IgG) SARS-CoV-2 antibodies in patient serum. This is subsequently extended by particle multiplexing to detect COVID-19 and Influenza A antibodies concurrently.

However, before serum can be used for immunoassays, as in Chapter 5, it needs to be obtained from whole blood. More specifically, whole blood needs to undergo external device treatment to rid the bio-fluid of cellular material, such as red blood cells (RBCs). Sample handlings outside the device are unwanted as they decrease its portability and application in resource-limited environments. Therefore, conventional POC-diagnostic tests, such as LFAs, are usually equipped with a filter membrane that enables the removal of cellular material on-chip. Unfortunately, due to electrostatic interactions, this

1. Introduction

filter membrane can retain up to 30% of the analyte or antibody under investigation, negatively impacting the performance of the assay.^{99,100} To this extent, we adapted the 3D profile in our nanofluidic device to make it compatible with whole blood immunoassays, reaching nanomolar sensitivities within 10 minutes. These results are reported in-depth in Chapter 6.

Lastly, parallel multiplexing is shown in Chapter 7, where simultaneous five-fold detection of biomarkers (cytokines) is performed within a single field-of-view of the microscope. The performed assay reached picomolar sensitivities within 20 minutes and was benchmarked against a conventional laboratory-based ELISA test.

1.5 Fabrication methods

A large part of the doctoral research was devoted to the development of a fabrication protocol that would enable nanoscale height control over a millimeter length scale while retaining the upscalability of device production for high volume manufacturing. Hence, it is of relevance to introduce conventional lithographic methods as well as grayscale patterning and the employed thermoplastic fabrication methods.

1.5.1 Optical and electron beam lithography

After the second world war, computational methods became ever more important. However, these methods primarily relied on vacuum tubes to control electronic circuits and elements (transistors). Consequently, the more complex the required numerical operations, the greater the complexity of the employed systems. For example, the first digital computer contained more than 17.000 vacuum tubes, greatly increasing possible downtime in case of errors, power consumption, and the physical system size.¹⁰¹ To this extent, the idea of system integration of these various elements on a single chip attracted an increasing amount of attention, leading to the development of the integrated circuit (IC) in 1959.¹⁰² In an IC, various electrical circuits are

1.5. Fabrication methods

patterned on a piece of semiconductor wafer. A key technology enabling this development was photolithography. In this process, a substrate, usually a silicon wafer, is spin-coated with a photo-sensitive material ('photoresist'). Subsequently, ultraviolet (UV) light passes through a mask containing transparent and opaque sections, defining the geometrical features of interest. The UV exposure induces a solubility switch of the photoresist in a so-called developer solution. Depending on resist type, the exposed areas are removed (positive-tone) or remain (negative-tone) on the silicon wafer. Afterward, this pattern can be transferred into the bulk material via a variety of etching strategies, aptly called pattern transfer (Fig. 1.8).¹⁰³ Via the use of projection optics, it is possible to further decrease the pattern size with respect to their size on the photomask. This, in turn, increases the number of attainable transistors on a given surface area. Ultimately, the minimum obtainable feature size is determined by the Rayleigh diffraction limit, restricting the smallest printable patterns to half the wavelength of the employed light source.¹⁰⁴ This has pushed the lithographical field to the use of extreme-ultraviolet (EUV) light at a wavelength of 13.5 nm.¹⁰⁵⁻¹⁰⁷

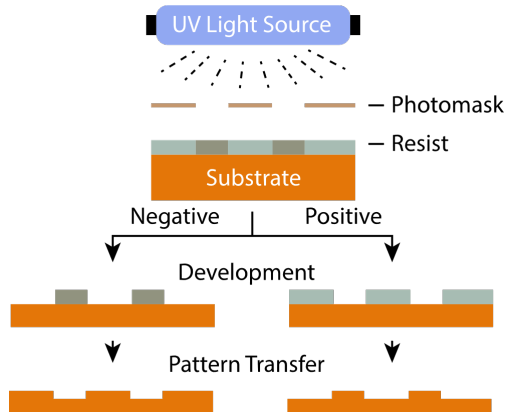


Figure 1.8. Overview of the photolithography process.

1. Introduction

Yet, a major drawback of conventional optical lithography is that a novel mask needs to be fabricated for each new pattern geometry, which is cumbersome, costly, and time-consuming. To this extent, maskless techniques have been developed that enable direct modification of a resist material. Examples of these techniques are laser lithography¹⁰⁸, thermal probe scanning lithography¹⁰⁹, focused ion beam systems¹¹⁰, or e-beam lithography¹¹¹. The latter has a significantly better resolution than optical systems, but as a single Gaussian electron beam is used for patterning, it is significantly slower.¹¹² Even so, it offers significant flexibility over pattern design. Instead of lenses, as with optical lithography, a beam deflection system containing a series of electromagnets is used to position and focus the incident electron beam on top of the sample's surface (Fig. 1.9a).¹¹³ The sample is coated with an e-beam resist, such as poly(methyl methacrylate) (PMMA), which undergoes chain scission upon electron exposure, locally reducing its molecular weight. This local polymer modification induces a solubility switch in a developer solution, much like in photolithography (Fig. 1.9b). The developer solutions can be a co-solvent system for high contrast development, such as a mixture of methyl isobutyl ketone (MIBK) & IPA, or water & IPA.¹¹⁴ Alternatively, for low contrast development, pure MIBK solutions have been used¹¹⁵.

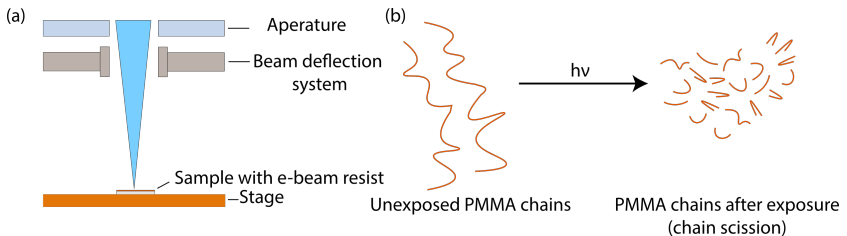


Figure 1.9. E-beam lithography. (a) e-beam exposure mechanism (b) polymer splicing upon electron exposure

1.5. Fabrication methods

1.5.2 Grayscale patterning

With the processes described above, it is only possible to pattern resist material in a two-dimensional (2D) or binary approach; meaning resist is either present or completely removed. This imposes an all-or-nothing illumination limitation on the patterning possibilities. However, in many fields, ranging from optics, to micro- and nanofluidics, 3D structuring is required.¹¹¹ This can be done through means of grayscale lithography. In this technique, the exposure dose is spatially modulated to tune the resist dissolution rate upon development locally. In conventional photolithography, this is possible by using so-called pixel density modulated masks.¹¹⁶ This poses an additional constraint on the already cumbersome mask making. In this regard, maskless techniques are more convenient and user-friendly. The presented work uses grayscale e-beam lithography as a method to accurately tune the resist development rate. Here, the electron dose is modulated to locally tune the molecular weight of polymer-based resists, such as PMMA. Thus, areas of lower molecular weight are associated with a higher development rate and vice versa.¹¹⁷ As the first step in this process, the resist contrast in a pure developer solution needs to be determined (Fig. 1.10a). For grayscale lithography, a low-contrast development is favored to decrease the binarity of the exposure and to make the process less sensitive to minute fluctuations in exposure dose.¹¹⁵ The resist's contrast curve allows to couple the electron exposure dose to an achieved depth. Secondly, a fluidic pattern design is needed. Such a design contains different layers, where each layer is representative of a specific target height (Fig. 10b).

1. Introduction

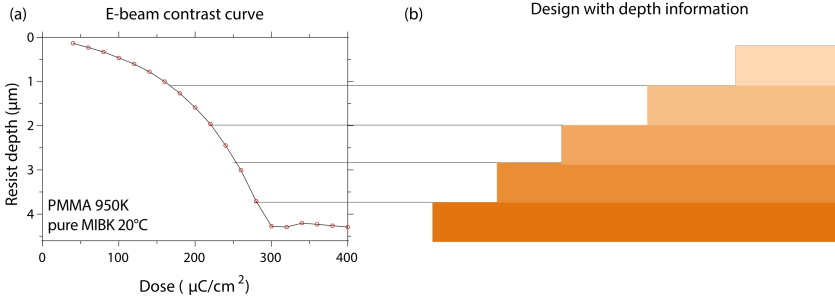


Figure 1.10. Grayscale e-beam procedure. (a) contrast curve of PMMA 950K developed in MIBK for 5 min at 20 °C (b) Cross-section of exposed staircase profile, where each layer (color) is representative of a different height in the resist material.

Still, before the pattern can be exposed, it is of paramount importance that the exposure matrix is corrected for the proximity effect. The latter causes areas adjacent to the scan area to receive a non-zero dose due to electron-material interactions.¹¹⁸ For binary lithography, this can be performed in 2D, but it is preferably done in 3D for grayscale lithography. This can be done using specialized software, such as BEAMER (GenISys GmbH), to combine the resist contrast curve, the pattern design and the electron point spread function (PSF) to expose the grayscale design correctly. The PSF describes the spatial function of the electron energy in function of the incident beam inside the resist material. 3D PEC helps to assure that the target depth is achieved. Still, when the technique was employed to fabricate 3D nanofluidic devices, it was found that there was a significant contribution of the time between electron exposure and development (t_{ED}) on obtained pattern topography (t_{ED}). This effect is extensively described and discussed in Chapter 2.

Furthermore, it was observed that an opposite dose-dependent effect occurred when e-beam-exposed PMMA is subject to dry rather than wet development. More specifically, exposed areas exhibit more etch resistance than their unexposed counterparts. This enables negative tone processing of a well-studied e-beam resist at much lower doses than previously reported.

1.5. Fabrication methods

Additionally, it facilitates simultaneous pattern development and transfer in a single step. This novel finding is outlined in Chapter 3.

1.5.3 Thermoplastic upscaling

It should be noted that despite the exciting technological progress in the last few decades regarding grayscale and maskless lithography methods, their upscalability remains limited. This makes them unsuitable to produce POC microfluidic devices directly. Instead, they are used to fabricate so-called master structures that can be used for pattern replication, much like the soft lithography process of PDMS. Even so, soft lithography techniques, albeit faster than direct writing, are inherently incompatible with industrial device production. Moreover, PDMS also has several other non-favorable features, such as small molecule absorption, fluid evaporation, and solvent-induced swelling.¹¹⁹ Its elastomeric behavior further complicates the fabrication of channel heights with sub-micron dimensions.¹²⁰ This led us to choose thermoplastics as the suitable device material for our 3D nanofluidic devices. They are chemically stable, non-gas permeable, low cost, and well-characterized in biological environments.¹²¹ Moreover, they are significantly less elastic than PDMS, which is essential for the fabrication of fluidic devices with shallow dimensions.

In the work discussed in this thesis, we used two thermoplastic patterning methods. More specifically, in Chapter 4, we describe the combination of grayscale e-beam lithography and injection molding as an upscalable fabrication route. Here, a grayscale e-beam exposed resist served as a substrate to fabricate a negative copy in a nickel mold directly. This mold could be used to injection mold the device design in thermoplastic materials. To do so, plastic granulate is liquefied and injected into the molding chamber. Once the latter is filled, cooling commences, and the plastic is solidified (Fig. 1.11 – Left). Due to its rapid thermal cycling, injection molding is often used for the industrial fabrication of plastic components.¹²² However, injection

1. Introduction

molding of sub-micron features is challenging and is highly dependent on a large variety of processes and geometrical parameters.¹²³ Furthermore, the fabrication of the molds is often time-consuming, expensive, and as a result, not compatible with device prototyping.

To this extent, we used hot-embossing to fabricate the devices in Chapters 5,6 and 7. Here, a negative copy was fabricated in a commercially available UV-cross-linkable polymer directly from grayscale e-beam patterned resist. Subsequently, a Plexiglas (PMMA) film was placed on top of the surface of the negative copy inside a hot-embossing chamber. The latter was homogeneously heated until the materials' glass transition temperature (T_g) was exceeded and the plexiglass softened. Afterward, the chamber pressure was increased to pattern the thermoplastic film. Once the pattern was imprinted, the temperature gradually decreased, and the plexiglass film was removed from the embossing chamber. This process enabled us to rapidly prototype and test novel design layouts within one day – including e-beam exposure, fabrication of the negative copy, and device bonding (Fig. 1.11 – Right). The developed methods contribute to the field of thermoplastic fluidics by not only providing a fabrication scheme for rapid device prototyping through hot embossing but also paving the way for viable upscaling of device fabrication through injection molding.

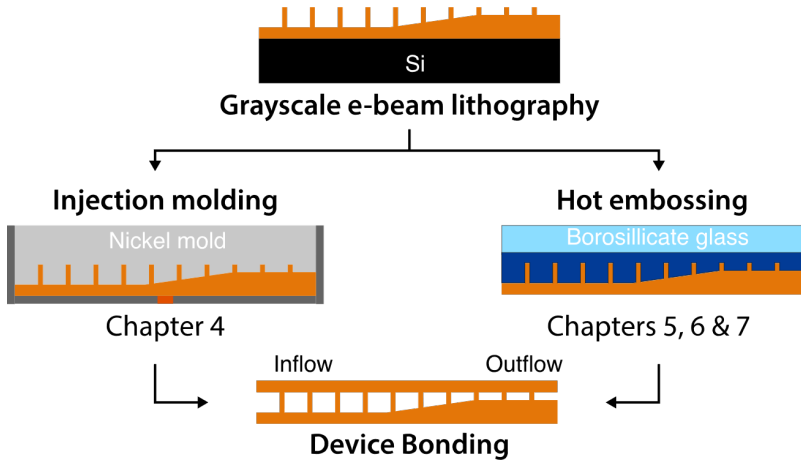
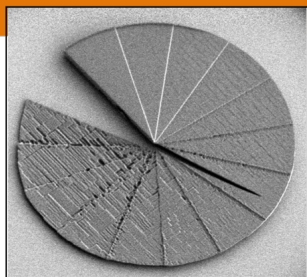


Figure 1.11. Fabrication of 3D nanofluidic devices. A grayscale e-beam exposure in PMMA950K on silicon is performed to pattern the initial device geometry. Afterward, injection molding (left) or hot embossing (right) is used to pattern the devices into thermoplastic materials cost-effectively.

Grayscale lithography for 3D patterning

2



The following section has been published in:
Microelectronic Engineering, Volume 225, 2020
<https://doi.org/10.1016/j.mee.2020.111272>.

Grayscale e-beam lithography: effects of a delayed development for well-controlled 3D patterning

**Thomas Mortelmans^{a,b,c}, Dimitrios Kazazis^a, Vitaliy A. Guzenko^a, Celestino Padeste^a,
Thomas Braun^b, Henning Stahlberg^b, Xiaodan Li^a, Yasin Ekinci^a**

^a Paul Scherrer Institute, 5232 Villigen PSI, Switzerland

^b Center for Cellular Imaging and NanoAnalytics (C-CINA),
Biozentrum, University of Basel, 4056 Basel, Switzerland

^c Swiss Nanoscience Institute, University of Basel, 4056 Basel,
Switzerland

Keywords: Grayscale e-beam lithography, 3D microstructuring, PMMA 950 K,
post-exposure bake, delayed development

*Corresponding author: thomas.mortelmans@psi.ch

2. Grayscale lithography for 3D patterning

2.1 Abstract

Grayscale electron beam lithography (g-EBL) is a fabrication technique that allows for tunable control of resist topography. In most cases, the height of the structures is in the submicron regime. Here, we present an extensive experimental characterization of the post electron beam exposure behavior of poly(methyl methacrylate) (PMMA) 950K for grayscale structuring with several micrometers in height. The obtained results show that the development depth for the same electron dose is dependent on the time between exposure and development. This dependence becomes more prominent at higher exposure doses. Additionally, it was found that a post-exposure bake influences the dose-response behavior of the resist material and, therefore, also the obtained three-dimensional (3D) structure. This work paves the way for controlled and reproducible 3D micrometer structuring via g-EBL.

2.2 Introduction

A large variety of scientific and technological applications in optics^{124,125}, spectrometry¹²⁶, life sciences^{127,128}, and micro- and nanofluidics¹²⁹⁻¹³¹ require three-dimensional (3D) material structuring. To achieve the desired topography, various well-established patterning methods have been employed, such as two-photon polymerization¹³², laser ablation¹³³, focused ion beam induced deposition (FIBID)¹³⁴, thermal probe scanning lithography¹³⁵, and grayscale lithography. The latter is a collective name for processes that enable the fabrication of complex 3D shapes with a single lithographic exposure.¹³⁶ To achieve grayscale patterning, the exposure dose during the patterning process is spatially modulated to locally increase or decrease the dissolution rate of the resist material during the subsequent development step. The resist material can be an ultraviolet (UV) sensitive polymer, called a photoresist, which can be used in conjunction with direct laser writing systems¹³⁶ or grayscale photomasks¹³⁰ to obtain 3D structures at the micrometer scale. An alternative direct writing strategy uses an electron beam with a spatially modulated dose to locally tune the polymer chain splicing of a resist such as poly(methyl methacrylate) (PMMA) and therefore tune its development rate.¹³⁷ This lithographic technique has significantly better resolution than the UV grayscale ones and has been used to make 3D structures with nanometer height precision.¹³⁸ Nevertheless, grayscale e-beam lithography (g-EBL) with PMMA-based resists has often only been employed to fabricate 3D structures with sub-micron sizes.^{126,139,140} In this chapter, we report on a systematic study of the PMMA resist behavior after electron beam exposure to extend the technique to 3D structures of several micrometers in height with no significant loss of vertical resolution. This work paves the way for applications in numerous fields of scientific research and technology.

2.3 Methods

2.3.1 Dose-response behavior of PMMA 950K

PMMA 950K 11% in anisol (AllResist GmbH) was spin-coated at 1000 rpm for 60 seconds on a 4" Si-wafer and baked at 175 °C for 25 min to achieve a 4- μm -thick film. An array of nineteen 500 \times 500 μm^2 squares with an inter-square spacing of 500 μm (Fig. 2.1) was exposed at different doses from 40 to 400 $\mu\text{C}/\text{cm}^2$ in steps of 20 $\mu\text{C}/\text{cm}^2$ by an electron beam lithography (EBL) system (Raith EBP 5000+), operated at 100 kV acceleration voltage. Hereafter the PMMA 950K was developed in pure methyl isobutyl ketone (MIBK, Technic France) at 20 °C, rinsed in isopropanol (IPA) for 20 s and blow-dried with nitrogen. After some initial tests, we noticed an irregularity in the results and figured out that the delay between the exposure and the development plays a significant role. To evaluate the dose-response behavior of PMMA over time, the array of squares was exposed 6 times on the same wafer. After the exposure, the wafer was cleaved in six pieces and kept in ambient conditions inside a cleanroom environment. Subsequently, the pieces were developed as previously described after 9, 13, 18, 37, 108 or 186 hours of delay after electron beam exposure. The development in pure MIBK provides a low resist contrast compared to the development in MIBK:IPA (1:3), a frequently used developer solution in binary EBL.^{141,142} The low-contrast behavior reduces the sensitivity to small fluctuations in exposure dose and allows for a wider range of doses to be used in resist patterning. This is an essential resist characteristic for grayscale lithography. The dose-response behavior over time was analyzed for doses below the dose-to-clear value through an exponential fitting of experimental data.

The influence of a post-exposure bake (PEB) on the dose-response behavior of PMMA 950K was investigated by heating the dose-test arrays on a hotplate for different amounts of time. After heating, the samples were left to cool down to room temperature before they were developed.

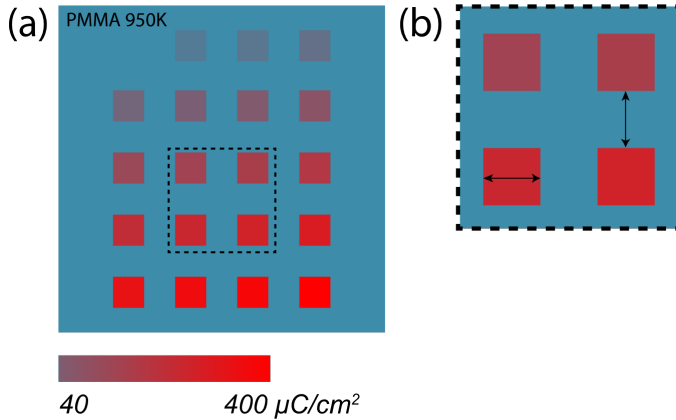


Figure 2.1. An array of squares exposed at different electron doses ($\mu\text{C}/\text{cm}^2$). (a) The exposure dose of the squares in the array ranges from 40 to 400 $\mu\text{C}/\text{cm}^2$ with 20 $\mu\text{C}/\text{cm}^2$ increments. (b) Zoomed-in picture of the patterned squares with arrows depicting a distance of 500 μm .

2.3.2 Grayscale electron beam lithography

The layout of a pie-chart shape with 6 slices (Fig. 2.2b) was made in the software Tanner L-Edit (Mentor Graphics), where each slice was defined as a separate layer. The height difference for each layer was 250 nm. The TRACER program (GenISys GmbH) was used to perform a Monte-Carlo simulation of the electron-solid interaction to provide the point spread function (PSF), which describes the deposited energy as a function of the distance of the incident beam inside the PMMA layer. Subsequently, the BEAMER program (GenISys GmbH) was used to perform a 3D proximity effect correction (3D PEC), which takes into account the PSF information, the contrast curve of the resist material and the layout. Thus, the EBL patterns were properly prepared by also encoding a modulation of the dose within the patterns. After the exposure, two pie-chart shapes were subject to different PEB conditions: one was heated at 45 °C for 5 min and the other at 60 °C for 10 min. The samples

2. Grayscale lithography for 3D patterning

were developed in the same way as the square dose-response arrays. A graphical representation of the experimental method is given in Fig. 2.

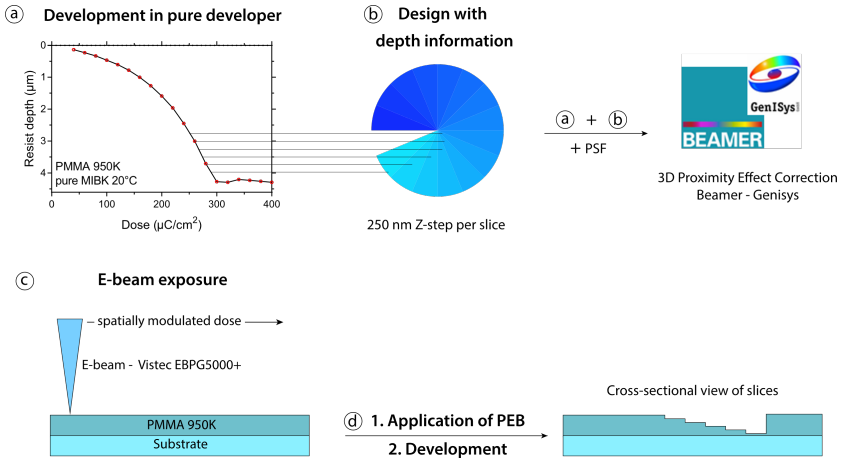


Figure 2.2. Schematic summary of the g-EBL procedure. (a) A contrast curve of PMMA 950K in a pure developer was used to correlate the desired 3D topography specified in the design (b) with the necessary exposure dose. (a) and (b) were combined with the PSF to perform a 3D-PEC in BEAMER. (c) PMMA 950K was exposed with a spatially modulated dose to achieve the required topography profile after development (d). The PEB at different temperatures is performed after step 3.

2.3.3 Metrology

The development depth for each square in the dose array was measured by using a profilometer (Veeco, Dektak 150) equipped with a 2.5 μm tip. Scanning electron microscopy (SEM) (Hitachi Regulus 8430) images are obtained at a low acceleration voltage of 0.5 kV, to image the sensitive and insulating PMMA films with no prior coating of a conductive layer. Atomic force microscopy (AFM) images were acquired with a Dimension Icon AFM (Bruker Corp.) in tapping mode.

2.4 Results and discussion

2.4.1 Change in dose-response behavior over time

Figure 2.3a shows the development depth of PMMA versus the exposure dose at different times between exposure and development (t_{ED}) fitted with an exponential function. It shows that if the resist material is developed shortly after e-beam exposure ($t_0 = 9\text{h}$), the development depth (d_0) differs significantly when compared to the resist depth for a development at large t_{ED} -values (d_{ss}).

Figure 3b shows that the variation in the dose-response behavior of the resist material follows an exponential relaxation behavior of the form:

$$d(t_{ED}) = (d_0 - d_{ss})e^{\left(\frac{-t_{ED}-t_0}{\tau}\right)} + d_{ss} \quad (1)$$

where $d(t_{ED})$ is the removed resist thickness from development at a delay time t_{ED} after the exposure, d_0 as well as d_{ss} can be extracted from the fit functions in figure 2.3a, and τ is a single time constant, extracted to be 15.2 h by fitting all the curves of Fig. 3b at once.

2. Grayscale lithography for 3D patterning

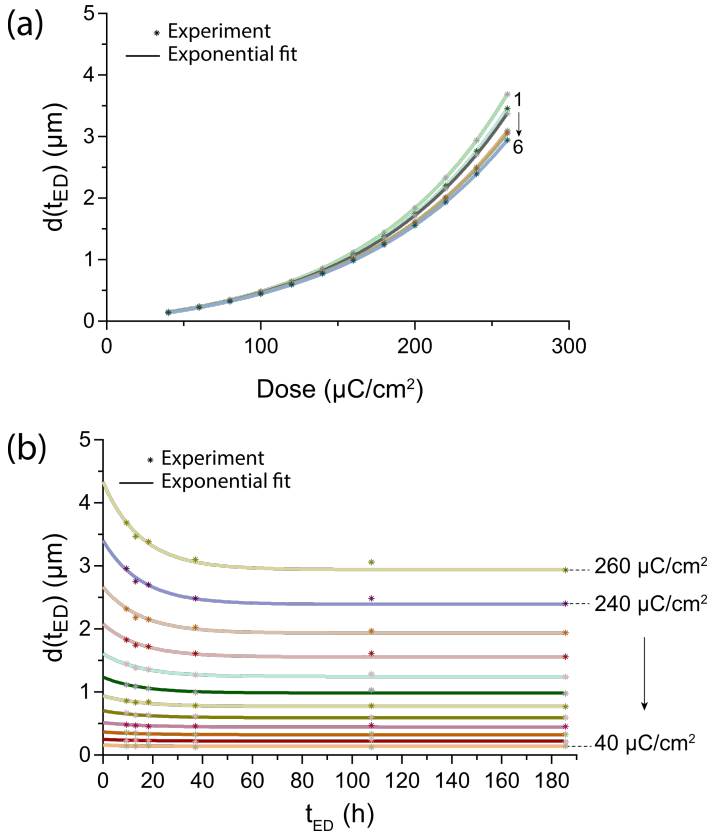


Figure 2.3. Development depth of PMMA 950K for different electron doses and different t_{ED} -values. (a) Measured depths in PMMA 950K when developed at 9, 13, 18, 37, 108, 186 hours (no. 1 to 6 respectively) after electron exposure. Solid lines are best-fit curve to an exponential function. (b) Development depth in PMMA 950K as a function of delay time (t_{ED}) for different exposure doses. The solid curve is the best-fit curve plotted using Eq. 1.

2.4. Results and discussion

The apparent relaxation process in Fig. 2.3b seems to reach a steady state after a period of t_{ss} which is longer for higher exposure doses. Additionally, our experiments demonstrate that the relaxation span (d_0-d_{ss}) increases with the exposure dose.

Furthermore, Eq. 1 allows for the approximation of the thickness/dose contrast curve of PMMA 950K at different t_{ED} -values by solely plugging in the electron exposure dose, as shown in Fig. 2.4. The fitted thickness/dose contrast curves show a significant influence of the delay time t_{ED} , which is more pronounced at higher exposure doses. This change also causes a shift of the dose-to-clear value towards higher electron doses. It should be noted that if the resist is exposed at relatively low exposure doses, the resist depth after development does not vary significantly over time. In contrast, if the resist is exposed at relatively high exposure doses, its depth after development decreases significantly more over time. This effect causes the slope of the contrast curve to decrease over time, enhancing its properties suitable for grayscale lithography ¹³⁹.

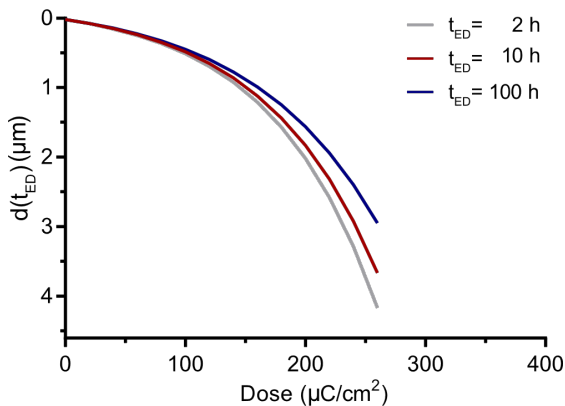


Figure 2.4. Predicted contrast curve of PMMA 950K at different t_{ED} values according to the exponential fit model of the measured data presented in Fig. 3b.

2. Grayscale lithography for 3D patterning

In standard binary electron beam lithography, where the PMMA resist is exposed and developed until it is fully removed, this dependence of the contrast curve on t_{ED} may also exist but is without influence and usually not observed. However, in 3D grayscale lithography, where a precise height control is essential, this effect is of great importance. To pattern micrometer-thick, 3D structures that require a wide range of electron exposure doses (see Fig. 2.2a), the resist relaxation must be taken into account for accurate and reproducible structuring. The mechanism behind this effect could be attributed to PMMA chain rearrangement after chain scission due to the electron beam exposure. However, this investigation is beyond the scope of the current work and will be the subject of future research.

2.4.2 Influence of PEB on contrast curve of PMMA 950K

In an effort to reduce the time t_{ss} , when the development depth of PMMA is practically not changing anymore, a PEB was applied at different temperatures for varying amounts of time. The effect of a PEB at 45 °C (Fig. 2.5a) was most pronounced at higher exposure doses and for longer heating times. The inset of Fig. 2.5c shows a reduction in resist depth of 175 nm at 260 $\mu\text{C}/\text{cm}^2$ after heating for 3 min. At a PEB temperature of 60 °C, the effect was more noticeable (Fig. 2.5b) and resist depth was reduced by 603 nm for the same exposure dose and after heating for 2.5 min. When a PEB was performed at 80 °C, the effect was even clearer and started to significantly affect the lower exposure doses. For a heating time of 1 min, the reduction in resist depth at 260 $\mu\text{C}/\text{cm}^2$ was 1289 nm. However, it should be noted that at this temperature significant amount of thermal stress is accumulated inside the resist material, causing cracking along the writing lines of the electron beam during exposure, as shown in the microscope image in the inset of Fig. 5c. This makes this PEB temperature impractical for application in 3D microstructuring.

2.4. Results and discussion

The results show that if a PEB is performed at elevated temperatures and for a longer time, the development depth for a given dose decreases, reaching steady state in a few minutes rather than several hours. The decrease in development depth after longer PEB times even goes below the d_{ss} seen at room temperature, which indicates that the removed resist after development is dependent on the temperature of the post-exposure conditions.

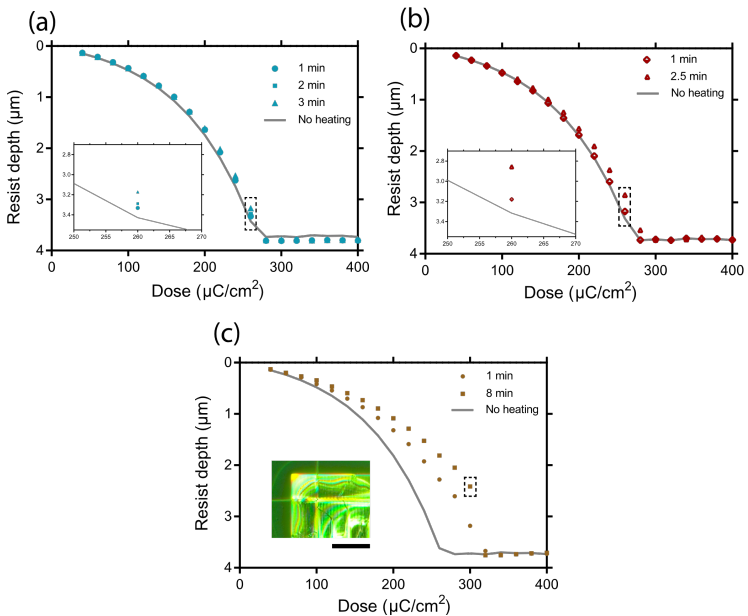


Figure 2.5. Influence of a PEB on the dose response behavior of PMMA 950K. Contrast curves are shown for PEB at 45 °C (a), 60 °C (b) and 80 °C (c). The curve showing no heating was extrapolated from Eq. 1 for the corresponding t_{ED} -values. The insets of figure (a) and (b) show a close up of the PEB effect at 260 μC/cm² for different times. The inset of (c) shows a light microscopy image of the top left corner of a developed square patterned in PMMA 950K at 300 μC/cm² after PEB at 80 °C for 8 min. The scale bar is 100 μm.

2.4.3 A practical example: changing a 3D shape by application of a PEB

The effect of PEB on the resist contrast curve and consequently on the resulting 3D topography is visualized in Fig 2.6. If PEB at 45 °C is performed for 5 min, slice No. 6 is absent, as shown in the SEM and AFM images of Fig. 2.6a and 2.6b, respectively. However, when PEB was performed at 60 °C for 10 min, this slice of the pie-chart remained after the development, with a significant height of 784 nm, as shown in the SEM and AFM images of Fig. 6c and 6d, respectively. The performed PEB led to a change in the dose-response behaviour of the resist material, causing more resist to remain after development for a given exposure dose (Fig. 2.5). This is in accordance with the results presented in the previous section. From the above discussion, we conclude that the obtained 3D structure can change not only by adjusting the e-beam exposure dose but also by the application of a PEB.

The images also show an increasing roughness at a higher electron dose (higher slice number in Fig. 2.6), which could be attributed to the shape of the contrast curve (Fig. 2.4). More specifically, the slope of the curve increases towards higher dose values. This has as an implication that even small changes in the exposure dose at a given area could cause noticeable changes in the removed resist. In addition, the closer the pattern is to the Si-substrate, the more important the contribution of backscattered electrons to the total dose is, making the 3D proximity effect correction nontrivial, which could also result in inaccurately corrected local doses.

2.4. Results and discussion

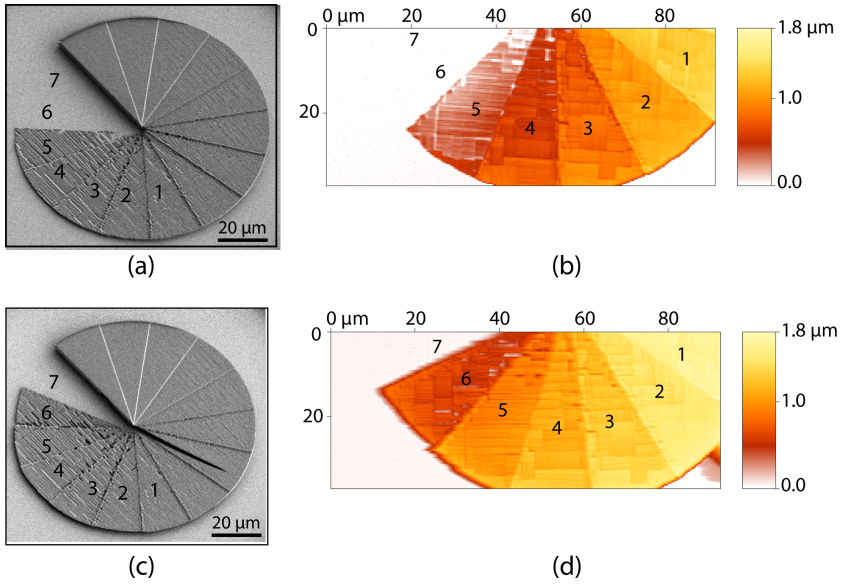


Figure 2.6. SEM and AFM images of a pie-chart shape subject to different PEB temperatures and times. (a) and (b) at 45 °C for 5 min. (c) and (d) at 60 °C and 10 min.

2.5 Conclusion and outlook

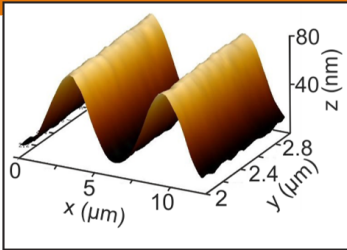
We have characterized the performance of PMMA 950K as a grayscale e-beam resist for 3D microstructures. It was shown that the dose-response behavior of the material depends on the time between exposure and development. This effect was accurately modeled through a unifying equation, showing that the removed resist for a given exposure dose stabilizes at long t_{ED} values. Moreover, it was found that the dose-response behavior of the resist also depends on the PEB conditions. In general, the application of PEB reduced the resist depth after development and was found to accelerate the relaxation process. The influence of PEB was proven to influence the resulting topography of a 3D microstructure. Further work is needed to study the detailed mechanism of the relaxation process after electron beam exposure. Nevertheless, our work not only shows that grayscale EBL can be used to reliably and reproducibly pattern 3D microstructures up to a total resist height of 4 μm , but it also provides a way to accurately model the dose-response behavior of PMMA versus the time between exposure and development. The presented results pave the way for applications in science and technology, ranging from micro-optics to 3D microfluidics and lab-on-a-chip applications.

2.6 Acknowledgments

This work was supported by the Swiss Nanoscience Institute.

Dry development of poly(methyl methacrylate)

3



The following section is based on
a manuscript in preparation

Dry development of poly(methyl methacrylate)

Furkan Ayhan^{a,b,c}, Thomas Mortelmans^{a,d}, Yasin Ekinci^a, and Dimitrios Kazazis*

^a Paul Scherrer Institute, 5232 Villigen PSI, Switzerland

^b Ecole Polytechnique Fédérale de Lausanne, 1015 Lausanne, Switzerland

^c CSEM (Centre Suisse d'Électronique et de Microtechnique) SA, 2002 Neuchâtel, Switzerland

^d Swiss Nanoscience Institute, University of Basel, 4056 Basel, Switzerland

Keywords: PMMA, electron beam lithography, grayscale lithography, dry development, negative tone, reactive ion etching.

*Corresponding author: dimitrios.kazazis@psi.ch

3. Dry development of poly(methyl methacrylate)

3.1 Abstract

We demonstrate a method for dry (plasma) development of e-beam exposed poly(methyl methacrylate) (PMMA). A reduced etch rate of PMMA in SF₆/O₂ plasma with increasing electron dose enables PMMA to be used as a negative-tone resist without the conventional wet development. Compared to the well-studied negative-tone behavior of PMMA at very high electron doses, this method works at lower electron doses. Using the dry development technique instead of a wet development allows the resist patterns to be developed and transferred to the substrate in the same step, enabling fast and robust fabrication. In addition, this method can be used for grayscale patterning for the fabrication of topographic structures. By spatially varying the electron dose, one can achieve the desired height profile of the three-dimensional microstructures. We showcase the capabilities of the proposed method by fabricating binary and grayscale structures in silicon with only e-beam lithography and subsequent reactive-ion etching. The underlying mechanism is hypothesized to be dose-dependent charging of the resist material as well as electron-dose-dependent fluorination of the PMMA, which results in a dose-dependent etch resistance in reactive-ion etching.

3.2 Introduction

Three-dimensional (3D) microstructures have several applications, such as diffractive optical elements (DOEs)¹⁴³, microlenses¹⁴⁴, and microfluidic devices¹⁴⁵. There are several techniques, mostly photon-based, that can be used for the fabrication of such devices with varying topography, including photolithography with gradient masks¹¹⁶, laser lithography^{108,146}, laser ablation¹⁴⁷, and two-photon polymerization (2PP)¹⁴⁸. These techniques can achieve lateral resolutions down to a few hundred nanometers. For 3D patterning in nanoscale, focused ion/electron beam induced deposition (FIBID/FEBID)^{149,150} thermal scanning probe lithography (t-SPL)¹⁵¹, and grayscale electron beam lithography (g-EBL) can be used.¹³⁸ In this work, we focus on g-EBL, which is a top-down patterning technique that can achieve lateral resolutions down to tens of nanometers. Compared to standard, binary e-beam lithography using positive-tone resists and wet development, whereupon the exposed resist is fully removed, in g-EBL the resist is only partially removed. This is achieved by spatially adjusting the electron dose and utilizing a low-contrast development process to achieve grayscale resist patterns. Although low contrast is not desired in binary lithography, it is crucial in g-EBL, and grayscale lithography in general, to achieve precise and reproducible 3D patterning. More specifically, the low-contrast process will make the resist less sensitive to minute changes in dose, enabling better control over development depth and reduced pattern roughness.

A widely-used resist in both binary and g-EBL is poly(methyl methacrylate) (PMMA). PMMA is a long polymer chain that undergoes main-chain scission during electron exposure. This fragments the polymer chains into smaller chains, decreases its average molecular weight, and consequently increases its solubility in various organic developers, e.g., methyl isobutyl ketone (MIBK).¹¹⁷ PMMA can also exhibit a negative-tone behavior at very high electron doses (an order of magnitude higher than for positive-tone), where crosslinking takes place that renders the exposed PMMA insoluble in

3. Dry development of poly(methyl methacrylate)

acetone.¹⁵² It is also possible to achieve low contrast and perform grayscale lithography in negative-tone PMMA processing.¹⁵³ However, this requires cryogenic cooling of the resist while patterning, making it impractical for most applications.

Resist development is a critical step of the lithographic process. The development conditions, such as the resist post-exposure bake, the development temperature and duration, the chemical composition and concentration of the developer, can have a significant effect on the resulting resist structures, their shape, and roughness. Resist swelling and cracking, pattern detachment from the substrate, and increased line edge roughness are only a few of the issues that a wet development method can cause. Moreover, when it comes to high aspect ratio patterns, wet development can be very problematic. During the drying step, after the development, the capillary forces that are exerted on the resist structures are strong enough to cause pattern collapse.¹⁵⁴ If the resist is compatible with supercritical drying, pattern collapse can be mitigated.¹⁵⁵ However, organic resists are incompatible with supercritical drying and therefore remain prone to pattern collapse during wet development. Lastly, wet development requires large amounts of chemicals to be consumed and disposed, that are potentially harmful to the environment.¹⁵⁶

Alternative to wet development, dry development techniques have also attracted increasing attention owing to several unique advantages. These techniques do not require large quantities of chemicals and they are, therefore, cheaper and more environmentally friendly. In addition, most of the aforementioned problems of wet development are absent and, notably, pattern collapse can be completely prevented, as there are no capillary forces during the dry development process. Dry development can be done by a post-exposure thermal treatment of the resist, during which the more volatile resist species that were formed during photon or electron exposure are removed.¹⁵⁷ Alternatively, electron or photon exposure can locally alter the plasma etch

3.2. Introduction

resistance of resists, and the pattern is developed owing to the etch resistance difference between exposed and unexposed regions.^{158,159} Such an increase in plasma etch resistance is, for example, attributed to crosslinking and to the formation of hydrogen bridges.¹⁶⁰ Dry etching has also been achieved by locally changing the electrical conductivity of a resist upon UV exposure. This, in turn, brings upon a change in the etch rate between the exposed and unexposed regions in a reactive ion etching (RIE) chamber.¹⁶¹ More recently, dry development has attracted a lot of attention for extreme ultraviolet (EUV) lithography, where it can be employed in a dry (deposited) metalorganic resist.¹⁶²

In this work, we propose a dry development scheme by combining g-EBL with RIE, using a well-established resist: PMMA. The electron-beam exposed samples are not subject to a wet-development step, nor are they subject to any other post-exposure treatment, but they are etched in an SF₆/O₂ plasma directly after the e-beam exposure. We show that the plasma etch rate of PMMA decreases with increasing electron dose, which means that PMMA behaves as a negative-tone resist in this case. In addition, the obtained contrast is low enough to enable grayscale patterning. A comparison of the standard wet development of PMMA (positive-tone) with the proposed dry development of PMMA (negative-tone) is shown in Fig. 3.1. Furthermore, since fluorine-based plasmas are also used to etch Si, the PMMA grayscale pattern can immediately be transferred to the Si substrate in a single etching step. This allows easier fabrication of grayscale Si structures with increased throughput, as a similar process by conventional means would require additional processing steps and optimization of the etching selectivity between Si and PMMA.

3. Dry development of poly(methyl methacrylate)

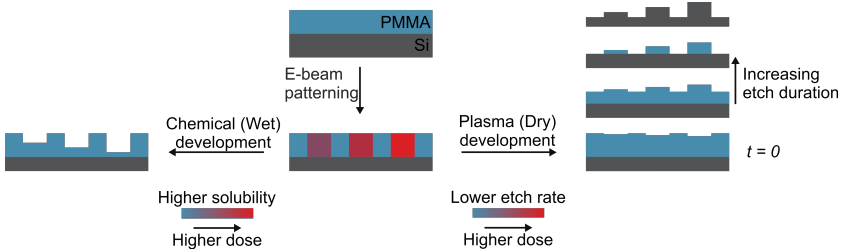


Figure 3.1 Working principle for wet and dry development of electron beam exposed PMMA for g-EBL. At the investigated exposure doses, the solubility of PMMA increases in a wet development step resulting in a positive tone behavior (left). For dry development (right), the etch rate in SF_6/O_2 plasma decreases with increasing electron dose, resulting in a negative tone behavior.

In Section 2, we describe our experimental methods, including sample preparation, EBL, and the associated data preparation and plasma etching. In Section 3, we present our main results on the dependence of the etching rate on the exposure dose and discuss the factors that influence the contrast of the plasma etching (henceforth called dry development). We also show examples of patterns achieved by this method. Finally, in Section 4, we summarize our results and discuss the possible applications and outlook of our work.

3.3 Methods

3.3.1 Measurement of the plasma etch rate of PMMA

Dry development of PMMA relies on the decrease of the plasma etch rate of PMMA with increasing electron dose during EBL. To study this effect quantitatively, the experiment starts with 4-inch silicon wafers spin-coated with PMMA 950K A11 (11% in anisole, Allresist GmbH) at 1000 rpm for 60 s and baked on a hotplate for 25 min at 175 °C. This process yields an average film thickness of 4 μm , as confirmed by reflectometry measurements (FTPadv, SENTECH). For thinner PMMA films, PMMA 950K A8 (8% in anisole, Allresist

3.3. Methods

GmbH) is used. When this is spin-coated at 1000 rpm for 60 s and baked at 175 °C for 10 min, a thickness of 1.66 µm is obtained. Spin-coating of same resist at 4000 rpm for 60 s and baking at 175 °C for 5 min, results in a thickness is 0.72 µm. To study the PMMA plasma etching, the wafer is patterned with an array of squares of 400 µm in width with varying electron doses. The patterning is done using a 100 keV EBL system (EBPG 5000Plus, Raith) with a beam current of 7 nA. After the e-beam exposure, the thickness of the unexposed region is measured using a reflectometer and of the exposed regions using a mechanical profilometer (Dektak 8, Veeco). Measurements at the exposed regions are necessary as electron irradiation of PMMA, even without any form of development, removes ester side groups from the main chain, along with several gaseous species like CO₂ and CH₃OH, leading to a material loss and shrinkage in the film.¹⁶³ Samples are, then, etched with a reactive-ion etcher (PlasmaLab 100, Oxford Instruments) using SF₆ and O₂ with several recipes listed in Table 3-1. The samples are etched with different etch durations, starting from 1 minute and going up to 6 minutes with one-minute increments, to capture the temporal change in etching rate. After etching, the samples are characterized again with reflectometry and profilometry to determine etched PMMA thickness and calculate the etching rates.

Table 3-1. Employed Etch Recipes

Recipe	Pressure (mTorr)	RF Power (W)	ICP Power (W)	SF₆ Flow Rate (sccm)	O₂ Flow Rate (sccm)
<i>RF200</i>	50	200	0	45	5
<i>RF300</i>	50	300	0	45	5
<i>ICP500</i>	25	50	500	45	5

3. Dry development of poly(methyl methacrylate)

3.3.2 Pattern transfer to Si

The contrast is one of the essential properties of a resist and critical in any lithographic process and is of utmost importance in grayscale lithography. In conventional EBL, a contrast curve simply maps the remaining resist thickness, after development, to electron dose. Here, since we develop and transfer the resist pattern into a Si substrate as in Fig. 3.2a using a single process, what is important, in the end, is the mapping between the Si pattern height after etching and the electron dose. The latter depends on both the resist etching rate at different electron exposure doses and the Si etch rate. To obtain such a mapping, the samples that were described in Section 2.1 are used. After e-beam exposure, the samples are etched in the same reactive-ion etcher using the same process parameters but for a longer time (to fully etch the PMMA resist) to ensure a complete pattern transfer to Si. Subsequently, the Si pattern heights are measured using a mechanical profilometer. The contrast curve obtained by this method is specific to the Si/PMMA system described here and the specified dry development (etching) conditions. In conventional EBL, the contrast curve mainly depends on the resist, developer, and development conditions but less on the substrate. In this case, the contrast curve can be fitted with a dose-response curve. Here, since the contrast curve also includes etching into the substrate, it is also heavily dependent on the substrate itself i.e., the etching selectivity between PMMA and Si. We have found that, in this case, the dose-response curve cannot provide a good fit to the measured data, while the data can be empirically fitted using a two-term exponential function as:

$$y = ae^{bx} + ce^{dx},$$

where x is the electron dose in $\mu\text{C}/\text{cm}^2$, y is the Si pattern height in μm , and, a , b , c and d are empirical fitting parameters. The fitted contrast curve for this method is shown in Fig. 3.2b.

3.3. Methods

After obtaining the contrast curve, g-EBL can be performed for the desired binary/grayscale patterns. First, the EBL data is prepared, including the computation of the spatial dose variation, by using the 3D proximity-effect correction (3D-PEC) module of BEAMER (GenISys GmbH), a commercial electron-beam and laser lithography software. First, the desired grayscale pattern is provided as a layered GDSII file. Each GDSII layer is mapped to a certain resist thickness. Second, the previously measured contrast curve is provided to determine the electron dose for the different layers. Last, a point spread function (PSF) is provided for the proximity effect correction. The PSF, which describes the deposited energy as a function of the distance from the incident electron beam, is obtained from TRACER (GenISys GmbH), a Monte Carlo simulation software for the electron-solid interaction and the associated energy deposition. The PSF function used for this work is obtained from a simulation for 4.05 μm thick PMMA on Si taken at 2.025 μm from the top of the resist (Fig. 3.2c). All of the above information is loaded into BEAMER (Fig. 3.2d), which corrects for the proximity effect by properly fracturing the layout and assigning different doses to the elementary shapes. After the e-beam patterning described in Section 2.1, the samples are etched using RIE with the same recipe that was used to obtain the contrast curve, yielding the intended binary or 3D patterns in Si. Atomic force microscopy (AFM) is used to characterize the dry-developed samples using a Dimension Icon (Bruker) AFM in tapping mode.

3. Dry development of poly(methyl methacrylate)

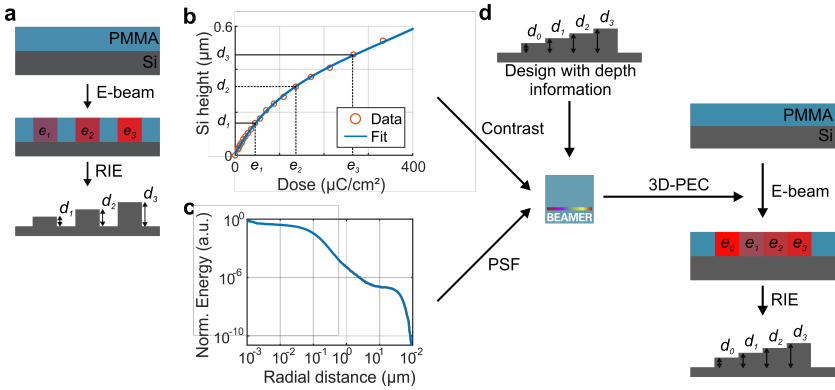


Figure 3.2. Process flow for g-EBL using dry development of PMMA. (a) Dose test procedure to obtain contrast. (b) Typical contrast for dry development of PMMA where different electron doses correspond to silicon pattern heights. (c) Typical point-spread function of lateral energy deposition computed for proximity effect correction. (d) Example of the process flow for grayscale lithography using dry development of PMMA.

3.4 Results and discussion

3.4.1 PMMA etch-rate dependence on electron dose

The dry development of e-beam exposed PMMA is based on the observed difference in plasma etching rate for PMMA exposed at different electron doses, as can be seen in Fig. 3.3a for a 4- μm -thick PMMA film etched with the RF200 recipe from Table 1. First, we observe an overall increase in the etching rate with time, regardless of the electron dose. This is likely due to the increasing temperature in the plasma chamber during etching, which increases the volatility of generated species and accelerates the etching of PMMA.¹⁶⁴ Second, the increase in etching rate with time is larger for lower doses as opposed to higher ones. This is apparent in Fig. 3.3b, where for the same etching duration, the unexposed PMMA is etched considerably more than the exposed PMMA. From Fig. 3.3, it is evident that PMMA behaves as a negative-tone resist when it is subject to dry development, contrary to its

3.4. Results and discussion

positive-tone behavior in wet development for the same range of electron doses (Fig. 3.1).

This increase in etch resistance with increasing electron dose could be attributed to several factors. First, it has previously been established that exposure of PMMA to fluorine-rich plasmas such as CF_4 or SF_6 leads to fluorination of the PMMA film.¹⁶⁵ This consequently increases its chemical etch resistance when the generated fluorine replaces hydrogen in the PMMA backbone, making it more difficult to fragment PMMA chains and remove them.¹⁶⁶ Additionally, fluorine-rich plasmas can form nonvolatile fluorocarbons on the surface and inhibit etching.¹⁶⁵⁻¹⁶⁷ This effect might be more prominent in e-beam exposed PMMA as the main-chain scission of the PMMA will create unsaturated bonds in its backbone¹⁶³, increasing the possibility of fluorine binding. This will make it more difficult to break these chains while etching due to fluorine's higher bonding strength to carbon compared to hydrogen.¹⁶⁸ This proposed mechanism is in agreement with the decreased etching rate as the electron dose is increased and with the observation that the etch rate contrast first appears after longer etching times, as shown in Fig. 3.3. From this fact, it is at least obvious that the plasma induces some changes in the PMMA, resulting in increased etch resistance, which is more pronounced for higher e-beam doses, i.e., PMMA with lower molecular weight. However, we note that the investigation of the exact mechanism is outside of the scope of this chapter and is the subject of future work, and our attempts to elucidate the underlying mechanisms using various spectroscopic methods were, so far, inconclusive. However, we should mention that preliminary experiments with etching PMMA with solely oxygen plasma showed similar, less pronounced effects. This indicates that polymer fluorination is not the only contributor to the tone reversal upon dry development.

3. Dry development of poly(methyl methacrylate)

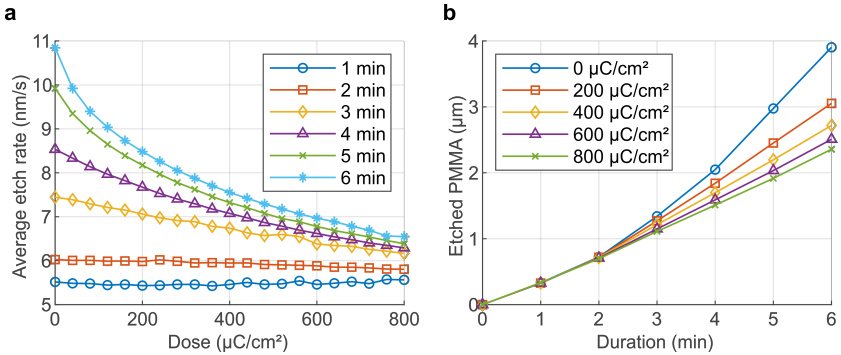


Figure 3.3. The dependence of etched PMMA on e-beam dose and etching time. (a) Average plasma etch rate of PMMA as a function of electron dose for varying etch durations. (b) Etched PMMA thickness as a function of time for different electron doses. The initial PMMA film thickness is 4 μm , and the used etching recipe is RF200 from Table 1.

3.4.2 Dry development of PMMA and pattern transfer to Si

We can take advantage of the variation of the etching rate with electron dose to plasma-develop PMMA and transfer the pattern into Si by prolonging the etching as explained in Section 2.2. To explore the effect of different process parameters on the contrast, we vary the PMMA thickness and the RIE power settings with recipes shown in Table 1. Higher PMMA thicknesses lead to a higher Si pattern height for the same electron dose, as shown in Fig. 3.4a. This is primarily because higher PMMA thicknesses enable longer etch durations in PMMA, thus longer exploitation of the etching rate difference between PMMA exposed at different doses and unexposed PMMA. For a 4- μm -thick PMMA film, the Si height is around 530 nm for an electron dose of 400 $\mu\text{C}/\text{cm}^2$, whereas the same dose yields Si heights of around 170 and 30 nm for PMMA thicknesses of 1.66 and 0.72 μm , respectively.

3.4. Results and discussion

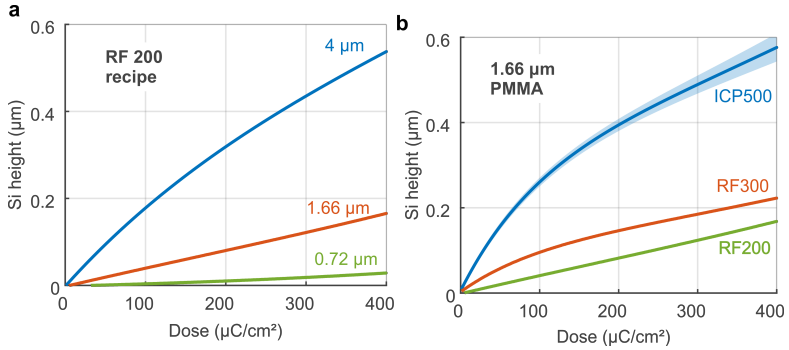


Figure 3.4. Change in contrast curve with different process parameters. (a) Contrast curve for different initial PMMA thicknesses. The etching recipe is RF200 from Table 1. (b) Contrast curve for different etching settings for an initial PMMA thickness of 1.66 μm. The shaded region for ICP500 represents $\pm 2\sigma$ taken from 6 independent measurements from different samples.

In addition, we investigate different power settings for etching. Increasing the RF power initially from 200 to 300 W leads to an increase in Si height after development. For an initial PMMA thickness of 1.66 μm and an electron dose of 400 μC/cm², the Si height increases from 170 nm to 220 nm. This increase becomes even more pronounced when inductively coupled plasma (ICP) is used. When ICP power of 500 W is introduced, the obtained Si height is 540 nm (Fig. 3.4b). As it appears, this recipe shows higher selectivity between PMMA and Si allowing for deeper Si etches. The method was also repeated several times to examine its reproducibility. The shaded area around the ICP500 curve in Fig. 3.4b shows the $\pm 2\sigma$ values calculated from 6 measurements taken from samples from different wafers. The Si height values for a given dose fall within 6 % of the mean value.

3. Dry development of poly(methyl methacrylate)

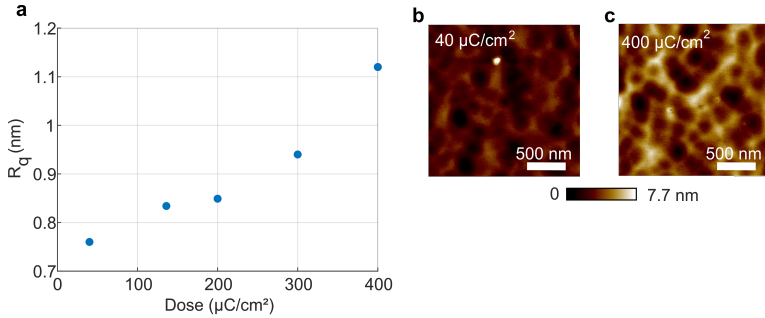


Figure 3.5. Si roughness for dry development of PMMA. (a) Si RMS roughness as a function of electron dose. Data are computed from $4 \mu\text{m}^2$ AFM micrographs taken after etching with the ICP500 recipe with an initial PMMA thickness of $1.66 \mu\text{m}$ (ICP500 in Fig. 3.4b). (b) and (c) are AFM micrographs for electron doses of 40 and $400 \mu\text{C}/\text{cm}^2$, respectively.

As it is known that aggressive plasma etching for extended periods of time can increase the roughness of Si structures¹⁶⁹, it is crucial to also investigate the roughness induced by our dry development procedure. Figure 3.5a shows the root mean square (RMS) roughness, R_q , computed from $2 \times 2 \mu\text{m}^2$ AFM micrographs taken from samples with $1.66 \mu\text{m}$ initial PMMA thickness and etched using the ICP500 recipe. With increasing dose, there is a gradual increase in roughness from 0.76 nm for $40 \mu\text{C}/\text{cm}^2$ (Fig. 3.5b) to 1.12 nm for $400 \mu\text{C}/\text{cm}^2$ (Fig. 3.5c). This increase is expected, as e-beam exposure is known to induce roughness on PMMA surface even without development, and these will be likely transferred to Si after etching.¹⁷⁰ However, the reported roughness values are still reasonable, especially considering that the Si height for an electron dose of $400 \mu\text{C}/\text{cm}^2$ is almost 600 nm. Such roughness values are within the specifications for several applications, including optics in the visible range, where a roughness below 5 nm is required.¹⁷¹ For negative-tone processing of PMMA, an RMS roughness of 2.66 nm has been reported for a similar development height¹⁵³ and 30.16 nm for conventional positive-tone lithography with PMMA.¹²⁶

3.4. Results and discussion

Using the established procedure in Section 2.2, we fabricated several binary and grayscale structures. Figures 3.6a and b show a line/space pattern with a 50% duty cycle (binary grating) and Figs. 3.6c-f a sawtooth grating as an example of grayscale patterning. With an initial PMMA thickness of 4 μm and using the RF200 recipe from Table 1, we have been able to resolve 2 μm wide lines, as shown in the AFM image of Fig. 3.6b, with an e-beam dose of 40 $\mu\text{C}/\text{cm}^2$. Additionally, by performing grayscale patterning with a dose-modulated exposure, as shown in Fig. 3.6c and subsequent dry development, successful fabrication of sawtooth structures with a 6 μm pitch in Si was achieved, as shown in the AFM images of Figs. 3.6d and e. The sawtooth profile is extracted from Fig. 3.6e across the grating and shown in Fig. 3.6f. The obtained structures highlight the patterning versatility of the method and show its application potential in different fields. To explore the ultimate resolution limit of the method, which is beyond the scope of this work, several steps in the fabrication can be optimized. For example, the spatial dose modulation should be well modeled and fine-tuned, with or without the 3D-PEC module of the BEAMER, which is, anyway, created and optimized for wet development and not for plasma development for etching into Si. In addition, there is a lot of room for optimization of the etching process, including the etching temperature, the gas composition, the chamber pressure, and the RIE and ICP powers.

3. Dry development of poly(methyl methacrylate)

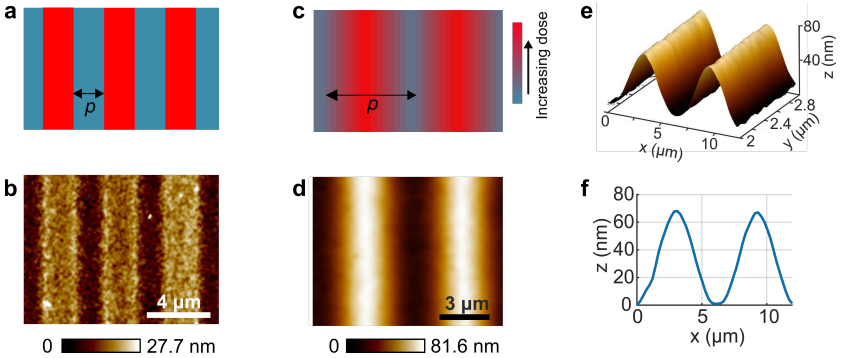


Figure 3.6. Binary and grayscale Si patterning using dry development of PMMA. (a) Exposure layout for binary lines with a pitch p and duty cycle of 50%. (b) AFM micrograph of binary lines in Si after etching with a pitch of 4 μm . Initial PMMA thickness is 4 μm and the electron dose is 40 $\mu\text{C}/\text{cm}^2$. (c) Dose distribution for a grayscale fabrication using dry development of PMMA. (d) and (e) are AFM micrographs of fabricated sawtooth gratings with a pitch of 6 μm . (f) The sawtooth profile of the grating extracted from (d).

3.5 Conclusions

We have studied the behavior of e-beam exposed PMMA during plasma etching and observed a decrease in the PMMA etching rate in SF_6/O_2 plasma as the electron dose is increased. The exact origin of this dependence is unclear, however, surface charging and dose-dependent fluorination of PMMA during etching are expected to play a significant role. Taking advantage of this effect, we have introduced a method to plasma-develop e-beam exposed PMMA on Si. The dry development technique not only eliminates the use of a chemical (wet) development process but also enables the negative-tone patterning using PMMA at much lower doses than conventionally done with PMMA cross-linking (by more than an order of magnitude). Moreover, the controllable variation of the etching rate with electron dose immediately enables this technique for grayscale lithography. Since fluorine plasma is also used for Si etching, PMMA can be developed and transferred to Si in the same

3.6. Acknowledgments

step, speeding up the processing and avoiding unnecessary steps that could lead to loss of pattern fidelity. This enables more streamlined processing for grayscale Si structures and eliminates etch selectivity optimization required for conventional fabrication of grayscale Si structures. The dry development method of PMMA is compatible with standard micro and nanofabrication techniques, making it readily available to be combined with other processes. Moreover, it can be useful for fabricating binary and grayscale structures for diffractive optical elements such as gratings and tapered structures for microfluidics which require both low surface roughness and high-fidelity grayscale patterning. Pushing the resolution of the technique to the nanoscale is also essential to enable it for a plethora of applications where a wet development would be problematic (e.g., pattern collapse). Finally, further investigations will be required to unveil and understand the underlying mechanism of the etch rate variation as a function of electron dose.

3.6 Acknowledgments

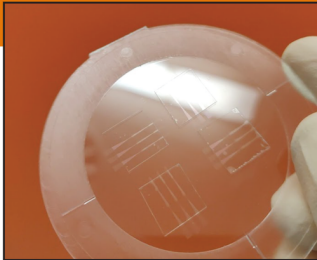
T.M. is supported by the Swiss Nanoscience Institute, Project Number 1702. F.A. was supported by PSI during his master internship and thesis.

3.7 Author contributions

F.A., T.M. and Y.E. conceived and designed the experiments. T.M. and F.A. designed and fabricated the samples. F.A. performed the etching, profilometry and AFM measurements. D.K. assisted with the nanofabrication and supervised the project. All authors contributed to the writing of the manuscript.

Thermoplastic injection molding for nanofluidic device fabrication

4



The following section is based
on a manuscript in preparation

Injection molding of thermoplastics for up scalable fabrication of 3D nanofluidic devices.

**Thomas Mortelmans^{a,b}, Dimitrios Kazazis^a, Jerome Werder^c, Per Magnus Kristiansen^{c,d},
and Yasin Ekinci^{a*}**

^a Paul Scherrer Institute, PSI, 5232 Villigen PSI, Switzerland

^b Swiss Nanoscience Institute, University of Basel, 4056 Basel, Switzerland

^c Institute of Polymer Nanotechnology, University of Applied Sciences and Arts
Northwestern Switzerland (FHNW), 5210 Windisch, Switzerland

^d University College Dublin, School of Mechanical and Materials Engineering, Belfield,
Dublin 4, Ireland

Keywords: 3D nanofluidics, nickel shim, injection molding, PMMA, COP,
grayscale e-beam lithography, particle trapping

*Corresponding author: yasin.ekinci@psi.ch

4. Thermoplastic injection molding for nanofluidic device fabrication

4.1 Abstract

Thermoplastic micro and nanofluidics are increasing in popularity as an alternative to the poly(dimethyl siloxane) (PDMS)-based devices more widely used in academia due to their favorable chemical and physical properties. Additionally, their fabrication is compatible with industrial processes, such as hot embossing and injection molding. Nevertheless, producing devices with sub-micron channel heights and low roughness while retaining high-throughput molding remains challenging. Here, we present the combination of grayscale e-beam lithography (g-EBL) and injection molding as a fabrication route for capillary 3D thermoplastic nanofluidic devices with unprecedented accuracy in the submicron range. We employed g-EBL to pattern the device profile in a poly(methyl methacrylate) (PMMA)-based resist, which served as a substrate for the subsequent fabrication of a negative nickel mold by means of electroforming. The latter was used to injection mold devices into PMMA and cyclic olefin polymer. We show that the 3D height profile of the nanofluidic devices is maintained throughout the entire replication cycle within very tight tolerances. Moreover, somewhat surprisingly, the roughness in the inflow section of the devices was significantly reduced, which we anticipate to be related to the fabrication procedure of the nickel mold due to the fabrication procedure. Lastly, we show that the capillary-based devices can be used to size-dependently trap six particles of various sizes, ranging from 2.16 to 0.75 μm , in a reliable and facile manner while only requiring a 4 μl sample volume. This passive device operation makes it easy in operation and versatile in application. The presented device and fabrication procedure paves the way for applications in various scientific fields, ranging from immunology to neurology and material science.

4.2 Introduction

Micro and nanofluidic devices enable highly precise handling and manipulations of fluids on a sub-mm or sub-micron scale, respectively.¹⁷² This allows for highly multiplexed analysis of a wide variety of samples, ranging from bio-fluids¹⁷³ to chemicals¹⁷⁴ or even cell cultures.¹⁷⁵ A key driving factor for this technology to be widely implemented is the accessibility of device fabrication through so-called soft lithography. This involves the casting of elastomeric materials, such as poly(dimethyl siloxane) (PDMS).¹⁷⁶ Due to its attractive property spectrum and simple processing, PDMS is currently one of the most used materials in academia to perform microfluidic experiments as well as device prototyping. These properties include low interfacial energy, chemical inertness, and high thermal stability as well as high replication fidelity.⁶⁶ However, PDMS also has several disadvantages, such as small molecule absorption, fluid evaporation, and solvent-induced swelling.¹¹⁹ In addition, due to its elastomeric properties, the fabrication of PDMS fluidic devices with sub-micron channel heights becomes difficult.¹⁷⁷ More importantly, the fabrication process used for PDMS-based devices is not upscalable and its commercial applicability is, therefore, inherently limited.¹²⁰

To this extent, thermoplastic materials offer a viable alternative. They are chemically stable, impermeable to gases, low cost, and well-characterized in a biological environment, such as cell culturing and tissue engineering.^{66,121} As its name implies, a thermoplastic material becomes softer and malleable at elevated temperatures. The softened material is, then, pressed or injected into a master mold and cooled in order to re-solidify.¹⁷⁸ One of the most straightforward and accessible thermoplastic patterning methods is hot embossing.¹⁷⁹ Here, a thermoplastic polymer film is placed on top of a master mold inside the chamber that is gradually and homogeneously heated above the glass transition temperature (T_g) of the material, where the material is subjected to substantial softening. Once softened, the pressure is subsequently increased to ensure that the semi-molten polymer flows into the

4. Thermoplastic injection molding for nanofluidic device fabrication

cavities of the master structure. After a given period of time, the chamber temperature is gradually reduced while retaining a high pressure. Once the demolding temperature is reached, the molding pressure is reduced, and the patterned film is removed from the master mold. The periodical heating and cooling of the chamber results in extended thermal cycles, which is time-consuming, limiting throughput and increasing cost. For microfluidic applications where devices are single-use, such as those in point-of-care diagnostics, this is a crucial factor that hinders many promising applications.¹⁸⁰

Alternative techniques, such as injection molding, offer a more commercially viable solution and have shown to enable high-throughput fabrication of microfluidic devices in a wide range of materials, such as polystyrene (PS)¹⁸¹, cyclic olefin copolymer (COC)¹⁸², and poly(methyl methacrylate) (PMMA).¹⁸³ In this technique, plastic granulate is melted and by means of a reciprocating screw, and subsequently pushed into a cavity containing the master structure or mold, at rather high pressures. Once the entire cavity is filled, the cooling process starts, and after solidification, the injection molded part is ejected. A major drawback of this fabrication route, however, is the expensive tooling costs associated with the fabrication of the master structure.¹⁸⁴ Also, the employed molds are often fabricated by micro milling or precision laser machining, which are inherently characterized by significant surface roughness.¹⁸⁵ This can lead to downstream problems with device bonding, introduce optical defects¹²¹ or cause fluid-flow inconsistencies and anomalies.⁷⁴ This becomes even more important when the channel heights are in the submicron regime. Furthermore, injection molding of such submicron features can be challenging and is highly dependent on a large variety of processes and geometrical parameters.¹²³

In this work, we use grayscale e-beam lithography (g-EBL)^{111,115,139} to pattern a mold substrate with a nanofluidic device design characterized by nanoscale height precision over a millimeter length scale, while retaining a high degree

4.2. Introduction

of design flexibility. This is, in turn, used for the cost-effective fabrication of an electroformed nickel mold. The mold consists of nanofluidic devices with different support structures, such as lines and pillars, which are modulated throughout the device to provide optimal support during bonding. In the first section, we discuss the geometry of the device and its different fluidic elements. The second section focuses on the pattern transfer fidelity throughout the fabrication process, as well as the roughness during each processing step. Afterward, the third section concentrates on the use of injection-molded PMMA and COC-based thermoplastic devices for nanofluidic experiments. The device function is evaluated by capillary-driven size-dependent sorting of calibration-grade polystyrene nanoparticles. Two major device advantages concerning its fabrication should be highlighted. Firstly, the minimum lateral features of the device are in the micron range, making molding significantly easier than that of devices with sub-micron features. The nanofluidic regime is achieved by Z-axis modulation, achieving extremely shallow channel profiles. Secondly, its completely passive operation means that it does not require cumbersome integration of inlet and outlet connectors. The presented devices can be used in a wide range of applications, from on-chip bead-based immunoassays for antibody or biomarker detection¹⁸⁶ to single cell analysis¹⁸⁷ and optical nanoparticle size determination.¹⁸⁸

4.3 Experimental section

4.3.1 Grayscale e-beam lithography and nickel-shim fabrication

The nanofluidic devices were patterned on a 4 μm thick PMMA 950K film spin-coated on a 4" silicon wafer following a protocol described elsewhere¹¹¹. The PMMA resist was exposed with a 100keV electron beam system (Raith EBPG 5000+) with a spatially modulated dose. Afterward, the resist was developed in pure methyl isobutyl ketone (MIBK) at 20°C for 5 min. The wafer was dip-rinsed in pure isopropyl alcohol for 20 s and blow-dried with nitrogen (Fig 4.1a). During the development, the areas which were exposed to higher electron doses, have a lower molecular weight and, therefore, a higher dissolution rate. Conversely, areas exposed with a lower electron dose have a relatively higher molecular weight and thus a lower dissolution rate. The patterned structures served as a template structure for electroforming (provided as a service by applied microSWISS) in order to fabricate a nickel shim mold for injection molding (Fig 4.1b). This was done as follows: The structured PMMA resist (on a silicon wafer) was PVD coated with a starting layer, followed by electroplating to produce a nickel shim with a thickness of around 3 mm. After stripping of the resist layer and removal of PMMA remnants by oxygen plasma treatment, the as produced shims were planarized on the back side and polished down to the target insert thickness of 2 mm and machined to the end contour of the insert geometry.

The surface metrology of the device topography at different steps in the fabrication process was performed with a Keyence VK-X1100 at a 50x magnification and a Bruker atomic force microscope (AFM) in tapping mode.

4.3.2 Injection molding and device bonding

Injection molding process

The devices were injection molded using an Arburg 320 (Lossburg, Germany) (Fig 4.1c). This system is characterized by a variety of attractive technical properties. For example, its hydraulic clamping unit can apply forces up to 600 kN. Furthermore, the electrical injection unit has a maximum injection velocity of $142 \text{ cm}^3 \text{ s}^{-1}$, facilitated by a 3-zone screw with a 30 mm diameter and an injection volume of 77 cm^3 . The maximum employable injection pressure was 2000 bar. A more in-depth explanation of the variothermal injection process is described elsewhere.¹⁸⁹

To finally achieve the ideal replication, particularly the injection speed and mold temperature were adjusted. In addition, the mold temperature control was changed from isothermal (IIM) to variothermal (VIM) in order to prevent freezing of the polymer melt during the injection phase, allowing a more accurate replication of the structures. During demolding, on the other hand, the mold temperature is lower to ensure the molded part is stiff enough to prevent deformation and also facilitate demolding. Based on the existing geometry of the mold, the injection speed and mold temperature were increased only moderately (Table 4-1).

Table 4-1. Injection molding parameters.

	Cylinder/ melt temperature at nozzle [degC]	Injection speed [cm ³ s ⁻¹]	T _{mold} isotherm [degC]	T _{mold} variotherm (at injection)	T _{mold} variotherm (at demolding)	P _{hold} (bar)
<i>COP-based devices</i>						
IIM	270	18	95	-	-	650
VIM	270	20	80	105	75	700
<i>PMMA-based devices</i>						
VIM	250	20	75	105	70	700

Device functionalization and bonding

After injection molding, both the PMMA and COP devices were subjected to Ultraviolet/Ozone (UV/O₃)-assisted bonding. The surfaces of the injection molded thermoplastic parts were exposed to highly energetic UV light at a wavelength of 172 nm using an excimer laser light source (Hamamatsu, L12530-01) for 30 s. Subsequently, the activated surfaces were spin-coated with poly(vinyl alcohol) (PVA) in MilliQ at 0.4% and 6000 RPM for 1 min. To enable device bonding, four unpatterned 200 μm thick films were similarly processed and aligned to the devices in the four quadrants. Thereafter, thermal bonding was performed in a Jenoptik Hex 03 at 45 °C and a pressure of 300 N for 1 min (Fig 4.1d).

4.3. Experimental section

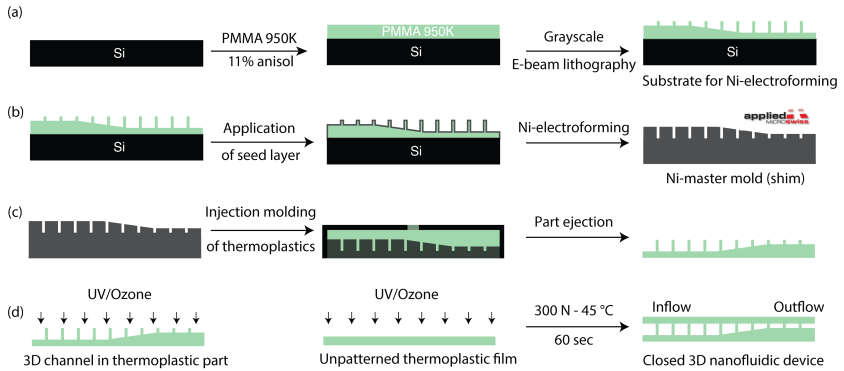


Figure 4.1. Schematic representation of the fabrication process. (a) grayscale e-beam patterning of a PMMA film on a Si substrate, serving as master structure for electroforming (b) Fabrication of the nickel mold by applied microSWISS (c) Injection molding of PMMA and COP onto nickel shim to fabricate 3D nanofluidic structures (d) UV/O₃-assisted bonding of 3D nanofluidic devices

4.3.3 Particle trapping experiments

The device function was evaluated by applying a droplet of a six-particle mixture dispersed in PBS at the inflow of the nanofluidic device. The mixture consisted of the following calibration-grade fluorescent PS particles: 0.5 μm (FlashRed, Bang Laboratories Inc., FSFR003), 0.75 μm (Yellow Green, Polysciences, 17153-10), 0.9 μm (EstaporX, Bangs Laboratories Inc., FC03F-1), 1.02 μm (Yellow green, Polysciences 17154-10), 1.744 μm (Dragon Green, Polysciences 683195) and 2.16 μm (Polychromatic Red, Polysciences 19508-2). Once the entire device was filled, a liquid droplet was added at the outflow in order to prevent the channel from drying out during microscopy. The latter was performed on a Leica DMI5000 microscope equipped with a Leica K5 monochromatic camera with a 10x objective, and a numerical aperture of 0.32. The sample was imaged using both dark-field and fluorescence microscopy. Due to hardware limitations, only the far red (Cy5) and orange (mOrange) spectral regions were imaged. All the images were used in

conjunction with a custom python script, using Scikit-image¹⁹⁰, Pandas¹⁹¹, and Numpy¹⁹² to find the average trapping position of each particle size.

4.4 Results and discussion

4.4.1 Geometry of 3D nanofluidic devices and injection molded parts

The circular injection molded part has a diameter of 65 mm and an inner diameter of 45 mm. The latter was divided into four equal quadrants (Fig 4.a). Each quadrant contained a nanofluidic device consisting of three parallel channels (Fig 4.2b). To operate the device, a 4 μl droplet is applied to the inflow region, where it is capillary-aspirated into the channels. The latter is 300 μm wide and has a depth of 2.6 μm . To reduce the influence of possibly bonding defects at the edge and to ensure a higher overall flow homogeneity, the inflow section is reduced to 100 μm , where it is kept for 500 μm and gradually returns to 300 μm over a distance of 2000 μm . This is denoted as the inflow resistor (I.R.) (Fig 4.2b top). Hereafter, the channel height is reduced from 2.6 to 0.5 μm over a distance of 1 mm. This region is defined as the trapping section (T.S.) and it contains circular distance markers adjacent to the channel to enable the analysis of the particle trapping positions. After the T.S., the height is kept constant at 0.5 μm for 150 μm . This is defined as the 'Shallow Region' (S.R.). This is important to ensure that during e-beam patterning, low-dose areas are not directly adjacent to areas patterned with a higher electron dose, which might influence pattern depth. Consequently, the integration of the S.R. enables greater control over the minimum channel height is obtained. To enable continuous fluid flow, each channel also contains a capillary pump (C.P.) composed of densely packed 20 μm pillars with a 30 μm pitch and a height of 1 μm . The C.P. is connected to the S.S. with a 100 μm connecting wedge (C.W.) that increases the channel height by 0.5 μm over a distance of 1 mm. As the channels are very shallow (for example the S.R. region has an aspect ratio of 600:1), supporting

4.4. Results and discussion

structures are needed to ensure flawless bonding and conservation of the height profile. To this extent, different types of supporting structures were implemented depending on the region. More specifically, three devices with different supporting structures in the inflow section and the T.S. were fabricated. Two devices contained 20 μm pillars organized in either a row or hexagonal array with respect to the fluid flow direction. The latter was arranged in such a way that the inter-pillar distance was 22.5 μm throughout the first section of the device (Fig. 4.3a). The row array had a horizontal pitch of 40 μm and a vertical shift of 20 μm between rows in an effort to ensure a more homogenous filling front (Fig 4.3b).⁷⁴ The third device type included 60 x 20 μm supporting lines that were organized in vertical rows with an inter-row pitch of 40 μm (Fig 4.3c). The corners of the individual lines were rounded to avoid fluidic pinning¹⁹³ or edge flow.⁷⁴ The supporting structures in the S.R., C.W. and C.P. remained the same for all the channels (Fig 4.3d-f). The S.R. was supported by 60 μm pillars with a pitch of 75 μm . Inside the C.W., the pillar diameter decreased to 15 μm at a pitch of 22.5 μm .

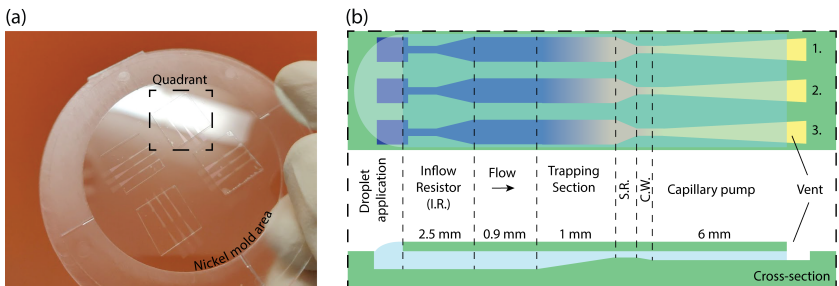


Figure 4.2. Injection molding layout and device specifications. (a) Injection molded part showing the four different quadrants, each containing three parallel fluidic channels. The transparent section shows the area of the nickel mold, whereas the rougher outside circle comes from a section of the injection molding chamber containing the ejector pins. (b) Technical layout of nanofluidic devices. The inflow region and trapping section are supported by either overlapping pillars.

4. Thermoplastic injection molding for nanofluidic device fabrication

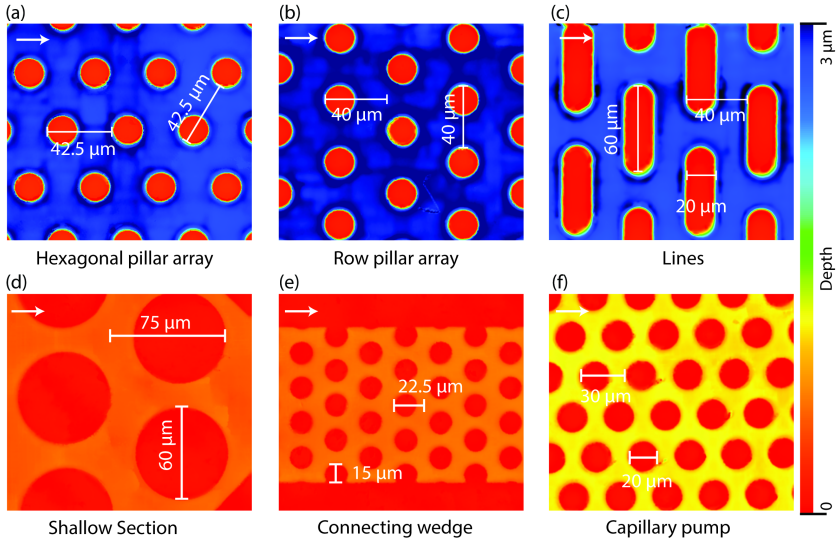


Figure 4.3. Supporting structures inside fluidic devices. (a), non-overlapping pillars (b) or lines (c) and are varied depending on the respective quadrant. The supporting structures in the rest of the device remain constant. The shallow section (S.R.) is supported by 60 μm pillars (d). The connecting wedge bridging the active trapping section to the capillary pump contains 15 μm pillars (e). The capillary pump contains 20 μm pillars (hf). The shown supporting structures were measured on a PMMA-injection molded part with optical laser profilometry. The color is indicative of the height. The flow direction in all regions is highlighted by an arrow.

4.4.2 Pattern transfer fidelity and roughness transfer

To evaluate the homogeneity of the injection molding, each quadrant of the mold also contained a wedge pattern without any supporting structures. The latter was measured at different steps along the fabrication process (Fig. 4.4a-d). The obtained depth after e-beam patterning was similar in all quadrants due to the use of a previously optimized procedure¹¹¹. Moreover, the depth of the patterns in the nickel mold compared were qualitatively similar to that of the g-EBL master. The nickel mold was subsequently used to injection mold

4.4. Results and discussion

the 3D nanofluidic channels into COP and PMMA. To achieve a high degree of pattern replication fidelity, optimization of the injection molding parameters was performed. More specifically, the injection speed was incrementally increased as well as the molding temperature. The latter was also variothermally controlled, meaning that it was higher at the time of injection than at demolding. However, it should be mentioned that due to the free-jetting cavity, the maximum attainable injection speed is inherently limited.

Overall, the fidelity of the wedge pattern in the nickel mold compared to the injection molded parts was high and the profile mostly overlapped in the sub-2 μm regime (Fig 4.4a). In the sections deeper than 2 μm , the largest depth decrease was less than 5% (Fig. 4.4c). As the largest particle size for the envisioned sorting was 2.16 μm , the decrease was not expected to impair the final device function, and it was out of the scope of the current work to further optimize the process. These results demonstrate that it is possible to replicate a g-EBL structure using injection molding in a highly reproducible manner and shows that it is a viable fabrication route for the production of 3D nanofluidic devices.

4. Thermoplastic injection molding for nanofluidic device fabrication

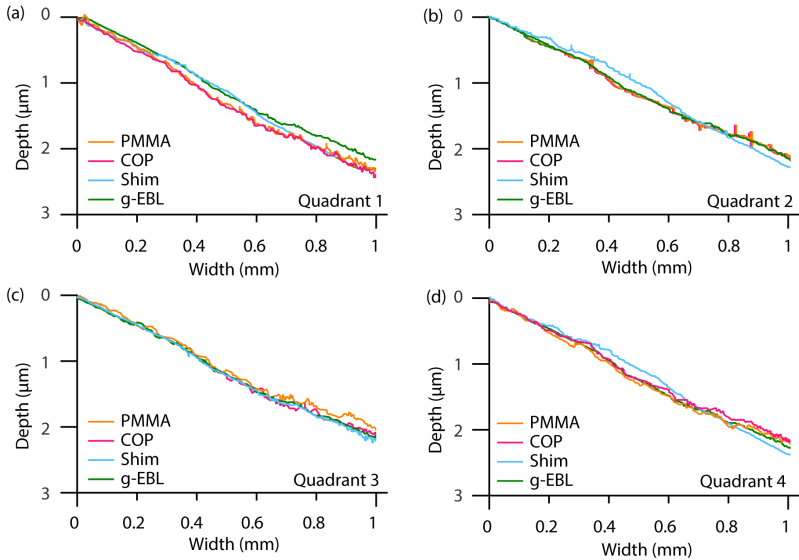


Figure 4.4 Wedge pattern transfer. Wedges without any supporting structures were patterned in all four quadrants of the injection molded part and measured at different points in the fabrication process. The zero point was taken at the shallowest point in the 3D nanofluidic device and served as an alignment point between different processing steps. (a-d).

In addition to the profile transfer fidelity, the roughness of the device was also monitored (Fig. 4.5a). This was done at three crucial points inside the channel. More specifically, in the inflow section, the S.R. and the C.P. For the g-EBL master structure, the largest roughness was seen in the inflow region. This coincides with our previous findings that the deeper g-EBL patterns are, the higher their associated roughness.¹¹¹ However, when the same region is compared between the g-EBL master and the nickel mold, a significant drop in roughness can be seen. This can be explained by the use of nickel electroplating to fabricate the mold. This process is known to decrease surface roughness in a process dependent-manner.¹⁹⁴ The surface smoothing can

4.4. Results and discussion

also be optically observed when comparing the inflow region in the g-EBL master structure (Fig 4.5b) and nickel mold (Fig 4.5c). In the other sections of the device, the roughness was constant during the different pattern transfer steps. Also, the roughness of the injection-molded devices was comparable for both COP and PMMA and similar to that of the nickel mold.

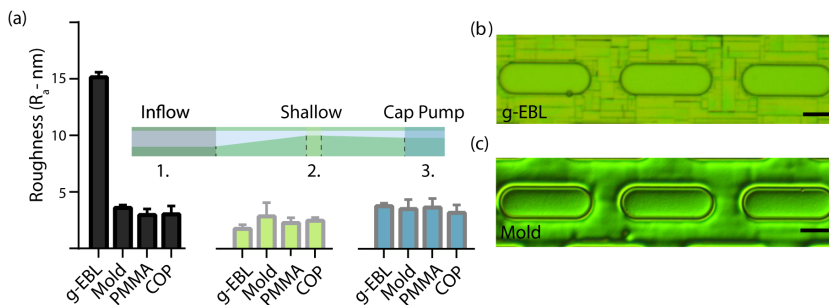


Figure 4.5. Roughness transfer during the fabrication process. The average roughness (R_a) at the inflow, the S.R., and C.P. of a device channel was monitored via tapping-mode AFM (a). The difference in roughness between the g-EBL structure and the nickel mold is highlighted via optical microscopy. (b) shows a bright-field microscopy image of supporting lines in the inflow. (c) shows a phase-contrast image of the nickel mold in the same region. The scale bar represents a length of 20 μm .

4.4.3 Nanoparticle trapping in injection-molded fluidics

The device's functionality was evaluated with respect to its ability to size-dependently immobilize five different particles with sizes ranging from 2.16 to 0.75 μm in a multi-particle mixture. As the S.R. of the devices was 550 nm on average, the multi-particle mixture also included 500 nm particles to investigate any height loss which might occur during the bonding procedure. It was observed that all the devices, regardless of supporting structure or thermoplastic material, retained their designed function (Fig. 4.6a-c). However, from the dark-field images, some small inter-device differences could be seen. For example, the overall trapping line deviation is smaller in

4. Thermoplastic injection molding for nanofluidic device fabrication

PMMA-based devices compared to their COP counterparts. This becomes increasingly evident when comparing devices with pillars in a row array (Fig. 4.6a). In the former, the trapping lines of particle numbers 3 to 5 have large dispersion in the COP-based devices, whereas this is small in the PMMA-based devices. Furthermore, in the case of supporting lines (Fig. 4.6c), the trapping line deviation is also greater in COP-based devices for particle numbers 1 and 2.

Upon quantification of the particle trapping position, the difference between both device materials becomes even more pronounced (Fig. 4.6d-f). In general, a right shift of the particle trapping positions along the T.S. can be seen in the COP devices when compared to the PMMA-devices. The degree of the right shift was greater for particle numbers 3 to 5, where the channel height is the lowest. This material-dependent shift in trapping position can be explained by the bonding procedure. More specifically, we use UV/O at 172 nm to induce the formation of polar functional groups¹⁹⁵ and to reduce the polymer molecular weight at the surface (for PMMA).^{196-198,196} Due to the short wavelength, the penetration depth into the material is only a few hundred of nanometers, depending on the processing conditions.¹⁹⁹ This leaves the bulk of the material unaffected and enables thermal bonding below the glass transition temperature of the material, without significant channel deformation or height loss. It should, however, be mentioned that the modification depth of the UV/O₃-exposure is not solely dependent on its spectral properties but also on the diffusion length of oxygen inside a specific material.²⁰⁰ It is well known that COP (like all polyolefins) contains certain antioxidants to protect the material from degradation during processing. The presence of small amounts of antioxidants is assumed to be sufficient to quench the generated ozone radicals, possibly reducing the oxygen diffusion length and photo-induced damage in COP. In contrast, PMMA does not contain any additives and thus is subjected to chain scission during exposure to UV/O₃,

4.4. Results and discussion

which reduces the T_g in the top layer of the surface. Furthermore, before UV/O₃ exposure, the glass transition temperature of the injection-molded COP was 102 °C and that of PMMA at 110 °C. This indicates that upon similar pre-treatment and bonding conditions, PMMA-based devices could suffer from greater height loss. As the bonding temperature was the same for both polymeric materials, the net temperature difference between $T_{g, \text{ surface}}$ and T_{bonding} is greatest for PMMA. As a result, particles of the same size will get immobilized earlier in the T.S. than in COP devices.

Also, it was seen that in devices with supporting lines, the trapping positions sometimes overlapped with the inter-line gaps, as in particle numbers 2 and 3 (Fig. 4.6c). Consequently, if the employed particle concentration was too high, a channel blockage could occur. For future device applications, such as particle size determination or on-chip immunoassays, clear trapping is of the utmost importance. From the obtained results, we can conclude that the particle trapping with the smallest dispersion was achieved with PMMA-based devices in a row-type array.

4. Thermoplastic injection molding for nanofluidic device fabrication

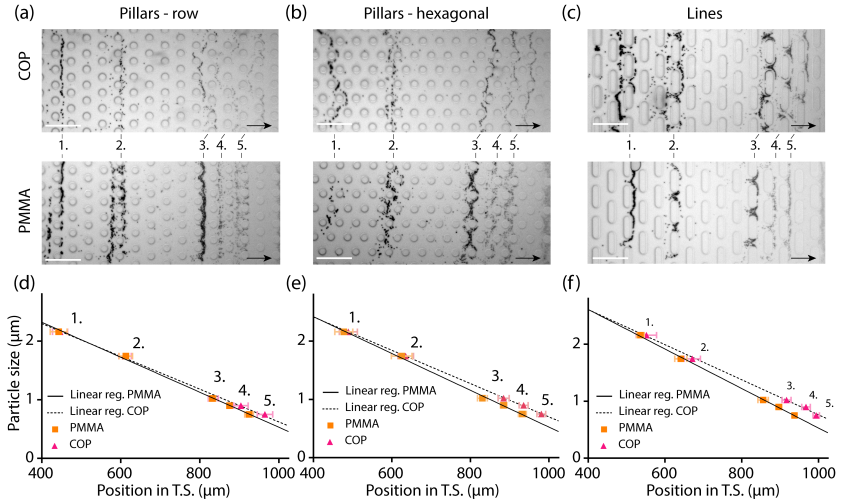


Figure 4.6. Nanoparticle trapping in injection molded 3D nanofluidic devices. Darkfield images of five particle (differing in size) trapping in 3D nanofluidic devices with different supporting structures: (a) pillars organized in a row array; (b) pillars organized in a hexagonal array and (c) elongated pillars with rounded edges. Particle trapping was performed in COP (top row) as well as PMMA (bottom row) injection molded devices. The black arrow indicates the direction of the fluid flow. All the scale bars represent a length of 100 μm. (d-f) Quantification of the respective trapping positions in the different devices. The error bars represent the standard deviation of the trapping positions.

As previously mentioned, the average height in the S.R. of both injection-molded devices was 550 nm. This implies that when bonding-induced height loss is negligible, particles with a 500 nm diameter should be able to flow through. However, when such an experiment was performed, clear trapping lines could be seen in the T.S. for PMMA-based devices containing supporting pillars. In the case of supporting lines, the particles got partially immobilized in the S.S (Fig. 4.7a). For the COP-based devices, no trapping line could be seen, regardless of the supporting structure. On top of this, when

4.5. Conclusion and outlook

investigating the C.P., one could see individual 500 nm particles, evidencing that they were able to flow through the T.S (Fig. 4.7b). These experiments corroborate the conclusion of the five-particle trapping experiments and are clear examples of the material-dependent height loss.

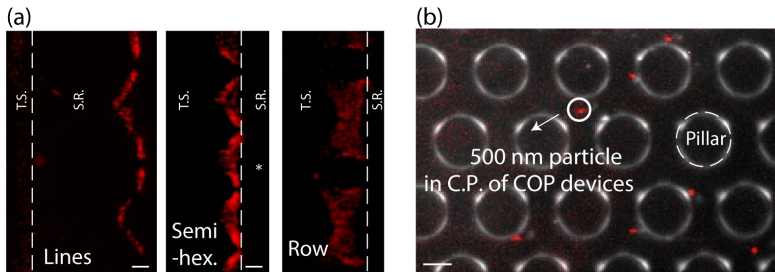


Figure 4.7. 500 nm particle trapping in PMMA-based devices. (a) Fluorescent micrographs of immobilized 500 nm particles in PMMA-based devices. The dashed line indicates the transition between the T.S. and the S.R. (b) An overlay of both a low-illumination dark field and a fluorescent micrograph in the C.P. region of COP-based devices showing flowing 500 nm particles as red dots.

4.5 Conclusion and outlook

We have highlighted the combination of g-EBL and injection molding as an upscalable fabrication route for thermoplastic 3D nanofluidic devices. We have shown that a complex capillary nanofluidic device can efficiently be transferred from e-beam resist to injection molded thermoplastics. During this procedure, the height profile was well maintained in all four quadrants of the fluidic chip, and due to the nickel shim fabrication method, a reduction in surface roughness could be observed. However, the latter also induced slight changes in pattern depth and morphology, which need to be considered for future device prototyping. Additionally, we showed that the devices operated well in both thermoplastic materials (COP and PMMA). The nanoparticle trapping lines were best defined in devices containing pillars in a row array, when compared

4. Thermoplastic injection molding for nanofluidic device fabrication

to the hexagonal pillar array and line structures. Moreover, the nanoparticle trapping experiments also showed that COP-based devices exhibited less bonding induced height reduction.

For future work, we would like to use the injection molded devices to perform on-chip immunoassays in similarity to thermoplastic devices fabricated through nano-imprint lithography¹⁸⁶. In addition, it would be of benefit to further explore alternate PVA functionalization and bonding strategies to increase the upscalability of the device fabrication. For example, it would be possible to use spray coating rather than spincoating to perform the surface functionalization²⁰¹, or alternatively atmospheric plasma modification followed by laser welding²⁰² or ultrasonic bonding²⁰³.

Moreover, as the focus of the current investigation was primarily on demonstrating the feasibility, the size of the capillary pumps was minimized to fit more devices on one injection molded part. Consequently, the concentration of the employed calibration beads had to be rather large. To this extent, it would be of interest to increase the dimensions of the capillary pump so that a larger sample volume can be flown through the T.S. and more dilute samples can be used for the particle trapping experiments.

4.6 Acknowledgments

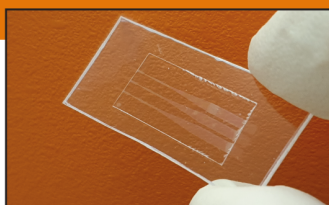
T.M. is supported by the Swiss Nanoscience Institute, Project Number 1702. The authors gratefully thank K. Vogelsang and H. Schiff for the insightful discussions. Roger Bischofberger is acknowledged for performing the electroplating and end-contour machining of the mold inserts used as an external service, which was financed by P.M.K. from FHNW.

4.7 Author contributions

T.M. and Y.E. conceived and designed the experiments. T.M. and J.W. designed and fabricated the devices. T.M. performed fluorescence microscopy and image analysis. D.K. assisted with the nanofabrication. J.W. and P.M.K. performed the injection molding of the devices. Y.E. and P.M.K. supervised the project. All authors contributed to the writing of the manuscript.

A 3D nanofluidic device for SARS-CoV-2 antibody detection

5



The following section has been published in:
ACS Applied Nanomaterials 2022, volume 5.
<https://doi.org/10.1021/acsnm.1c03309>.

Poly(Methyl Methacrylate)-Based Nanofluidic Device for Rapid and Multiplexed Serological Antibody Detection of SARS-CoV-2

Thomas Mortelmans^{a,d}, Dimitrios Kazazis^a, Celestino Padeste^b, Philipp Berger^b, Xiaodan Li^c and Yasin Ekinci^{a*}

^a Laboratory for Micro and Nanotechnology, PSI, 5232 Villigen PSI, Switzerland

^b Laboratory of Nanoscale Biology, PSI, 5232 Villigen, Switzerland

^c Laboratory of Biomolecular Research, PSI, 5232 Villigen, Switzerland

^d Swiss Nanoscience Institute, University of Basel, 4056 Basel, Switzerland

Keywords: 3D nanofluidics, gray-scale e-beam lithography, immunoassay, biofunctionalized nanoparticles, Sars-Cov-2, Influenza A, PMMA

*Corresponding author: yasin.ekinci@psi.ch

5. A 3D nanofluidic device for SARS-CoV-2 antibody detection

5.1 Abstract

The outbreak of SARS-CoV-2 emphasized the value of point-of-care diagnostics, as well as reliable and cost-effective serological antibody tests to monitor the viral spread and contain pandemics and endemics. Here, we present a three-dimensional (3D) nanofluidic device for rapid and multiplexed detection of viral antibodies. The device is made from poly(methyl methacrylate) and contains 3D fluidic channels with nanoscale topography variations on the millimeter length scale, enabled by combining grayscale e-beam lithography and nanoimprint lithography. It works with capillary pumps only and does not require a complex microfluidic setup and pumps, which hinder the widespread usage of micro and nanofluidic devices. The device is designed to size-dependently immobilize particles from a multi-particle mixture at predefined positions in nanochannels, resulting in distinct trapping lines. We show that it can be used as an on-chip fluorescence-linked immunosorbent assay for highly specific and sensitive multiplexed detection of serological antibodies against different viral proteins. Further test flexibility is demonstrated by on-bead color multiplexing for simultaneous detection of IgG and IgM antibodies in convalescent human serum. The particle sorting is further leveraged to enable concurrent detection of anti-spike (SARS-CoV-2) and anti-hemagglutinin (Influenza A) antibodies. The device's applications can be further extended to detect a large variety of diseases simultaneously in a reliable and straightforward manner.

5.2 Introduction

The SARS-CoV-2 pandemic showed the significance of immunoassays for rapid diagnosis to contain further disease spread.² Currently, the state-of-the-art laboratory testing primarily consists out of conventional enzyme-linked immunosorbent assays (ELISAs), which provide a quantifiable insight into anti-SARS-CoV-2 antibody levels.²⁰⁴ However, as it requires extensive sample handling, the procedure is inherently lengthy, cumbersome, and tedious.⁸ In an effort to overcome this, previously commercialized lateral flow immunoassays (LFAs) show an increased potential for point-of-care application due to their shorter incubation time and low cost. Yet, they are characterized by a limited sensitivity and reproducibility and only provide binary information (*yes/no*) on a previous infection.^{205–207} As such, there is a clear benefit for devices and methods that can provide sensitive and specific multiplexed testing rapidly and cost-effectively. In light of this, microfluidic and nanofluidic approaches are of interest because they only require a small sample volume, are characterized by their high throughput and multiplexed testing.²⁰⁸ They are an ideal candidate to overcome the shortcomings of LFAs. However, most of the microfluidic and nanofluidic devices employ micropumps which hinder their widespread usage.

In this chapter, we address these shortcomings by firstly introducing a 3D poly(methyl methacrylate) (PMMA) nanofluidic particle sorter fabricated by state-of-the-art nanofabrication methods. We then demonstrate the potential of the device to perform on-chip multiplexed serological assays for anti-spike (SARS-CoV-2) IgG while providing semi-quantitative data with high sensitivity and specificity. The proposed device is based on fluorescence measurements of trapped biofunctionalized nanoparticles, allowing for high sensitivity as well as point-of-care use²⁰⁹, in contrast to other on-bead or microfluidic methods.^{210,211} The device's versatility and performance are shown by simultaneous on-bead testing of different antibody sub-types as well as concurrent detection of SARS-CoV-2 and Influenza A antibodies. As both

infections provoke similar symptoms²¹², this kind of differential testing would allow the treating physician to provide the correct diagnosis and treatment rapidly and accurately.

Our nanofluidic device is designed to be low-cost and easy to operate. It is entirely made of PMMA and contains only passive capillary microfluidic elements to control the fluid flow without the need for external loading mechanisms, such as syringes or pressure pumps. The latter usually hampers the point-of-care applicability of micro – and nanofluidic devices due to their complex setup and low degree of portability.²⁰⁸ The device is characterized by a unique combination of nano-and microfluidics, which reduces the required sample volume while simultaneously decreasing the microscopical detection volume. The latter has the advantage that the signal is extremely localized and is characterized by a low background signal as this scales well with decreasing dimensions of the detection volume.^{69,70} Our nanofluidic devices feature a 3D wedge profile that allows for the trapping of nanoparticles at predetermined locations, allowing for particle size sorting and size determination (Table S1).

5.3 Methods

5.3.1 Grayscale e-beam lithography

The nanofluidic device was designed using a custom-developed Python script in a GDSII format, where each layer was correlated with a different height to achieve the desired 3D topography in the trapping region and the connecting wedge. The contrast curve, PSF, and nanofluidic design were loaded into the BEAMER software (GenISys GmbH) to perform a 3D proximity effect correction (3D PEC) to ensure a proper dose modulation during subsequent e-beam exposure. An array of 6 devices consisting of three channels was exposed with a base dose of 80 $\mu\text{C}/\text{cm}^2$, after which the resist was developed

as previously described. For a more in-depth explanation of the grayscale e-beam lithography procedure, we would like to refer you to our earlier work.¹¹¹

5.3.2 Nanofluidic master fabrication and nanoimprint lithography

A 4-inch borosilicate wafer was cleaned with acetone and subsequently in IPA, blow-dried with nitrogen, and activated with an oxygen plasma (RIE80, Oxford Instruments) at 40W with a pressure of 20 mTorr for 1 min. The adhesion promoter Ormoprime (Microresist) was spin-coated on the activated surface at 4500 rpm for 45 s and baked on a hotplate at 150 °C for 5 min. 1 mL of the UV crosslinking polymer GMN-PS90 (Optool) was pipetted directly on the surface of the developed e-beam structure, on top of which the borosilicate wafer was placed. The GMN-PS90 was allowed to spread for 20 min to ensure that all the nanofluidic cavities were filled. Subsequently, the polymer was cured under UV light at 365 nm for 6 min at a power of 300 mW/cm². As the GMN-PS90 polymer is inherently anti-sticking, the cured polymer can easily be demolded from the e-beam structures and was immediately ready for further downstream fabrication steps. More specifically, this Optool nanofluidic master was put into a Jenoptik Hex 03 imprinting tool with a 1 mm free-standing PMMA film on top of it. To ensure a homogeneous imprinting, an anti-adhesion coated silicon wafer was placed on the backside of the PMMA film, with a poly(amide)-PDMS-poly(amide) sandwich to equalize the imprinting pressure. A touch force of 300 N was applied and the imprinting chamber was steadily heated to a temperature of 130 °C at 9°/min before the force increased to 17 500 N, where it was kept for 15 min. The chamber was then cooled to 60 °C within 15 minutes before opening and demolding the imprinted PMMA film from the GMN-PS90 master. The device topography was characterized by using a confocal laser scanning microscope (Keyence VK-X1100) at 440 nm with a 150 × magnification.

Afterward, the free-standing PMMA film was activated by oxygen plasma at 80W and a pressure of 0.8 mbar for 20 s and spin-coated with a protective

5. A 3D nanofluidic device for SARS-CoV-2 antibody detection

layer of 10% Dextran (66 kDa, Roth Industries) solution in deionized water at 3000 rpm for 60 s. The array of 6 devices was then mechanically cut into two separate 3×1 devices and the particle protecting Dextran layer was removed by submerging the chips in MilliQ water for 10 min and subsequent drying in a vacuum chamber at 9 mbar for 10 min.

5.3.3 Poly(vinyl alcohol) (PVA) functionalization and bonding

The PMMA surfaces of the 1 mm patterned film and a 200 μm unpatterned film were activated by UV/O-activation at 172 nm for 30 s. This reduces the molecular weight of surface polymer chains and consequently also the surface glass transition temperature ($T_{g, \text{surface}}$) with respect to the bulk material. This leads to increased interactions of PMMA chains and the surface contact area, much like in a nanovelcro-like system. Subsequently, a 0.5% PVA (Polysciences, 15132-500) solution in PBS pH 7.4 was spin-coated at 2000 rpm for 1 min. To remove any excess PVA and aid film homogeneity, the surface of the PMMA nanofluidic chip was spin-washed with deionized water at 2000 rpm for 1 min. Afterward, the patterned and unpatterned PMMA films were aligned and bonded at 750 N and 45°C for 1 min.

5.3.4 Trapping of calibration grade fluorescent polystyrene particles

A five-particle mixture in PBS was made with calibration grade fluorescent polystyrene particles of the following sizes and dyes: 0.9 μm (EstaporX, Bangs Laboratories Inc., FC03F-1), 1.02 μm (Yellow green, Polysciences 17154-10), 1.744 μm (Dragon Green, Polysciences 683195), 2.12 μm (Polychromatic red, Polysciences 19508-2), 3.16 μm (Yellow green, Polysciences 18861-1). A 4 μl droplet was put onto the inlet of the nanofluidic device and after the liquid reached the end of the capillary pump region, a droplet of PBS was placed at the outflow to prevent premature drying of the sample. The fluorescence microscopy was done with a Leica DMi8 microscope using a 40x objective with 0.95 numerical aperture. A custom python script was used to analyze the

5.3. Methods

average trapping positions of the particles and corresponding standard deviation. To compensate for the lateral height discrepancy in the channel, only the trapping in the central region of the channel was considered for the calculation of the trapping position. The particle sizes specified by the supplier were used to fit a linear regression curve to the particle trapping position. The mean particle size and coefficient of variation were recalculated from the linear regression fit.

5.3.5 Fluorescence microscopy

The trapped particles in the active region of the nanofluidic device were fluorescently investigated with a Leica DMI8 microscope using a 10x objective with a 0.32 numerical aperture. The microscope is equipped with an LED light source with a tunable excitation wavelength and a Leica-K5-14400713 detector. To ensure proper filtration of the emission light, filter cubes for the following wavelengths were used: 700, 585, 527, and 470 nm. The same setup was employed when examining the filling of the device's capillary pump region with ATTO 448. For the on-chip SARS-CoV-2 and Influenza A antibody assays, a 40x objective with a 0.95 numerical aperture was used. All the shown fluorescent images were thresholded at the same relative intensity. Hence, brighter beads, which emit more fluorescent light, might appear bigger than their actual diameter.

5.3.6 Preparation of Dynabeads M-280 and MyOne T1 with spike-RBD and hemagglutinin

Dynabeads M-280 (Thermo Fischer Scientific, 11205D) were added to 1 mL of PBS and left on the Spin Magnet (Thermo Fischer Scientific, 12320D) for 4 min to ensure proper magnetic isolation of the beads. Afterward, the beads were washed twice with the same volume of PBS before suspending the washed beads in the final volume used for labeling at a concentration of 700 µg/mL. These suspensions were mixed together with the biotinylated receptor-binding domain (RBD) spike protein (Sino Biological, 40592-V08B-

B) at 600 rpm and 25 °C for 2 h at a concentration of 50 µg/mL, with resuspending the mixture every 30 min. The concentration ratio of beads to spike RBD was kept constant for all the experiments. Subsequently, the beads were washed three times in PBS as previously described. For the COVID-19 only experiments, the particles were blocked with Superblock PBS (Thermo Fischer Scientific, 37580) for 30 min at 600 rpm and 25 °C, whereas for the influenza multiplexing experiments, 0.9 mg/mL free biotin (Thermo Fischer Scientific, 29129) was added during the blocking step to saturate all remaining open streptavidin binding pockets. Biotin was only added when multiplexing experiments were performed to inhibit particle aggregation, possibly stemming from the interaction of available biotin-moieties and empty streptavidin binding pockets between different particle sizes. Dynabeads MyOne T1 (Thermo Fischer Scientific, 65601; 240 µg/mL) were washed as described above and were labeled with biotinylated Influenza A H1N1 Hemagglutinin (A/California/04/2009, Sino Biological, 11055-V08B-B; 5 µg/mL). The beads were subsequently blocked in Superblock PBS containing 0.9 mg/mL free biotin for 30 min at 600 rpm and 25 °C. The concentration ratio of beads: was kept constant for all the experiments.

5.3.7 Serological immunoassay – limit-of-detection and test validation

The proof-of-principle of on-bead and on-chip immunoassay was performed by using a chimeric antibody (Sino Biological, 40150-D001; cross-reactivity with SARS-CoV Spike S1) and diluting it in COVID-19 negative human serum (Sigma-Aldrich, H4522). The serum was diluted 1:4 with a spike RBD-functionalized Dynabead 280 suspension in a final volume of 20 µl and left to incubate at 600 rpm for 1 h at 25 °C) after which it was washed three times with PBS (pH 7.4). To validate the binding of the anti-S-RBD antibodies to the antigen-coated beads, the washed particles were incubated with Cy5 donkey anti-human IgG (5 µg/mL). This was done for 1 h at 25°C and 600 rpm, with three subsequent washing steps. To control the flow and trapping functionality

5.3. Methods

of the device, 0.9 μm non-magnetic Estaporix-loaded polystyrene beads were added to the suspension. A 4 μl droplet of the suspension was then loaded onto the 3D nanofluidic PMMA chip and after the liquid reached the end of the capillary pump, a droplet of PBS (pH 7.4) was pipetted on the outflow region to halt the further fluid flow. The fluorescent signal in the relevant trapping region was quantified by using a custom Python image analysis script. The script used the *scikit-image* module to identify the relevant fluorescent pixels, perform the background subtraction and the equalization with a top-hat filter. Afterward, NumPy and Pandas were used to calculate the mean signal of the acquired image. The LOD was calculated as specified by *Pum et al.*²¹³ resulting in a fluorescence limit of 3956 arbitrary units. The latter was correlated with the concentration of anti-spike RBD antibodies through a non-linear fit function. It should be mentioned that the number of beads or fluorescent pixels was not characterized. *Assay Validation.* The assay described above was performed with a commercially available patient sample set acquired from Anawa GmbH, COV-POSSET-S, consisting of 19 IgG positive and 10 IgG negative patients. The supplier prepared the serum by collecting whole blood into a tube without any additives and subsequently keeping it at room temperature for 20 minutes. Afterward, the sample was centrifuged for 10 minutes at 3000 RPM and aliquot into small tubes. They were stored at -80 °C until shipment on dry ice. All of the IgG-positive patients had a positive PCR test for COVID-19, whereas the IgG-negative patients had a negative PCR test. The PCR-positive patients were also characterized by the supplier through qualitative indirect ELISA and serological lateral flow tests. In the former, 18 out of 19 patients showed an above threshold value for anti-spike IgG antibodies. The 19th patient had a questionable ELISA readout. However, both the PCR and antibody lateral flow tests of the patient confirmed the presence of SARS-CoV-2 viral RNA and associated antibodies, respectively. Moreover, when tested with the developed device, the patient exhibited a positive result for anti-spike IgG. To this extent, the patient was still included in the IgG-positive population. The highest fluorescence signal of the

negatively-tested patient population was taken as a cut-off value at 6.159 arbitrary units. A higher signal was considered to be a positive result.

5.3.8 Antibody and disease multiplexing

Antibody multiplexing. Dynabeads M-280 were labeled with the COVID-19 spike RBD as previously outlined. Afterward, they were mixed in a 3:4 ratio and incubated with serum from a positive patient control with a high ELISA titer for IgG and IgM antibodies against the spike RBD as well as with a negative patient control, which was tested PCR negative for COVID-19. For color-multiplexed antibody detection, two secondary antibodies were added to the particle suspension: a donkey anti-human IgM Alexa 488 (Bioconcept, 2020-30; 5 µg/mL) and a donkey anti-human IgG Cy5 (Jackson Immuno, AB_2340539; 5 µg/mL). Both were incubated with the washed particle suspension as described in the previous section. The device loading and investigation, as well as associated analysis, were performed in the same fashion. *Disease multiplexing.* As a proof-of-principle, a particle suspension containing spike RBD functionalized Dynabeads M-280 and hemagglutinin functionalized Dynabeads MyOne T1 particles were mixed with purified polyclonal rabbit anti-spike (Sino Biological, 40592-T62; cross-reactivity with SARS-CoV Spike S1) and purified polyclonal rabbit anti-hemagglutinin (Sino biological, 11055-RP01) in PBS. The beads were then immunostained with donkey anti-rabbit Cy3 (Jackson Immuno, AB_2307443) for 1 h at 25°C and 600 rpm, after which the suspension was washed three times with PBS (pH 7.4). 0.9 µm Estaporix flow control beads were added before loading the particles into the nanofluidic device. The relevant trapping lines were investigated and analyzed as previously described.

5.4 Results and discussion

5.4.1 Design, fabrication, and functionalization of a 3D nanofluidic particle sorter

The 3D nanofluidic device necessitates nanoscale topography control over several millimeters and simultaneous integration of various micro and nanofluidic components. To overcome these challenging fabrication requirements, high precision grayscale e-beam lithography (g-EBL) is employed to pattern the master stamp of the nanofluidic device following a process that we developed recently through extensive process optimization (Fig. 5.1a).¹¹¹ g-EBL enables a high degree of control over channel topography down to the sub-micron regime and allows for facile integration of numerous 3D profiles with different height profiles. This is in contrast to non-lithographical techniques, such as HF-dipping, which also allow for the fabrication of wedge-shaped profiles in fluidic devices for similar applications.^{11,188} Additionally, the referenced devices require active pumping, significantly larger samples volumes, do not achieve sub-micron channel heights, and have very limited design flexibility. Our g-EBL high-resolution structure is subsequently replica-molded to obtain numerous negative daughter stamps (Fig. 5.1b). These can be used to nanoimprint the devices into PMMA films with high precision and excellent retention of the channel dimensions (Fig. 5.1c). The combination of g-EBL and nanoimprint lithography makes the device fabrication upscalable and cost-effective. For device bonding, a patterned and an unpatterned PMMA film are activated by exposure to UV/Ozone at 172 nm wavelength. In doing so, the molecular weight of the surface PMMA chains is reduced and consequently also the surface glass transition temperature ($T_{g, \text{ surface}}$) with respect to the bulk material.^{140,214} The latter is favorable for bonding purposes, as it enables bonding at reduced temperatures due to the increased interactions of PMMA chains at the surface, much like in a nanovelcro-like system.²¹⁵ After activation, both PMMA films are functionalized with poly(vinyl alcohol) (PVA) to block non-specific binding

5. A 3D nanofluidic device for SARS-CoV-2 antibody detection

sites on the PMMA²¹⁶ (Fig. S2) and allow for more controlled surface wetting²¹⁷. The functionalized films were then bonded at slightly elevated pressures and temperatures (Fig. 5.1d).

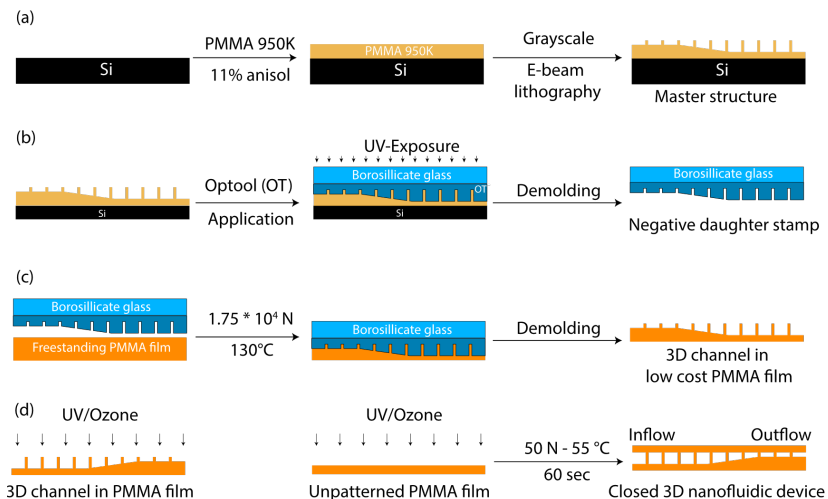


Figure 5.1 The fabrication process for 3D PMMA nanofluidics. (a) g-EBL fabrication of the nanofluidic device in PMMA 950K by exposing the material with a spatially dose-modulated electron beam and development in temperature-controlled pure developer (b) high-resolution replication of the 3D e-beam pattern by using OpTool (OT) GMN PS90, a commercially-available UV-crosslinking polymer with inherent anti-adhesion properties (c) Nano-imprinting the negative master copy into a free-standing, low-cost PMMA film (d) UV/Ozone-assisted bonding of a patterned and unpatterned PMMA film.

Once closed, liquid can be passively aspirated into the 300- μm -wide inflow, enhanced pillars with a 20 μm diameter and 40 μm pitch (Fig. 5.2a-c). The channels containing various passive flow elements were optimized for a controlled and reproducible flow. More specifically, the size and pitch of the incorporated pillars were altered throughout the device (Fig. 5.2c-e) to modulate fluid flow rate and to provide necessary mechanical support against

the collapse of these relatively broad but extremely shallow channels (aspect ratio 375:1) due to the capillary forces (Fig. S1). The chip's inflow region consists of three parallel channels with separate inlets to enable redundancy in testing or multiplexing (Fig. 5.2f). Furthermore, to minimize premature drying of the liquid inside the nanofluidic device and to ensure a constant fluid filling velocity, an inflow resistor (I.R.) was incorporated (Fig. 5.2b - IR). This was achieved by narrowing the channel width after the inflow region to 100 μm and keeping it constant for a length of 500 μm . Afterward, the width is gradually increased to 300 μm . The IR is followed by the trapping region (TR), i.e., a wedged channel of a linearly decreasing height from 3.4 to 0.8 μm over a distance of 1.2 mm (Fig. 5.3a-b).

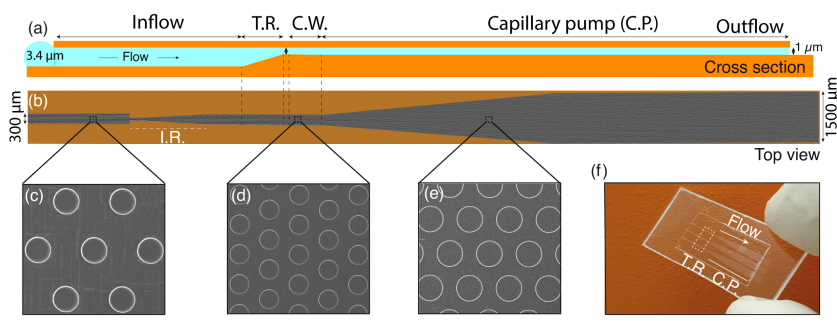


Figure 5.2. Geometry of a 3D nanofluidic PMMA Device. (a), Cross-sectional view of the changing height profile inside the device (b), Scanning Electron Microscopy (SEM) top view image of the device, with the inflow resistor (I.R.) marked by a white dashed line (c-e), SEM images of supporting pillars with a diameter of 20 μm (c,e) and 15 μm (d) in the different regions of the device (f), photograph of the 3D PMMA nanofluidic device showing the narrower inflow and broader capillary pump region. Each device contains three channels which have the same geometrical layout to allow for multiple measurements of the same sample on one device

After the TR, the channel height is kept constant at 0.8 μm for 100 μm before a secondary wedge increases the total height to 1 μm over 1 mm to decrease flow resistance during filling. This connecting wedge (CW) couples the active

device region to a capillary pump containing 20 μm pillars with a 30 μm pitch to enable flow control (Fig. 5.2e). In addition to the capillary pump, the application procedure of PVA was shown to influence the flow behavior of the particles in the TR. This was extensively optimized to maintain a steady flow rate during the entire particle trapping experiment (Fig. 5.3c). More specifically, it was seen that when drop-casting PVA on the PMMA surface, the particle flow significantly slowed down over time. In comparison, when the same solution was spin-coated, nanoparticles kept flowing steadily over time (Video S1). When monitoring the filling velocity of functionalized and non-functionalized devices, an average difference of 3.67% could be seen (Fig. S3b), confirming that the functionalization does not impair device function. The latter is evidenced by the absence of corner flow in the capillary pump region and improvement of the filling front (Fig. S3; Video S2).

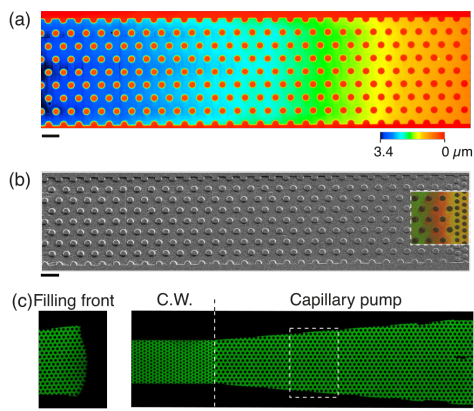


Figure 5.3. Profile of trapping region and capillary filling. (a), topographical confocal laser scanning image of the trapping region showing the decreasing channel height over the channel length (b), SEM image of the trapping region recorded at a 30° tilt-angle with an inset of a light microscopy image of a bonded device at the transition between the trapping and connecting region. (c), Fluorescent image of the filling of the connecting wedge and capillary pump region with ATTO488 and the associated filling front as indicated by the white dashed square

5.4. Results and discussion

The device concept with various micro and nanofluidic components in combination with specific surface chemistry allows for facile device operation that can be used in various applications. This includes particle size determination, sorting, and immobilization, as well as paving the way for applications such as point-of-care diagnostics.

5.4.2 Size-dependent separation of a multi-particle mixture

The ease of use and the performance of the device were highlighted by passive size-dependent particle immobilization of five different fluorescent polystyrene calibration grade particles in the TR (Fig. 5.4a-c). The relationship between the particle trapping position and its nominal diameter was shown to be highly linear ($R^2 = 0.998$; Fig. 5.4b) and could be used to effortlessly determine mean particle sizes with nanometer accuracy (Table S1). Extrapolation from the linear fit (Fig. 5.4c) amounts to a minimal TR channel height of 720 nm, indicating a reduction of roughly 45 nm when compared to the unbonded height of 765 nm. This can be attributed to the surface selective bonding process^{140,214,215} and also highlights the necessity of supporting pillars inside the nanofluidic channel to avoid the collapse of the channel (Fig. 5.3b, inset; Fig. S1).

5. A 3D nanofluidic device for SARS-CoV-2 antibody detection

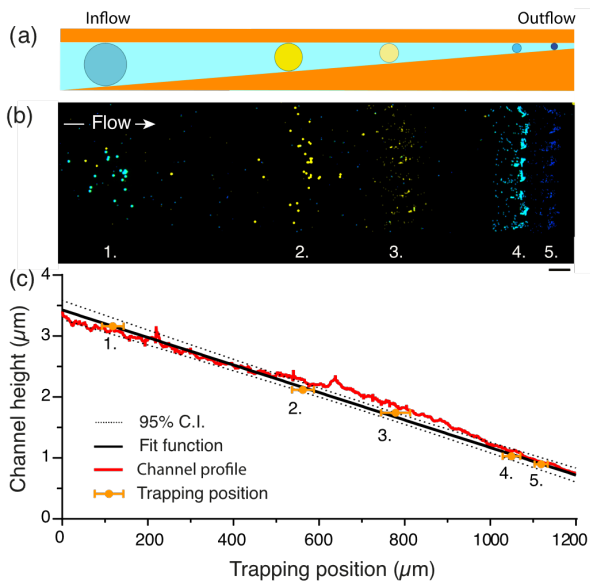


Figure 5.4. Size-dependent trapping of calibration-grade PS nanoparticles. (a) Cross-sectional sketch illustrating the immobilization of calibration grade particles of different sizes and colors (b) Fluorescent micrograph of trapped fluorescent polystyrene calibration grade particles (c) Plot correlating the mean trapping position with the mean particle size. The error bars represent the standard deviation of the trapping position. The dotted lines show the 95% confidence interval of the linear regression fit. All scale bars represent a 50 μm length.

5.4.3 Evaluation of on-chip capillary immunoassays for SARS-CoV-2 IgG antibodies

By using the size-dependent immobilization properties of our nanofluidic device, we developed an on-bead immunoassay for the detection of specific SARS-CoV-2 antibodies in human serum by concentrating the relevant nanoparticles at predetermined locations. Our immune system fights infection and eliminates foreign bodies using innate and adaptive mechanisms, where the latter requires growth and rearrangement of gene elements to produce antibodies that specifically bind to invading antigens. The most commonly found antibody type in human serum is immunoglobulin G (IgG)²¹⁸, making it a valuable target for immune status characterization. One of the major antigens of SARS-CoV-2 associated IgG antibodies is the surface trimeric spike (S) protein, which plays a vital role in facilitating the entry of the SARS-CoV-2 into human cells.²¹⁹ The receptor-binding domain (RBD) of the S-protein (S-RBD) is an immunodominant target for SARS-CoV-2 antibodies²²⁰. To enable their on-chip detection, we used the high-affinity interaction between streptavidin and biotin to couple biotinylated S-RBD to the surface of 2.8 μm streptavidin-coated beads (Fig. 5.5; top).

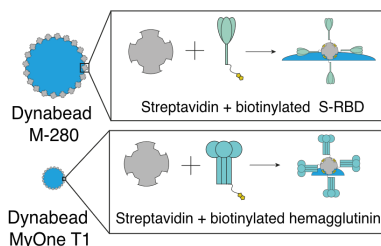


Figure 5.5 Antigen functionalization of nanoparticles. Top: Functionalization of streptavidin-coated Dynabeads M-280 the receptor-binding domain (RBD) of the spike protein. For simplicity, the entire trimeric protein is drawn with a single biotin moiety. The smaller Dynabeads MyOne T1 beads (bottom) are similarly functionalized with a biotinylated hemagglutinin protein.

5. A 3D nanofluidic device for SARS-CoV-2 antibody detection

Once functionalized, the beads were mixed with human serum. If the patient was previously exposed to SARS-CoV-2, the serum will contain antibodies with a specific antigen-binding site for S-RBD and bind to the beads. The latter can be fluorescently visualized by conventional immunostaining procedures. In our case, a donkey-originating antibody conjugated with a red fluorescent dye (Cy5) was used that specifically binds to human IgG (Fig. 5.6a; left). All the previously mentioned functionalization steps, as well as incubation with human serum and the secondary detection antibody, took place out of the device. To benchmark the serological immunoassay, the lowest detectable concentration of a purified humanized anti-S-RBD IgG antibody in human serum was determined. To evaluate the nanofluidic device function, non-functionalized 0.9 μm calibration-grade particles were added to the suspension before applying the particle mixture onto the device's inflow region. The calibration particles serve as a flow control to ensure that the device was fabricated and sealed correctly. Analysis of the corresponding fluorescent signal of the trapped beads revealed a limit-of-detection (LOD) of 0.8 nM (Fig. 5.6b). It should also be mentioned that there are alternative methods of micro/nanoparticle-based microfluidic assays that have achieved sub-nanomolar detection limits for different analytes.^{221,222} However, an LOD of 0.8 nM is comparable to the state-of-the-art microfluidic devices that test for COVID-19 associated IgG antibodies.^{208,211,223} Furthermore, in recent studies, the physiologically relevant concentration of this specific type of anti-spike IgG antibody in recovered COVID-19 infected patients has been shown to be in the range of 9.6 – 28 880 nM.²²⁴ This shows that the developed on-bead and on-chip nanofluidic device operates well within the physiologically relevant concentrations. For future work, we aim to ameliorate the LOD by decreasing non-specific antibody binding²²⁵ or by using brighter and more stable fluorophores.²²⁶

5.4. Results and discussion

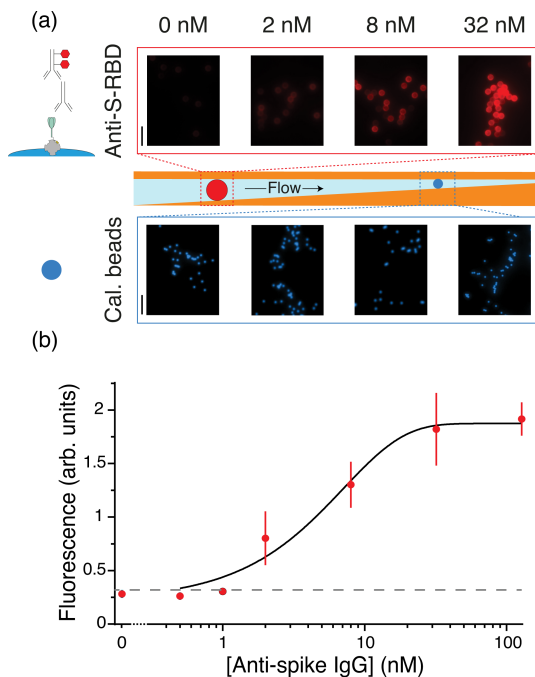


Figure 5.6 Limit-of-detection determination of COVID-19 antibody immunoassay. (a) Top: Fluorescence images of trapped Dynabeads M-280 mixed with a given concentration of anti-S-RBD antibodies in human serum. Middle: cross-section of the trapping region. Bottom: Trapped $0.9\ \mu\text{m}$ EstaporX flow control beads (b) quantification of anti-human IgG Cy5 fluorescent signal on trapped Dynabeads M-280 for a given anti-spike IgG concentration. The dashed line represents the estimated LOD. All the scale bars represent $10\ \mu\text{m}$.

5.4.4 Test validation with COVID-19 patient serum

Additionally, the assay was validated using a patient serum set containing both PCR positive ($n = 19$) and PCR negative ($n = 10$) patients (Fig. 5.7). From the 29 different samples, 28 could be identified correctly according to infection status, with one false-negative result. The signal distribution of

positive cases is to be expected, as immune responses are highly individual and dependent on the infection history of the patient. This corresponds to a test sensitivity of 94.7% (99-65) with a specificity of 100% (100-72) and an area under the curve of 0.95 ($\sigma_{\bar{x}} = 0.05$) according to receiver operator characteristic analysis (ROC) performed in the data-analysis software Graphpad Prism. We note that the false negative was retested and showed a signal above the threshold value. Although we could not reconstruct the root cause of the initial false negative during the blind experimental run, the overall results show the performance of the devices in this early development phase and highlight the potential for further optimization. These findings evidence the applicability of the assay in a real-world setting for the IgG serological characterization of suspected COVID-19 patients²²⁷.

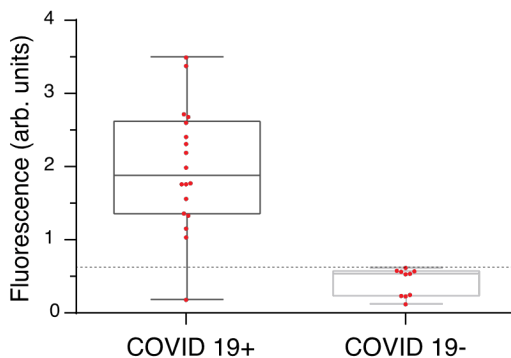


Figure 5.7. COVID-19 antibody test validation. Validation of on-chip anti-spike IgG immunoassay using COVID-19 PCR positive and negative patient samples. Each data point represents the mean signal of each patient. The box plot has whiskers from the minimum to the maximum value, whereas the dashed line graphically indicates the cut-off value separating negative from positive values

5.4.5 Multiplexed detection of SARS-CoV-2 IgG and IgM antibodies

Even though IgG is the dominant immunoglobulin subtype in human serum, it is mainly associated with late-stage and memory-related immune responses. In the case of SARS-CoV-2 infection, specific IgG antibodies become prominent within 7 days post-infection. This hampers the applicability of IgG-specific antigen assays for early-stage disease detection. However, other antibody sub-types, such as immunoglobulin M (IgM), can already be found in human serum 4 days post-infection.²²⁸ Hence, the on-bead and on-chip assay was further developed to include color-multiplexing for simultaneous detection of both antibody subtypes (Fig. 5.8a; Fig. S4). More specifically, the immunostaining solution contained anti-human IgM antibodies conjugated with a green fluorescent dye (Alexa 488) as well as anti-human IgG antibodies conjugated with a red fluorescent dye (Cy5). The anti-IgG fluorescent signal of the COVID-19 positive patient was 25.5 times greater than that of the negative control. Similarly, the anti-IgM signal was 4.9 times higher (Fig. 5.8b). This difference between IgG and IgM is to be expected, given that the investigated COVID-19 positive serum was taken 33 days after symptom onset. As is well known, IgM antibody levels start to decline roughly 21 days after infection, explaining the findings.²²⁹ This experiment shows the potential of color multiplexing to monitor the IgG and IgM response of suspected SARS-CoV-2 infected people.

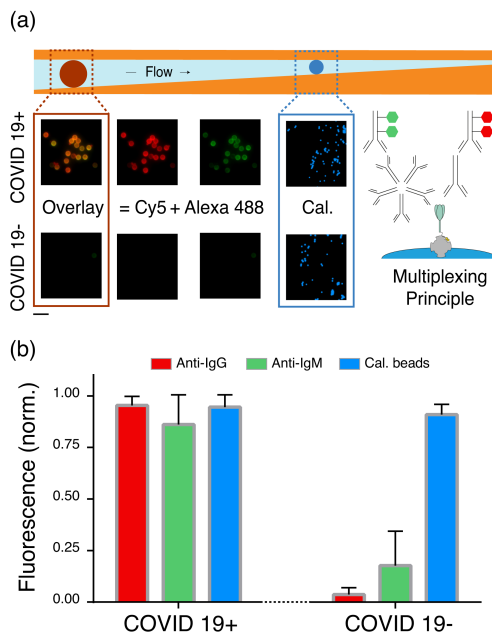


Figure 5.8. On-particle multiplexed antibody detection. (a) Top: The schematic of a color multiplexed IgM and IgG on-bead immunoassay. Bottom: the measured fluorescent signal resulting from the on-chip immunoassay for a COVID-19 positive and – patient. (b) Normalized signal of anti-human IgG cy5, anti-human IgM Alexa 488 and calibration bead fluorescent signal. All scale bars represent 10 μm.

5.4.6 Particle multiplexing for concurrent detection of SARS-CoV-2 and Influenza A antibodies

Furthermore, it is of interest to perform simultaneous differential testing for the presence of antibodies against diseases with similar symptoms. In the case of COVID-19, one of the most symptomatically similar and prevalent viral infections is Influenza A. The latter causes yearly epidemics, and it is one of the major targets of annual vaccination campaigns.²³⁰ To demonstrate the on-chip multiplexing of disease-specific antibodies, 1-μm-size streptavidin-

5.4. Results and discussion

coated beads were labeled with biotinylated hemagglutinin, i.e., immunodominant influenza A-associated protein (Fig 5.5; bottom).²³¹The surfaces of the 1 μm and 2.8 μm particles biofunctionalized with hemagglutinin and S-RBD, respectively, were saturated with free biotin before being added together. This successfully inhibited the aggregation of the SARS-CoV-2 and Influenza A functionalized particles (Fig. S4) and enabled size separation in the 3D nanofluidic device. As a proof-of-principle experiment, the multi-particle suspension was mixed with various combinations of purified polyclonal rabbit antibodies, targeting either the S-RBD or hemagglutinin protein (Fig 5.9a). The beads were subsequently immunostained with a Cy3 anti-rabbit antibody. The obtained signal at their trapping positions is shown to correlate very well with the presence or absence of the relevant antibodies for either S-RBD (SARS-CoV-2) or hemagglutinin (Influenza A), respectively (Fig. 5.9b). This proof-of-principle experiment further emphasizes the versatility of our 3D nanofluidic device within the framework of serological multiplexed immunoassays. The need for such multiplexed testing is further evidenced by a growing body of literature reporting the use of commercially available multiplexed immunoassays.²³²⁻²³⁴ Mostly, these technologies use spatially immobilized antigen spots to perform multiplexed testing, much like in the current rapid tests. This is time-consuming as it requires either manual spotting of the capture antibodies, or advanced patterning techniques, such as inkjet printing.²³⁵ In contrast, the reported device only requires a very small sample volume to be applied at the inlet, as spatial immobilization of the different targets is enabled by the 3D channel profile. As an alternative, bead-based assays have been shown to contribute significantly to the multiplexed testing landscape by enabling analysis of multiple antibody types with a high degree of sensitivity and throughput.^{210,236-239} Nevertheless, they require highly costly dedicated laboratory infrastructure and their analysis is subject to significant supplier variability.^{36,240} Conversely, the presented technology only requires a conventional fluorescent microscope for readout and therefore retains a high degree of usability and has lower up-front costs. The featured

5. A 3D nanofluidic device for SARS-CoV-2 antibody detection

device paves the way for large-scale rapid antibody testing and, in doing so, addresses key shortcomings of currently available lateral flow assays, lacking the possibility for signal quantification.^{205–207}

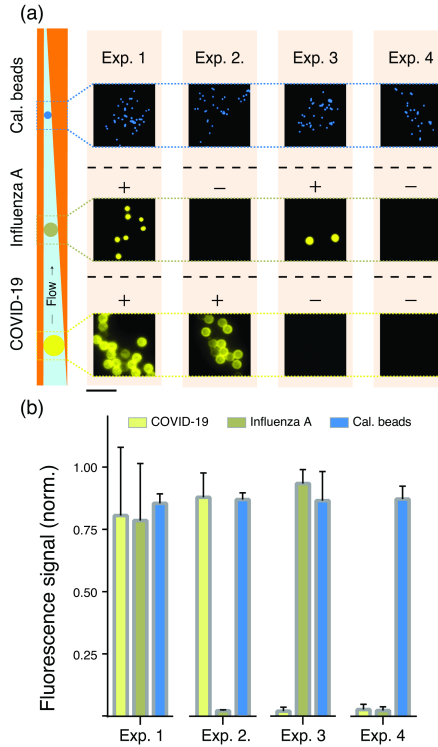


Figure 5.9. Multiplexed viral antibody detection. (a) Left: Schematic of a multiplexed on-chip immunoassay for simultaneous detection of anti-spike (SARS-CoV-2) and anti-hemagglutinin H1N1 (Influenza A) antibodies. Right: fluorescent micrograph of trapped particles of different sizes and different antigen functionalities. (b) Normalized anti-rabbit Cy3 signal at the trapping lines for Dynabeads M-280 and MyOne T1, testing for the presence of SARS-CoV-2 and Influenza A antibodies, respectively. All scale bars represent 10 μm .

5.5 Conclusions

In this chapter, a novel approach towards multiplexed antibody and disease testing by using a novel 3D PMMA-based nanofluidic device was shown. Proof of principle was obtained by showing that calibration-grade particles can be size-dependently immobilized, and their size can be accurately determined from their trapping positions. The size sorting capability of the device was used to concentrate and trap S-RBD-functionalized beads in an IgG SARS-CoV-2 serological assay with a detection limit well within the range of conventional immunoassays and state-of-the-art microfluidic approaches.^{208,211,223} This all while retaining a straightforward and handy operation principle. The test was further cross-validated with PCR and ELISA-tested patient samples, showing a high degree of sensitivity and specificity. Moreover, on-bead color multiplexing has demonstrated the potential to simultaneously monitor the presence of both IgG and IgM antibodies in human sera on single particles for future time-dependent antibody studies. Additionally, we have highlighted the versatility and applicability of the 3D nanofluidic device by detecting anti-S-RBD (SARS-CoV-2) and anti-hemagglutinin (Influenza A) antibodies in control samples using different bead sizes.

Here, we showed multiplexing in two dimensions by employing different particle sizes and conjugated dye colors of the detection antibody. For future work, we aim to extend this by using various fluidic channels for different immunoassays and using color-coded beads of the same size.³⁷ We believe that by this multiplexing capability in four dimensions, i.e., size, bead color, channel and dye color, concurrent detection of more than 100 antibodies on a single chip can be achieved. Moreover, we aim to transfer the fluorescence detection to a portable and compact microscope and eventually adaptable to smartphones, since the devices do not necessitate state-of-the-art infrastructure for immunoassay readout.

5. A 3D nanofluidic device for SARS-CoV-2 antibody detection

The advantages of the developed 3D nanofluidic device in terms of simplicity of operation, reduced sample volume, reduced incubation time, multiplexing capabilities, and cost-effectiveness make it a general-purpose immunoassay method. Moreover, in comparison to conventional ELISA assays, the required sample volume in the reported assay is significantly less. In the aforementioned technique 100 μ l sample is usually required to perform a single assay, excluding duplicate or triplicate testing.²⁴¹ In contrast, the presented method allows for multiplexed detection of various antibody types in 4 μ l human serum. Additionally, by using smaller sample volumes and biofunctionalized particles, reagent cost can also be significantly reduced.³⁵ The functionality of the device can be further enhanced by the incorporation of other capabilities of microfluidic techniques such as preconcentration, mixing, and blood filtration. The applications of the 3D nanofluidic device presented in this work are not limited to on-chip serological immunoassays but can further be extended to various disciplines of biomedical sciences to address key research questions, ranging from mitochondrial size determination in Parkinson's disease²⁴² to nanoparticle-based cancer therapeutics²⁴³, sickle-cell diagnosis²⁴⁴ and many more.

5.6 Supporting Information

Optical micrographs of the device with supporting pillars, filling of the capillary pump region, additional information with respect to disease multiplexing. Supplementary videos showing device filling. These can be found under the following link: <https://pubs.acs.org/doi/10.1021/acsanm.1c03309> and in the thesis appendix.

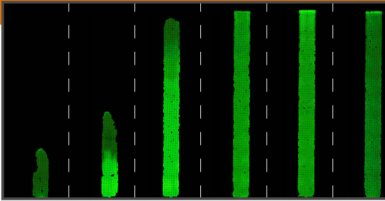
5.7 Acknowledgments

This work is in part supported by the Swiss Nanoscience Institute, Project Number 1702. The authors gratefully thank T. Braun, H. Stahlberg, Gabriel Aeppli, Helmut Schiff, and G.V. Shivashankar for the insightful discussions.

5.8 Author contributions

T.M., Y.E., and X.L. conceived and designed the experiments. T.M. and Y.E. designed the devices. D.K. assisted with the nanofabrication and acquired the SEM images of the devices. T. M. optimized the device fabrication and immunoassays and performed all the experiments and data analysis. P.B. set up the fluorescence microscopy and validated the image analysis. C.P. assisted with and advised on the surface functionalization and device materials. Y.E. and X.L. supervised the project. All authors contributed to the writing of the manuscript.

Multiplexed immunoassays in whole blood



The following section is based on
a manuscript in preparation

A three-dimensional microfluidic capillary system for rapid on-bead multiplexed immunoassays in whole blood

**Thomas Mortelmans^{a,d}, Balz Marty^a, Dimitrios Kazazis^b, Celestino Padeste^b,
Xiaodan Li^c and Yasin Ekinci^{a*}**

^a Laboratory for Micro and Nanotechnology, PSI, 5232 Villigen PSI, Switzerland

^b Laboratory of Nanoscale Biology, PSI, 5232 Villigen, Switzerland

^c Laboratory of Biomolecular Research, PSI, 5232 Villigen, Switzerland

^d Swiss Nanoscience Institute, University of Basel, 4056 Basel,
Switzerland

Keywords: whole blood, FLISA, microfluidics, on-bead, point-of-care,
PMMA, e-beam lithography, hot embossing

*Corresponding author: yasin.ekinci@psi.ch

6. Multiplexed immunoassays in whole blood

6.1 Abstract:

Here, we present a three-dimensional (3D) poly (methyl methacrylate) (PMMA) device that enables on-chip fluorescence-linked immunosorbent assays in a rapid and multiplexed manner. In a linearly tapered channel segment, realized with grayscale lithography, antigen bio-functionalized particles are size-dependently immobilized, after which the device is vacuum dried. The pre-trapped beads serve as the substrate for on-bead fluorescence-linked immunosorbent assays, which reach nanomolar sensitivities without filtering or incubation and washing steps, thereby substantially simplifying the preparation of the immunoassays. Moreover, by leveraging the shallow device dimensions of the device, we show that device read-out is possible in less than 10 min and does not require washing steps due to the small detection volume inside the microfluidic channels. The height profile of the device was further optimized to allow red blood cells to flow through easily. This enables whole blood immunoassays, without the need for sample pretreatment steps. We show that compared to a pure buffer solution, the presence of red blood cells has no detrimental effect on the sensitivity of the assay. Lastly, the device's versatility is highlighted by pre-trapping particles of two sizes, each functionalized with a different antigen, to perform multiplexed on-chip whole-blood capillary immunoassays.

6.2 Introduction

Immunoassays are antibody-based analytical methods for the detection of specific analytes in a wide range of samples.⁹ They are often used in a pharmaceutical and biological research setting²⁴⁵ but also as a diagnostic tool²⁴⁶. They can prevent, manage and monitor disease progression.⁴⁷ However, as they are an inherently labor-intensive procedure and require relatively large sample volumes, their application in a resource-limited environment where rapid read-out is hampered.¹² Alternate methods that can provide rapid and cost-effective diagnosis are therefore needed. An example of such a method are point-of-care (POC) devices, such as lateral flow assays (LFAs).²⁴⁷⁻²⁴⁹ The societal role of LFAs was evidenced by its role in combatting the recent global outbreak of COVID-19.^{4,250}

LFAs can investigate the presence of analytes in a wide variety of bio-fluids, of which plasma is one of the most commonly used. It contains a large variety of proteins that are essential to maintain bodily hemostasis and that can be used as valuable biomarkers. Its composition can reveal infections²⁵¹, autoimmune diseases²⁵² and help the identification of many other disorders.²⁵³⁻²⁵⁵ It also accounts for 55% of whole blood volume. The remaining volume consists of cells, the most abundant of which are the red blood cells (RBCs) or erythrocytes. These are biconcave disks with a thickness of 2.5 μm at the edges and 1 μm in the center. They are rich in hemoglobin, an iron-containing protein that enables the transport of oxygen from the lungs throughout the body and gives them their distinctive red color.²⁵⁶

However, as the read-out mechanism of LFAs is mostly colorimetric, the intense red color of RBCs is known to introduce severe optical or colorimetric interference effects. This translates to significant masking of the signal from the target analyte.²⁵⁷ As a result, numerous methods exist to remove all cellular material from whole blood prior to performing immunoassays with a colorimetric read-out. These include centrifugation²⁵⁸, agglutination²⁵⁹, or

6. Multiplexed immunoassays in whole blood

whole blood filtration²⁶⁰. In LFAs, the last two are often combined in membrane-based dead-end filtration techniques.²⁶¹ Nevertheless, a major downside of using such membranes is that they do not only retain RBCs but due to electrostatic effects, also retain up to 30% of potential plasma biomarkers, effectively reducing the concentration before it reaches the testing area.^{99,100} Furthermore, such filtration could possibly cause hemolysis, ostensibly increasing analyte concentration.²⁶²

Moreover, the flow properties of LFAs are largely determined by the used membrane, which is subject to significant supplier variability.⁷ Also, the employed membranes do not allow for easy flow customization, which hamper the multiplexing potential of such devices. To this extent, micro – and nanofluidic systems offer a viable alternative. Their geometry and flow properties can be precisely tuned depending on the wanted application, by the integration of various fluidic elements, such as resistors, valves, multiple inlets and mixers.⁷⁴ Nevertheless, the integration of filter membranes in micro- and nanofluidic systems is not straightforward and poses significant fabrication challenges. To overcome this, it is possible to integrate on-chip blood plasma separation by exploiting various fluidic principles, such as deterministic lateral displacement²⁶³ or the Zweifach-Fung effect.²⁶⁴ Yet, this necessitates meticulous control over the flow rate by means of active pumping, significantly hampering the applicability of such assays in a POC setting.²⁶⁵ Additionally, as with LFAs, microfluidic POC-devices still require cumbersome pre-patterning of the functional area^{13,16}, which reduces the upscalability.

Here, we propose a poly(methyl methacrylate) (PMMA) three-dimensional (3D) microfluidic device which is capable of performing fluorescence-linked immunosorbent on-bead and on-chip immunoassays directly in whole blood, without the need for sample pre-processing, active pumping strategies or external device pre-patterning. The reported device has a 3D channel profile which enables size-dependent immobilization of biofunctionalized particles.¹⁸⁶

6.2. Introduction

In typical microfluidic devices fabricated through binary lithography, the channel heights remain constant. Grayscale lithography, on the other hand, makes it possible to accurately modulate the channel topography. This introduces an additional degree of freedom, which considerably increases the possible fluid manipulations.

In the 3D channel, the particles are pre-immobilized at a given position in the channel, and whole blood is subsequently flushed through the channel in a second loading step. In the first section of the chapter, we outline the optimization of the channel topography on the one hand to efficiently pre-trap the particles and on the other hand to ensure the easy flow of whole blood through the device.

In the second section of the chapter, we use a channel profile that enables whole blood flow to perform on-chip immunoassays. As a read-out technique, we use an indirect fluorescence immunoassay and thus reduce the optical influence of RBCs. Furthermore, the incubation of the different immunoassays reagents happens concurrently on-chip and because of the reduced channel height, their diffusion distance is significantly reduced in comparison to incubation in standard 96-well plates.^{95,186,266} Consequently, the time it takes for an assay to be read-out is significantly shortened, while simultaneously avoiding cumbersome sample handling steps, such as washing and sequential addition of assay reagents. We show that by pre-trapping two sizes of bio-functionalized beads, it is possible to perform multiplexed detection of antibodies against different antigen targets. Due to the size-dependent particle separation, deposition of such bead-testing lines is straightforward in comparison to LFAs.^{235,267} The device is purely driven by capillary forces and therefore self-powered. This makes its operation uncomplicated and paves the way for extensive application in a POC setting.

6.3 Methods

6.3.1 Device design and grayscale e-beam patterning

The devices consist out of two plexiglass substrates that are bonded together to realize the 3D channels as well as the inlets and outlets. More specifically, a 1 mm plexiglass sheet is patterned with nano-imprint lithography, for which the master stamps are fabricated using e-beam lithography. This is bonded to a 200 μm optical grade PMMA sheet to close the device. The devices were designed using the open-source GDS II-based PHIDL Python module.²⁶⁸ As GDS II files are inherently two-dimensional, the 3D topography of the device's structure was defined by using a separate layer per distinct height level. In total, 1000 layers or gray levels were used. A 4" Si wafer is patterned to contain 2x9 arrays of fluidic channels. Each array of 9 channels was considered to be one fluidic chip (Fig. 6.1a). A more in-depth description of the grayscale e-beam lithography fabrication procedure can be found in our earlier work.^{111,186}

6.3.2 Fabrication of daughter stamps and devices with nanoimprint lithography

After patterning with the e-beam lithography, this negative copy is used for nanoimprint lithography of the microfluidic structures. To do so, a 4" borosilicate wafer was cleaned in acetone for 30 s and subsequently in isopropyl alcohol (IPA) for the same time. Afterward, the wafer was blow dried with nitrogen, and its surface was activated with oxygen plasma in a PlasmaLab 80 RIE (Oxford Instruments) at 20 W with a pressure of 20 mTorr for 1 min. The activated wafer was spin-coated with an adhesion promoter (Ormoprime, Microresist) at 4500 rpm for 45 s. The spin-coated wafer was baked on a hotplate at 150 °C for 5 min. Subsequently, 1 mL of a photo-curable polymer (GMN PS-90, Optool) was pipetted onto the e-beam structure. The coated borosilicate wafer was then carefully placed on top of the master stamp. The GMN-PS90 was left to spread between the glass wafer

6.3. Methods

and the master stamp for a minimum of 20 min. Subsequently, the polymer was exposed to UV light at 365 nm with a power of 300 mW/cm² for 6 min. GMN-PS90 has inherent anti-adhesive properties, so that after curing, the hardened polymer (daughter stamp) could easily be removed from the master stamp.

The daughter stamp was used to hot emboss the negative structures into a 1 mm thick PMMA sheet. To do so, the daughter stamp and the PMMA sheet were put into a Jenoptik Hex 03 hot embossing chamber. A flat 4" silicon wafer with an anti-adhesion coating was placed onto the backside of the PMMA sheet, followed by a poly(amide)- poly(dimethyl siloxane) – poly(amide) sandwich to equalize the pressure on the surface of the PMMA film. Afterward, a touch force of 300 N was applied, and the imprinting chamber was heated to 160 °C at 9 °C/min. Afterward, the force increased to 10 000 N, where it was kept for 15 min. The chamber was then cooled to a demolding temperature of 60 °C before the PMMA sheet was removed from the imprinting chamber (Fig. 6.1b). The topography of the devices was investigated via optical and contact profilometry, with a Keyence VK-X1100 at a 150x magnification and a Veeco Dektak 150 equipped with a 2.5 μm stylus, respectively. On a 4" PMMA two arrays of 9 devices are obtained, which were diced into the single devices. We note the fabrication process described here, makes the device production relatively cheap, since the most expensive step is the fabrication of the master stamp with e-beam lithography from which a large multitude of devices can be obtained.

6.3.3 Device functionalization and bonding

After hot-embossing, the PMMA sheets were activated with oxygen plasma at 80W and 0.8 mbar for 20 s (Tepla AG). This temporarily rendered the PMMA sheet hydrophilic, enabling the spin-coating of a water-soluble protection layer (10% Dextran in MilliQ; 66kDa Roth Industries) at 3000 rpm for 60 s. The PMMA sheet was cut into two chips, each containing 9 devices. Afterward, the protective layer was dissolved by submerging the single chips in deionized water for 15 min. The chips were blow dried with nitrogen and placed under vacuum for a minimum period of 10 min to ensure that the PMMA was fully dried before further processing.

Afterward, the patterned PMMA was activated together with an unpatterned 200 μm thick optical-grade film by UV/ozone irradiation at 172 nm for 30 s. In doing so, the molecular weight of the polymer chains at the surface is reduced and consequently also the glass transition temperature with respect to the bulk material¹⁹⁶. The surfaces of both PMMA films were spin-coated with poly(vinyl alcohol) (PVA; 0.5% in phosphate buffered saline (PBS) with a pH of 7.4) at 2000 rpm for 1 min to prevent unspecific interactions between biomolecules and the surface of the PMMA²¹⁶. Excess PVA was removed by spin-washing with deionized water at 2000 rpm for 1 min. Once coated, both PMMA surfaces were thermally bonded at 750 N and 45 °C for 1 min in a Jenoptix Hex 03 press (Fig. 6.1c).

6.3.4 Capillary filling as a function of wedge profile

The filling of the capillary pump was investigated using a Leica DMI8 microscope equipped with a Leica-K5-14400713 detector. A 5x objective with a numerical aperture of 0.12 was used to have a large field of view. The influence of the wedge profile and the blood concentration on the flow properties of the 3D microfluidic device were investigated by using nine unique channel profiles, in combination with three concentrations of ethylenediaminetetraacetic acid (EDTA)-treated rabbit whole blood

6.3. Methods

(Undiluted, 1:2, 2:40; Envion). To simplify the tracking of the fluid, a fluorescent dye (ATTO488) was added 1:10 to all three solutions to reach a final concentration of 125 μM . During device loading, a time-lapse series was acquired to monitor the evolution of the flow velocity during filling. Also, five minutes after loading the device, a stitched image was taken to assess the filling factor of the capillary pump. The images were analyzed with a custom Python script, where image segmentation was performed to identify the number of fluorescent pixels and determine the corresponding volume. These data were subsequently used to obtain the average flow rate during capillary filling.

6.3.5 Bovine Serum Albumin (BSA) bead functionalization and pre-trapping

Streptavidin-coated 2.8 μm magnetic beads (Dynabeads™ M-280 Streptavidin, ThermoFisher Scientific, 11205D) were washed three times in PBS. Afterward, the desired number of beads was resuspended in a PBS solution containing 160 pmol of biotinylated BSA per μg beads (Pierce™ Bovine Serum Albumin, Biotinylated, ThermoFisher Scientific, 29130). The protein-bead mixture was incubated at 600 rpm and 25 °C for 2 h with periodic vortexing every 30 min and finally washed three times with PBS (Fig. 6.1d). The functionalized beads were diluted in deionized water and applied to the inlet of the microfluidic device so that the trapped beads formed a discernable line in the trapping region upon complete filling of the capillary pump. The filled devices were dried in vacuum for 1.5 h (Fig. 6.1e).

6.3.6 Time-lapse of BSA immunoassay

To investigate the time evolution of the signal when loading the device, a 2 μl PBS-droplet containing 130 nM diluted anti-BSA antibody (Bethyl Laboratories; Bovine Albumin Polyclonal Antibody, A10-127A) and 50 nM Cy5 donkey anti-rabbit antibody was applied onto the inlet of the device. The fluorescence of the beads was monitored over time at 45-second intervals to

minimize bleaching for a total time of 390 s (Fig. 6.1f). As a negative control, a PBS solution solely containing Cy5 donkey anti-rabbit antibody was used and monitored over the same amount of time. The fluorescent images were subjected to a rolling-ball background correction, and the previously obtained particle positions were used to extract the median bead pixel intensity for a given concentration. To do so, image processing algorithms from Scikit-image²⁶⁹ as well as data processing through NumPy²⁷⁰ and Pandas were used¹⁹¹.

6.3.7 Limit-of-detection (LOD) of BSA antibodies

Devices with a minimum channel height of 2.2 μm and containing pre-trapped 2.8 μm BSA-functionalized beads were used to perform a proof-of-principle immunoassay in diluted whole blood (1:40). More specifically, the diluted, EDTA-treated rabbit whole blood (Envion) was spiked with varying concentrations of rabbit anti-BSA antibodies (Bethyl Laboratories; Bovine Albumin Polyclonal Antibody, A10-127A). As secondary detection antibodies, Cy5-conjugated donkey anti-rabbit antibodies (JacksonImmuno, AB_2340607) were added to the spiked samples at 50 nM immediately before filling the capillary devices. The experiment was repeated three times for each anti-BSA antibody concentration. Six minutes after device filling, a fluorescent and a brightfield image of the trapping region was taken. The latter enabled easy identification of the beads via the same Python script described in the previous section. As a comparison, the same experiment was performed in PBS, devoid of any whole blood. The median fluorescence per bead was fit with a sigmoidal function, which was used to calculate the limit-of-detection as the median signal of the control sample that is devoid of anti-BSA antibodies (blank) plus three times its standard deviation.

6.3.8 Multiplexed detection of horseradish peroxidase (HRP) and BSA in whole blood

The 3D profile of the device was slightly adjusted to a minimum channel height of 1.9 μm to enable multiplexed detection of two different antigens in a proof-of-principle setting. More specifically, in addition to the 2.8 μm BSA-functionalized beads, 2 μm functionalized beads (Creative Diagnostics, WHM-G187) were similarly functionalized by incubating them in a PBS solution containing 25 pmol of biotinylated HRP (Thermo Fischer Scientific, 29139) per μg beads. After functionalization, the particles were incubated with a 0.9 mg/mL free biotin (Thermo Fischer Scientific, 29129) at room temperature for 30 min at 600 rpm to reduce cross-particle aggregation. Hereafter, both bead suspensions were added together and pre-trapped in the device as previously described. Subsequently, 50 nM Cy5 donkey anti-rabbit antibody was added to EDTA-treated rabbit whole blood (1:40 in PBS). The latter was spiked with rabbit anti-BSA and/or rabbit anti-HRP at 130 nM to showcase different immunological outcomes. Immediately afterward, a 2 μl droplet of the solution was applied to the inlet of the capillary microfluidic device and left to flow for 6 min. The bead fluorescence at the relevant trapping lines was imaged using a Leica DMi8 equipped with a 40x objective (NA: 0.95) and numerically analyzed with a custom Python script.

6. Multiplexed immunoassays in whole blood

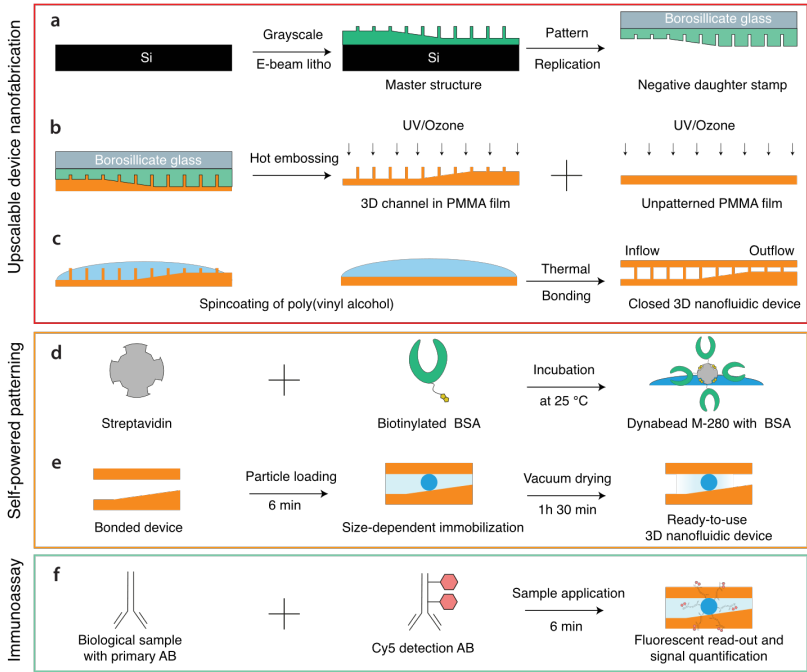


Figure 6.1 Overview of the 3D nanofluidic immunoassay process. (a) Preparation of master structure through grayscale e-beam lithography in PMMA 950K, spincoated on a silicon wafer. The master structure was subject to pattern replication to fabricate a negative daughter stamp for nano-imprint lithography. (b) Hot-embossing of a flat PMMA sheet with the negative daughter stamp, followed by UV/Ozone-activation at 172 nm. (c) Functionalization of the PMMA surface with PVA through spincoating and spinwashing. The two PMMA films were aligned and thermally bonded. (d) Functionalization of 2.8 μm particles with bovine serum albumin via the high-affinity interaction of streptavidin and biotin. Similar functionalization was performed for HRP beads (e) Size-dependent immobilization of bio-functionalized particles and vacuum drying to finalize self-powered patterning of testing lines (f) One drop immunoassay by mixing the sample under investigation with detection antibodies and loading it into the device through capillary forces.

6.4 Results and Discussion

6.4.1 Design of a capillary device with a 3D profile

By varying the channel height inside a microfluidic device, many new functionalities can be obtained, such as advanced flow focusing¹³¹ and on-chip particle size determination¹⁸⁸. We have previously exploited the effect of topographical variations inside fluidic channels to develop a capillary-driven device that can geometrically trap particles in the submicron regime. This effect was exploited to enable multiplexed antibody detection in patient serum.¹¹¹ Nevertheless, the previously reported process required samples to undergo various processing steps outside the device, including serum incubation and secondary antibody labeling. Moreover, due to the submicron channel height, the device was incompatible with whole blood samples. To this extent, we adapted the device geometry, resulting in a self-powered 3D microfluidic device consisting of an inlet, inflow resistor (I.R.), an adapted 3D-region (3DR), and a capillary pump (Fig. 6.2a). In the proposed device, biofunctionalized particles are, first, size-dependently immobilized, and then the device is vacuum dried. This enables on-chip immunoassays without any incubation steps outside of the device. Once dried, a 2 μ l sample droplet can be applied at a 300 μ m inflow channel at a depth of 4 μ m (Fig. 6.2b – left). Here, due to surface tension, the sample will be aspirated into the channel. Subsequently, the sample will flow through an I.R., which is 100 μ m wide and 500 μ m long. These dimensions increase the fluidic resistance and ensure a more homogeneous filling front.⁷⁴ The I.R. is succeeded by the 3DR, which consists of two topographically distinct sections. Firstly, the channel height decreases over 1 mm to ensure size-dependent immobilization of biofunctionalized particles. The second section of the 3DR brings the channel height back to 4 μ m over a distance of 0.5 mm (Fig. 6.2c) and couples the active region of the device to a capillary pump (CP) (Fig. 6.2b - right). The CP is 4 μ m deep, 2 mm wide, and 22.5 mm long, resulting in a total filling

6. Multiplexed immunoassays in whole blood

capacity of ~ 150 nL. It contains pillars with a diameter of $30\ \mu\text{m}$ and a pitch of $75\ \mu\text{m}$ that contribute to flow control during the on-chip immunoassay.⁷⁴

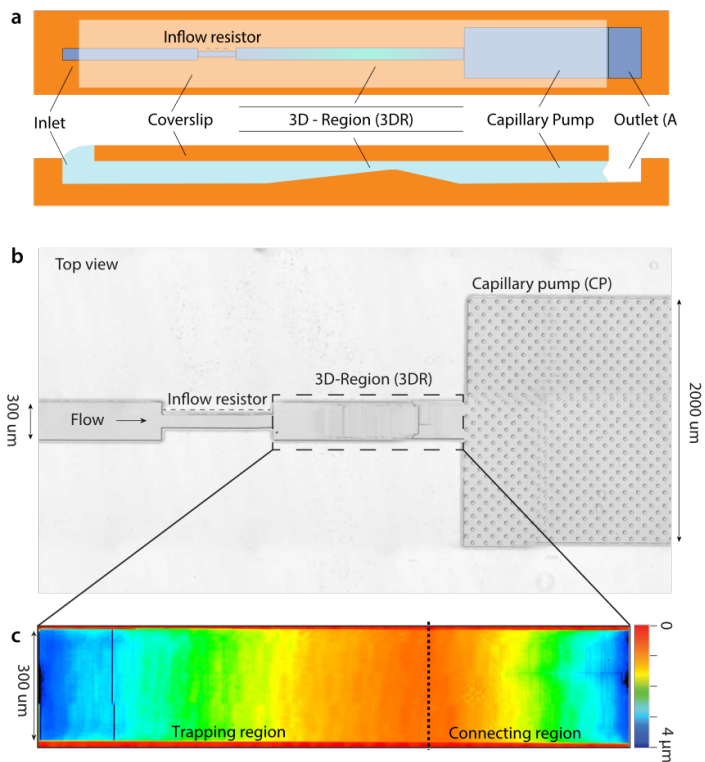


Figure 6.2 3D microfluidic device geometry. (a) Schematic showing the different microfluidic components of the capillary device. The top section shows a top view, and the bottom section is a cross-section to highlight the change in channel topography. (b) Brightfield image of a bonded microfluidic device, showing the flow direction as well as the 3-dimensional region (3DR). (c) Confocal micrograph of the three-dimensional topography in the 3DR of a device with an outflow height of $800\ \text{nm}$.

6.4.2 Adapting the 3D channel profile for uninterrupted flow of whole blood

In order to enable whole blood assays to be easily performed on chip, it is of paramount importance that RBCs do not get halted in the 3DR. When they flow through the aforementioned section, they undergo three phases. Firstly, they flow freely (Fig. 6.3 (i)), after which they gradually compress and expand laterally until the shallowest point of the 3DR is reached (Fig. 6.3 (ii)). Subsequently, if they do not get stuck at this position, they will continue to flow to the capillary pump and decompress to their normal shape (Fig. 6.3 (iii)). The region where cellular compression takes places is defined as the trapping region (T.R.) and where decompression occurs is termed the connecting region (C.R.).



Figure 6.3 Red blood cell flow in 3D channels. Graphical illustration of the three phases a red blood cell undergoes in the channel: i. normal flow ii. compression in shallow region iii. decompression in the capillary pump region.

To identify the appropriate height profile of the device, which would prevent RBC blockage, nine devices were patterned with changing 3DRs. More specifically, the shallowest point was systematically decreased in $\approx 0.2 \mu\text{m}$ increments, while simultaneously retaining a maximum depth of $4 \mu\text{m}$ in the inflow section (Fig. 6.4a). These nine devices were patterned on the same chip by grayscale e-beam lithography followed by nanoimprint lithography into a PMMA sheet (Fig. 6.4b).¹⁸⁶

6. Multiplexed immunoassays in whole blood

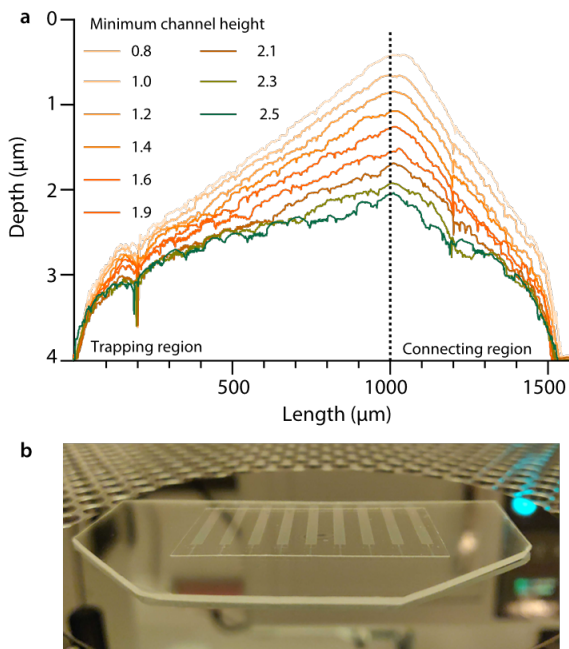


Figure 6.4. On-chip height screening. (a) Profiles of the 9 different wedge topographies which were used to find the ideal outflow height. The trapping region indicates where the particle immobilization takes place. The connecting region is representative of the tapering that connects the trapping region with the capillary pump. (b) Photograph showing a PMMA-based chip containing 9 different devices with different channel topography on top of a 4" Si-wafer as a reference

To enable pre-loading of bio-functionalized beads and to increase the device's hydrophilicity¹⁸⁶, the surfaces of both a patterned and unpatterned PMMA sheet were blocked with poly(vinyl alcohol) (PVA) before sealing the device through UV/O-assisted thermal bonding (see *Methods*). Afterward, the devices were loaded with whole blood at different concentrations, and the filling fraction in the capillary pump region was monitored after 5 min (Fig. 6.5). Here, it becomes noticeable that undiluted blood does not reach the

capillary pump region in the devices with a shallower 3DR due to clogging effects. A qualitative change in the filling fraction of undiluted whole blood can be seen between channels with a minimum depth of 1.6 and 1.9 μm . When an increased dilution is used, this transition in filling fraction is shifted towards smaller minimum channel heights.

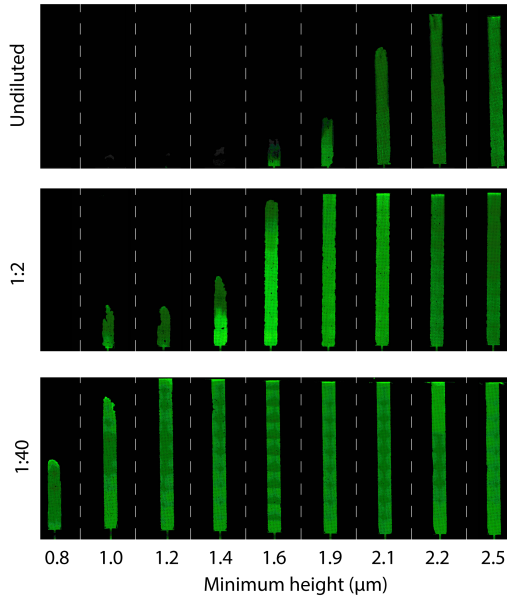


Figure 6.5. Fluorescence images of whole blood flowing through devices with different outflow heights. The shown channels have a width of 2000 μm . The investigated dilutions were: undiluted, 1:2, 1:40 in PBS.

To monitor this effect more quantitatively, a timelapse series was acquired at the beginning of the capillary pump region to monitor the initial filling behavior of the devices (Fig. 6.6). The obtained data was fit with a segmental linear regression to obtain an estimation of the transition height between flow regimes. For more concentrated blood samples, the major transition in filling rate occurs between 1.6 and 1.9 μm . For a more dilute sample, the flow rate

6. Multiplexed immunoassays in whole blood

seems to decrease linearly, dependent on the minimum channel height. This is highly likely due to an increase in the fluidic resistance caused by narrower channels.²⁷¹ It is interesting to note that the aforementioned transition point is around the minimal reported red blood cell thickness of $1.7 \mu\text{m}$.²⁷² To this extent, a new chip containing 9 devices of an equal minimal outflow height of $2.2 \mu\text{m}$ was fabricated.

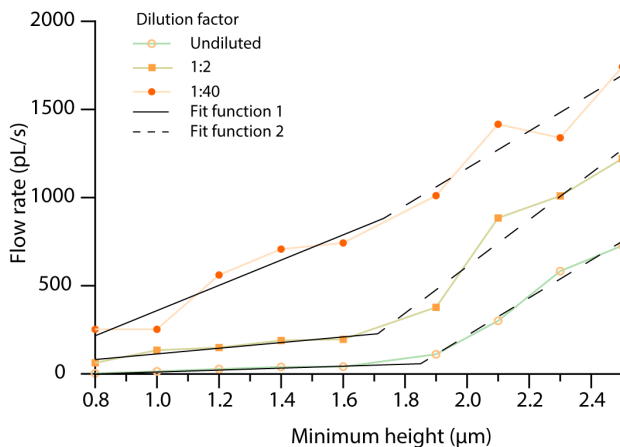


Figure 6.6 Filling velocity of the capillary pump region at different concentrations of whole blood and for various outflow heights. The data was fit with a segmental linear regression fit. The two fit functions are given by the dotted and non-dotted black lines.

6.4.3 Preparation of 3D microfluidic devices to enable on-chip immunoassays

As previously mentioned, LFAs are attractive POC tools because of their rapid readout and the small, required sample volume. Yet, they only provide a binary answer and are characterized by a limited sensitivity.⁶ Alternatively, laboratory-based enzyme-linked immunosorbent (ELISA) assays allow for a high degree of sensitivity and biomarker quantification. Nevertheless, a major

shortcoming is their labor-intensive and time-consuming protocol. For example, a classical sandwich ELISA requires overnight plate functionalization and numerous consecutive sample loading steps with extensive intermediate washing. It is estimated that such an assay takes 5-7 hours for an experienced operator to perform.²⁴¹ Moreover, ELISAs require a minimum sample volume of 100 μ L per well or condition when using conventional 96 well plates, excluding sample volume required for possible duplicate or triplicate testing²⁷³. This is not optimal, as in many life-science research fields, such as structural biology²⁷⁴ or high-throughput drug discovery²⁷⁵, sample volumes are a limiting factor. To address the shortcomings of both POCs and ELISAs, we used the optimized 3D microfluidic device to perform on-chip immunoassays directly in whole blood. This device allows for rapid readout and analysis of small sample volumes, while at the same time, it avoids numerous sample-handling steps. The immunoassay was structured similarly to an indirect ELISA. In these assays, the antigen is pre-functionalized on the plate's surface, and the concentration of the antigen-specific primary antibody in the sample is determined using a secondary antibody conjugated with an enzyme. In our case, we functionalized 2.8 μ m streptavidin-coated particles with biotinylated bovine serum albumin, acting as an antigen (Fig. 6.1d). This was done in phosphate buffered saline (PBS) at a pH of 7.4. Afterward, the functionalized beads were diluted in distilled water and loaded into the device. Once the capillary pump region was filled, the loaded devices were left to dry in vacuum for a period of 1.5 h. Distilled water rather than PBS was used for the final particle dilution to prevent the formation of salt crystals and ensure proper and homogenous drying of the device. The pre-loading of the functionalized beads is similar to the overnight plate functionalization in indirect ELISAs but requires almost 23 hours less time, while retaining a high degree of antibody stability.¹⁶

6.4.4 Rapid one-drop detection of anti-BSA antibodies directly in whole blood

Once the device is properly prepared, on-chip immunoassays can rapidly be performed. As a proof-of-principle experiment, a 2 μ l PBS droplet containing diluted rabbit anti-BSA antibody as well as Cy5-conjugated donkey anti-rabbit antibody was applied onto the inflow region of the device. The former acts as a primary antibody against the antigen target, whereas the latter functions as a secondary fluorescent detection antibody. Hereafter, the liquid was passively aspirated into the fluidic channel and flowed over the pre-immobilized BSA functionalized particles. Due to the large surface-to-volume ratio, attributable to the shallow device dimensions as well as the spherical bead geometry, mass transport is increased, and diffusion times are considerably reduced in comparison to ELISA.^{14,276} This enables rapid binding of the primary anti-BSA antibodies to its antigen. Simultaneously, the secondary anti-rabbit antibodies conjugated with a fluorescent dye will bind to the primary antibodies on top of the beads. This enables indirect fluorescent detection of the binding event between the primary antibody and its antigen. The accumulation of fluorescent signal on the beads was monitored by means of a time-lapse series (Fig. 6.7a). The signal steadily increased over time, reaching a maximum around 360 s. When visually comparing the different fluorescent images (Fig. 6.7b), the intensity difference between positive and negative control samples could already be seen after 45 seconds. Additionally, in the negative control experiment, the fluorescent signal on the particles did not increase over time, evidencing the absence of non-specific binding of the secondary antibody to the bead surface. On the contrary, a slight decrease over time can be seen. This can be explained by partial bleaching of the autofluorescence of the bead, some minor defocusing during time-lapse acquisition as well as bleaching of the unbound secondary antibodies inside the fluidic channel. The bleaching effect also becomes apparent after around 10 min in the case of the BSA-positive control sample. However, it should be

mentioned that based on the previously acquired flow rates, the capillary pump is estimated to be filled after around 100 s, whereas the maximum signal was seen after 360 s. This could imply that not all the available binding sites on the bio-functionalized particles are saturated. For future considerations, it is worth adapting the capillary-pump region to increase the volume of analyte that is flushed over the beads, and therefore the number of primary antibodies on top of the beads' surface.

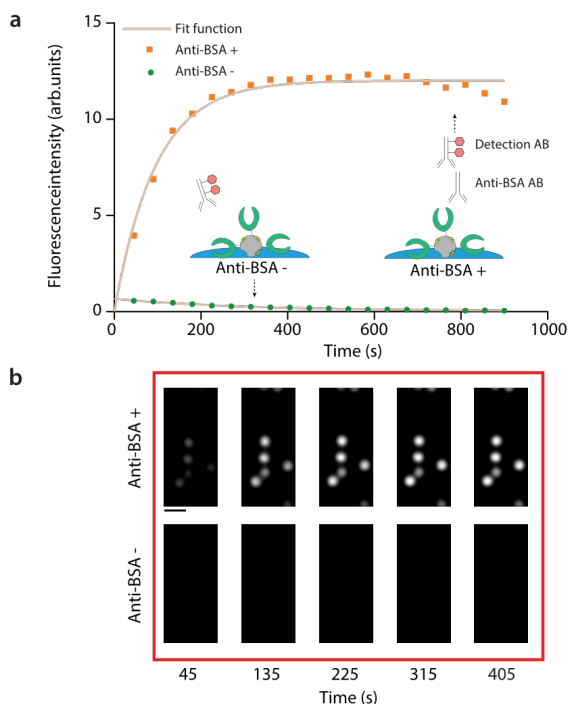


Figure 6.7. On-chip fluorescent immunosorbent assays in whole blood. (a) timelapse showing change in fluorescent signal of the trapped particles over time, both for BSA+ and BSA- samples (b) fluorescent micrographs of BSA+ and BSA- samples at different times after device loading. The scale bar represents 10 μm .

Also, it is important to note that because of device operation, no washing steps were performed, and unbound fluorescent detection antibodies remained in the channel. Consequently, the background signal increases and could potentially mask the fluorescent signal on top of the bead's surface. Other microfluidic assays have addressed this issue by additional washing steps or complex pre-deposition antibodies to decrease the background signal over time and enable signal readout.¹⁶ However, this can be cumbersome and time-consuming. The presented device inherently mitigates this issue because of its shallow dimensions and small detection volume. This ensures that the fluorescent signal in a given region of interest is primarily dominated by the up concentrated fluorescent detection antibodies on the biofunctionalized particles rather than the background.²⁷⁷

6.4.5 On-chip immunoassays reveal a 2 nM limit-of-detection

In the previous subsection, it was shown that it is possible to rapidly detect the presence of BSA-specific antibodies in a physiological buffer solution. As a next step, the whole blood assay was benchmarked against its limit-of-detection in PBS. This was done by determining the lowest detectable concentration of rabbit anti-BSA antibody, while keeping the concentration of secondary detection antibodies constant (Fig. 6.8a). Each sample was left to flow over the pre-immobilized beads for 6 min to ensure maximal binding of all the assay constituents. Afterward, a brightfield and fluorescent micrograph of the beads in the trapping region were acquired and the corresponding fluorescence intensity quantified (Fig. 6.8b - top). The quantified data revealed an LOD of 11 nM in PBS. The same experiment was repeated for diluted whole blood (1:40) and revealed an ameliorated LOD at 2 nM. This discrepancy can be possibly attributed to the blocking effect of serum constituents, which reduces non-specific binding interactions²⁷⁸. This is evidenced by the higher signal of the PBS control in comparison to that in whole blood. Additionally, various other factors, such as pH²⁷⁹ or flow velocity²⁸⁰ can play a significant role. Nevertheless, the achieved LODs, both

for PBS and whole blood, are in the relevant range for a variety of analytes²⁸¹ and disease-specific antibodies²²⁴. The bright field micrographs of the whole blood samples (Fig. 6.8b – bottom) show that even though the hematocrit is drastically reduced by the increased dilution, RBCs are still present in the microfluidic channels. At this point, it is worth emphasizing that due to geometrical size constraints, the RBCs can't cover the pre-immobilized particles on their top and bottom surfaces. This means that from a top view, the RBCs cannot conceal the beads, which ensures that the fluorescent signal originating from the surface of the beads is not diminished by possible scattering and absorption effects.^{282,283} Additionally, it should be mentioned that due to the small height in the trapping region, it is not possible for multiple RBCs to stack on top of each other, further reducing the influence of signal diminishing effects. These experiments highlight that the LOD of BSA-specific antibodies is not negatively impacted by the presence of diluted whole blood.

6. Multiplexed immunoassays in whole blood

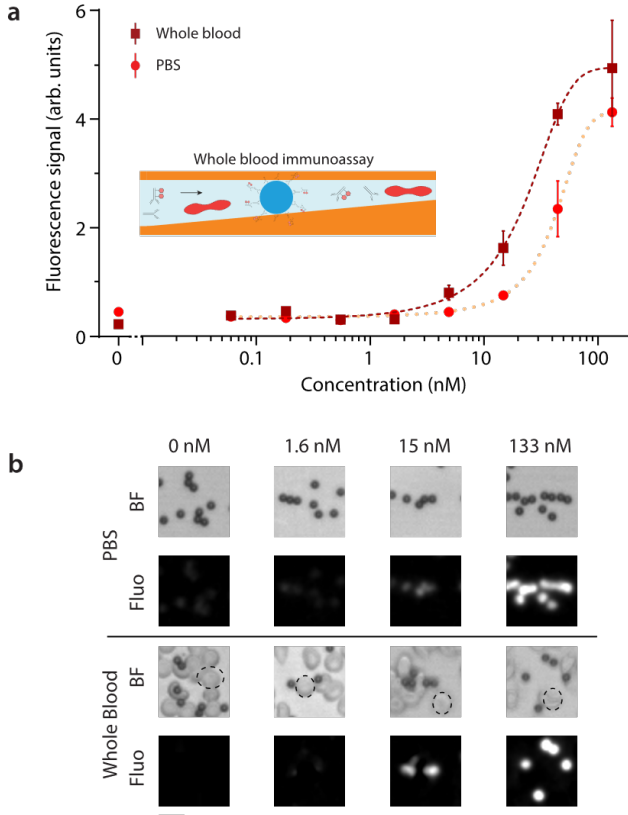


Figure 6.8. Limit-of-detection of immunosorbent assays in whole blood and PBS. (a) limit-of-detection curve showing the fluorescent intensity for different concentrations of anti-BSA antibody in whole blood (red dotted line) and PBS (orange dotted line) (b) Brightfield and fluorescent micrographs of biofunctionalized particles in the TR when loaded with different concentrations of anti-BSA antibody in PBS (top) or whole blood (bottom). The red blood cells are outlined by a dashed line. The scale bar represents 10 μm

6.4.6 Passive particle size-separation enabling facile two-fold multiplexed antibody detection

The passive size-dependent particle immobilization of the device has previously been shown to enable on-chip multiplexed detection of antibodies with distinct antigen targets¹⁸⁶. Here, we show that similar assays are possible using whole blood assays. To do so, the shallowest point of the device was slightly reduced from 2.2 μm to 1.9 μm . This decrease in minimum channel outflow height enabled the trapping of smaller, 2 μm particles. The latter were functionalized with biotinylated HRP added to a suspension consisting of 2.8 μm BSA functionalized beads. Subsequently, both particles were pre-trapped in the trapping section of the 3DR, as explained previously. As a proof-of-principle experiment, diluted whole blood samples (1:40) containing controlled combinations of rabbit anti-HRP and rabbit anti-BSA antibodies were loaded into the device. The evaluation of the binding event of the primary antibodies with their respective antigen targets on the different bead sizes was enabled by the addition of a Cy5-conjugated fluorescent anti-rabbit detection antibody. After an incubation time of 6 min, high magnification fluorescent micrographs were taken at the positions inside the trapping section (Fig. 6.9a). From these images, it becomes clear that the fluorescence intensity at the edges of the biofunctionalized particles is greater than the intensity in the middle. This is to be expected, as the particles are geometrically immobilized by the tapered wedge profile inside the fluidic channel on their top and bottom surfaces. Consequently, the largest interaction between the primary antibodies and their antigen targets occurs on the bead's surface facing the volume of the channel. This is in contrast with other immunoassay technologies that leverage the same effect of decreased channel heights, but where only one of the channel walls is biofunctionalized.⁹⁵ The use of biofunctionalized particles increases the surface-to-volume ratio and the associated reaction field. Consequently, the diffusion distance is even further reduced, possibly increasing reaction rates.^{75,284} The

6. Multiplexed immunoassays in whole blood

quantification of the bead's fluorescent signal is in agreement with the presence or absence of the respective primary antibodies (Fig. 6.9b). More specifically, in exp. 1 (BSA+/HRP+), a large fluorescent signal can be seen at both pre-trapped biofunctionalized particles. However, when either the primary HRP (exp. 2) or BSA (exp. 3) antibody is removed, the obtained fluorescent signal at the relative trapping position drops sharply. If both primary antibodies are removed, and only whole blood spiked with fluorescent detection antibodies is loaded into the device (exp. 4), the signal at the trapping positions drops even further.

This proof-of-principle experiment highlights that by using distinct biofunctionalized particles of different sizes, it is possible to perform on-chip multiplexed antibody detection against different antigen targets or diseases in whole blood samples. This while retaining a low sample volume and rapid sample read-out. The reported device can deliver the results on a similar timescale as LFAs, but provide the possibility for semi-quantitative signal analysis, which is in sharp contrast to the binary result which is obtained by the aforementioned POC devices. Nevertheless, a drawback of the presented technology remains the need for a fluorescent microscope for signal read-out. To this extent, we are currently working on a smartphone-based fluorescent microscope for portable on-chip immunoassays.

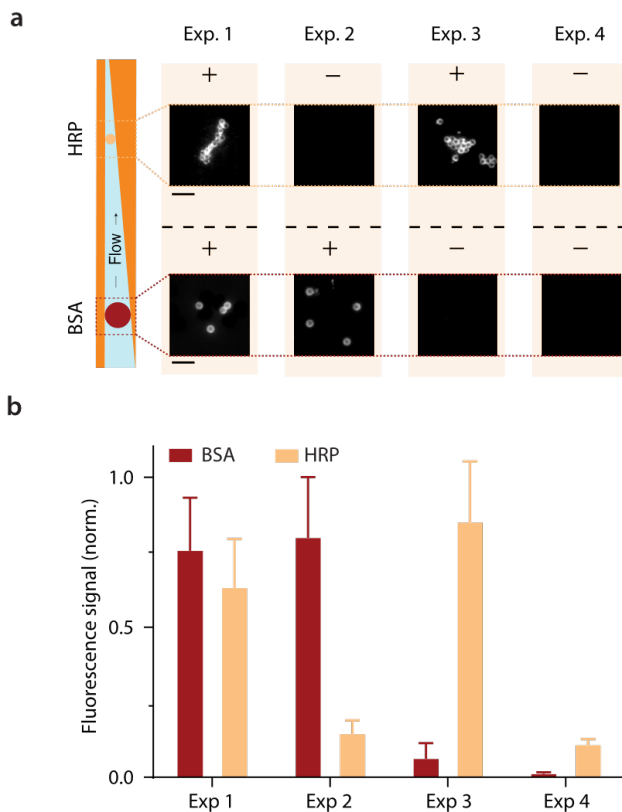


Figure 6.9 Multiplexed on-chip immunoassays. (a) fluorescent images of 2 μm HRP and 2.8 μm biofunctionalized particles in different experimental conditions to show the multiplexing capabilities of the 3D microfluidic device (b) Quantified fluorescent signal from particles shown in (g). The error bars represent the standard error of the mean ($N = 3$). All the scale bars represent 10 μm

6.5 Conclusions and Outlook

The results presented in this chapter show that it is possible to perform immunoassays directly in whole blood by using capillary-driven microfluidic devices with a changing channel topography. The 3D profile inside the microfluidic channel proved to have a critical impact on the filling behavior of both undiluted and diluted whole blood samples. More specifically, it was found that a minimum channel height of 1.7 μm is required to enable facile passage of the RBCs through the trapping region and to reach the capillary pump. It was shown that an optimized 3DR enables efficient pre-trapping of biofunctionalized particles, and due to the high surface-to-volume ratio, sub-10 min sample readout can be achieved. Moreover, we highlight that the presence of whole blood does not negatively affect the limit-of-detection when compared to standard PBS. An adapted version of the 3DR allowed for concurrent pre-trapping of two different particle sizes, each functionalized with a different antigen. This permitted twofold multiplexing in a series of proof-of-principle experiments while retaining very low volume requirements, rapid sample readout, and quantitative analysis.

To increase the portability of the proposed on-chip immunoassay our aim is to develop and use a smartphone-based fluorescence microscope. This technology has a proven track record in the field of fluorescent immunoassays, showing LODs in physiological relevant ranges for a wide range of analytes and diseases.^{58,285} Additionally, we aim to further reduce the limit-of-detection. This can be done in a variety of ways. One could increase the total volume of the capillary pump in an effort to increase the number of bound antibodies on the biofunctionalized particles. Also, the use of brighter and more photostable fluorophores, such as quantum dots²⁸⁶ or the addition of anti-fading chemicals²⁸⁷ could potentially lead to a better signal-to-noise ratio.

Furthermore, even though in the current chapter only twofold multiplexing is presented, it should be emphasized that this can easily be extended by several strategies. More specifically, we have previously reported on the use of color-multiplexing for the simultaneous detection of various antibody types on one single bio-functionalized particle.¹⁸⁶ In addition, it would be possible to use multiple channels within a given microscopic field-of-view. This form of parallel multiplexing can be complemented by increasing the number of particle sizes pre-trapped in the microfluidic channels. Thus, many more analytes could be concurrently analyzed with one single fluorescent micrograph.

On the device fabrication side, we would like to investigate alternate combinations of nanofabrication methods to render the entire process even more cost-effective and upscalable. For instance, one could go from a 4-inch process to an 8-inch one and replace hot-embossing by other high-throughput methods, such as roll-to-roll embossing²⁸⁸ or injection molding¹⁸⁴.

The 3D microfluidic device further extends the use of the previously developed 3D nanofluidic device towards whole blood assays. For future research endeavors, it would be of interest to adapt it to various bio-fluids, such as saliva or urine to increase the device's versatility. Subsequently, by combining this with smartphone fluorescent microscopy, the technology has the potential to make a meaningful impact on the biomarker detection landscape.

6.6 Acknowledgments

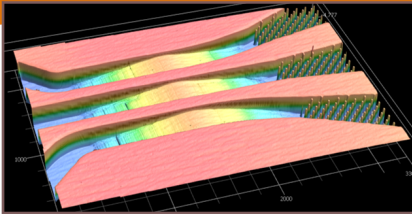
T.M. is supported by the Swiss Nanoscience Institute, Project Number 1702. The authors gratefully thank P. Berger, K. Vogelsang and H. Schift for insightful discussions.

6.7 Author contributions

T.M., Y.E. and B.M. conceived and designed the experiments. B.M. and T.M. designed and fabricated the devices. They also performed the image analysis. D.K. assisted with the nanofabrication. B.M adapted the device's operating principle and geometry to accommodate whole blood assays. T.M. performed the immunoassays, bead functionalization, and fluorescence microscopy. C.P. assisted with and advised on the surface functionalization and device materials. Y.E. and X.L. supervised the project. All authors contributed to the writing of the manuscript.

The power of one F.O.V.: five-fold cytokine screening

7



The following section is based on
a manuscript in preparation

Multiplexed detection of cytokines in 3D nanofluidics with picomolar sensitivity

Thomas Mortelmans^{a,e}, Saša Štefanić^d, Dimitrios Kazakis^a, Balz Marty^a
Celestino Padeste^b, Xiaodan Li^c and Yasin Ekinci^{a*}

^a Laboratory for Micro and Nanotechnology, PSI, 5232 Villigen PSI, Switzerland

^b Laboratory of Nanoscale Biology, PSI, 5232 Villigen, Switzerland

^c Laboratory of Biomolecular Research, PSI, 5232 Villigen, Switzerland

^d Nanobody Service Facility, Institute of Parasitology, University of Zurich, 8057 Zürich

^e Swiss Nanoscience Institute, University of Basel, 4056 Basel, Switzerland

Keywords: ELISA, nanofluidics, PMMA, multiplex, immunoassay, cytokines, biomarkers, sepsis

*Corresponding author: yasin.ekinci@psi.ch

7. The power of one F.O.V.: five-fold concurrent cytokine detection

7.1 Abstract

Sepsis is a major cause of mortality in non-coronary intensive care units. The heterogeneity of the disease and its late-stage recognition attribute to a delayed treatment and a low survivability. To this extent, diagnostic methods which can identify sepsis at an early stage are of significant interest. As dysregulated cytokine release is a hallmark of acute phase sepsis, their multiplexed analysis has been proposed as a technique that could accelerate disease diagnosis. Consequently, laboratory-based immunoassays have been developed that concurrently screen for a multitude of cytokine-associated biomarkers. Albeit more rapid than classical approaches, they are cumbersome and require a centralized laboratory. Hence, cost-effective, rapid, and multiplexed diagnostic tools are needed to increase patient survivability. Here, we present a 3D nanofluidic device that can perform multiplexed assaying of cytokines using a fluorescent immunosorbent assay (FLISA) in an on-particle and on-chip format. To do so, the devices contain three parallel channels which can be individually pre-loaded with distinctly bio-functionalized particles. This allowed imaging of multiple particles in one microscopical field-of-view, facilitating five-fold multiplexed detection. Furthermore, we show that all channels have similar nanoscale topographies and enable size-dependent immobilization of calibration-grade particles down to a diameter of 0.9 μm . The on-chip FLISA could be read-out in 20 min and reached picomolar sensitivities. To enable high precision patterning while retaining scalability, the devices were fabricated by combining grayscale e-beam lithography with nano-imprint lithography. The modular and sensitive detection mechanism of the presented devices will enable applications in immunoassay fields where multiplexed analyte detection is of interest.

7.2 Introduction

Upon infection, various biological pathways are activated to efficiently identify and combat the invading pathogen.²⁸⁹ However, if these mechanisms are dysregulated, an overresponse of the immune system could occur. This can possibly lead to sepsis, an immunological syndrome with potentially lethal consequences.²⁹⁰ The syndrome can be described as a systemic inflammatory response, mostly following either a bacterial²⁹¹ or viral²⁹² infection. If not appropriately identified and treated, it can cause multiple organ failure (severe sepsis), and hemodynamic instability (septic shock).²⁹³ Its difficult diagnosis and complex immunological profile makes timely treatment challenging. Recently, biomarkers, such as cytokines, have been increasingly acknowledged as a viable alternative to the lengthy classical culture diagnosis.²⁹⁴ Cytokines are low molecular weight proteins that play an important role in various cellular processes. They are key regulators in many immunological and homeostatic responses. To this extent, their intra-cellular production is tightly regulated by elaborate signal-transduction pathways.^{295,296} At normal homeostatic conditions, cytokines are present at concentrations of several pg/mL (fM to pM). Only when a person is diseased, do their concentrations increase (up to 1000 fold).²⁷ In addition to sepsis, they serve as relevant biomarkers for a large variety of different diseases, such as asthma²⁹⁷, heart disease²⁹⁸, and various cancers.^{299,300} To this extent, it is of the utmost importance to develop technologies that can rapidly, accurately, and quantitatively characterize their concentration in bodily fluids.

Additionally, it should be noted that the physiological effects of cytokines are highly dependent on relative concentrations of several cytokine combinations at any given time.³⁰¹ In view of this, it is insufficient to monitor single biomarker levels for accurate diagnostics. Rather, multiplexed detection panels should be used.³⁰² Such panels have previously been commercialized, mostly in a bead-based immunoassay format, and can concurrently screen up

7. The power of one F.O.V.: five-fold concurrent cytokine detection

to 25 cytokines.³⁰³ Regrettably, they are usually lengthy, cumbersome, and require a significant patient sample volume. To this extent, it is of relevance to develop technologies that provide the same quantifiable insights in a rapid and cost-effective manner while reducing the required sample volume and required infrastructure.

An alternative candidate that could potentially match the requirements of multiplexed cytokine detection is microfluidics. This technique allows for the integration and miniaturization of various laboratory handlings while reducing incubation times, enabling precise and controlled fluid manipulations as well as different multiplexing strategies.²⁹ However, a significant drawback of multiplexed microfluidic assays is that their functionalization with capture antibodies is usually lengthy, cumbersome and requires advanced patterning methods and multiple washing steps.³⁰⁴

In this work, we report on the development of a capillary-powered 3D nanofluidic device, which employs size-dependent trapping of beads functionalized with cytokine-specific capture antibodies. As the device is purely passively operated, a single suspension of the functionalized particles could be used to pre-patterning numerous test regions in different microfluidic channels, without the need for costly peripheral infrastructure. Furthermore, many of these functional trapping regions could be fitted into a singular microscopical field-of-view (F.O.V.) to enable rapid multiplexed analyte detection.

This unique fluidic system was used to perform on-chip fluorescent immunosorbent assays for six sepsis-associated cytokines within 20 min without necessitating cumbersome washing steps. The device is made from commercially available plexiglass and is patterned using nanoimprint lithography, which is a relatively low-cost fabrication method. In the first section, we outline the device geometry, evaluate its 3D pattern, and investigate its ability to size-dependently sort calibration-grade particles. In

7.2. Introduction

the second section, the device's used for on-chip fluorescent immunoassays (FLISA) and benchmarked against a conventional enzyme-linked immunosorbent assay (ELISA) with respect to its sensitivity, specified by the assays limit-of-detection (LOD). The latter of both methods are discussed, and their respective advantages and shortcomings are outlined. Lastly, the chapter highlights the multiplexing capabilities of the device by performing concurrent on-chip detection of five different cytokines. This is done by employing particle multiplexing and channel parallelization. The presented devices can offer a viable alternative for rapid biomarker quantification in the picomolar regime. In addition to their potential role as a contributor in the field of sepsis diagnosis, the concurrent detection of different biomarkers can pave the way for applications in various other biomedical research fields. For example, the device's could be used for so-called molecular patient fingerprinting in an effort to not only provide quantifiable data, but also specific disease diagnosis.³⁰⁵⁻³⁰⁷

7.3 Methods

7.3.1 Enzyme-linked immunosorbent assays

The enzyme-linked immunosorbent assays (ELISA) were performed by adapting a commercial kit. The kit contained a purified analyte (cytokine) and an ELISA antibody pair of which one was biotinylated. This was used to couple the antibody to either a streptavidin-coated 96-well plate (4 °C overnight at 10 µg/mL) for the conventional ELISA-assay or to the surface streptavidin-coated beads (11205D, ThermoFischer) in the case of the nanofluidic assay (Fig. 7.1a). Commercial kits were purchased for six different cytokines: TNF- α (DY210-05, BioTechne), IL-8 (DY208-05, BioTechne), IL-1 β (DY201-05, BioTechne), IL-6 (DY206-05, BioTechne), IL-10 (DY417-05, BioTechne) and IL-2 (DY202-05, BioTechne). The standard was reconstituted in distilled water according to the supplier's recommendations. The capture antibody was reconstituted in reagent buffer (PBS pH 7.4, 1% Bovine Serum Albumin (BSA)) to a concentration of 10 µg/mL. The detection antibody was reconstituted in the same buffer, according to the supplier's instructions. It should be mentioned that because of the employed detection scheme the denotation for the detection and capture antibodies presented in this chapter are reversed with that specified by the supplier. The reconstituted reagents were left on a rotating wheel for a period of 30 min to ensure a homogenous dissolution. The capture antibody for all analytes, except for IL-8, was diluted to a working concentration of 1.5 µg/mL using reagent buffer. Due to reagent limitations, the IL-8 capture antibody was diluted to 0.3 µg/mL. After diluting the antibody, 100 µL was added to the wells of streptavidin-coated 96-well (Nunc MaxiSorp™) plates and was incubated at room temperature (RT), while continuously shaken at 200 RPM for 1 h. Afterward, all the wells were washed four times with washing buffer (PBS pH 7.4 - 0.05% Tween-20). Subsequently, the cytokines were added to their respective wells at concentrations in the supplier's specified range, including three wells without

7.3. Methods

any analyte to determine the median blank signal. The plate was left to incubate at RT for 1 hr at 200 RPM, after it was washed as previously described. 100 μ L of mouse monoclonal detection antibodies at a concentration of 4 μ g/mL was then added to the wells and similarly incubated. After incubation, the plate was washed, and a secondary anti-mouse F(ab₂)-fragment conjugated with alkaline phosphatase (ALP) was added at concentration of 0.06 μ g/mL. The assay was finalized by a last washing step and addition of reagent buffer containing 1 mg/mL 4-Nitrophenyl phosphate, disodium salt hexahydrate (71768, Sigma-Aldrich). The latter serves as a substrate for ALP, resulting in the formation of nitrophenol and yellow liquid coloration³⁰⁸ (Fig. 7.1b). The substrate incubation was performed at a temperature of 37 °C to ensure optimal enzymatic activity. The resulting coloration was quantitatively read-out using a 96-well plate-reader at a wavelength of 405 nm (reference 630 nm) at different incubation times: 10, 20, 50, 65, 80 and 100 min (Multiskan RC, Thermo LabSystems, Waltham, USA). The LOD was defined as the signal of blank + 3x its standard deviation at an incubation time of 100 min. The obtained optical density was fit with a non-linear fit function and functioned as a benchmark for the 3D nanofluidic particle sorting device.

7. The power of one F.O.V.: five-fold concurrent cytokine detection

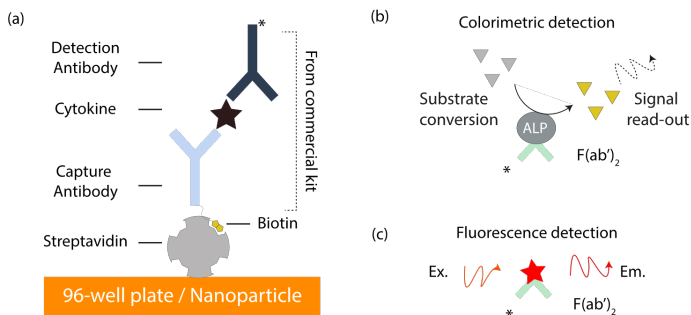


Figure 7.1. Schematic illustration of the different immunoassays. (a) General detection scheme. The asterisk represents the difference in secondary antibody reporter molecule between the ELISA and nanofluidic immunoassay. (b) Secondary antibody conjugated with ALP for colorimetric detection in ELISA (c) Secondary antibody conjugated with Alexa647 for fluorescence detection in the on-particle and on-chip nanofluidic immunoassay. Ex. represents the excitation light, whereas Em. denotes the emission light.

7.3.2 Fabrication of a 3D nanofluidic particle sorter

The 3D nanofluidic device was fabricated using methods outlined elsewhere.^{111,186} Briefly, grayscale electron-beam lithography was used to pattern the nanofluidic devices into a 4 μm thick layer of poly(methyl methacrylate) 950K (AllResist GmbH) on a silicon wafer, which served as a master structure. The master was then copied into several negative daughter stamps made from the UV-curable GMN-PS90 (OpTool) through soft-lithography. These daughter stamps were used to nanoimprint the devices into a 1 mm thick PMMA (plexiglass) sheet. The latter was exposed together with a 200 μm thick unpatterned PMMA sheet to UV/Ozone at 172 nm (Hamamatsu, Excimer Light Source L12530-01) and spincoated with poly(vinyl alcohol) (PVA; 0.4% in MilliQ) at 6000 RPM. Afterward, the two sheets were bonded together at 45 $^{\circ}\text{C}$ with a pressure of 2500 N for 1 min. The 3D topography of the devices was evaluated using Keyence VK-X1100 at a 50x magnification before bonding.

7.3.3 Trapping of calibration grade particles

The particle trapping homogeneity in the three different channels (*see Results & Discussion*) was evaluated via the application of a five-particle mixture in PBS at the inflow region of the device. The following particle sizes were size-dependently immobilized: 0.9 μm (EstaporX, Bangs Laboratories Inc., FC03F-1), 1.02 μm (Yellow green, Polysciences 17154-10), 1.744 μm (Dragon Green, Polysciences 683195), 2.16 (Polychromatic Red, Polysciences 19508-2) and 3.16 μm (Yellow Green, Polysciences 18861-1). A darkfield image of the trapping region in the different channels was acquired with a Leica DMI5000 microscope equipped with a Leica K5 monochromatic camera using a 10x objective (N.A. 0.32). A custom Python script was used to identify the median trapping position for each particle size. This was plotted using GraphPad Prism 8.

7.3.4 Pre-trapping of bio-functionalized particles

Streptavidin-coated beads at a concentration of 1 mg/mL (11205D / ThermoFischer, 65601) were functionalized with a biotinylated capture antibody at 10 $\mu\text{g/mL}$ in PBS pH 7.4 for 1.5 h at 25 °C on a rotating wheel. This was the same for all cytokines, except for IL-8, where the beads were incubated with the capture antibodies at 0.3 $\mu\text{g/mL}$. Afterward, the beads were washed three times with reagent buffer. They were then blocked using the same buffer (PBS pH 7.4, 1% BSA) for 1.5 h at 25°C and 600 RPM. The blocked and functionalized beads were diluted in MilliQ containing 0.125% Trehalose Dihydrate (8897.2, Carl Roth).³⁰⁹ The diluted beads were loaded onto the inflow region of the device and were left to flow until the liquid meniscus reaches the end of the capillary pump was reached (+/- 7 minutes). Finally, the devices were vacuum dried for at least 1.5 h to ensure no liquid remained in the nanofluidic channel.

7.3.5 On-chip limit-of-detection of cytokines

Devices containing pre-trapped bio-functionalized beads were taken out of the vacuum and loaded with a droplet containing a purified cytokine, the associated detection antibody, and a secondary anti-mouse F(ab₂)-fragment conjugated with Alexa647. The solution also contained 0.05% Tween-20 and 2 mM Trolox to respectively ensure a better flow homogeneity and ameliorated fluorescent imaging.^{310,311} As it was evident from preliminary experiments that the nanofluidic assay could not reach the same LOD as conventional ELISA, the screened concentration range was accordingly adapted. More specifically, a serial dilution in PBS was made ranging from 1120 to 4.3 pM. Images were acquired with the same microscopy setup described previously. An LED-based excitation source (pE-300 white, CoolLED) was used at 100% intensity to excite the Alexa647 fluorophore. Flow issues Excitation/emission filtration was done via a Cy5-filter cube (1150471, Leica Microsystems). In conjunction with a fluorescent image, a darkfield image was acquired of the trapped particles to identify the region-of-interest (ROI). This enabled measuring of the median fluorescence in a background-corrected fluorescent micrograph. All these operations were performed using a custom Python which employed NumPy¹⁹², Pandas¹⁹¹ and scikit-image²⁶⁹.

7.3.6 Multiplexed screening of cytokines with one field-of-view

The device was used for five-fold multiplexed detection of cytokines in a proof-of-principle experiment. To do so, three parallel channels were pre-loaded with different combinations of bio-functionalized particles. More specifically, the 2.8 μm particles were functionalized as previously described with either IL-2, IL-1 β or IL-10. Additionally, 1 μm particles (65601, Thermofischer) were functionalized with IL-6 and TNF- α . After functionalization with the relevant biotinylated capture antibodies, any free biotin-binding sites on streptavidin were blocked by an additional incubation step with PBS containing 20 $\mu\text{g}/\text{mg}$ of free biotin (29129, Thermofischer). Three two-particle combinations were

made: IL-2 & TNF-Alpha, IL-1 β & IL-6, IL-10 & blank 1 μm . The blank functioned as a control trapping line, indicating any unspecific binding that might invalidate the assay. The three combinations were each loaded into a different channel, enabling simultaneous imaging of six different particles. Three droplets containing relevant cytokines, detection antibodies and a secondary anti-mouse F(ab₂)-fragment conjugated with Alexa647 were applied at the device's inflow region. After a period of 20 min, darkfield and fluorescent images were acquired and quantified as previously described.

7.4 Results and discussion

7.4.1 The geometry and operation of a multiplexed nanofluidic device

In an effort to provide rapid disease diagnosis, a 3D nanofluidic device, consisting entirely of plexiglass, was developed (Fig. 7.2a). The device was functionalized with PVA prior to bonding to prevent the biofunctionalized particles from adhering to the PMMA. In contrast with previous work¹⁸⁶, no post-functionalization spin wash step was performed and the bonding pressure was adapted. As a consequence, bonding without pattern collapse and without the need for supporting pillars was achieved.

Once bonded, a droplet was applied to the inflow section (Fig. 7.2b). Here, three inlets with a depth of 4 μm , a width of 300 μm , and an inter-inlet distance of 4450 μm are present. The large space between different inlets made it possible to individually load the channels. After loading, the fluid moves from the inflow towards the functional device region, consisting of the trapping region (T.R) and connecting wedge (C.W.). The former gradually reduces the channel height from 4 μm to 0.9 μm over 1000 μm , which is immediately followed by the C.W. that brings the channel height back to 4 μm to couple the T.R. to the capillary pump (C.P.) region. The active device region fits within a single microscopical F.O.V. at a 100x magnification. This enables

7. The power of one F.O.V.: five-fold concurrent cytokine detection

concurrent visualization of all three channels, while simultaneously allowing for them to be loaded with distinct sample solutions or different particle suspensions. The liquid flows through the C.P., where the channel width is gradually increased from 300 μm to 2500 μm to enable a larger filling capacity. The topographical transition between the device's inflow region and C.P. is shown in Figure 7.2c. When the profiles of the 3D channels are superimposed, it can be seen that there is a little topographical variance (Fig. 7.2d). More specifically, the shallowest point in the device (between the T.R. and C.W.) is at the same height the same for all channels, highlighting the patterning reproducibility. This is crucial as it not only determines the minimum trappable particle size, but as fluidic resistivity increases with a cubic dependency on the channel height⁷⁴, it will limit the fluid flow velocity. However, it should also be noted that there are some slight topographical discrepancies. The most noteworthy is the presence of an e-beam stitching line in Channel 3. This locally modifies the channel's height profile and influences particle trapping homogeneity.

7.4. Results and discussion

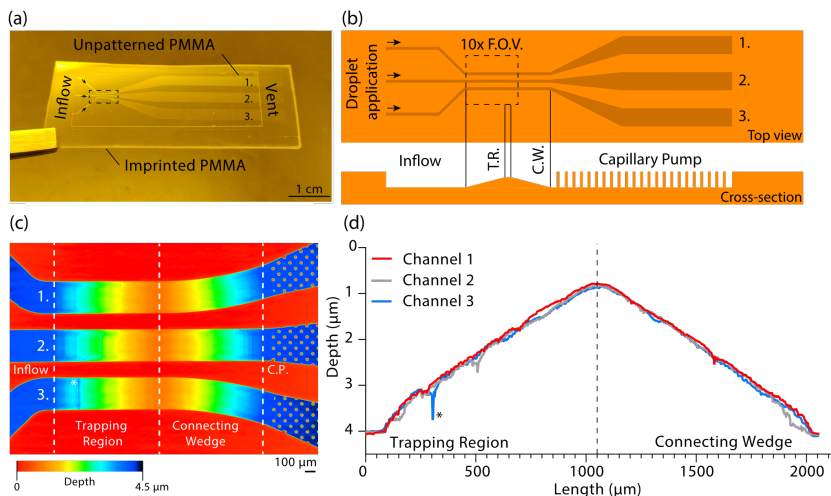


Figure 7.2. Outline of device characteristics. (a) Photography of a bonded 3D nanofluidic device. The dashed lines indicate the trapping regions and 10X FOV, which is used for multiplexed particle analysis. (b) Schematic illustrating the different device components as a top-view and cross-sectional drawing. (c) Confocal microscopy image showing the different height profiles in the parallel 3D channels. (d) Topographical profile of the functional device area. The asterisk represents the presence of an e-beam stitching line.

The core device functionality is size-dependent particle trapping. This was leveraged in our previous work to perform concurrent detection of SARS-CoV-2 and Influenza A antibodies by using particle multiplexing in a single channel.¹⁸⁶ Here, we present the parallelization of particle trapping in a single F.O.V. by using three distinctly loadable inlets. However, as a first step, the particle trapping capabilities of each channel needed to be evaluated to validate the device function. This was done by using a suspension consisting of five different particle sizes, ranging from 3.16 μm to 0.9 μm. The same suspension was loaded into the three different inlets and left to flow until the end of the C.P. was reached (Fig. 7.3a). Afterward, a droplet was applied onto

7. The power of one F.O.V.: five-fold concurrent cytokine detection

the venting section of the fluidic device to halt particle flow. Upon analysis of the median particle trapping position (see *Methods*), the topographical similarity between the three channels is confirmed by their large overlap in particle trapping positions (Fig. 7.3b). Also, the trapping position of the 3.16 μm particles in Channel 3 is highly disperse, attributable to the presence of the previously discussed e-beam stitching line. Nevertheless, within a single F.O.V., 15 different particle trapping lines can be seen. Even though these are non-functionalized calibration-grade particles, it highlights the potential of channel parallelization for multiplexed on-bead and on-chip immunoassays.

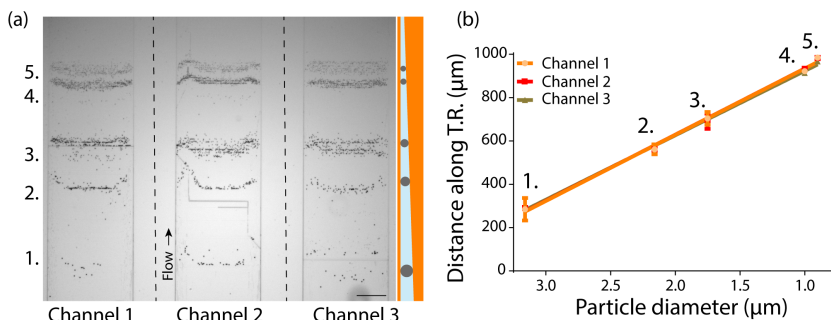


Figure 7.3. Trapping of five calibration grade particles in three parallel nanofluidic channels. (a) Left: the darkfield image of size-dependently immobilized particles. Right: cross-section schematic of the particle trapping positions (b) The median particle distance inside the T.R. versus their diameter. The scale bar represents a length of 100 μm .

7.4.2 On-chip detection of cytokines with picomolar sensitivity

Sepsis is a complex immunological response where both pro-inflammatory and anti-inflammatory cytokines are concurrently expressed.³¹² To this extent, it was chosen to screen for both these sub-types as proof-of-principle analytes for the development of our multiplexed nanofluidic FLISA. More specifically, IL-10 was chosen as it plays a significant role in the suppression of pro-inflammatory cytokines in a large variety of cell types.³¹³ Furthermore, elevated serum IL-10 serum levels have been linked to an increased mortality.³¹⁴ IL-6 was added to the multiplexing panel as it is known to have a bi-modal inflammatory role and is highly elevated in patients who suffered from septic shock.³¹⁵ TNF- α was included as it is a key mediator in the acute phase of systemic inflammation and has been extensively studied in the context of sepsis.³¹⁶ IL-1 β plays an important role in the inflammatory response and is elevated in patients with septic shock.²⁹³ However, its exact role remains unclear. Additionally, IL-2 provides insights into the origins of infection, as it is produced upon exposure to gram-positive bacteria.³¹⁷ Lastly, IL-8 was selected for its contribution to neutrophil chemotaxis and its reputation as a predictive biomarker for sepsis-related mortality.³¹⁸

Once the cytokines were selected, the novel nanofluidic method needed to be benchmarked and validated against a well-established method. To do so, ELISA, the gold standard of laboratory-based assays, was chosen. A commercially available kit optimized for a direct non-competitive sandwich assay was adapted to an indirect assay using a secondary antibody conjugated with ALP (*see Methods*). To enable comparison between the two assays, the same secondary antibody, but conjugated with a far-red fluorophore, was used in the nanofluidic FLISA. Once the enzymatic substrate was added, the optical density was measured after different reaction times. During the first 20 min, little increase in optical density could be seen, however, after a period of 50 min, it started steadily increasing (Fig. 7.4). The LOD of the assay was

7. The power of one F.O.V.: five-fold concurrent cytokine detection

determined after an incubation period of 100 min and was in accordance with the suppliers' specifications. As expected, the resulting LODs were all in the sub-picomolar range, except for IL-2. Also, it should be noted that for IL-8, of which less capture antibody was used (*see Methods*), the obtained optical density was significantly higher in comparison to that of the other cytokines. This likely is attributable to an increased antibody-antigen binding affinity. Overall, the obtained ELISA results exemplify the sensitivity needed to monitor homeostatic concentrations of cytokines. However, excluding plate functionalization, the assay took a full day to perform, which can be detrimental for patients who are suspected of suffering from sepsis. For example, it has been shown that with each hour appropriate treatment is delayed, 72-hour patient survival rates drop by 7.6%.³¹⁹ Therefore, the time-to-result has a significant practical influence and exemplifies why assay sensitivity is not the only relevant parameter to consider when employing diagnostic immunoassays.

7.4. Results and discussion

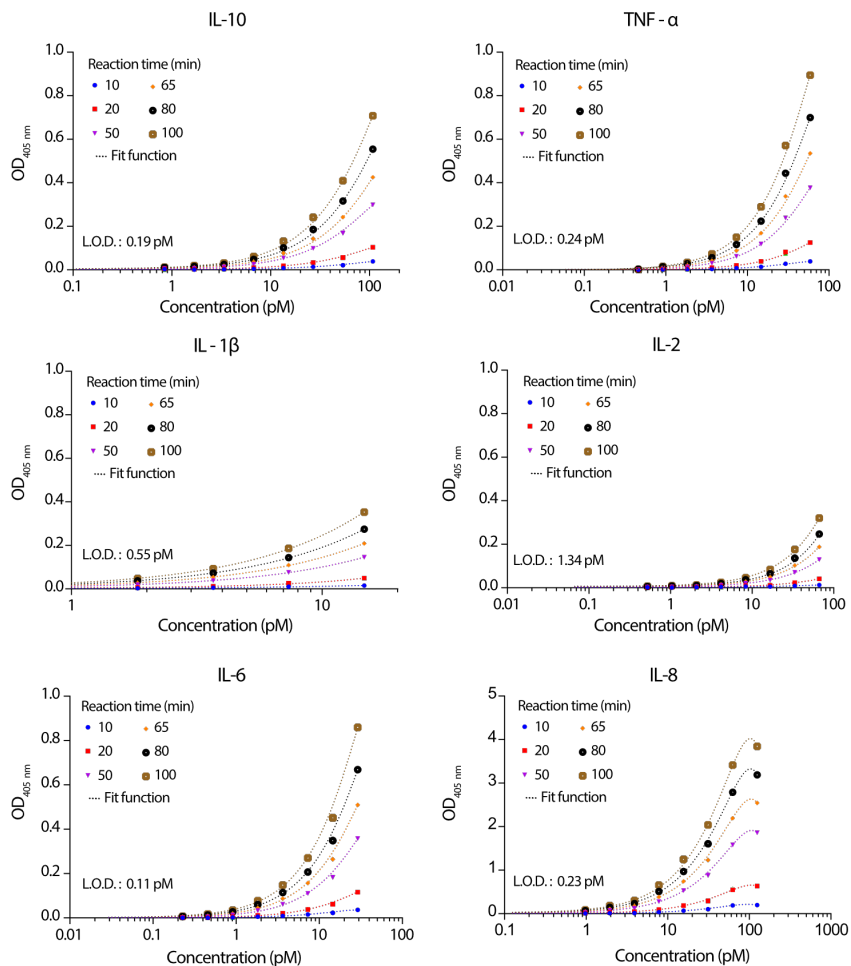


Figure 7.4. Colorimetric optical densities for different cytokines after various reaction times. Colorimetric readings were performed after different reaction times ranging from 10 to 100 minutes. The LOD was calculated as the optical density signal of a blank sample + 3x its standard deviation. To convert it into the associated concentration, the data was fitted with a non-linear fit equation, represented by the dashed lines.

7. The power of one F.O.V.: five-fold concurrent cytokine detection

To enable on-chip immunoassays inside the 3D nanofluidic device, particles functionalized with cytokine-specific capture antibodies were size-dependently immobilized, after which the device was vacuum dried. This step is denoted as particle pre-loading and enables to load the capillary-powered device with an analyte-containing sample in a second phase. The sample consisted of a cytokine, a detection antibody, and a secondary antibody (Fig. 7.1). Once the sample was loaded onto the chip, it was left to flow until the end of the C.P. was reached. Afterward, the particles inside the T.R. were imaged and their fluorescence was quantified (Fig. 7.5). Due to inexplicable variations of the blank samples, the LOD for all cytokine assays had to be visually estimated, resulting in values between 10 – 100 pM. This is two to three orders of magnitude less sensitive than the previously obtained ELISA LODs. Nevertheless, the on-chip immunoassay only required one 20 μ L sample droplet and was performed within 20 minutes. This means that it also is one order of magnitude faster. Assay speed, as mentioned previously, is a key parameter for sepsis-related immunoassays in order to commence appropriate treatment as soon as possible. Also, LOD in the ELISA assay after a reaction time of 20 min, was around the 1 pM range. This implies that for similar reaction times, the fluidic FLISA is one order of magnitude less sensitive.

In all the nanofluidic FLISA assays (except for IL-6), the plateau at low sample concentrations was characterized by relatively high fluorescence intensities of the trapped particles, implying a high degree of unspecific binding. For future work, we aim to reduce this as much as possible in an effort to increase the assay's sensitivity. Hence, it is of relevance to screen for different blocking solutions^{278,320}, adapt the drying procedure³²¹ and screen antibody compatibility. Furthermore, by optimizing the drying procedure, antibody binding affinities of the pre-immobilized antibodies should also be more well-maintained³²², increasing analyte capture at the trapping lines. Lastly, alternate fluorophores, such as Quantum Dots, offer increased brightness and

7.4. Results and discussion

have been previously employed to increase the assay sensitivity of microfluidic FLISAs.^{61,323}

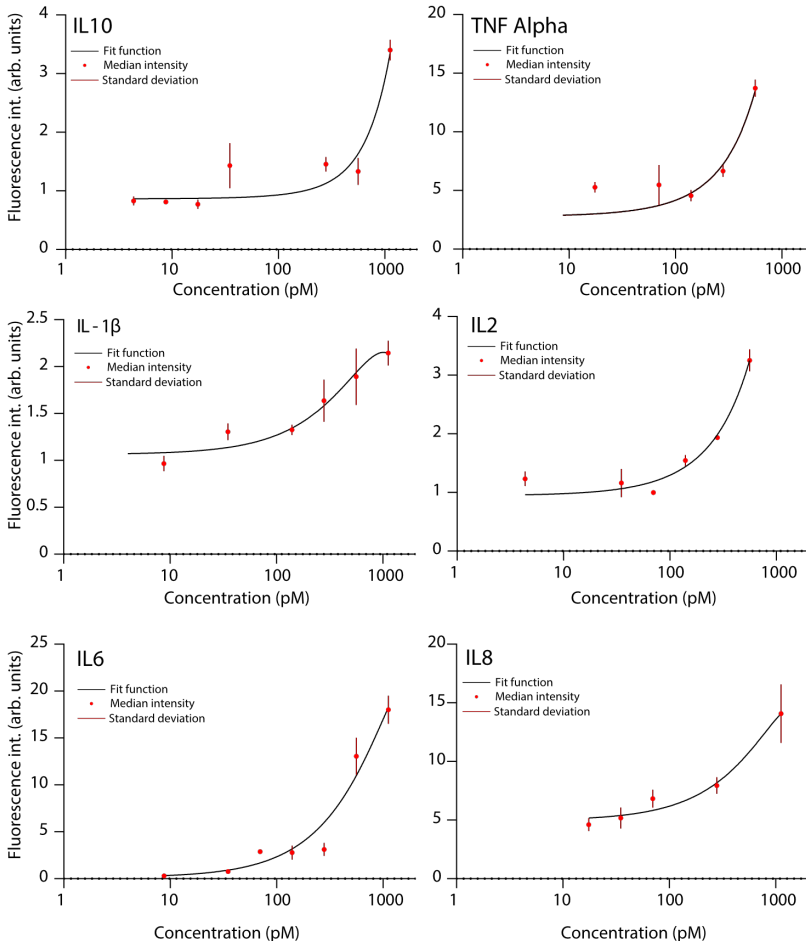


Figure 7.5. Fluorescence particle intensities for different cytokines in a 3D nanofluidic FLISA assay. The data was fitted with a non-linear fit function represented by a black line. The error bars represent the standard deviation.

7.4.3 Five-fold multiplexed detection of cytokines with one micrograph

In previous work, we employed both color-multiplexing and particle multiplexing to leverage the versatility of the 3D nanofluidic device.¹⁸⁶ However, it is possible to further extend the multiplexing possibilities of the device through means of parallelization. As previously described, the T.R. of three devices can be concurrently visualized within one microscopical F.O.V. This was combined with particle size multiplexing. In the pre-loading step, three different particle suspensions, each consisting of a 2.8 μm and 1 μm particle, were loaded into three separate channels (Fig. 7.6a). In doing so, six immunoassays can be concurrently performed on the nanofluidic chip (Fig. 7.6b). In the proof-of-principle experiment, one trapping line consisting of unfunctionalized streptavidin-coated particles was employed to monitor possible unspecific antibody binding to the beads' surface. An increased signal in the 'blank' trapping line would invalidate the performed assay.

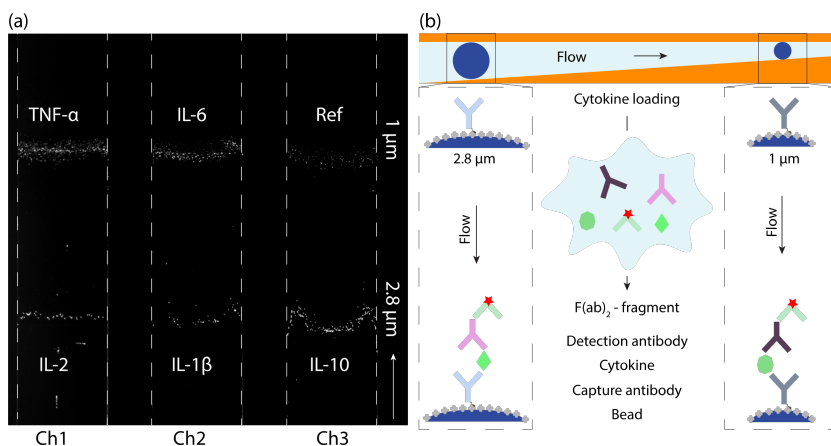


Figure 7.6. Multiplexed cytokine detection in a single FOV. (a) Low-illumination dark-field microscopy image of trapped bio-functionalized particles. The arrow indicates the flow direction. The 300 μm channel is outlined by two parallel dashed lines. 'Blank' marks unfunctionalized 1 μm particles. (b) Schematic illustrating multiplexed detection principle. A device containing two pre-trapped particle sizes (2.8 μm & 1 μm) are functionalized with cytokine-specific capture antibodies. A droplet is applied onto the inlet containing a mixture of: two cytokines, two detection antibodies, one $\text{F}(\text{ab})_2$ -fragment conjugated with Alexa647. This droplet is flown over the pre-immobilized beads for 20 min before imaging.

Three different experiments were performed to validate the multiplexed assay. In each experiment, three different droplets containing the relevant detection antibodies, a secondary antibody, and cytokines were added to the respective inflow sections. After an incubation period of 20 min, the trapped beads were imaged, and their median fluorescence was analyzed. Firstly, a negative control experiment consisting solely of the detection antibody and secondary antibody was used to set a baseline fluorescence. Subsequently, two proof-of-principle experiments, each containing different combinations of

7. The power of one F.O.V.: five-fold concurrent cytokine detection

cytokines (at high concentrations), were used to evaluate the multiplexing capabilities. The quantified results are presented in Figure 7.7. As can be seen, there is a clear relationship between the fluorescence intensity and the presence/absence of the cytokines in the assayed sample. Also, across all the experiments, the blank intensity remained constant. These experiments highlight the feasibility of using the fabricated device for rapid cytokine detection. However, a few considerations should be made. Firstly, the raw median fluorescence of the 1 μm beads was significantly lower than that of the 2.8 μm particles, attributable to their smaller surface area and capture antibody density. For future experiments, it would be of interest to use longer acquisition times, different fluorophores, or brighter excitation light to partially compensate for this effect. Secondly, the control signal of IL-2 was relatively elevated, indicating a high degree of unspecific binding. This most likely originates from the presence of both the IL-2 and TNF- α detection antibodies inside the applied droplet, rather than that of the secondary antibodies. To this extent, cross-adsorbed cytokine detection antibodies should be used prior to the multiplexed detection experiments. Lastly, there is a significant variation in fluorescence intensities of the positive control samples (e.g. IL-10 and IL-6). The root cause of this variation is unclear and will need to be identified and resolved. In spite of the clear shortcomings, these experiments highlight that five-fold multiplexed of cytokines on a single device is feasible but will require more work before reliable quantification is possible.

7.4. Results and discussion

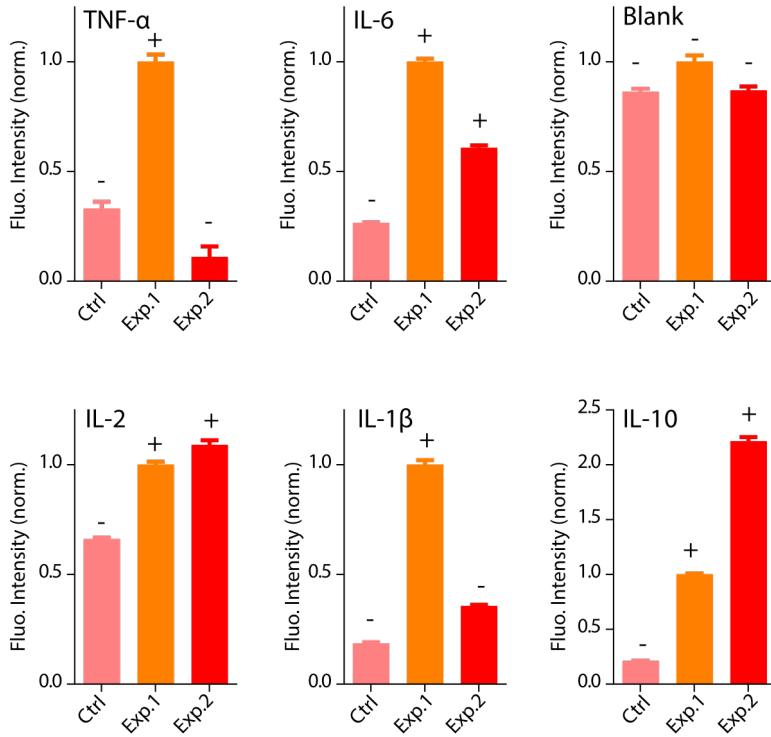


Figure 7.7. Multiplexed cytokine detection in one 10x F.O.V. Ctrl is representative of a negative control experiment that did not contain any cytokines. Exp. 1 and 2 represent different sample combinations of cytokines. Their absence or presence in the sample solutions is respectively indicated by a '-' or '+' on top of the bar graphs. The error bars represent the standard error of mean. The fluorescence was normalized with respect to Exp. 1.

7.5 Conclusions and outlook

The work presented in this chapter showed the applicability of 3D nanofluidic devices for on-chip FLISAs in the framework of multiplexed cytokine quantification. Firstly, we showed that it is possible to cost-effectively fabricate three separately loadable channels in plexiglass using both grayscale e-beam lithography and nano-imprint lithography. The parallelization capabilities of the 3D nanofluidic devices were highlighted by trapping 15 calibration grade particles in a single F.O.V. We have subsequently shown that an adapted ELISA assay reaches homeostatic relevant cytokine concentrations within 12 hours, whereas the nanofluidic device has limited sensitivity, but provides quantifiable results within 20 minutes. Furthermore, the multiplexing capabilities of the device were highlighted by the concurrent detection of five different cytokines, with an integrated control for unspecific binding.

For future work, we would like to increase the sensitivity of the assays in order for the device to be applicable in real-world scenarios. To do so, it would be of interest to use an alternate patterning method, such as grayscale laser lithography³²⁴, which would allow for the fabrication of deeper channels. This would permit an increase in the filling volume of the C.P. and consequently facilitate on the pre-immobilized beads. Also, as mentioned before, it would be possible to use different fluorophores, such as Quantum Dots, which have increased brightness and are resistant to photo-bleaching. Furthermore, by using laser rather than LED-based excitation, the intensity of the excitation light could be increased, possibly resulting in a greater fluorescent signal.¹¹ On top of this, it is required that unspecific antibody binding is reduced to a minimum. This can be done by screening for different blocking reagents²⁷⁸ or adding stabilizers during bead pre-trapping³²². Regardless of the current limitations, the developed device is an excellent example of how innovative micro and nanofabrication techniques can be employed to make a meaningful impact on the diagnostic landscape. The presented results pave the way for

7.6. Acknowledgments

applications in various fields where rapid multiplexed detection is needed, such as allergy-determination³²⁵, the use of illicit substances in high-performance sports³²⁶, or diagnosis of tick-borne diseases³²⁷.

7.6 Acknowledgments

T.M. is supported by the Swiss Nanoscience Institute, Project Number 1702.

7.7 Author contributions

T.M., Y.E. and S.S. conceived and designed the experiments. T.M. and B.M. designed the devices. T.M. fabricated the devices. T.M. performed fluorescence microscopy and image analysis. D.K. assisted with the nanofabrication. S.S. assisted with the ELISA experiments. C.P. assisted with and advised on the surface functionalization and device materials. Y.E. and X.L. supervised the project. All authors contributed to the writing of the manuscript.

Conclusions and future outlook



8. Conclusions and outlook

The development of rapid and cost-effective point-of-care (POC) diagnostics that provide quantifiable results has attracted significant attention in the last years. This was further substantiated by the COVID-19 pandemic, where lateral flow assays (LFA) were one of the key technologies used to contain and to reduce disease spread. Regrettably, these are only characterized by a binary response (*yes/no*) and have a limited sensitivity and specificity. To this extent, micro- and nanofluidic systems could provide a viable alternative to integrate the lab on a chip and overcome the drawbacks of classical LFAs. The goal of the presented research was to develop a passive fluidic device capable of size-dependent particle immobilization in order to facilitate rapid on-chip fluorescent immunosorbent assays. Its applications for the detection of various analytes in different fluids was highlighted in the different chapters of this thesis. The device and fabrication insights that resulted from this work, will pave the way for applications within a wide range of scientific research fields where multiplexed analysis or 3D patterning is required. This chapter provides a concise and comprehensive overview of the main conclusions of the performed work and offers a perspective for future work and applications in different fields.

8.1 Conclusions and considerations

8.1.1 g-EBL exposed PMMA permits nanoscale topography control and dry development

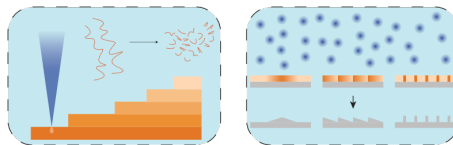
To bring laboratory-grade immunoassays to the patient's bedside, it is of great importance to develop assays that are easy in operation and versatile in application. The device operation is therefore completely passive and only requires the application of a microliter-sized droplet. As the device's core functionality is a sloped channel profile, it was essential to achieve a high degree of topographical control for the fluid flow to behave in a reproducible and predictable manner. To do so, we have developed a g-EBL grayscale exposure protocol using a PMMA-based resist in combination with delayed development. The experimental characterization of the fabrication protocol led to the formation of a unifying equation that accurately describes the achieved resist depth as a function of the time between exposure and development (t_{ED}). In general, little depth variation occurs after a t_{ED} of 72 hours. The underlying cause of this dependency is yet to be elucidated, but it was found that the application of a PEB can significantly accelerate the time until a steady-state depth is achieved. This controlled development procedure enabled the fabrication of micro and nanofluidic master structures with nanoscale topography variations on a millimeter length scale.

Furthermore, PMMA is an extensively studied resist for e-beam patterning and can be both processed as a positive-tone resist at low electron doses or as a negative-tone resist at higher electron doses. However, in the presented work, a novel dry development procedure for negative-tone processing at low electron doses was developed. This was done by using an SF_6/O_2 -plasma, which showed that the greater the electron dose, the larger the etch resistance. This effectively enabled negative tone processing at electron doses which are an order of magnitude lower than in classical wet development. Furthermore, as fluorine ions were included in the plasma, the exposed

8. Conclusions and outlook

patterns could be simultaneously transferred into the silicon substrate. In doing so, it was possible to fabricate binary and grayscale patterns with micron-sized lateral features in silicon directly from g-EBL exposed PMMA.

Further work is, however, needed to study the underlying mechanisms responsible for the observed electron dose dependent effects. For example, it would be of interest to use surface characterization methods, such as Fourier-transformation infrared spectroscopy (FT-IR) or x-ray photoelectron spectroscopy (XPS)¹⁶³, to monitor the possible formation of different chemical bonds in a dose and time-dependent manner. Furthermore, a growing hypothesis regarding the PMMA tone reversal during dry development is the formation of surface charges during etching, effectively providing a repulsive force to the incident ions and in doing so, reducing the etch rate.³²⁸ It would be of interest to test this hypothesis by using different sample immobilization strategies, such as electro-static clamping, rather than physical clamping.³²⁹ On top of this, the resolution of the current dry development technique is still characterized by micron-sized lateral dimensions. Further investigations will be needed to identify and resolve the resolution limitations of this alternate development path. Eventually, this could be a useful technique for the development of small feature sizes which are prone to capillary-induced pattern collapse, a common problem of wet development.



8.1.2 Upscalable device fabrication is enabled via thermoplastic patterning

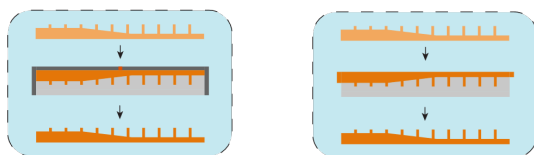
g-EBL, albeit very precise and versatile, is an expensive and slow patterning technique. Therefore, it does not lend itself to the fabrication of POC diagnostic devices. In an effort to overcome this drawback, two different thermoplastic patterning methods were explored within this thesis. Firstly, nano-imprint lithography or hot embossing was used to perform device prototyping and rapidly test new channel geometries. To do so, the grayscale patterned e-beam resist served as a substrate for the fabrication of negative daughter stamps in a UV-curable polymer through soft lithography. Two different polymeric materials were explored as potential candidates for the fabrication of the so-called daughter stamps. Firstly, OrmoStamp (MicroResist GmbH) was employed due to its established reputation within the field of imprint lithography.³³⁰ This material is characterized by a high-resolution and long lifetime. However, a significant drawback is its adhesion to the PMMA resist upon UV crosslinking. Therefore, the pattern can be replicated, but the original e-beam structure is lost. Additionally, it significantly shrinks upon UV exposure, causing pattern and substrate bending. To this extent, for all the work reported in this thesis, we used an alternate stamp material: GMN PS-90 (OpTool). This silane-containing material has extremely low shrinkage and is inherently anti-adhesive.³³¹ Consequently, multiple daughter stamps can be effortlessly made from a single e-beam master. The pattern transfer protocol was optimized such that the 3D profile could be precisely replicated into a low-cost, commercially available plexiglass film. This enabled us to test novel fluidic geometries within a single day.

Nevertheless, nano-imprint lithography suffers from extended thermal cycles, limiting its production capability. To this extent, injection molding was explored as a substitute thermoplastic patterning method. It was shown that it is possible to fabricate a nickel mold directly from grayscale exposed e-beam resist, while reducing patterning roughness and retaining 3D

8. Conclusions and outlook

topography. The nickel mold was used to pattern the device in two different materials: COP and PMMA. Both material types enabled size-dependent particle trapping, but COP showed less height loss due to the bonding process. Furthermore, the nanofluidic devices contained supporting structures, such as lines and pillars, to enable collapseless bonding. It was found that pillars organized in a row-type array showed the most homogenous trapping lines.

Yet, even though throughput is increased by using injection molding as a patterning technique, later processing steps still require a significant amount of sample handling. For example, the functionalization of the device with PVA requires sequential spincoating. Additionally, it is only possible to activate single chips with UV-O before bonding. To this extent, more work is needed to optimize the device's surface activation and bonding procedure. This could be done by using in-line processes, in resemblance to that of a commercial foundry³³² or by using roll-to-roll embossing with integrated functionalization and bonding modules.³³³



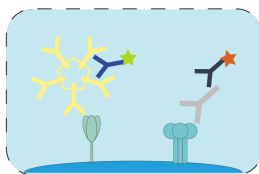
8.1.3 3D nanofluidic devices for viral antibody detection

At the time of the doctoral research, the COVID-19 pandemic was in full upswing. Hence, a key biomedical application of the developed device was the multiplexed antibody detection in the context of viral diseases. More specifically, it was shown that thanks to the size-dependent immobilization properties of the device, S-RBD functionalized beads could be used to perform a FLISA for SARS-CoV-2 related antibodies inside patient serum. By using

8.1. Conclusions and considerations

secondary antibodies specific for short-term (IgM) and long-term (IgG) antibodies, color multiplexing was achieved. The nanofluidic immunoassays were benchmarked with respect to its LOD, reaching 0.8 nM. As the average COVID-19 patient produces between 9.6 and 28 880 nM of antibodies, it puts the device in the relevant physiological range. This was further emphasized by the high sensitivity (94.7%) and specificity (100 %) of the assay when used in conjunction with real patient samples. The color multiplexing was extended by particle size multiplexing. In doing so, it was possible to concurrently detect both SARS-CoV-2 and Influenza A antibodies on a single device. The device's advantages are in sharp contrast with commercially available and widely implemented methods. For example, semi-quantifiable information could be obtained, in comparison to LFAs that only provide a binary answer. Also, with respect to the lab-based on-bead platform Luminex, the developed device requires less expensive infrastructure and less sample volume.

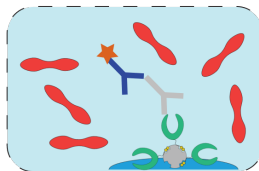
The multiplexed antibody detection is a great example of the advantages of the device with respect to its ease of operation, small required sample volume, cost-effectiveness and versatility. In addition to the presented on-bead FLISA application, the device can be applied to address research questions in many more scientific disciplines, e.g. it can function as a tool to offer laboratory-grade experiments in resource-limited environments.



8.1.4 Whole blood immunoassays through adaptation of channel topography

Thus far, the device operation was only compatible with bead pre-incubation in the sample outside of the device, significantly contributing to the total assay time. Furthermore, it was only validated with serum, which required an additional whole blood processing step. To this extent, it was of relevance to adapt the device geometry to make it compatible with whole blood assays. It was shown that a minimum channel height of 1.7 μm was required for the red blood cells to effortlessly flow through the capillary-driven device. Additionally, by pre-immobilizing the beads within the 3D fluidic channel prior to sample loading, sub-10 min FLISAs with nanomolar sensitivity could be performed. The whole blood FLISA was compared to a PBS-based assay and no detrimental effect regarding its sensitivity could be noted. Also, by using particle size multiplexing, it was possible to detect two antigen-specific antibodies in whole blood with a high degree of sensitivity and specificity.

For future device applications, it would be of benefit to test a large variety of additional bio-fluids, such as saliva and urine, to monitor the devices compatibility as well as sensitivity. Furthermore, the current experiments were performed with rabbit blood treated with anti-coagulants and spiked with a known antigen concentration. For the device to be compatible with human blood samples, further validation in a clinical testing environment is required.



8.1.5 Three-dimensional multiplexing: color, size, and channel

The whole-blood adapted device only reports two distinct multiplexing strategies, i.e., color and particle size-multiplexing. However, for many diseases, such as sepsis, it is of the utmost importance that more analytes can be concurrently assayed in an effort to provide accurate disease diagnosis. To this extent, we have parallelized three nanofluidic channels to fit within a single microscopic field-of-view. In doing so, it was possible to visualize 15 calibration beads in a single image and perform five-fold multiplexed FLISAs. Additionally, the fluidic assay was benchmarked against a lab-based ELISA assay and highlighted key differences. For example, in comparison to the ELISA, the fluidic assay was characterized by a reduction in sensitivity but was able to provide quantifiable results an order of magnitude faster.

Further work is required to bring the sensitivity of the fluidic assay within the relevant homeostatic range. To do so, several possibilities exist. Firstly, the capillary pump could be enlarged to increase the fluid volume being flushed over the pre-immobilized particles. In doing so, there would be a larger degree of analyte up concentration and hence, a more amplified fluorescent signal. Secondly, a significant amount of unspecific binding could also be seen. Therefore, different blocking and pre-loading strategies should be explored to reduce this to a minimum. For example, the addition of stabilizing agents³²² would enable a better retention of antibody binding affinities upon drying. Lastly, it would be interesting to explore different fluorescent labeling and excitation strategies. More specifically, the use of brighter and more stable fluorophores should provide an increased signal. In addition, alternative excitation sources, such as laser illumination, should increase the fluorescent brightness.

8.2 Outlook

Even though many device shortcomings were identified and addressed during this thesis, several important remaining drawbacks would need to be resolved before the developed platform could be applied in the field of POC diagnostics. The following section identifies key aspects which still would need to be addressed for the device to fully translate from a lab-based environment to widespread application in resource-limited environments.

Additionally, the g-EBL and nano-imprint protocol established during this thesis laid the foundation for various fluidic projects with applications in different fields. One of these are briefly discussed, and its importance is highlighted.

8.2.1 Mobile fluorescence detection

While the device fabrication and the device itself can be described as upscalable, rapid and cost-effective, the current immunoassay read-out was performed using a conventional tabletop fluorescent microscope. This severely limits the test's portability. To this extent, proof-of-principle experiments were performed to develop device-compatible mobile read-out systems.

Firstly, a current globally omnipresent tool, available to a wide proportion of the population, is the smartphone. These portable devices are characterized by a high computational power, miniaturized optics, and sensitive cameras.³³⁴ They are the ideal candidate to develop a fluorescent detection platform for the developed the device. A proof-of-principle mobile microscopy setup was developed consisting out of two distinct parts: the smartphone itself and the auxiliary hardware (Fig. 8.1). The Oppo Find X3 Pro smartphone was chosen due to its high pixel density, quality optics and already integrated microscopy function.³³⁵ Furthermore, previous Oppo models that were adapted for fluorescence microscope and were characterized by a very good signal-to-noise ratio.³³⁶ The smartphone could be mounted on a custom 3D-printed

8.2. Outlook

enclosure consisting out of an LED-excitation source, a short-pass filter, a sample stage capable of XYZ manipulations, and a commercially available smartphone objective (DIPLE³³⁷) and a long-pass filter for filtration of the emission light. Furthermore, special inserts were included to integrate possible diffusers of neutral density filters to reduce the excitation light intensity. The entire imaging system is enclosed by a dark cover to ensure no stray ambient light reaches the detector during image acquisition.

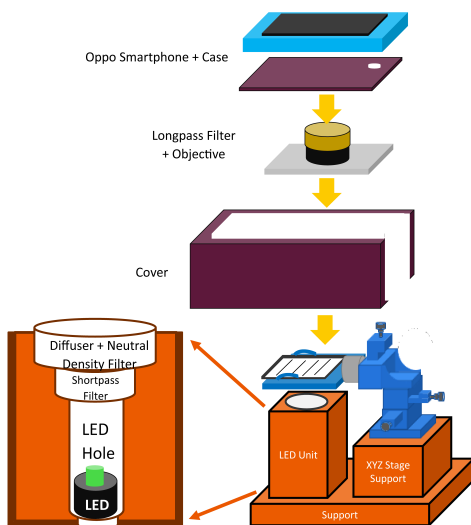


Figure 8.1. Schematic of a portable fluorescence microscope.³³⁸

To evaluate the function of the mobile microscope, calibration-grade particles characterized by a far-red emission, were imaged using a 75x objective (Fig. 8.2a). The images are collected in a JPEG format, of which the red channel was isolated (Fig. 8.2b). The obtained image was characterized by significant background fluorescence. To this extent, the algorithm used for FLISA image analysis was used to perform appropriate background correction (Fig. 8.2c). The normalized fluorescence data shows that it allows to appropriately

subtract the background, while maintaining the intensity profile of the fluorescent particles (Fig. 8.2d)

Even though these beads were imaged on a microscopy slide rather than inside a nanofluidic device, it evidences the use of a smartphone-based read-out system for portable FLISAs. Regrettably, such systems are characterized by two significant drawbacks. Firstly, there is a considerable smartphone-to-smartphone variation regarding optical characteristics, detector sensitivity and geometry.³³⁹ These differences imply that for each smartphone model, a different auxiliary system would need to be developed. Secondly, it is difficult to obtain regulatory approval for smartphone-based read-out systems, stemming from the different regulatory requirements of consumer electronics and POC diagnostics.³⁴⁰ This hampers their eventual applicability as portable read-out systems in a real-world setting.

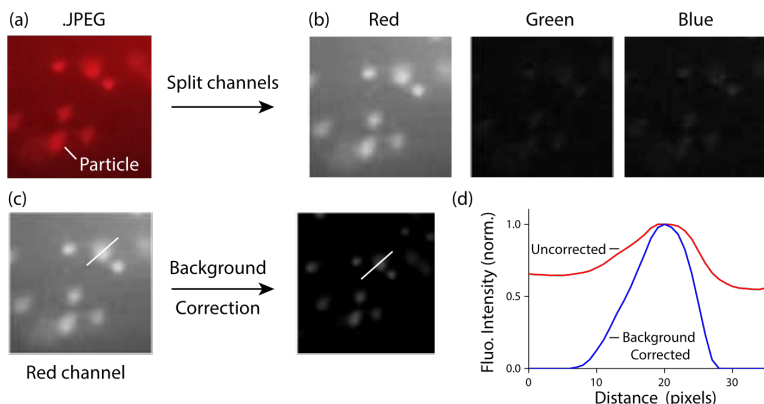


Figure 8.2. Overview of particle imaging using a fluorescent smartphone microscope. (a) Original image directly from a smartphone in a JPEG-format. The imaged particles have a diameter $2.16 \mu\text{m}$ (b) Segmentation of the JPEG image into the three different RGB channels (c) Background correction of the image using a custom Python code using a rolling ball algorithm. The white line indicates the measured intensity profile (d) Normalized intensities of the corrected and uncorrected particle profiles.

8.2. Outlook

Secondly, as an alternative mobile detection platform, a series proof-of-principle experiments were performed in collaboration with the research group of Dr. Stefano Cattaneo at CSEM Landquart using their low-cost (< 1000 CHF) laser-based read-out system. The parallel multiplexing devices presented in Chapter 7 were used to trap 2.8 μm and 1 μm beads functionalized with biotinylated Alexa647 to perform a preliminary feasibility evaluation. Even though the setup is characterized by a limited resolution (30 μm), the particle trapping lines are clearly visible in all channels (Fig. 8.3a). Furthermore, the obtained signal-to-noise is excellent for such a low-cost system, evidencing its applicability for portable FLISAs (Fig. 8.3b). Nevertheless, additional work is required to determine the ideal optical system characteristics, such as resolution, excitation source and filters, to ensure optimal imaging conditions.

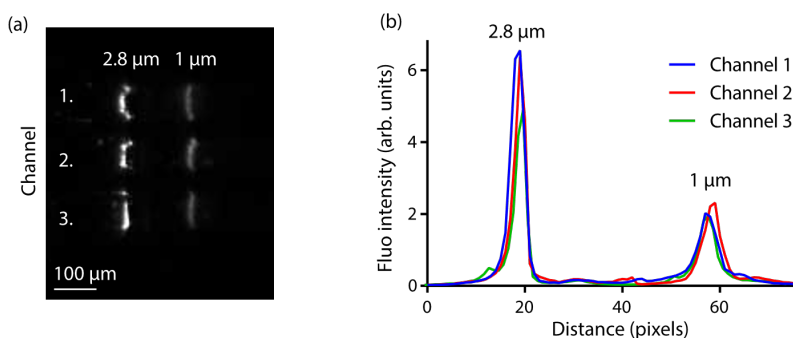


Figure 8.3. Imaging of Alexa 647 functionalized particles with a portable microscopy setup. (a) Fluorescent image of region-of-interest (b) Quantified fluorescent intensities along channel length.

8.2.2 Further optimization of the nanofluidic devices

Though the g-EBL patterning protocol was highly optimized for accurate topography control, the possible pattern depth was limited to 4 μm , attributable to the spincoatable resist thickness. Furthermore, e-beam exposures of devices with micron-sized lateral dimensions can be lengthy and

therefore also expensive. The limited pattern depth poses two important constraints on the device. Firstly, it restricts the employable particle size to be within 0.9 – 4 μm . Secondly, it limits the depth and thus the volume of the capillary pump ($V_{C.P.}$), resulting in a reduced up concentration of the analyte on the pre-immobilized particles. A greater $V_{C.P.}$ is one of the crucial device adjustments needed to ameliorate the fluidic assays LOD (Fig. 8.4). A viable alternative to g-EBL as a patterning method would be grayscale laser lithography. This technique is compatible with thick resist layers ($> 20 \mu\text{m}$) and offers accelerated patterning times.³⁴¹

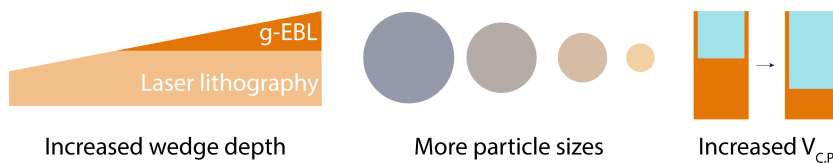


Figure 8.4. Advantages of employing a different patterning method.

In addition to having an increased $V_{C.P.}$, it would be of benefit to have multiple C.P.s with different volumes on a single chip (Fig. 8.5a). More specifically, a larger $V_{C.P.}$ would enable the detection of minute analyte concentrations, but it would concurrently also cause a signal saturation for higher analyte concentrations. In contrast, smaller $V_{C.P.}$ would reduce the signal of low analyte concentrations, but simultaneously also enable quantification of higher analyte concentrations. This would allow to extend the immunoassays dynamic range (Fig. 8.5b).

8.2. Outlook

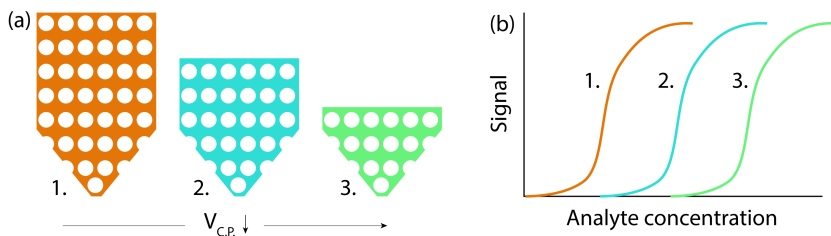


Figure 8.5. Dynamic range adjustment by tuning capillary pump volume. (a) Capillary pumps of sequentially reducing width and filling volume (b) Shift in fluorescent signal depending on the sample volume flushed over the pre-immobilized beads. The larger the $V_{C.P.}$, the greater the signal at lower analyte concentrations and vice versa.

8.2.3 Biomedical applications

Currently, the device has been primarily used to perform detection of analytes present in either whole-blood or serum. However, both of these bio-fluids require invasive methods, such as a fingerpick, to acquire.²⁵⁸ To this extent, other, more accessible bio-fluids, such as urine and saliva, should also be validated with the developed device.

On the one hand, saliva has mostly been used for the diagnosis of oral diseases, but recently, it has attracted increasing attention as a biofluid for the detection of systemic diseases, such as HIV.³⁴² Furthermore, saliva contains a plethora of different analytes, ranging from hormones and steroids to cytokines, proteins and drugs, making it useful for a wide range of diagnostic applications.³⁴³

On the other hand, urine has a long-standing reputation as an important bio-fluid for diagnostic purposes.³⁴⁴ For example, the urinary concentration of albumin has been used as a predictor for acute kidney injury.³⁴⁵ As an added benefit, urine is not influenced by homeostatic mechanisms as much as whole blood composition. Consequently, analyte fluctuations in urine offer unique insights into a different perspective on various physiological changes, such as

8. Conclusions and outlook

pregnancy and aging.³⁴⁶ On top of this, recent literature has identified urine as a promising bio-fluid for the diagnosis of brain-diseases³⁴⁷, such as Alzheimer's³⁴⁸ and Parkinson's disease³⁴⁹.

Regrettably, as the analyte concentration in saliva and urine is usually in the order of a few picomolar, their detection and quantification require highly sensitive and specific methods.³⁵⁰ It is therefore of the utmost importance that the device's LOD is ameliorated prior to performing validation experiments with other bio-fluids.

Furthermore, in recent years, exosomes, rather than single bio-active compounds, have been identified as biomarkers for various diseases. Exosomes are 40 to 100 nm large vesicles secreted by various cell types.³⁵¹ They contain a wide range of molecules from their cell of origin, including proteins, nucleic acids as well as lipids, and are found in multiple extracellular environments.³⁵² Consequently, they play a significant role in cell-to-cell signaling. Over the last decade, it has been shown that cancer patients display an increased number of circulatory exosomes as compared to healthy individuals.³⁵³ As a result, they are an interesting disease biomarker to enable minimally invasive cancer detection.³⁵⁴

In addition to applications within the immunoassay field, the device could also be used as a pathophysiological investigative method for different diseases. For example, by performing organelle isolation and size-characterization. A key sub-cellular entity that takes part in a large variety of pathways that control essential cellular process are the mitochondria. Their impairment plays a key role in numerous pathological conditions, including neurodegenerative diseases.^{242,355-357} With respect to the latter, it has been found that their size and number change depending on the cellular disease state.³⁵⁸ Nevertheless, geometrical monitoring of mitochondria is cumbersome, time-consuming, and requires advanced imaging techniques such as transmission electron

microscopy (TEM). To this extent, self-powered micro – and nanofluidic devices offer a cost-effective alternative.

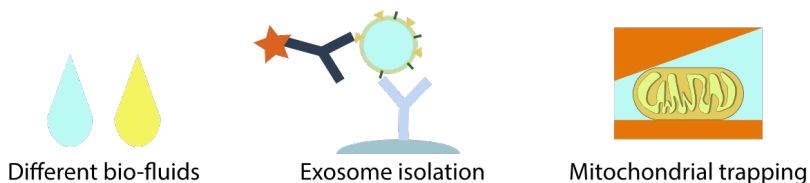


Figure 8.6. Future biomedical applications.

8.2.4 Alternate application of e-beam patterned fluidics: horizontal nanopores

The reported immunoassays allow for accurate protein analysis and quantification in aqueous environments for POC applications. However, this requires the use of specialized antibodies, fluorophore labels, functionalized particles, and a unique fluidic construct. Furthermore, the performed analysis does not provide an indication of analyte volume or any other biophysical properties. To this extent, label-free methods that can provide detailed protein information in a native physiological environment are of high interest. A microfluidic method technique that is a candidate to do so, are nanopore-based systems. This technology uses nanometer-sized holes within a thin insulating membrane, such as silicon nitride, to characterize proteins with respect to a plethora of biophysical parameters, e.g. volume, shape, dipole moment and rotational diffusion coefficient.³⁵⁹ Even though this technique is a highly promising alternative to current state-of-the-art protein analysis methods, it is still characterized by several important shortcomings. Firstly, their employed fabrication scheme, consisting out of a series of lithographical, etching and deposition steps, negatively impacts the pore geometry. More specifically, it deviates from an ideal cylinder and causes local resistance changes, negatively impacting protein measurements. Secondly, as

nanopore-based devices only contain a single pore, they are characterized by a limited throughput. To this extent, it is of importance to use fabrication schemes that can produce extensive arrays of horizontal nanopores to parallelize protein detection and characterization. The g-EBL fabrication scheme presented in Chapter 2 was used as a proof-of-principle method to pattern 50 nm horizontal nanopores, connecting two microfluidic cavities in a single lithographic exposure (Fig. 8.7a-b). To ensure an optimal liquid flow, the transition between the micro – and nanofluidic channels contained a 3D wedge that reduced the height of the channel to 32.5 nm (Fig. 7c). Furthermore, in comparison to an abrupt micro to nano transition, such a tapered segment has the added advantage that analyte flow is greatly enhanced while simultaneously ensuring retention of biomolecule structure.¹¹⁰ However, before this pattern could be used inside a microfluidic device, future work is still needed. For example, the current channel geometry is characterized by a relatively sharp reduction in channel width, giving rise to resist cracks.³⁶⁰ Furthermore, the channel was only fabricated in e-beam resist, and subsequent processing using pattern replication and thermoplastic patterning will be needed to enable microfluidic device fabrication. In spite of this, this feasibility investigation highlighted the use of g-EBL for the possible fabrication of horizontal nanopores for label-free and multiplexed protein detection.

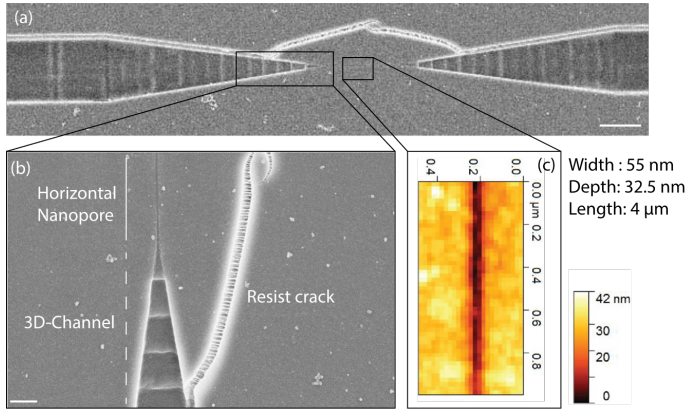


Figure 8.7. Overview of horizontal 3D nanopore geometry. (a) SEM-image of two microfluidic channels (left and right) connected by a nanochannel function as a nanopore (middle) (b) Bridging section between the micro and nanochannel, highlighting the 3D steps and the nanopore. The scale bars in the SEM-images represent 500 nm (c) AFM-image of the nanopore and specified geometry.

8.3 Concluding statement

In summary, the device presented within this doctoral thesis is characterized by several unique features and advantages that can be listed as follows:

- Nanoscale channel topography on a millimeter length scale
- Fabrication methods compatible with state-of-the-art foundries for high-volume manufacturing
- Nano functionality in the vertical axis for simplified pattern replication
- Only passive components and no need for peripheral flow control – easy in operation and versatile in application
- Size-dependent trapping of specific particle sizes at pre-determined locations with nanometer accuracy
- Compatibility with protein-coated particles through surface functionalization strategies
- Three levels of analyte detection:
 - Color multiplexing for determination of antibody type
 - Particle multiplexing for differential disease diagnosis
 - Channel parallelization
- Modular immunoassay platform for antigen and antibody detection
- One drop FLISAs without the need for washing steps facilitated by the shallow device dimensions
- Compatible with various fluids: buffer, serum, and whole blood
- Sub-nanomolar limit-of-detection of different analytes

8.3. Concluding statement

These unique characteristics were employed for a variety of biomedical applications, ranging from viral antibody detection to cytokine quantification. However, to bring the device from the lab to the patient's bedside, several shortcomings will need to be addressed. It is of paramount importance that a mobile fluorescent reader is developed to facilitate assaying in resource-limited environments. Also, the fluidic design will need to be optimized to enable the use of more particle sizes and to push the limit-of-detection into the sub-picomolar regime. Regardless of this, the technological and scientific advancements made in the past four years provide an excellent platform to do so and will pave the way for many more applications within numerous research fields, ranging from biomedicine to material science and chemistry.

To developing novel solutions for unmet needs and improving the well-being of humankind.

References

9. References

1. Robert, K. & Arkadiusz, D. Molecular and Serological Tests for COVID-19 . A Comparative Review of SARS-CoV-2 Coronavirus Laboratory and Point-of-Care Diagnostics. *Diagnostics* **10**, (2020).
2. Vandenberg, O., Martiny, D., Rochas, O., van Belkum, A. & Kozlakidis, Z. Considerations for diagnostic COVID-19 tests. *Nat. Rev. Microbiol.* **19**, 171–183 (2021).
3. Yager, P., Domingo, G. J. & Gerdes, J. Point-of-care diagnostics for global health. *Annu. Rev. Biomed. Eng.* **10**, 107–144 (2008).
4. Whitman, J. D. *et al.* Evaluation of SARS-CoV-2 serology assays reveals a range of test performance. *Nat. Biotechnol.* **38**, 1174–1183 (2020).
5. Deng, Y., Jiang, H., Li, X. & Lv, X. Recent advances in sensitivity enhancement for lateral flow assay. *Microchim. Acta* **188**, (2021).
6. Bishop, J. D., Hsieh, H. V., Gasperino, D. J. & Weigl, B. H. Sensitivity enhancement in lateral flow assays: A systems perspective. *Lab Chip* **19**, 2486–2499 (2019).
7. Hemmig, E., Temiz, Y., Gökçe, O., Lovchik, R. D. & Delamarche, E. Transposing lateral flow immunoassays to capillary-driven microfluidics using self-coalescence modules and capillary-assembled receptor carriers. *Anal. Chem.* **92**, 940–946 (2020).
8. Sakamoto, S. *et al.* Enzyme-linked immunosorbent assay for the quantitative/qualitative analysis of plant secondary metabolites. *J. Nat. Med.* **72**, 32–42 (2018).
9. Hage, D. S. Immunoassays. *Anal. Chem.* **71**, 294R–304R (1999).
10. DeMello, A. J. Control and detection of chemical reactions in microfluidic systems. *Nature* **442**, 394–402 (2006).
11. Krausz, A. D., Korley, F. K. & Burns, M. A. A variable height microfluidic device for multiplexed immunoassay analysis of traumatic brain injury biomarkers. *Biosensors* **11**, 1–17 (2021).
12. Ng, A. H. C., Uddayasankar, U. & Wheeler, A. R. Immunoassays in microfluidic systems. *Anal. Bioanal. Chem.* **397**, 991–1007 (2010).
13. Gökçe, O., Castonguay, S., Temiz, Y., Gervais, T. & Delamarche, E. Self-coalescing flows in microfluidics for pulse-shaped delivery of reagents. *Nature* **574**, 228–232 (2019).
14. Cesaro-Tadic, S. *et al.* High-sensitivity miniaturized immunoassays for tumor necrosis factor α using microfluidic systems. *Lab Chip* **4**, 563–569 (2004).

8.3. Concluding statement

15. Arango, Y., Temiz, Y., Gökçe, O. & Delamarche, E. Electrodrives for stop-and-go control of liquid flow in microfluidics. *Appl. Phys. Lett.* **112**, (2018).
16. Gervais, L. & Delamarche, E. Toward one-step point-of-care immunodiagnosics using capillary-driven microfluidics and PDMS substrates. *Lab Chip* **9**, 3330–3337 (2009).
17. Zimmermann, M., Bentley, S., Schmid, H., Hunziker, P. & Delamarche, E. Continuous flow in open microfluidics using controlled evaporation. *Lab Chip* **5**, 1355–1359 (2005).
18. Habli, Z., Saleh, S., Zaraket, H. & Khraiche, M. L. COVID-19 in-vitro Diagnostics: State-of-the-Art and Challenges for Rapid, Scalable, and High-Accuracy Screening. *Front. Bioeng. Biotechnol.* **8**, 1–14 (2021).
19. Liu, J., Zanardi, S., Powers, S. & Suman, M. Development and practical application in the cereal food industry of a rapid and quantitative lateral flow immunoassay for deoxynivalenol. *Food Control* **26**, 88–91 (2012).
20. Moser, A. C. & Carlson, T. L. General principles of immunoassays. *Nov. Approaches Immunoassays* 7–19 (2014). doi:10.2217/EBO.13.617
21. Wang, X., Cohen, L., Wang, J. & Walt, D. R. Competitive Immunoassays for the Detection of Small Molecules Using Single Molecule Arrays. *J. Am. Chem. Soc.* **140**, 18132–18139 (2018).
22. Kobayashi, N. & Goto, J. Noncompetitive immunoassays for small molecules with high sensitivity and specificity. *Advances in Clinical Chemistry* **36**, 139–170 (2001).
23. Roth, S. *et al.* Improving the Sensitivity of Fluorescence-Based Immunoassays by Photobleaching the Autofluorescence of Magnetic Beads. *Small* **15**, 1–9 (2019).
24. Grossberg, A. N. *et al.* A multiplex chemiluminescent immunoassay for serological profiling of COVID-19-positive symptomatic and asymptomatic patients. *Nat. Commun.* **12**, (2021).
25. Hosseini, S., Vázquez-Villegas, P., Rito-Palomares, M. & Martínez-Chapa, S. O. *Advantages, Disadvantages and modifications of conventional ELISA. SpringerBriefs in Applied Sciences and Technology* (Springer, 2018). doi:10.1007/978-981-10-6766-2_5
26. Zhang, S. *et al.* Predicting detection limits of enzyme-linked immunosorbent assay (ELISA) and bioanalytical techniques in general. 439–445 (2014). doi:10.1039/c3an01835k
27. Schenk, T. *et al.* Potential of on-line micro-LC immunochemical detection in the bioanalysis of cytokines. *J. Pharm. Biomed. Anal.* **26**, 975–985 (2001).

9. References

28. Mikulskis, A., Yeung, D., Subramanyam, M. & Amaravadi, L. Solution ELISA as a platform of choice for development of robust , drug tolerant immunogenicity assays in support of drug development. *J. Immunol. Methods* **365**, 38–49 (2011).
29. Lim, C. T. & Zhang, Y. Bead-based microfluidic immunoassays: The next generation. *Biosens. Bioelectron.* **22**, 1197–1204 (2007).
30. Verpoorte, E. Beads and chips: new recipes for analysis. *Lab Chip* **3**, 60N–68N (2003).
31. Qu, Z. *et al.* Ultrasensitive ELISA using enzyme-loaded nanospherical brushes as labels. *Anal. Chem.* **86**, 9367–9371 (2014).
32. Elshal, M. F. & McCoy, J. P. Multiplex bead array assays: Performance evaluation and comparison of sensitivity to ELISA. *Methods* **38**, 317–323 (2006).
33. Wu, D. & Voldman, J. An integrated model for bead-based immunoassays. *Biosens. Bioelectron.* **154**, 112070 (2020).
34. Sheehan, P. E. & Whitman, L. J. Detection limits for nanoscale biosensors. *Nano Lett.* **5**, 803–807 (2005).
35. Huergo, L. F. *et al.* Magnetic Bead-Based Immunoassay Allows Rapid, Inexpensive, and Quantitative Detection of Human SARS-CoV-2 Antibodies. *ACS Sensors* **6**, 703–708 (2021).
36. Khalifian, S., Raimondi, G. & Brandacher, G. The Use of Luminex Assays to Measure Cytokines. *J. Invest. Dermatol.* **135**, 1 (2015).
37. Germeraad, E. *et al.* The development of a multiplex serological assay for avian influenza based on Luminex technology. *Methods* **158**, 54–60 (2019).
38. van der Wal, F. J., Bergervoet, J. H. W., Achterberg, R. P. & Haasnoot, W. Bead-based immunoassays. *Nov. Approaches Immunoassays* 53–71 (2014). doi:10.2217/EBO.13.560
39. Tan, X. *et al.* Glass capillary based microfluidic ELISA for rapid diagnostics. *Analyst* **142**, 2378–2385 (2017).
40. Tomás, A. L. *et al.* Development of a Gold Nanoparticle-Based Lateral-Flow Immunoassay for Pneumocystis Pneumonia Serological Diagnosis at Point-of-Care. *Front. Microbiol.* **10**, (2019).
41. Koczula, K. M. & Gallotta, A. Lateral flow assays. *Essays Biochem.* **60**, 111–120 (2016).
42. Liu, J., Mazumdar, D. & Lu, Y. A simple and sensitive 'dipstick' test in serum based on lateral flow separation of aptamer-linked nanostructures. *Angew. Chemie - Int. Ed.* **45**, 7955–7959 (2006).

8.3. Concluding statement

43. Özalp, V. C. *et al.* Small molecule detection by lateral flow strips via aptamer-gated silica nanoprobe. *Analyst* **141**, 2595–2599 (2016).
44. Jönsson, C. *et al.* Silane-dextran chemistry on lateral flow polymer chips for immunoassays. *Lab Chip* **8**, 1191–1197 (2008).
45. Liu, Y., Zhan, L., Qin, Z., Sackrison, J. & Bischof, J. C. Ultrasensitive and Highly Specific Lateral Flow Assays for Point-of-Care Diagnosis. *ACS Nano* **15**, 3593–3611 (2021).
46. Amanda, M., Esther Serrano-Pertierra, M. S., Carlos Martínez-García, J., Rivas, M. & Blanco-López, M. C. Magnetic Lateral Flow Immunoassays. *Diagnostics* **10**, 288 (2020).
47. Kim, H., Chung, D. R. & Kang, M. A new point-of-care test for the diagnosis of infectious diseases based on multiplex lateral flow immunoassays. *Analyst* **144**, 2460–2466 (2019).
48. Linares, E. M., Kubota, L. T., Michaelis, J. & Thalhammer, S. Enhancement of the detection limit for lateral flow immunoassays: Evaluation and comparison of bioconjugates. *J. Immunol. Methods* **375**, 264–270 (2012).
49. Nagatani, N. *et al.* Gold nanoparticle-based novel enhancement method for the development of highly sensitive immunochromatographic test strips. *Sci. Technol. Adv. Mater.* **7**, 270–275 (2006).
50. Mei, Z. *et al.* One-step signal amplified lateral flow strip biosensor for ultrasensitive and on-site detection of bisphenol A (BPA) in aqueous samples. *Biosens. Bioelectron.* **49**, 457–461 (2013).
51. Omidfar, K. *et al.* Colloidal nanogold-based immunochromatographic strip test for the detection of digoxin toxicity. *Appl. Biochem. Biotechnol.* **160**, 843–855 (2010).
52. Serebrennikova, K., Samsonova, J. & Osipov, A. Hierarchical Nanogold Labels to Improve the Sensitivity of Lateral Flow Immunoassay. *Nano-Micro Lett.* **10**, 1–8 (2018).
53. Rodríguez, M. O., Covián, L. B., García, A. C. & Blanco-López, M. C. Silver and gold enhancement methods for lateral flow immunoassays. *Talanta* **148**, 272–278 (2016).
54. Quesada-González, D. *et al.* Iridium oxide (IV) nanoparticle-based lateral flow immunoassay. *Biosens. Bioelectron.* **132**, 132–135 (2019).
55. Shirshahi, V., Nasrollah, S., Hatamie, S. & Saber, R. Functionalized reduced graphene oxide as a lateral flow immuneassay label for one-step detection of Escherichia coli O157: H7. *J. Pharm. Biomed. Anal.* **164**, 104–111 (2019).
56. Sun, W. *et al.* A novel multi-walled carbon nanotube-based antibody conjugate for quantitative and semi-quantitative lateral flow assays. *Biosci. Biotechnol. Biochem.* **81**, 1874–1882 (2017).

9. References

57. Nguyen, V., Song, S., Park, S. & Joo, C. Recent advances in high-sensitivity detection methods for paper-based lateral-flow assay. *Biosens. Bioelectron.* **152**, (2020).
58. Rong, Z. *et al.* Smartphone-based fluorescent lateral flow immunoassay platform for highly sensitive point-of-care detection of Zika virus nonstructural protein 1. *Anal. Chim. Acta* **1055**, 140–147 (2019).
59. Lichtman, J. W. & Conchello, J. A. Fluorescence microscopy. *Nat. Methods* **2**, 910–919 (2005).
60. Lee, L. G., Nordman, E. S., Johnson, M. D. & Oldham, M. F. A low-cost, high-performance system for fluorescence lateral flow assays. *Biosensors* **3**, 360–373 (2013).
61. Sapountzi, E. A., Tragoulias, S. S., Kalogianni, D. P., Ioannou, P. C. & Christopoulos, T. K. Lateral flow devices for nucleic acid analysis exploiting quantum dots as reporters. *Anal. Chim. Acta* **864**, 48–54 (2015).
62. Peeling, R. W., Olliaro, P. L., Boeras, D. I. & Fongwen, N. Scaling up COVID-19 rapid antigen tests: promises and challenges. *Lancet Infect. Dis.* **21**, e290–e295 (2021).
63. Terry, S. C., Herman, J. H. & Angell, J. B. A Gas Chromatographic Air Analyzer Fabricated on a Silicon Wafer. *IEEE Trans. Electron Devices* **26**, 1880–1886 (1979).
64. Manz, A., Graber, N. & Widmer, H. M. Miniaturized total chemical analysis systems: A novel concept for chemical sensing. *Sensors Actuators B. Chem.* **1**, 244–248 (1990).
65. Duffy, D. C., McDonald, J. C., Schueller, O. J. A. & Whitesides, G. M. Rapid prototyping of microfluidic systems in poly(dimethylsiloxane). *Anal. Chem.* **70**, 4974–4984 (1998).
66. Gencturk, E., Mutlu, S. & Ulgen, K. O. Advances in microfluidic devices made from thermoplastics used in cell biology and analyses. *Biomicrofluidics* **11**, (2017).
67. Kim, J. *et al.* Applications, techniques, and microfluidic interfacing for nanoscale biosensing. *Microfluid. Nanofluidics* **7**, 149–167 (2009).
68. Sachdeva, S., Davis, R. W. & Saha, A. K. Microfluidic Point-of-Care Testing: Commercial Landscape and Future Directions. *Front. Bioeng. Biotechnol.* **8**, 1–14 (2021).
69. Kovarik, M. L. & Jacobson, S. C. Nanofluidics in lab-on-a-chip devices. *Anal. Chem.* **81**, 7133–7140 (2009).
70. Chansin, G. A. T. *et al.* Single-molecule spectroscopy using nanoporous membranes. *Nano Lett.* **7**, 2901–2906 (2007).

8.3. Concluding statement

71. Reynolds, O. An experimental investigation of the circumstances which determine whether the motion of water shall be direct or sinuous, and of the law of resistance in parallel channels. *Philos. Trans. R. Soc. London* **174**, 935–982 (1883).
72. Convery, N. & Gadegaard, N. 30 Years of Microfluidics. *Micro Nano Eng.* **2**, 76–91 (2019).
73. Tabeling, P. *Introduction to Microfluidics*. (Oxford University Press on Demand, 2005).
74. Olanrewaju, A., Beaugrand, M., Yafia, M. & Juncker, D. Capillary microfluidics in microchannels: From microfluidic networks to capillary circuits. *Lab Chip* **18**, 2323–2347 (2018).
75. Sato, K. *et al.* Integration of an immunosorbent assay system: Analysis of secretory human immunoglobulin A on polystyrene beads in a microchip. *Anal. Chem.* **72**, 1144–1147 (2000).
76. Dong, J. & Ueda, H. ELISA-type assays of trace biomarkers using microfluidic methods. *Wiley Interdiscip. Rev. Nanomedicine Nanobiotechnology* **9**, 1–19 (2017).
77. Sultan, F., Chimie, M., Jansen, M., Henry, S. & Martinez, L. M. *Magnetic bead coatings: Today and tomorrow*. (Sepmag).
78. Dundas, C. M., Demonte, D. & Park, S. Streptavidin-biotin technology: Improvements and innovations in chemical and biological applications. *Appl. Microbiol. Biotechnol.* **97**, 9343–9353 (2013).
79. Weber, P. C., Ohlendorf, D. H., Wendoloski, J. J. & Salemme, F. R. Structural origins of high-affinity biotin binding to streptavidin. *Science (80-.)*. **243**, 85–88 (1989).
80. Chivers, C. E., Koner, A. L., Lowe, E. D. & Howarth, M. How the biotin-streptavidin interaction was made even stronger: Investigation via crystallography and a chimaeric tetramer. *Biochem. J.* **435**, 55–63 (2011).
81. Huang, C. Y. *et al.* AMPFLUID: Aggregation Magnified Post-Assay Fluorescence for Ultrasensitive Immunodetection on Digital Microfluidics. *Proc. IEEE* **103**, 225–235 (2015).
82. Schmidli, C. *et al.* Microfluidic protein isolation and sample preparation for high-resolution cryo-EM. *Proc. Natl. Acad. Sci. U. S. A.* **116**, 15007–15012 (2019).
83. Andersson, H., Jönsson, C., Moberg, C. & Stemme, G. Patterned self-assembled beads in silicon channels. *Electrophoresis* **22**, 3876–3882 (2001).
84. Gubala, V., Harris, L. F., Ricco, A. J., Tan, M. X. & Williams, D. E. Point of care diagnostics: Status and future. *Anal. Chem.* **84**, 487–515 (2012).

9. References

85. Sia, S. K. & Kricka, L. J. Microfluidics and point-of-care testing. *Lab Chip* **8**, 1982–1983 (2008).
86. Weigl, B., Domingo, G., LaBarre, P. & Gerlach, J. Towards non- and minimally instrumented, microfluidics-based diagnostic devices. *Lab Chip* **8**, 1999–2014 (2008).
87. Lynn, N. S. & Dandy, D. S. Passive microfluidic pumping using coupled capillary/evaporation effects. *Lab Chip* **9**, 3422–3429 (2009).
88. Lillehoj, P. B., Wei, F. & Ho, C. M. A self-pumping lab-on-a-chip for rapid detection of botulinum toxin. *Lab Chip* **10**, 2265–2270 (2010).
89. Dutse, S. W. & Yusof, N. A. Microfluidics-based lab-on-chip systems in DNA-based biosensing: An overview. *Sensors* **11**, 5754–5768 (2011).
90. Zimmermann, M., Schmid, H., Hunziker, P. & Delamarche, E. Capillary pumps for autonomous capillary systems. *Lab Chip* **7**, 119–125 (2007).
91. 1Drop Diagnostics. Available at: <https://www.1dropdx.com/technology/>. (Accessed: 12th April 2022)
92. Durand, N. F. Y. *et al.* Direct observation of transitions between surface-dominated and bulk diffusion regimes in nanochannels. *Anal. Chem.* **81**, 5407–5412 (2009).
93. Durand, N. F. Y. & Renaud, P. Label-free determination of protein-surface interaction kinetics by ionic conductance inside a nanochannel. *Lab Chip* **9**, 319–324 (2009).
94. Abionic. Available at: <https://abionic.com/de>. (Accessed: 12th April 2022)
95. Putallaz, L., Bogaard, P. van den, Laub, P. & Rebeaud, F. Nanofluidics Drives Point-of-care Technology for on the Spot Protein Marker Analysis with Rapid Actionable Results. *J. Nanomed. Nanotechnol.* **10**, 1–7 (2019).
96. Zimmermann, M., Hunziker, P. & Delamarche, E. Valves for autonomous capillary systems. *Microfluid. Nanofluidics* **5**, 395–402 (2008).
97. Korczyk, P. M. *et al.* Accounting for corner flow unifies the understanding of droplet formation in microfluidic channels. *Nat. Commun.* **10**, 1–9 (2019).
98. Arango, Y., Temiz, Y., Gökçe, O. & Delamarche, E. Electro-actuated valves and self-vented channels enable programmable flow control and monitoring in capillary-driven microfluidics. *Sci. Adv.* **6**, 1–13 (2020).
99. Hauser, J. *et al.* High-Yield Passive Plasma Filtration from Human Finger Prick Blood. *Anal. Chem.* **90**, 13393–13399 (2018).
100. Tang, R. H. *et al.* A review on advances in methods for modification of paper supports for use in point-of-care testing. *Microchim. Acta* **186**, (2019).
101. Goldstine, H. H. & Goldstine, A. Electronic numerical integrator and computer (ENIAC). *Math. Tables Other Aids to Comput.* **15**, 97–110 (1946).

8.3. Concluding statement

102. Lakatoş, E. Ş. 60 Years From the Invention of the Integrated Circuits. *EEA - Electroteh. Electron. Autom.* **66**, 72–80 (2018).
103. Dill, F. H. Positive optical lithography. *Dig. Tech. Pap. - IEEE Int. Solid-State Circuits Conf.* 54–55 (1975). doi:10.1109/ISSCC.1975.1155417
104. Al-Amri, M., Liao, Z. & Zubairy, M. S. *Beyond the Rayleigh Limit in Optical Lithography. Advances in Atomic, Molecular and Optical Physics* **61**, (Elsevier Inc., 2012).
105. Fallica, R., Kirchner, R., Schiff, H. & Ekinci, Y. High-resolution grayscale patterning using extreme ultraviolet interference lithography. *Microelectron. Eng.* **177**, 1–5 (2017).
106. Ekinci, Y., Vockenhuber, M., Hojeij, M., Wang, L. & Mojarad, N. M. Evaluation of EUV resist performance with interference lithography towards 11 nm half-pitch and beyond. *Extrem. Ultrav. Lithogr. IV* **8679**, 867910 (2013).
107. Tasdemir, Z. *et al.* Evaluation of EUV resists for 5nm technology node and beyond. 19 (2018). doi:10.1117/12.2502688
108. McKenna, C., Walsh, K., Crain, M. & Lake, J. Maskless direct write grayscale lithography for MEMS applications. *Bienn. Univ. Microelectron. Symp. - Proc.* (2010). doi:10.1109/UGIM.2010.5508906
109. Wolf, H. *et al.* Thermal Scanning Probe Lithography (t-SPL) for Nano-Fabrication. *2019 Pan Pacific Microelectron. Symp. Pan Pacific 2019* 1–9 (2019). doi:10.23919/PanPacific.2019.8696898
110. Esmek, F. M. *et al.* Sculpturing wafer-scale nanofluidic devices for DNA single molecule analysis. *Nanoscale* **11**, 13620–13631 (2019).
111. Mortelmans, T. *et al.* Grayscale e-beam lithography: Effects of a delayed development for well-controlled 3D patterning. *Microelectron. Eng.* **225**, 111272 (2020).
112. Pain, L., Tedesco, S. & Constancias, C. Direct write lithography: the global solution for R&D and manufacturing. *Comptes Rendus Phys.* **7**, 910–923 (2006).
113. Vieu, C. *et al.* Electron beam lithography: Resolution limits and applications. *Appl. Surf. Sci.* **164**, 111–117 (2000).
114. Yasin, S., Hasko, D. G. & Ahmed, H. Comparison of MIBK/IPA and water/IPA as PMMA developers for electron beam nanolithography. *Microelectron. Eng.* **61–62**, 745–753 (2002).
115. Kirchner, R. *et al.* Bio-inspired 3D funnel structures made by grayscale electron-beam patterning and selective topography equilibration. *Microelectron. Eng.* **141**, 107–111 (2015).
116. Sure, A. *et al.* Fabrication and characterization of three-dimensional silicon tapers. *Opt. Express* **11**, 3555 (2003).

9. References

117. Schleunitz, A., Guzenko, V. A., Schander, A., Vogler, M. & Schiff, H. Selective profile transformation of electron-beam exposed multilevel resist structures based on a molecular weight dependent thermal reflow. *J. Vac. Sci. Technol. B* **29**, 06F302 (2011).
118. Chang, T. H. P. Proximity Effect in Electron-Beam Lithography. *J Vac Sci Technol* **12**, 1271–1275 (1975).
119. Raj M, K. & Chakraborty, S. PDMS microfluidics: A mini review. *J. Appl. Polym. Sci.* **137**, (2020).
120. Moschou, D. & Tserepi, A. The lab-on-PCB approach: tackling the μ TAS commercial upscaling bottleneck. *Lab Chip* **17**, 1388–1405 (2017).
121. Berthier, E., Young, E. W. K. & Beebe, D. Engineers are from PDMS-land, biologists are from polystyrenia. *Lab Chip* **12**, 1224–1237 (2012).
122. Ogorodnyk, O. & Martinsen, K. Monitoring and Control for Thermoplastics Injection Molding A Review. *Procedia CIRP* **67**, 380–385 (2018).
123. Muntada-López, O. *et al.* Replication of nanoscale surface gratings via injection molding. *Micro Nano Eng.* **3**, 37–43 (2019).
124. Guo, C. F. *et al.* Grayscale photomask fabricated by laser direct writing in metallic nano-films. *Opt. Express* **17**, 19981–19987 (2009).
125. Deng, Q. *et al.* Fabrication of micro-optics elements with arbitrary surface profiles based on one-step maskless grayscale lithography. *Micromachines* **8**, 314–326 (2017).
126. Zhang, S. *et al.* Multistep Aztec profiles by grayscale electron beam lithography for angle-resolved microspectrometer applications. *J. Vac. Sci. Technol. B, Nanotechnol. Microelectron. Mater. Process. Meas. Phenom.* **32**, 06F504 (2014).
127. Baac, H. *et al.* Submicron-scale topographical control of cell growth using holographic surface relief grating. *Mater. Sci. Eng. C* **24**, 209–212 (2004).
128. Choi, C. H. *et al.* Cell interaction with three-dimensional sharp-tip nanotopography. *Biomaterials* **28**, 1672–1679 (2007).
129. Skaug, M. J., Schwemmer, C., Fringes, S., Rawlings, C. D. & Knoll, A. W. Nanofluidic rocking Brownian motors. *Science (80-.)*. **359**, 1505–1508 (2018).
130. Stavis, S. M. *et al.* Nanofluidic structures with complex three-dimensional surfaces. *Nanotechnology* **20**, 7 (2009).
131. Paiè, P. *et al.* Particle focusing by 3D inertial microfluidics. *Microsystems Nanoeng.* **3**, 1–8 (2017).
132. Zhou, X., Hou, Y. & Lin, J. A review on the processing accuracy of two-photon polymerization. *AIP Adv.* **5**, (2015).

8.3. Concluding statement

133. Heyl, P., Olschewski, T. & Wijnaendts, R. W. Manufacturing of 3D structures for micro-tools using laser ablation. *Microelectron. Eng.* **57–58**, 775–780 (2001).
134. Erdmanis, M. & Tittonen, I. Focused ion beam high resolution grayscale lithography for silicon-based nanostructures. *Appl. Phys. Lett.* **104**, 10–15 (2014).
135. Lisunova, Y. & Brugger, J. Combination of thermal scanning probe lithography and ion etching to fabricate 3D silicon nanopatterns with extremely smooth surface. *Microelectron. Eng.* **193**, 23–27 (2018).
136. Loomis, J., Ratnayake, D., McKenna, C. & Walsh, K. M. Grayscale lithography—automated mask generation for complex three-dimensional topography. *J. Micro/Nanolithography, MEMS, MOEMS* **15**, 013511 (2016).
137. Schleunitz, A., Spreu, C., Vogler, M., Atasoy, H. & Schiff, H. Combining nanoimprint lithography and a molecular weight selective thermal reflow for the generation of mixed 3D structures. *J. Vac. Sci. Technol. B, Nanotechnol. Microelectron. Mater. Process. Meas. Phenom.* **29**, 06FC01 (2011).
138. Kirchner, R., Guzenko, V. A. & Schiff, H. Single-digit 6-nm multilevel patterns by electron beam grayscale lithography. *Adv. Opt. Technol.* **8**, 175–180 (2019).
139. Piaszenski, G. *et al.* 3D structures for UV-NIL template fabrication with grayscale e-beam lithography. *Microelectron. Eng.* **84**, 945–948 (2007).
140. Schleunitz, A. *et al.* Novel 3D micro- and nanofabrication method using thermally activated selective topography equilibration (TASTE) of polymers. *Nano Converg.* **1**, 7 (2014).
141. Murali, R., Brown, D. K., Martin, K. P. & Meindl, J. D. Process optimization and proximity effect correction for gray scale e-beam lithography. *J. Vac. Sci. Technol. B Microelectron. Nanom. Struct.* **24**, 2936–2939 (2006).
142. Schleunitz, A. & Schiff, H. Fabrication of 3D patterns with vertical and sloped sidewalls by grayscale electron-beam lithography and thermal annealing. *Microelectron. Eng.* **88**, 2736–2739 (2011).
143. Fujita, T., Nishihara, H. & Koyama, J. Blazed gratings and Fresnel lenses fabricated by electron-beam lithography. *Opt. Lett.* **7**, 578 (1982).
144. Fujita, T., Nishihara, H. & Koyama, J. Fabrication of micro lenses using electron-beam lithography. *Opt. Lett.* **6**, 613 (1981).
145. Nock, V. & Blaikie, R. J. Fabrication of optical grayscale masks for tapered microfluidic devices. *Microelectron. Eng.* **85**, 1077–1082 (2008).
146. Totsu, K., Fujishiro, K., Tanaka, S. & Esashi, M. Fabrication of three-dimensional microstructure using maskless gray-scale lithography. *Sensors Actuators, A Phys.* **130–131**, 387–392 (2006).

9. References

147. Silvennoinen, M., Kaakkunen, J., Paivasaari, K. & Vahimaa, P. Parallel femtosecond laser ablation with individually controlled intensity. *Opt. Express* **22**, 2603 (2014).
148. Geng, Q., Wang, D., Chen, P. & Chen, S. C. Ultrafast multi-focus 3-D nano-fabrication based on two-photon polymerization. *Nat. Commun.* **10**, 1–7 (2019).
149. Reyntjens, S. & Puers, R. Focused ion beam induced deposition: fabrication of three-dimensional microstructures and Young's modulus of the deposited material. *J. Micromechanics Microengineering* **10**, 181–188 (2000).
150. Fernández-Pacheco, A. *et al.* Three dimensional magnetic nanowires grown by focused electron-beam induced deposition. *Sci. Rep.* **3**, 3–7 (2013).
151. Pires, D. *et al.* Nanoscale three-dimensional patterning of molecular resists by scanning probes. *Science (80-.)*. **328**, 732–735 (2010).
152. Zailer, I., Frost, J. E. F., Chabasseur-Molyneux, V., Ford, C. J. B. & Pepper, M. Crosslinked PMMA as a high-resolution negative resist for electron beam lithography and applications for physics of low-dimensional structures. *Semicond. Sci. Technol.* **11**, 1235–1238 (1996).
153. Schnauber, P. *et al.* Using low-contrast negative-tone PMMA at cryogenic temperatures for 3D electron beam lithography. *Nanotechnology* **27**, (2016).
154. Tanaka, T., Morigami, M. & Atoda, N. Mechanism Of Resist Pattern Collapse During Development Process. *Jpn. J. Appl. Phys.* **32**, 6059–6064 (1993).
155. Mojarad, N., Kazazis, D. & Ekinci, Y. Fabrication of high aspect ratio and tilted nanostructures using extreme ultraviolet and soft x-ray interference lithography. *J. Vac. Sci. Technol. B* **39**, 042601 (2021).
156. Yoon, C. *et al.* Chemical Use and Associated Health Concerns in the Semiconductor Manufacturing Industry. *Saf. Health Work* **11**, 500–508 (2020).
157. Auzelyte, V., Langner, A. & Solak, H. H. Thermal development of a calixarene resist. *J. Vac. Sci. Technol. B Microelectron. Nanom. Struct.* **27**, 2990 (2009).
158. Tsuda, M. *et al.* Novel Plasma Developable Resist Compositions and Performance of Total Dry Microfabrication in Submicron Lithography. *J. Vac. Sci. Technol.* **19**, 1351–1357 (1981).
159. Tsuda, M. *et al.* Dry development and fine pattern fabrication PMIPK-Azide dry-developable resist in electron beam lithography. *Microelectron. Eng.* **2**, 105–112 (1984).
160. Tsuda, M. & Oikawa, S. (Invited) mechanism of dry development and dry etch resistance of resist. *Jpn. J. Appl. Phys.* **21**, 135 (1982).

8.3. Concluding statement

161. Bargon, J., Baumann, R. R. & Boeker, P. Dry development of resist patterns using RIE based on different electrical conductivity. *Adv. Resist Technol. Process. IX* **1672**, 441 (1992).
162. Wise, R. S. Breaking stochastic tradeoffs with a dry deposited and dry developed EUV photoresist system. in *Proc.SPIE* **11612**, (2021).
163. Choi, J. O. Degradation of poly(methylmethacrylate) by deep ultraviolet, x-ray, electron beam, and proton beam irradiations. *J. Vac. Sci. Technol. B Microelectron. Nanom. Struct.* **6**, 2286 (1988).
164. Katsuhiko, H. Plasma etching durability of PMMA. *J. Appl. Polym. Sci.* **26**, 1961 (1981).
165. Zanini, S. *et al.* Sulfur hexafluoride (SF₆) plasma treatment of medical grade poly(methyl methacrylate). *Coatings* **10**, 1–14 (2020).
166. Grigaliūnas, V. *et al.* Effects of 3D microlens transfer into fused silica substrate by CF₄/O₂ dry etching. *Appl. Surf. Sci.* **393**, 287–293 (2017).
167. Schwartzman, M., Mathur, A., Hone, J., Jahnes, C. & Wind, S. J. Plasma fluorination of carbon-based materials for imprint and molding lithographic applications. *Appl. Phys. Lett.* **93**, 6–9 (2008).
168. Kim, S. H., Moon, H. & Ahn, J. Effects of SF₆ addition to O₂ plasma on polyimide etching in ECR plasma etcher. *Dig. Pap. - 2000 Int. Microprocess. Nanotechnol. Conf. MNC 2000* 214–215 (2000). doi:10.1109/IMNC.2000.872718
169. Pétri, R. *et al.* Silicon roughness induced by plasma etching. *J. Appl. Phys.* **75**, 7498–7506 (1994).
170. Nathawat, R., Kumar, A. & Vijay, Y. K. Morphological changes of electron-beam irradiated PMMA surface. *Proc. IEEE Part. Accel. Conf.* 2745–2747 (2007). doi:10.1109/PAC.2007.4440562
171. Kirchner, R., Chidambaram, N., Altana, M. & Schift, H. Surface smoothing of the inherent roughness of micro-lenses fabricated with 2-photon lithography. **10456**, 64 (2018).
172. Sackmann, E. K., Fulton, A. L. & Beebe, D. J. The present and future role of microfluidics in biomedical research. *Nature* **507**, 181–189 (2014).
173. Nie, S. *et al.* An automated integrated platform for rapid and sensitive multiplexed protein profiling using human saliva samples. *Lab Chip* **14**, 1087–1098 (2014).
174. Moon, H., Wheeler, A. R., Garrell, R. L., Loo, J. A. & Kim, C. J. An integrated digital microfluidic chip for multiplexed proteomic sample preparation and analysis by MALDI-MS. *Lab Chip* **6**, 1213–1219 (2006).
175. Zhang, C. *et al.* Ultra-multiplexed analysis of single-cell dynamics reveals logic rules in differentiation. *Sci. Adv.* **5**, 1–11 (2019).

9. References

176. Rogers, J. A. & Nuzzo, R. G. Recent progress in soft lithography. *Mater. Today* **8**, 50–56 (2005).
177. Gerspach, M. A., Mojarad, N., Sharma, D., Pfohl, T. & Ekinici, Y. Soft electrostatic trapping in nanofluidics. *Microsystems Nanoeng.* **3**, 0–10 (2017).
178. Deshmukh, S. S. & Goswami, A. Hot Embossing of polymers - A review. *Mater. Today Proc.* **26**, 405–414 (2019).
179. Sun, J. *et al.* Development and Application of Hot Embossing in Polymer Processing: A Review. *ES Mater. Manuf.* **6**, 3–17 (2019).
180. Scott, S. M. & Ali, Z. Fabrication methods for microfluidic devices: An overview. *Micromachines* **12**, (2021).
181. Kim, Y. *et al.* High-throughput injection molded microfluidic device for single-cell analysis of spatiotemporal dynamics. *Lab Chip* **21**, 3150–3158 (2021).
182. Marshall, L. A., Rogacs, A., Meinhart, C. D. & Santiago, J. G. An injection molded microchip for nucleic acid purification from 25 microliter samples using isotachopheresis. *J. Chromatogr. A* **1331**, 139–142 (2014).
183. Ma, X. *et al.* Injection molding and characterization of PMMA-based microfluidic devices. *Microsyst. Technol.* **26**, 1317–1324 (2020).
184. Lee, U. N. *et al.* Fundamentals of rapid injection molding for microfluidic cell-based assays. *Lab Chip* **18**, 496–504 (2018).
185. Zhou, Z., Chen, D., Wang, X. & Jiang, J. Milling positive master for polydimethylsiloxane microfluidic devices: The microfabrication and roughness issues. *Micromachines* **8**, (2017).
186. Mortelmans, T. *et al.* Poly(methyl methacrylate)-Based Nanofluidic Device for Rapid and Multiplexed Serological Antibody Detection of SARS-CoV-2. *ACS Appl. Nano Mater.* **5**, 517–526 (2022).
187. Han, J. Y., Wiederoder, M. & DeVoe, D. L. Isolation of intact bacteria from blood by selective cell lysis in a microfluidic porous silica monolith. *Microsystems Nanoeng.* **5**, (2019).
188. Mena, S. E. *et al.* Variable-height channels for microparticle characterization and display. *Lab Chip* **20**, 2510–2519 (2020).
189. Rytka, C., Kristiansen, P. M. & Neyer, A. Iso- and variothermal injection compression moulding of polymer micro- and nanostructures for optical and medical applications. *J. Micromechanics Microengineering* **25**, 16 (2015).
190. Walt, V. Der *et al.* Scikit-image: Image processing in python. *PeerJ* **2014**, 1–18 (2014).
191. McKinney, W. Data Structures for Statistical Computing in Python. *Proc. 9th Python Sci. Conf.* **1**, 56–61 (2010).

8.3. Concluding statement

192. Harris, C. R. *et al.* Array programming with NumPy. *Nature* **585**, 357–362 (2020).
193. Eijkel, J. C. T. & Van Den Berg, A. Young 4ever - The use of capillarity for passive flow handling in lab on a chip devices. *Lab Chip* **6**, 1405–1408 (2006).
194. Jang, Y. R., Jeong, R., Kim, H. S. & Park, S. S. Fabrication of solderable intense pulsed light sintered hybrid copper for flexible conductive electrodes. *Sci. Rep.* **11**, 1–15 (2021).
195. Horiuchi, S., Hakukawa, H., Jong Kim, Y., Nagata, H. & Sugimura, H. Study of the adhesion and interface of the low-temperature bonding of vacuum ultraviolet-irradiated cyclo-olefin polymer using electron microscopy. *Polym. J.* **48**, 473–479 (2016).
196. Tsao, C. W., Hromada, L., Liu, J., Kumar, P. & DeVoe, D. L. Low temperature bonding of PMMA and COC microfluidic substrates using UV/ozone surface treatment. *Lab Chip* **7**, 499–505 (2007).
197. Aderneuer, T. *et al.* Surface topology and functionality of freeform microlens arrays. *Opt. Express* **29**, 5033 (2021).
198. Jakubowsky, M., Werder, J., Rytka, C., Kristiansen, P. M. & Neyer, A. Design, manufacturing and experimental validation of a bonded dual-component microstructured system for vertical light emission. *Microsyst. Technol.* **26**, 2087–2093 (2020).
199. Chidambaram, N. *et al.* Selective Surface Smoothing of Polymer Microlenses by Depth Confined Softening. *Adv. Mater. Technol.* **2**, (2017).
200. Kim, Y. J. & Sugimura, H. Effects of irradiation atmosphere on vacuum ultraviolet-induced surface modification of cyclo-olefin polymer substrates. *Appl. Phys. Express* **12**, (2019).
201. Couto, R. *et al.* Microfluidic supercritical antisolvent continuous processing and direct spray-coating of poly(3-hexylthiophene) nanoparticles for OFET devices. *Chem. Commun.* **51**, 1008–1011 (2015).
202. Volpe, A. *et al.* Welding of PMMA by a femtosecond fiber laser. *Opt. Express* **23**, 4114 (2015).
203. Zhang, Z., Wang, X., Luo, Y., He, S. & Wang, L. Thermal assisted ultrasonic bonding method for poly(methyl methacrylate) (PMMA) microfluidic devices. *Talanta* **81**, 1331–1338 (2010).
204. Gaebler, C. *et al.* Evolution of antibody immunity to SARS-CoV-2. *Nature* **591**, 639–644 (2021).
205. Guglielmi, G. Rapid coronavirus tests: a guide for the perplexed. *Nature* **590**, 202–205 (2021).
206. Rubin, R. The Challenges of Expanding Rapid Tests to Curb COVID-19. *JAMA - J. Am. Med. Assoc.* **324**, 1813–1815 (2020).

9. References

207. Corman, V. M. *et al.* Comparison of seven commercial SARS-CoV-2 rapid point-of-care antigen tests: a single-centre laboratory evaluation study. *The Lancet Microbe* **2**, e311–e319 (2021).
208. Hartanto, H., Wu, M., Lam, M. L. & Chen, T. H. Microfluidic immunoassay for detection of serological antibodies: A potential tool for rapid evaluation of immunity against SARS-CoV-2. *Biomicrofluidics* **14**, 1–13 (2020).
209. Ung, Y. U. S., Ampa, F. E. C. & Hih, W. E. I. H. S. Open-source do-it-yourself multi-color fluorescence smartphone microscopy. *Biomed. Opt. Express* **8**, 236–247 (2017).
210. Mariën, J. *et al.* Evaluating SARS-CoV-2 spike and nucleocapsid proteins as targets for antibody detection in severe and mild COVID-19 cases using a Luminex bead-based assay. *J. Virol. Methods* **288**, (2021).
211. Swank, Z. *et al.* A high-throughput microfluidic nanoimmunoassay for detecting anti-SARS-CoV-2 antibodies in serum or ultralow-volume blood samples. *Proc. Natl. Acad. Sci. U. S. A.* **118**, 1–9 (2021).
212. Bhatraju, P. K. *et al.* Covid-19 in Critically Ill Patients in the Seattle Region — Case Series. *N. Engl. J. Med.* **382**, 2012–2022 (2020).
213. Pum, J. *A practical guide to validation and verification of analytical methods in the clinical laboratory.* *Advances in Clinical Chemistry* **90**, (Elsevier Inc., 2019).
214. Mironov, A. E. *et al.* Photolithography in the vacuum ultraviolet (172 nm) with sub-400 nm resolution: Photoablative patterning of nanostructures and optical components in bulk polymers and thin films on semiconductors. *Nanoscale* **12**, 16796–16804 (2020).
215. Bhattacharyya, A. & Klapperich, C. M. Mechanical and chemical analysis of plasma and ultraviolet-ozone surface treatments for thermal bonding of polymeric microfluidic devices. *Lab Chip* **7**, 876–882 (2007).
216. Rodda, D. J. & Yamazaki, H. Poly(vinyl alcohol) as a blocking agent in enzyme immunoassays. *Immunol. Invest.* **23**, 421–428 (1994).
217. Khodayari Babil, A. & Kim, J. A capillary flow-driven microfluidic system for microparticle-labeled immunoassays. *Analyst* **143**, 3335–3342 (2018).
218. Chaplin, D. D. Overview of the immune response. *J. Allergy Clin. Immunol.* **125**, S3–S23 (2010).
219. Chi, X. *et al.* A neutralizing human antibody binds to the N-terminal domain of the Spike protein of SARS-CoV-2. *Science (80-.)*. **369**, 650–655 (2020).
220. Premkumar, L. *et al.* The receptor-binding domain of the viral spike protein is an immunodominant and highly specific target of antibodies in SARS-CoV-2 patients. *Sci. Immunol.* **5**, 1–10 (2020).

8.3. Concluding statement

221. Choi, J. *et al.* Portable , one-step , and rapid GMR biosensor platform with smartphone interface. *Biosens. Bioelectron.* **85**, 1–7 (2016).
222. Tekin, H. C., Cornaglia, M. & Gijs, M. A. M. Attomolar protein detection using a magnetic bead surface coverage assay. *Lab Chip* **13**, 1053–1059 (2013).
223. Rodriguez-Moncayo, R. *et al.* A high-throughput multiplexed microfluidic device for COVID-19 serology assays. *Lab Chip* **21**, 93–104 (2021).
224. Tan, X. *et al.* Rapid and quantitative detection of SARS-CoV-2 specific IgG for convalescent serum evaluation. *Biosens. Bioelectron.* **169**, (2020).
225. Liu, G. & Rusling, J. F. COVID-19 Antibody Tests and Their Limitations. *ACS Sensors* **6**, 593–612 (2021).
226. Miller, B. S. *et al.* Spin-enhanced nanodiamond biosensing for ultrasensitive diagnostics. *Nature* **587**, 588–593 (2020).
227. West, C. P., Montori, V. M. & Sampathkumar, P. COVID-19 Testing: The Threat of False-Negative Results. *Mayo Clin. Proc.* **95**, 1127–1129 (2020).
228. Liu, X. *et al.* Patterns of IgG and IgM antibody response in COVID-19 patients. *Emerg. Microbes Infect.* **9**, 1269–1274 (2020).
229. Long, Q. X. *et al.* Antibody responses to SARS-CoV-2 in patients with COVID-19. *Nat. Med.* **26**, 845–848 (2020).
230. Li, X. *et al.* The role of children in transmission of SARS-CoV-2: A rapid review. *J. Glob. Health* **10**, 1342–1343 (2020).
231. Dilillo, D. J., Tan, G. S., Palese, P. & Ravetch, J. V. Broadly neutralizing hemagglutinin stalk-specific antibodies require FcR interactions for protection against influenza virus in vivo. *Nat. Med.* **20**, 143–151 (2014).
232. Gillot, C. *et al.* An original elisa-based multiplex method for the simultaneous detection of 5 sars-cov-2 igg antibodies directed against different antigens. *J. Clin. Med.* **9**, 1–13 (2020).
233. Ghosh, S. *et al.* A new microchannel capillary flow assay (MCFA) platform with lyophilized chemiluminescence reagents for a smartphone-based POCT detecting malaria. *Microsystems Nanoeng.* **6**, 1–18 (2020).
234. Favresse, J. *et al.* An original multiplex method to assess five different SARS-CoV-2 antibodies. *Clin. Chem. Lab. Med.* **59**, 971–978 (2021).
235. Guo, X., Chen, Y., Zhang, L. & Liu, W. An inkjet printing paper-based immunodevice for fluorescence determination of immunoglobulin G. *Anal. Methods* **11**, 3452–3459 (2019).
236. Chen, J. H. K. *et al.* Clinical performance of the luminex nxtag cov extended panel for sars-cov-2 detection in nasopharyngeal specimens from covid-19 patients in Hong Kong. *J. Clin. Microbiol.* **58**, 1–6 (2020).

9. References

237. Bray, R. A. *et al.* Development and Validation of a Multiplex, Bead-based Assay to Detect Antibodies Directed against SARS-CoV-2 Proteins. *Transplantation* **105**, 79–89 (2021).
238. Wagner, T. R. *et al.* NeurobodyPlex—monitoring SARS-CoV-2 neutralizing immune responses using nanobodies. *EMBO Rep.* **22**, 1–16 (2021).
239. Den Hartog, G. *et al.* SARS-CoV-2-Specific Antibody Detection for Seroepidemiology: A Multiplex Analysis Approach Accounting for Accurate Seroprevalence. *J. Infect. Dis.* **222**, 1452–1461 (2020).
240. Lynch, H. E. *et al.* Development and implementation of a proficiency testing program for Luminex bead-based cytokine assays. *J. Immunol. Methods* **409**, 62–71 (2014).
241. Kohl, T. O. & Ascoli, C. A. Immunometric double-antibody sandwich enzyme-linked immunosorbent assay. *Cold Spring Harb. Protoc.* **2017**, 458–462 (2017).
242. Bose, A. & Beal, M. F. Mitochondrial dysfunction in Parkinson’s disease. *J. Neurochem.* **139**, 216–231 (2016).
243. Davis, M. E., Chen, Z. G. & Shin, D. M. Nanoparticle therapeutics: An emerging treatment modality for cancer. *Nat. Rev. Drug Discov.* **7**, 771–782 (2008).
244. Rees, D. C., Williams, T. N. & Gladwin, M. T. Sickle-cell disease. *Lancet* **376**, 2018–2031 (2018).
245. Pinho, A. R. *et al.* Comparison of ELISA and HPLC-MS methods for the determination of exenatide in biological and biotechnology-based formulation matrices. *J. Pharm. Anal.* **9**, 143–155 (2019).
246. de Bruin, E., Duizer, E., Vennema, H. & Koopmans, M. P. G. Diagnosis of Norovirus outbreaks by commercial ELISA or RT-PCR. *J. Virol. Methods* **137**, 259–264 (2006).
247. Tenforde, M. W. *et al.* Diagnostic accuracy of the biosynex cryptops cryptococcal antigen semiquantitative lateral flow assay in patients with advanced HIV disease. *J. Clin. Microbiol.* **59**, (2021).
248. Dector, A. *et al.* Towards autonomous lateral flow assays: Paper-based microfluidic fuel cell inside an HIV-test using a blood sample as fuel. *Int. J. Hydrogen Energy* **42**, 27979–27986 (2017).
249. Sastre, P. *et al.* Development of a novel lateral flow assay for detection of African swine fever in blood. *BMC Vet. Res.* **12**, 1–8 (2016).
250. Corman, V. M. *et al.* Comparison of seven commercial SARS-CoV-2 rapid point-of-care antigen tests: a single-centre laboratory evaluation study. *The Lancet Microbe* **5247**, 1–9 (2021).

8.3. Concluding statement

251. Klinger, M. H. F. & Jelkmann, W. Role of blood platelets in infection and inflammation. *J. Interf. Cytokine Res.* **22**, 913–922 (2002).
252. Thewissen, M. *et al.* Analyses of immunosenescent markers in patients with autoimmune disease. *Clin. Immunol.* **123**, 209–218 (2007).
253. Duffy, M. J. & O'Byrne, K. *Tissue and Blood Biomarkers in Lung Cancer: A Review. Advances in Clinical Chemistry* **86**, (Elsevier Ltd, 2018).
254. Jickling, G. C. & Sharp, F. R. Blood Biomarkers of Ischemic Stroke. *Neurotherapeutics* **8**, 349–360 (2011).
255. Olsson, B. *et al.* CSF and blood biomarkers for the diagnosis of Alzheimer's disease: a systematic review and meta-analysis. *Lancet Neurol.* **15**, 673–684 (2016).
256. Ford, J. Red blood cell morphology. *Int. J. Lab. Hematol.* **35**, 351–357 (2013).
257. Mielczarek, W. S., Obaje, E. A., Bachmann, T. T. & Kersaudy-Kerhoas, M. Microfluidic blood plasma separation for medical diagnostics: Is it worth it? *Lab Chip* **16**, 3441–3448 (2016).
258. Zheng, X. H., Cui, C., Zhou, X. X., Zeng, Y. X. & Jia, W. H. Centrifugation: An important pre-analytic procedure that influences plasma microRNA quantification during blood processing. *Chin. J. Cancer* **32**, 667–672 (2013).
259. Yang, X., Forouzan, O., Brown, T. P. & Shevkoplyas, S. S. Integrated separation of blood plasma from whole blood for microfluidic paper-based analytical devices. *Lab Chip* **12**, 274–280 (2012).
260. Homsy, A. *et al.* Development and validation of a low cost blood filtration element separating plasma from undiluted whole blood. *Biomicrofluidics* **6**, (2012).
261. Guo, W., Hansson, J. & Van Der Wijngaart, W. Synthetic Paper Separates Plasma from Whole Blood with Low Protein Loss. *Anal. Chem.* **92**, 6194–6199 (2020).
262. Baviera, G. *et al.* The Effect of Sample Hemolysis on Cardiac Troponin I and T Assays. *Clin. Chem.* **56**, 1355–1357 (2010).
263. Holmes, D. *et al.* Separation of blood cells with differing deformability using deterministic lateral displacement. *Interface Focus* **4**, (2014).
264. Yang, S., Ündar, A. & Zahn, J. D. A microfluidic device for continuous, real time blood plasma separation. *Lab Chip* **6**, 871–880 (2006).
265. Tripathi, S., Varun Kumar, Y. V. B., Prabhakar, A., Joshi, S. S. & Agrawal, A. Passive blood plasma separation at the microscale: A review of design principles and microdevices. *J. Micromechanics Microengineering* **25**, (2015).

9. References

266. Fomitcheva-Khartchenko, A., Pereiro, I. & Kaigala, G. V. Shake it or shrink it: Mass transport and kinetics in surface bioassays using agitation and microfluidics. *MicroTAS 2020 - 24th Int. Conf. Miniaturized Syst. Chem. Life Sci.* 589–590 (2020).
267. Taranova, N. A. *et al.* Integration of lateral flow and microarray technologies for multiplex immunoassay: Application to the determination of drugs of abuse. *Microchim. Acta* **180**, 1165–1172 (2013).
268. McCaughan, A. N. *et al.* PHIDL: Python -based layout and geometry creation for nanolithography . *J. Vac. Sci. Technol. B* **39**, 062601 (2021).
269. Walt, V. Der, Sch, J. L. & Nunez-iglesias, J. scikit-image : image processing in Python. *PeerJ* 1–18 (2014). doi:10.7717/peerj.453
270. Harris, C. R. *et al.* Array programming with NumPy. *Nature* **585**, 357–362 (2020).
271. Bruus, H. Theoretical microfluidics. *Physics (College. Park. Md)*. **18**, 363 (2008).
272. Monica Diez-Silva, Ming Dao, Jongyoon Han, Chwee-Teck Lim, and S. S. A. Shape and Biomechanical Characteristics of Human Red Blood Cells in Health and Disease. *MRS Bull.* **35**, 382–388 (2010).
273. Wild, D. *The immunoassay handbook*. (2013).
274. Schmidli, C. *et al.* Microfluidic protein isolation and sample preparation. 1–6 (2019). doi:10.1073/pnas.1907214116
275. Fung, E., Sugianto, P., Hsu, J., Damoiseaux, R. & Ganz, T. High-Throughput Screening of Small Molecules Identifies Hepcidin Antagonists s. **2**, 681–690 (2013).
276. Lionello, A., Josserand, J., Jensen, H. & Girault, H. H. Protein adsorption in static microsystems: Effect of the surface to volume ratio. *Lab Chip* **5**, 254–260 (2005).
277. Leichlé, T. & Chou, C. F. Biofunctionalized nanoslits for wash-free and spatially resolved real-time sensing with full target capture. *Biomicrofluidics* **9**, (2015).
278. Péterfi, Z. & Kocsis, B. Comparison of blocking agents for an ELISA for LPS. *J. Immunoassay* **21**, 341–354 (2000).
279. Tochi, B. N. *et al.* Monoclonal antibody for the development of specific immunoassays to detect Enrofloxacin in foods of animal origin Monoclonal antibody for the development of specific immunoassays to detect Enrofloxacin in foods of animal origin. (2015). doi:10.1080/09540105.2015.1089844
280. Selmi, M., Gazzah, M. H. & Belmabrouk, H. Optimization of microfluidic biosensor efficiency by means of fluid flow engineering. *Sci. Rep.* **7**, 1–11 (2017).

8.3. Concluding statement

281. Tehrani, Z. *et al.* Generic epitaxial graphene biosensors for ultrasensitive detection of cancer risk biomarker. *2D Mater.* **1**, (2014).
282. Gienger, J., Gross, H., Ost, V., Bär, M. & Neukammer, J. Assessment of deformation of human red blood cells in flow cytometry: measurement and simulation of bimodal forward scatter distributions. *Biomed. Opt. Express* **10**, 4531 (2019).
283. Nitzan, M., Romem, A. & Koppel, R. Pulse oximetry: Fundamentals and technology update. *Med. Devices Evid. Res.* **7**, 231–239 (2014).
284. Sato, K., Tokeshi, M., Kimura, H. & Kitamori, T. Determination of carcinoembryonic antigen in human sera by integrated bead-bed immunoassay in a microchip for cancer diagnosis. *Anal. Chem.* **73**, 1213–1218 (2001).
285. Di Nonno, S. & Ulber, R. Smartphone-based optical analysis systems. *Analyst* **146**, 2749–2768 (2021).
286. Resch-Genger, U., Grabolle, M., Cavaliere-Jaricot, S., Nitschke, R. & Nann, T. Quantum dots versus organic dyes as fluorescent labels. *Nat. Methods* **5**, 763–775 (2008).
287. Takasaki, K. T., Ding, J. B. & Sabatini, B. L. Live-cell superresolution imaging by pulsed STED two-photon excitation microscopy. *Biophys. J.* **104**, 770–777 (2013).
288. Liedert, C. *et al.* Roll-to-Roll Manufacturing of Integrated Immunodetection Sensors. *ACS Sensors* **5**, 2010–2017 (2020).
289. Carr, E. A. *Systemic Inflammatory Response Syndrome. Robinson's Current Therapy in Equine Medicine: Seventh Edition* (StatPearls Publishing, Treasure Island, 2015). doi:10.1016/B978-1-4557-4555-5.00177-1
290. Chaudhry, H. *et al.* Role of cytokines as a double-edged sword in sepsis. *In Vivo (Brooklyn)*. **27**, 669–684 (2013).
291. Marsh, C. B. & Wewers, M. D. The pathogenesis of sepsis: Factors that modulate the response to gram- negative bacterial infection. *Clin. Chest Med.* **17**, 183–197 (1996).
292. Lin, G. L., McGinley, J. P., Drysdale, S. B. & Pollard, A. J. Epidemiology and Immune Pathogenesis of Viral Sepsis. *Front. Immunol.* **9**, 1–21 (2018).
293. Bozza, F. A. *et al.* Cytokine profiles as markers of disease severity in sepsis: A multiplex analysis. *Crit. Care* **11**, 1–8 (2007).
294. Valera, E. *et al.* A microfluidic biochip platform for electrical quantification of proteins. *Lab Chip* **18**, 1461–1470 (2018).
295. Anderson, P. Post-transcriptional control of cytokine production. *Nature Immunology* **9**, 353–359 (2008).

9. References

296. Kruijs, V. & Huez, G. Translational control of cytokine expression by 3' UA-rich sequences. *Biochimie* **76**, 862–866 (1994).
297. Kim, C. K. *et al.* Bronchoalveolar lavage cytokine profiles in acute asthma and acute bronchiolitis. *J. Allergy Clin. Immunol.* **112**, 64–71 (2003).
298. Kaptoge, S. *et al.* Inflammatory cytokines and risk of coronary heart disease: New prospective study and updated meta-analysis. *Eur. Heart J.* **35**, 578–589 (2014).
299. Chen, Z. Y. *et al.* Cytokine profile and prognostic significance of high neutrophil-lymphocyte ratio in colorectal cancer. *Br. J. Cancer* **112**, 1088–1097 (2015).
300. Li, L. *et al.* Serum cytokine profile in patients with breast cancer. *Cytokine* **89**, 173–178 (2017).
301. Wakita, T., Shintani, F., Yagi, G., Asai, M. & Nozawa, S. Combination of inflammatory cytokines increases nitrite and nitrate levels in the paraventricular nucleus of conscious rats. *Brain Res.* **905**, 12–20 (2001).
302. Vincent, J. L. The Clinical Challenge of Sepsis Identification and Monitoring. *PLoS Med.* **13**, 1–10 (2016).
303. Moncunill, G., Aponte, J. J., Nhabomba, A. J. & Dobaño, C. Performance of Multiplex Commercial Kits to Quantify Cytokine and Chemokine Responses in Culture Supernatants from *Plasmodium falciparum* Stimulations. *PLoS One* **8**, (2013).
304. Jones, A., Dhanapala, L., Kankanamage, R. N. T., Kumar, C. V. & Rusling, J. F. Multiplexed immunosensors and immunoarrays. *Anal. Chem.* **92**, 345–362 (2020).
305. Feng, S. *et al.* A noninvasive cancer detection strategy based on gold nanoparticle surface-enhanced raman spectroscopy of urinary modified nucleosides isolated by affinity chromatography. *Biosens. Bioelectron.* **91**, 616–622 (2017).
306. Kim, M. *et al.* Detection of ovarian cancer via the spectral fingerprinting of quantum-defect-modified carbon nanotubes in serum by machine learning. *Nat. Biomed. Eng.* **6**, 267–275 (2022).
307. Poon, T. C. W. *et al.* Diagnosis of Gastric Cancer by Serum Proteomic Fingerprinting. *Gastroenterology* **130**, 1858–1864 (2006).
308. La Farré, M. *et al.* Evaluation of 4-nitrophenol ELISA kit for assessing the origin of organic pollution in wastewater treatment works. *Environ. Sci. Technol.* **33**, 3898–3904 (1999).
309. Asghar, W. *et al.* Engineering long shelf life multi-layer biologically active surfaces on microfluidic devices for point of care applications. *Sci. Rep.* **6**, 1–10 (2016).

8.3. Concluding statement

310. Glière, A. & Delattre, C. Modeling and fabrication of capillary stop valves for planar microfluidic systems. *Sensors Actuators, A Phys.* **130–131**, 601–608 (2006).
311. Dave, R., Terry, D. S., Munro, J. B. & Blanchard, S. C. Mitigating unwanted photophysical processes for improved single-molecule fluorescence imaging. *Biophys. J.* **96**, 2371–2381 (2009).
312. Chaudhry, H. *et al.* Role of cytokines as a double-edged sword in sepsis. *In Vivo* **27**, 669–684 (2013).
313. Opal, S. M. & DePalo, V. A. Anti-inflammatory cytokines. *Chest* **117**, 1162–1172 (2000).
314. Gogos, C. A., Drosou, E., Bassaris, H. P. & Skoutelis, A. Pro- versus anti-inflammatory cytokine profile in patients with severe sepsis: A marker for prognosis and future therapeutic options. *J. Infect. Dis.* **181**, 176–180 (2000).
315. Wu, H. P. *et al.* Serial cytokine levels in patients with severe sepsis. *Inflamm. Res.* **58**, 385–393 (2009).
316. Kox, W. J., Volk, T., Kox, S. N. & Volk, H. D. Immunomodulatory therapies in sepsis. *Intensive Care Med. Suppl.* **26**, 124–128 (2000).
317. Sagy, M., Al-Qaqaa, Y. & Kim, P. Definitions and pathophysiology of sepsis. *Curr. Probl. Pediatr. Adolesc. Health Care* **43**, 260–263 (2013).
318. Mera, S. *et al.* Multiplex cytokine profiling in patients with sepsis. *Apmis* **119**, 155–163 (2011).
319. Kumar, A. *et al.* Duration of hypotension before initiation of effective antimicrobial therapy is the critical determinant of survival in human septic shock. *Crit. Care Med.* **34**, 1589–1596 (2006).
320. Studentsov, Y. Y. *et al.* Enhanced enzyme-linked immunosorbent assay for detection of antibodies to virus-like particles of human papillomavirus. *J. Clin. Microbiol.* **40**, 1755–1760 (2002).
321. Jiang, X. & Lillehoj, P. B. Lateral flow immunochromatographic assay on a single piece of paper. *Analyst* **146**, 1084–1090 (2021).
322. Park, J. W. *et al.* Comparison of stabilizing effect of stabilizers for immobilized antibodies on QCM immunosensors. *Sensors Actuators, B Chem.* **91**, 158–162 (2003).
323. Eberle, P. *et al.* Single entity resolution valving of nanoscopic species in liquids. *Nat. Nanotechnol.* **13**, 578–582 (2018).
324. Erjawetz, J. *et al.* Bend the curve – shape optimization in laser grayscale direct write lithography using a single figure of merit. *Micro Nano Eng.* **15**, (2022).

9. References

325. Jakob, T., Forstenlechner, P., Matricardi, P. & Kleine-Tebbe, J. Molekulare allergiediagnostik im multiplex-verfahren: Teil 21 der Serie Molekulare Allergie. *Allergo J.* **24**, 42–56 (2015).
326. Tort, N., Salvador, J. P. & Marco, M. P. Multiplexed immunoassay to detect anabolic androgenic steroids in human serum. *Anal. Bioanal. Chem.* **403**, 1361–1371 (2012).
327. Tokarz, R. *et al.* A multiplex serologic platform for diagnosis of tick-borne diseases. *Sci. Rep.* **8**, 1–10 (2018).
328. Wu, B., Kumar, A. & Pamarthy, S. High aspect ratio silicon etch: A review. *J. Appl. Phys.* **108**, (2010).
329. Daviet, J. -F., Peccoud, L. & Mondon, F. Electrostatic Clamping Applied to Semiconductor Plasma Processing: II . Experimental Results. *J. Electrochem. Soc.* **140**, 3256–3261 (1993).
330. Schiff, H. *et al.* Transparent hybrid polymer stamp copies with sub-50-nm resolution for thermal and UV-nanoimprint lithography. *J. Vac. Sci. Technol. B Microelectron. Nanom. Struct.* **27**, 2846 (2009).
331. Asif, M. H., Graczyk, M., Heidari, B. & Maximov, I. Comparison of UV-curable materials for high-resolution polymer nanoimprint stamps. *Micro Nano Eng.* **14**, (2022).
332. Chrostowski, L. *et al.* Silicon Photonic Circuit Design Using Rapid Prototyping Foundry Process Design Kits. *IEEE J. Sel. Top. Quantum Electron.* **25**, 1–26 (2019).
333. Feysa, B. *et al.* Patterned Immobilization of Antibodies within Roll-to-Roll Hot Embossed Polymeric Microfluidic Channels. *PLoS One* **8**, (2013).
334. Kim, H. *et al.* LudusScope: Accessible interactive smartphone microscopy for life-science education. *PLoS One* **11**, 1–16 (2016).
335. Wang, H., Heintzmann, R. & Diederich, B. The power in your pocket - uncover smartphones for use as cutting-edge microscopic instruments in science and research. *Adv. Opt. Technol.* **10**, 89–108 (2021).
336. Cai, F., Wang, T., Lu, W. & Zhang, X. High-resolution mobile bio-microscope with smartphone telephoto camera lens. *Optik (Stuttg.)*. **207**, 164449 (2020).
337. Cesaretti, M. *et al.* Accurate assessment of nonalcoholic fatty liver disease lesions in liver allograft biopsies by a smartphone platform: A proof of concept. *Microsc. Res. Tech.* **83**, 1025–1031 (2020).
338. Nur, E. D. Internship Report. (2021).
339. McCracken, K. E. & Yoon, J. Y. Recent approaches for optical smartphone sensing in resource-limited settings: A brief review. *Anal. Methods* **8**, 6591–6601 (2016).

8.3. Concluding statement

340. Kwon, L., Long, K. D., Wan, Y., Yu, H. & Cunningham, B. T. Medical diagnostics with mobile devices: Comparison of intrinsic and extrinsic sensing. *Biotechnol. Adv.* **34**, 291–304 (2016).
341. Grushina, A. Direct-write grayscale lithography. *Adv. Opt. Technol.* **8**, 163–169 (2019).
342. Parisi, M. R. *et al.* Offer of rapid testing and alternative biological samples as practical tools to implement HIV screening programs. *New Microbiol.* **32**, 391–396 (2009).
343. Malamud, D. Saliva as a Diagnostic Fluid. *Dent. Clin. North Am.* **55**, 159–178 (2011).
344. Pisitkun, T., Johnstone, R. & Knepper, M. A. Discovery of urinary biomarkers. *Mol. Cell. Proteomics* **5**, 1760–1771 (2006).
345. Bolisetty, S. & Agarwal, A. Urine albumin as a biomarker in acute kidney injury. *Am. J. Physiol. - Ren. Physiol.* **300**, 626–627 (2011).
346. Wu, J. & Gao, Y. Physiological conditions can be reflected in human urine proteome and metabolome. *Expert Rev. Proteomics* **12**, 623–636 (2015).
347. An, M. & Gao, Y. Urinary Biomarkers of Brain Diseases. *Genomics, Proteomics Bioinforma.* **13**, 345–354 (2015).
348. Fukuhara, K. *et al.* NMR-based metabolomics of urine in a mouse model of Alzheimer's disease: Identification of oxidative stress biomarkers. *J. Clin. Biochem. Nutr.* **52**, 133–138 (2013).
349. Luan, H. *et al.* LC – MS-Based Urinary Metabolite Signatures in Idiopathic Parkinson ' s Disease. *J. Proteome Res.* **15**, 567–478 (2015).
350. Khan, A. Detection and quantitation of forty eight cytokines, chemokines, growth factors and nine acute phase proteins in healthy human plasma, saliva and urine. *J. Proteomics* **75**, 4802–4819 (2012).
351. Yu, X., Harris, S. L. & Levine, A. J. The regulation of exosome secretion: A novel function of the p53 protein. *Cancer Res.* **66**, 4795–4801 (2006).
352. Raposo, G. & Stoorvogel, W. Extracellular vesicles: Exosomes, microvesicles, and friends. *J. Cell Biol.* **200**, 373–383 (2013).
353. Samanta, S. *et al.* Exosomes: New molecular targets of diseases. *Acta Pharmacol. Sin.* **39**, 501–513 (2018).
354. Kanwar, S. S., Dunlay, C. J., Simeone, D. M. & Nagrath, S. Microfluidic device (ExoChip) for on-chip isolation, quantification and characterization of circulating exosomes. *Lab Chip* **14**, 1891–1900 (2014).
355. Nunnari, J. & Suomalainen, A. Mitochondria: In sickness and in health. *Cell* **148**, 1145–1159 (2012).

9. References

356. Faustini, G. *et al.* Mitochondria and α -synuclein: Friends or foes in the pathogenesis of Parkinson's disease? *Genes (Basel)*. **8**, 1–9 (2017).
357. Reeve, A. K. *et al.* Mitochondrial dysfunction within the synapses of substantia nigra neurons in Parkinson's disease. *npj Park. Dis.* **4**, 9 (2018).
358. DuBoff, B., Feany, M. & Götz, J. Why size matters - balancing mitochondrial dynamics in Alzheimer's disease. *Trends Neurosci.* **36**, 325–335 (2013).
359. Yusko, E. C. *et al.* Real-time shape approximation and fingerprinting of single proteins using a nanopore. *Nat. Nanotechnol.* **12**, 360–367 (2017).
360. Kim, M., Ha, D. & Kim, T. Cracking-assisted photolithography for mixed-scale patterning and nanofluidic applications. *Nat. Commun.* **6**, 1–8 (2015).

Publications

10. Publications

10.1 Publications in peer-reviewed journals

Mortelmans, T.; Kazazis, D.; Guzenko, V. A.; Padeste, C.; Braun, T.; Stahlberg, H.; Li, X.; Ekinci, Y. Grayscale E-Beam Lithography: Effects of a Delayed Development for Well-Controlled 3D Patterning. *Microelectron. Eng.* **2020**, 225

Mortelmans, T.; Kazazis, D.; Padeste, C.; Berger, P.; Li, X.; Ekinci, Y. Poly(Methyl Methacrylate)-Based Nanofluidic Device for Rapid and Multiplexed Serological Antibody Detection of SARS-CoV-2. *ACS Appl. Nano Mater.* **2022**.

10.2 Publications in preparation

Ayhan F.; Mortelmans T.; Ekinci Y.; Kazazis D. Dry development of poly(methyl methacrylate),

Mortelmans, T.; Kazazis, D.; Werder J.; Kristiansen P.M.; Ekinci, Y. Poly(methyl methacrylate) and cyclic olefin polymer injection molded 3D nanofluidic devices for particle sorting

Mortelmans, T.; Marty B.; Kazazis D.; Padeste, C.; Li X.; Ekinci, Y. A three-dimensional microfluidic capillary system for rapid on-bead multiplexed immunoassays in whole blood

Mortelmans, T.; Štefanić S.; Kazazis D.; Marty B.; Padeste C.; Li X.; Ekinci, Y. Multiplexed detection of cytokines in 3D nanofluidics with picomolar sensitivity

10.3 Annual reports

A venture into grayscale lithography for nanofluidic device fabrication in the context of neurodegenerative diseases

Mortelmans, T.; Kazazis, D.; Guzenko, V. A.; Padeste, C.; Braun, T.; Stahlberg, H.; Li, X.; Ekinci, Y. – SNI Annual Report 2018

Grayscale nanolithography for 3D microfluidic devices towards the diagnosis of Parkinson's disease

Mortelmans, T.; Kazazis, D.; Padeste, C.; Braun, T.; Stahlberg, H.; Li, X.; Ekinci, Y. – SNI Annual Report 2019

10.4. Poster presentations

Development of a 3D poly(methyl methacrylate) microfluidic device for biomedical applications

Mortelmans, T.; Kazazis, D.; Padeste, C.; Li, X.; Ekinci, Y. – SNI Annual Report 2020

A 3D nanofluidic device for rapid and multiplexed diagnosis: SARS-CoV-2 and Influenza antibody detection

Mortelmans, T.; Kazazis, D.; Padeste, C.; Berger P.; Li, X.; Ekinci, Y. – SNI Annual Report 2021

10.4 Poster presentations

50 shades of blue: grayscale lithography for 3D micro-structuring

Mortelmans, T.; Kazazis, D.; Guzenko, V. A.; Padeste, C.; Braun, T.; Stahlberg, H.; Li, X.; Ekinci, Y. – 2018 Nano in the Snow, Braunwald

On-chip particle size determination by 3D microfluidics

Mortelmans, T.; Kazazis, D.; Guzenko, V. A.; Padeste, C.; Braun, T.; Stahlberg, H.; Li, X.; Ekinci, Y. – 2019 Murten, Biozentrum PhD-retreat

Grayscale e-beam lithography for the fabrication of 3D microfluidics

Mortelmans, T.; Kazazis, D.; Guzenko, V. A.; Padeste, C.; Braun, T.; Stahlberg, H.; Li, X.; Ekinci, Y. – 2019 Lenzerheide, SNI Annual Event

Grayscale e-beam lithography for the fabrication of 3D microfluidics

Mortelmans, T.; Kazazis, D.; Guzenko, V. A.; Padeste, C.; Braun, T.; Stahlberg, H.; Li, X.; Ekinci, Y. – 2019 Lausanne, Swiss Nanoconvention

Nanofluidic device for rapid and multiplexed immunoassays

Mortelmans, T.; Kazazis, D.; Padeste, C.; Berger P.; Li, X.; Ekinci, Y. – Virtual, Biozentrum PhD-retreat, 2021

A PMMA-based nanofluidic device for on-chip immunoassays

Mortelmans, T.; Kazazis, D.; Padeste, C.; Berger P.; Li, X.; Ekinci, Y. – 2021 Virtual, Swiss NanoConvention

Nanofluidic device for rapid and multiplexed immunoassays

Mortelmans, T.; Kazazis, D.; Padeste, C.; Berger P.; Li, X.; Ekinci, Y. – 2021 Lenzerheide, SNI Annual Event

A 3D nanofluidic device for COVID-19 and Influenza A detection

Mortelmans, T.; Kazazis, D.; Padeste, C.; Berger P.; Li, X.; Ekinci, Y. – 2021 Montreux, NanoBioTech Montreux

10.5 Talks

Grayscale e-beam lithography for 3D microfluidics

Mortelmans, T.; Kazazis, D.; Guzenko, V. A.; Padeste, C.; Braun, T.; Stahlberg, H.; Li, X.; Ekinci, Y. – 2018, Rhodos, MNE

A 3D nanofluidic device for size-dependent particle sorting

Mortelmans, T.; Kazazis, D.; Padeste, C.; Li, X.; Ekinci, Y. – 2019, Lauenen, Nano in the Snow

Microfluidics: an interdisciplinary overview

Mortelmans, T.; Kazazis, D.; Padeste, C.; Li, X.; Ekinci, Y. – 2020, Virtual, Nano in the Snow

Thermoplastic 3D nanofluidic devices for bio-sensing

Mortelmans, T.; Kazazis, D.; Padeste, C.; Berger P.; Li, X.; Ekinci, Y. – 2021, Invited, Virtual, Polymer Replication on Nanoscale

Acknowledgements

11. Acknowledgments

“Let us be grateful to people who make us happy; they are the charming gardeners who make our souls blossom.” – *Marcel Proust*

Scientific research requires discussion, communication, creativity and collaboration. More often, it is a feat facilitated by a variety of people rather than individuals. Over the last four years, I had the absolute pleasure of working together with great scientists and amazing people. Now, as I am concluding my doctoral studies, I would like to take the opportunity to extend my gratitude and appreciation to everyone that has helped me along this path.

Firstly, I would like to thank my main supervisor **Dr. Yasin Ekinci** for the opportunity to work on this exciting and innovative project. It has laid the foundation to revolutionize immunoassays and change people’s lives. Over the course of my studies, Yasin’s office door was always open, whether it was for personal or professional discussions. When my father passed away, Yasin’s sympathy, empathy and understanding had a major impact on my life and made the grieving period a lot easier. Thank you. Yasin’s in-depth engagement in every scientific discussion had a large contribution to the success of this work. He seemingly always has novel ideas and makes creative thinking look easy. Our conversations motivated me to continuously improve as a researcher and ameliorate my work ethic, something I will take with me for the rest of my life.

Secondly, my deep gratitude goes out to my ‘colleague’ **Dr. Dimitrios Kazazis**. When starting at the Paul Scherrer Institute, I had little idea about the relevant nanofabrication processes nor their crucial parameters. It was only because of the weekly, daily and sometimes hourly discussions with Dimitrios that I was able to fabricate the 3D nanofluidic devices in my first year. He carefully introduced me to the foundations of nanofabrication, with an emphasis on e-beam lithography, and inspired me to fully immerse myself

in this fascinating discipline. Dimitrios' nanofabrication expertise was not only invaluable to my project but was the foundation for many collaborative efforts. This motivated me to always share my experience with others in an effort to help them resolve their issues: science is collaboration. On a personal level, Dimitrios has become a close friend over the last couple of years. He taught me to become not only a better researcher, but also a better person. It goes without saying that it was an absolute pleasure to work together with Dimitrios on this project.

I would also like to thank **Dr. Celestino Padeste** for all of his vital contributions to the project. More specifically, a large part of the presented work involved polymer science and surface chemistry. Celestino's experience and extensive knowledge regarding the use of polymeric materials for biosensing applications allowed us to thoroughly develop this interdisciplinary research topic. I am also very grateful for Celestino's help in learning German; something is not easy when working at an international research institute. This is something that has had and will have a profound impact on my life. Thank you.

Also, I would like to thank **Dr. Xiaodan Li**, whose optimism, bright smile and experience helped me immensely throughout the last years. Xiaodan, together with Yasin, laid the foundation for this project and defined it. It was only because of her input and interdisciplinary scientific interest that this PhD was possible. Xiaodan always was open to a quick brainstorming session and provided indispensable scientific input regarding the biological experiments. It was a pleasure to perform my PhD-research under her supervision.

My gratitude goes out towards **Dr. Philipp Berger**, who helped me in setting up all the immunoassays and fluorescence microscopy experiments to push the applications of our device for rapid and cost-effective antibody detection. Without his extensive knowledge regarding antibody-antigen interactions and fluorophore selection, this would not have been possible. It was because his

innovative ideas and approaches that we could perform multiplexed antibody detection in our devices. Moreover, if I had a question or a new experiment to run, Philipp's office door was always open to discuss.

I am grateful to **Prof. Dr. Henning Stahlberg** for being the initial University thesis supervisor and to **Prof. Dr. Roderick Lim** for taking over this role at a later stage during the project. Both offered tremendous support during my research period. I would like to specifically thank Roderick for always making me feel welcome, being open for questions and for the opportunity to work on the nucleus-on-a-chip project.

Also, I would like to thank **Dr. Thomas Braun** for his insights and ideas regarding biomedical applications of the nanofluidic particle sorter, for his administrative, scientific and personal support and encouragement. Thomas' attitude towards collaborative scientific projects had a large role in the success of this work. His insights permitted to cross the boundaries of different scientific domains. I am also gratefully indebted to **Rosemarie Sütterling** for introducing me to the basic principles of cell culturing, fluorescence microscopy and immunostaining. My gratitude extends to **Dr. Saša Štefanić** for showing me the basic principles of an ELISA-assay, discussing various aspects of immunoassays, and highlighting important aspects of an academic researcher.

I would also like to acknowledge the efforts of my second supervisor **Prof. Dr. Richard Neher and Dr. Thomas Pfohl**, as external expert. Without their valuable and insightful feedback on the thesis and research, this would not have been possible. Thank you.

I would also like to express my deepest appreciation to the **Swiss Nanoscience Institute** for their financial support and for the organization of two great annual events. Personally, I think that the SNI is one of the best institutes in which to perform PhD-research. It is a textbook example what interdisciplinary and inter-institutional research can

accomplish. To Claudia Wirth, thank you very much for the administrative support over the last few years. To Christel Möller, thank you for the outreach possibilities and making the viral video that very nicely highlighted our research. To Andreas Baumgartner, thank you for support and the interesting discussions at the poster sessions. Of course, also thank you to all the other members of the SNI-organization for making this an unforgettable experience.

Further, I would like to thank all of the scientist and **technical staff at PSI**. In particular, Eugen Deckardt, Michaela Vockenhuber, Stefan Stutz, Anja Weber, Markus Kropf, Dario Marty, Christopher Wild and Konrad Vogelsang. Without all of your knowledge regarding nanofabrication processes, many things wouldn't have been possible. I also would like to thank **Dr. Helmut Schift and Konrad Vogelsang** for all the discussion regarding nano-imprint lithography, polymer films, bonding strategies and stamp fabrication. Hot embossing has been one of the key techniques that was used over the last years and without your support, it would not have been possible to make such shallow devices with this degree of accuracy. However, before we could perform nano-imprint lithography, we had to obtain a high-quality grayscale e-beam master. This was achieved with help of **Dr. Vitaliy Guzenko** and his extensive knowledge regarding grayscale patterning.

My gratitude extends to a variety of people at the **Fachhochschule Nordwestschweiz** in Brugg. Firstly, I would like to thank **Prof. dr. Per Magnus Kristiansen** for the opportunity of exploring injection molding as an alternate device fabrication route, the nice conversations, and the Friday beers. Secondly, my gratitude extends towards **Jerome Werder** for working together on this inter-institutional program and for all the insights regarding molding techniques and processes. Lastly, I would like to thank **Agnieszka Karpik** for being the bridge between FHNW and PSI, for becoming a very close friend over these last few years and for the skiing and biking trips. I am already looking forward to your wedding!

Being an SNI PhD-student, you meet a large number of like-minded people and form meaningful friendships. That being said, I would like to thank **Dr. Luc Driencourt and Dr. Tamara 'Abenteuer'** for all the good times and exciting discussions. I could always count on you for advice, support and reminding me that there is a life outside of research. I will cherish our skiing and biking trips for many years to come. Thank you.

During my time at PSI, I was part of the Advanced Lithography and Metrology group within the Laboratory of Micro – and Nanotechnology. My gratitude and appreciation go out to all the current and former **group members** for the stimulating and motivating scientific discussions. Thank you to Dr. Iacopo Mochi, Dr. Uldis Locans, Atoosa Dejkameh, Dr. Ricarda Nebling, Dr. Prajith Karadan, Dr. Hyun-Su Kim, Dr. Peng Tian, Dr. Deepika Sharma, Dr. Mohammed Saifullah, Corinna Burri and Dr. Jan Ravnik.

It was my pleasure to share **the office** with a large variety of people. Thank you to Dr. Rajeev Rajendran, Dr. Li-Ting Tseng, Dr. Zuhail Tasdemir, Dr. Sara Fernandez Fernandez, Chia-Kai Yeh, Dr. Xiaolong Wang and Dr. Iason Giannopoulos for the conversations, support, laughs and insights. My special thanks go out to **Tao Shen** for being my fellow 'Brugger' in the office and always being up for a beer, hike or bike trip. Also, to resident snowboarder **Dr. Timothée 'Yellow Shirt' Allenet**, I would like to say thank you for all the fun times together. Your attitude towards life and never-ending positivity is inspiring.

I also had the honor of mentoring and supervising three great young scientists who will no doubt have beautiful and extraordinary careers ahead of them. Thank you **Furkan Ayhan, Balz Marty and Elif Dayi Nur** for sharing parts of this experience with me.

"Keep the ones that heard you when you never said a word". I think that quote very nicely exemplifies the tremendous support I've received from my friends back in Belgium. Even though we didn't see each other frequently in the last couple of years, they always kept in touch, and more than once, came for a visit. Consequently, I've also been Mt. Rigi more than ten times... My special thanks go to **S.C. H.O.C.K.E.Y.** and **De Zuipers**. Hockey provided me with a still ongoing connection to my previous Alma Mater, while simultaneously keeping me involved in an abundance of leisurely activities. Thank you. De Zuipers, or also known as **Ferre, Yannick, Ine and Andreas**, I would like to thank for the joyful conversations, late nights, and being there for me in my hour of need. I am looking forward to spending more time together.

I would also like to thank my **family** for their support during these past few years:

Thank you to my mother, **Kathleen Hubrechts**, for the continuous encouragement throughout my years of study, for always allowing me to chase my dreams and desires and for giving me the opportunity to learn and continuously develop. This accomplishment would not have been possible without you. I know me moving to Switzerland was not easy for you, but you always allowed and encouraged me to follow my passion and interest. Thank you for being the most loving, caring, understanding and supporting mother one could wish for. *Love you hé, ciao*

Thank you to my father, **Steven Mortelmans**, for being a key driving factor behind my success. Your positivity and interest in my doctoral studies always drove me to be the best version of myself. Your pride for what I achieved made me hungry for more and larger success stories. It gave me the necessary motivation and confidence to be a dream-chaser. Even though you are not here with us now, I felt your warmth during the difficult times and your support when making tough decisions. Thank you for being my father. May our path's cross again. *Ma alé Thomas*

Thank you to my siblings, **Michiel and Marie Mortelmans**, for being the best brother and sister one could dream of and being so supportive of my decisions. It has been my absolute pleasure to grow up together with you and I am looking forward to seeing how we grow up together in the future. To more memories together. *Kom e pie - Balou is ni dik*

Thank you to my grandmother, **Jaja**, for all the love and support growing up. For all your advice, wisdom and for your encouragement to tackle this challenge head-on with determination. *Ich ben zoewe bliji dè ge hie ziet en veur dezze iene kier, gen eirmke geiven hé*

Lastly, my most profound gratitude goes out to my girlfriend, **Lotte Jaeken**, for without you this would not have been possible. Your love, attention, unwavering support and caring personality helped me tremendously during the past few years. It still amazes me how fast the last four years went by. I still remember how I told you that I wanted to apply for a PhD-position in Switzerland. Even then, you were immediately supportive. You moved to a foreign country, without knowing the language, without expressing any doubt. Thank you for your trust and for chasing our dreams together. This accomplishment is as much mine as it is yours. Also: *See you up!*

だってばよ - Dattebayo - Believe



THOMAS MORTELMANS

DEVELOPING NOVEL SOLUTIONS FOR UNMET NEEDS TO IMPROVE THE WELL-BEING OF HUMAN KIND

- Passionated by health care, science and innovation
- Comfortable with change and do well in uncertainty
- Motivated by opportunities and challenges
- Language fluency in German, English and Dutch

PROFILE

Goal Oriented & Entrepreneurial Mindset
 Excellent academic track record
 High Ethical Standards - Diversity & Inclusion
 Multi-Country Experiences (EU & OC)
 Courageous, Curious & Creative
 Critical Thinker
 Quick Learner
 Team Player
 Humble
 Agile & Resilient
 Independent & Decisive

SKILLS

Data analysis & visualization
 Combining Science and Business
 Document review - Patents / Scientific Papers
 Science and Technology
 Technical Software & Writing
 Stakeholder Management
 Multi-Lingual
 Analytical testing & characterization
 Coding - Python
 Interdisciplinary Communication
 Problem Solving & Time Management

CONTACT

NATIONALITY: BELGIAN
D.O.B.: 30.11.1994
PHONE: +41(0) 76 343 72 53
MAIL
 thomasmortelmans94@gmail.com
ADDRESS
 Dahlienstrasse 9
 5200 Brugg AG, Switzerland

EXPERIENCE

Sept. 2018-
Aug. 2022



PHD STUDENT - POINT-OF-CARE DIAGNOSTICS

UNIVERSITY OF BASEL - SWITZERLAND
ADVANCED LITHOGRAPHY & METROLOGY - PAUL SCHERRER INSTITUTE

- Fabrication of polymer point-of-care diagnostic devices - incl. **design and validation**
- **Cost optimization** of device fabrication - from 3k CHF to 5 CHF
- Material functionalization - incl. quality control of **raw materials & manufactured devices**
- Python for **data** processing and analysis - image analysis, **statistics &** reporting
- Technical documentation - Reports and scientific publications
- Physical and chemical device **characterization** and optimization
- Co-Inventor of two diagnostic **patents** - from ideation to application (Tech Transfer)
- **Mentored** three master thesis students - Robotics / Bio-Eng. / Microtechnology

BIOZENTRUM - UNIVERSITÄT BASEL

- Quantitative fluorescence microscopy
- Optical **sensing** in various biological samples - whole blood & serum

July 2018



MERCK INNOVATION CUP - TEAM LITHOGRAPHY

INNOVATION INCUBATOR - MERCK KGAA

- Conceptualization of a novel **quality control** method
- **Pitching** of scientific ideas in a highly competitive environment
- Product pipeline: Discovery - Development - Market introduction
- Transferring **academic projects to industry**
- Selected out of 3000+ Ph.D. level applicants - **Top 2%**

Nov. 2017-
May, 2018



MASTER THESIS - NANO DRUG DELIVERY FOR STEM CELLS

INSTITUTE FOR MATERIALS RESEARCH (IMO) - BELGIUM

- Chemical **analysis** with FT-IR spectroscopy
- Physical analysis - Dynamic Light Scattering
- **Sterilization** of drug delivery nanoparticles (Gamma-radiation)
- Human anatomy & physiology
- Toxicity studies of primary human dental pulp stem cells

Sept. 2017-
Aug. 2019



PRODUCT INVENTION AND DEVELOPMENT - CLOUDY GIN

ALL INCLUDES EVENT MANAGEMENT

- **Product launch**
- Sales operations
- **Marketing** and advertising strategies
- Customer creation
- **Regulatory** requirements

Sept. 2015-Aug. 2016
Sept. 2017-Aug. 2018



PRESIDENT OF STUDENT ORGANIZATION

- Administrative relationships with college facilities and local government
- General **management** of the organization - Leadership
- Coordination of large scale events (2000+ attendees)
- **Financial planning** - including subsidies, fundraising and taxes

Aug. 2012-
Aug. 2013




ROTARY EXCHANGE STUDENT: BELGIUM - AUSTRALIA


- Youth ambassador for Rotary Belgium in rural Australia
- **Voluntary services** in construction, food distribution and **health-care fundraising**
- **Culturally diverse** environment
- Advanced English course

EDUCATION


- 2018-PRESENT




Doctorate of Philosophy
Swiss Nanoscience Institute - University of Basel, Switzerland
 Ph.D. Project on the Interface of Physics, Chemistry, Material Science And Biomedicine
- 2016-2018




Master of Biomedical Sciences - Bio-electronics and Nanotechnology, MSc
Hasselt University - Diepenbeek, Belgium
 Academic Master - Grade 7 of Flemish Education System
- 2013-2016



Bachelor of Biomedical Sciences - BSc
Hasselt University - Diepenbeek, Belgium
 Academic Bachelor - Grade 6 of Flemish Education System
- 2012-2013

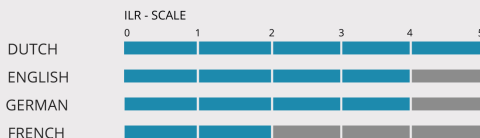


Year 12 - Advanced Mathematics, Narrabri High School
 Narrabri, New South Wales, Australia
- 2006-2012



Economics and Modern Languages (Dutch, English, German and French)
Sint-Janscollege - Meldert, Belgium
 Includes certificate of **Business Management**

LANGUAGES



AWARDS & PUBLICATIONS

- Best Poster Prizes**

 - 2021 NanoBioTech Montreux Conference
Title: "A 3D Nanofluidic Device for COVID-19 and Influenza-A Detection"
 - 2021 Annual Event of The Swiss Nanoscience Institute
Title: "Nanofluidic Device for Rapid and Multiplexed Immunoassays"
 - 2019 Annual Event of The Swiss Nanoscience Institute
Title: "Grayscale E-beam Lithography for the Fabrication of 3D Microfluidics"
 - 2019 Ph.D. Retreat of The Biozentrum - University of Basel
Title: "On-Chip Particle Size Determination By 3D Microfluidics"
-
- Talks**
- Invited Talk at the Polymer Replication on Nanoscale Conference 2021**
Best Talk as Young Scientist
Title: "Thermoplastic 3D Nanofluidic Devices for Biosensing"
 - Nano In The Snow Ph.D. School 2021 - Swiss Nanoscience Institute**
Best Talk Award
Title: "Microfluidics: an interdisciplinary overview"
 - Conference on Micro- and Nano-Engineering (MNE) - Rhodos, Greece**
Title: "Grayscale E-beam Lithography for the Fabrication of 3D Microfluidic Devices"
- Various**

 - Innovation Workshop - University of Basel
Best Start-up Pitch
Title: "MognoCell: Enabling the next-generation of fuel-cells"
-
- Selected first-author publications**
- Grayscale E-beam lithography: Effects of a delayed development for well-controlled 3D patterning**
Microelectron. Eng. 2020, 225 (November 2019), 111272.
 - Poly(Methyl Methacrylate)-based Nanofluidic Device for Rapid and Multiplexed Serological Antibody Detection of SARS-CoV-2**
Acs Applied Nanomaterials - DOI: 10.1021/ACSANM.1C03309
 - A Three-Dimensional Microfluidic Capillary for Rapid On-Bead Immunoassays in Whole Blood**
Manuscript in preparation

REFERENCES

References can be provided upon request

Appendix

13. Appendix

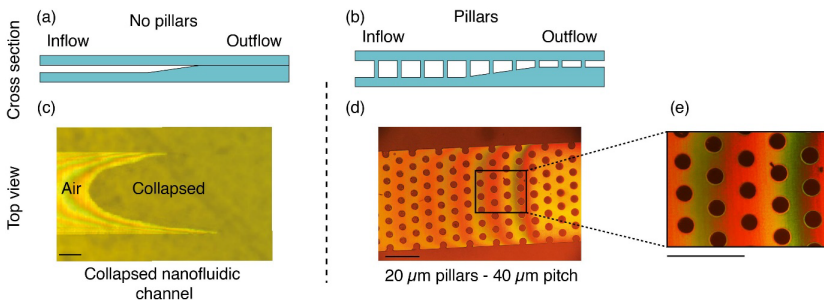


Figure S1. Light microscopy images evidencing the role of supporting pillars for successful uncollapsed bonding in a 3D nanofluidic device with an outflow of 500 nm. **a**, the cross-section of a collapsed nanofluidic channel without supporting pillars and associated top view light microscopy image shown in **b**, **c**, a cross-section of a nanofluidic channel containing supporting pillars with 20 μm pillars and a 40 μm pitch and the corresponding light microscopy image in **d**, with a zoomed-in section shown in **e**. Scale bars represent 100 μm .

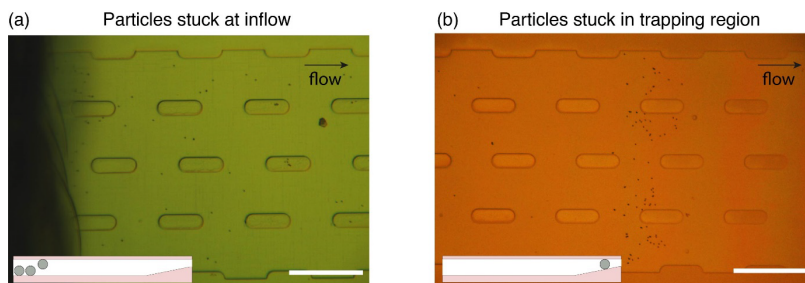


Figure S2. Influence of PVA on the non-specific binding of streptavidin-coated Dynabeads MyOne T1 in a 3D nanofluidic device with supporting lines. **a**, Sticking of Dynabeads MyOne T1 to non-functionalized PMMA. **b**, Trapping of Dynabeads MyOne T1 in a functionalized device. The scale bars represent 100 μm .

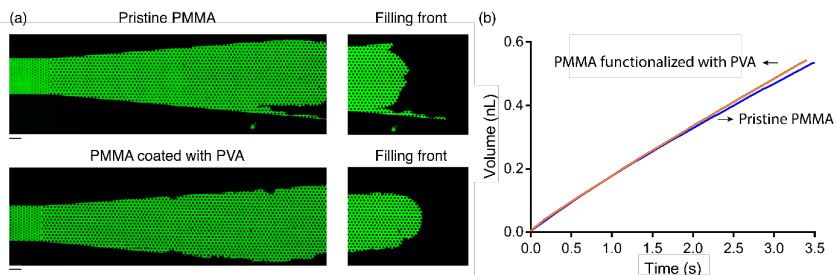


Figure S3. Filling of the capillary pump and connecting wedge region of devices with and without PVA functionalization. **a**, ATTO 448 filled section of the capillary pump and connecting wedge with associated filling fronts **b**, Filling volume as a function over being loaded into the capillary pump section. This was determined using the Skimage Python package in conjunction with Pandas and NumPy. The scale bar represents 50 μm .

Table S1. The nominal particle diameter in comparison to the calculated diameter according to the linear regression curve of the 3D nanofluidic device. The associated coefficient of variation for both mean particle diameters is given between brackets. N.A. signifies missing supplier information.

Nominal diameter (μm)	3.16 (3%)	2.12 (1%)	1.74 (1%)	1.03 (1%)	0.9 (N.A.)
Calculated diameter (μm)	3.16 (1,8%)	2.15 (2,7%)	1.67 (4,6%)	1.06 (4,4%)	0.9 (3,9%)

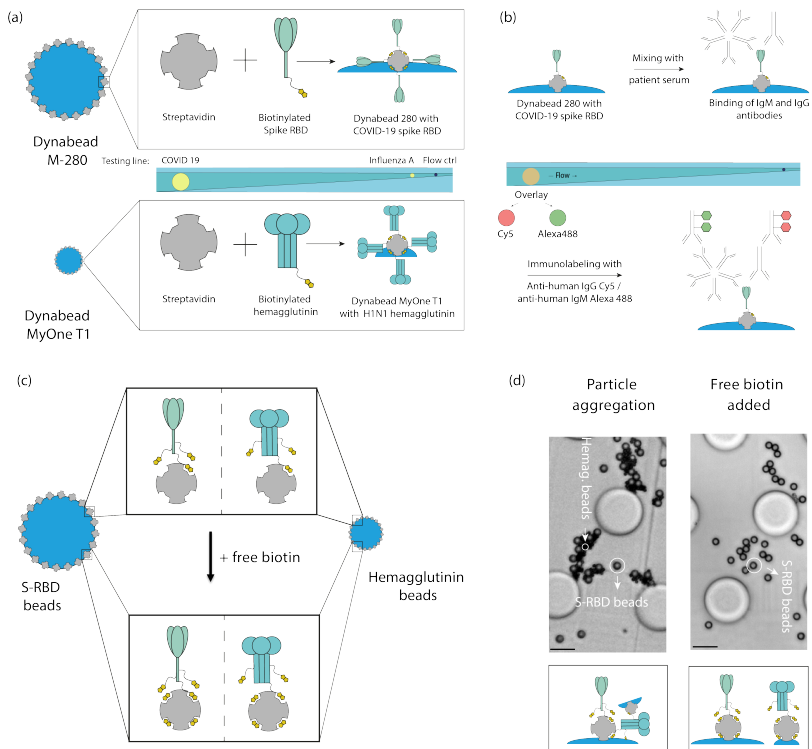


Figure S4. Conceptual drawing illustrating the on-chip multiplexing concept of simultaneous detection of IgG and IgM antibodies and disease multiplexing. **a**, Top: functionalization of streptavidin-coated Dynabeads M-280 with the receptor-binding domain (RBD) of the spike protein. The entire trimeric protein with only one biotin moiety is drawn for simplification purposes. Middle: Schematic illustrating the on-chip disease multiplexing principle by using the two different sizes of Dynabeads. Bottom: The smaller Dynabeads MyOne T1 beads are similarly functionalized with a biotinylated hemagglutinin protein (Influenza A H1N1/California/2009). **b**, Top and bottom: Schematic representation of the color multiplexing principle for simultaneous detection of IgG and IgM antibodies. Middle: Cross-sectional sketch showing trapped Dynabeads 280 and 0.9 μm flow control calibration beads. **c**, Schematic illustrating the influence of free-biotin added during the blocking step on the available biotin-binding sites. **d**, 40x microscopy images of the Dynabead M-280 trapping line, with no free-biotin added (left) and free biotin added (right). The scale bars represent 10 μm.

